



TECHNISCHE
UNIVERSITÄT
WIEN

Dissertation

**Mechanistic Studies on $\text{TiO}_2\text{-SiO}_2$
Core-shell Nanoparticles for
Photocatalytic Hydrogen Production
and Degradation of Organics**

carried out for the purpose of obtaining the degree of

Doctor rerum naturalium (Dr. rer. nat.),

submitted at TU Wien, Faculty of Chemistry, by

Ariane Giesriegl M.Sc.

Matr.Nr.: 00726700

under the supervision of

Univ.Prof. Dr. Dominik Eder

Wien, am October 15, 2021

Name of Reviewer 1: Prof. Dr. **Roland Marschall**
Lehrstuhl Physikalische Chemie III
Universität Bayreuth
Universitätsstraße 30, 95440 Bayreuth, Deutschland

Name of Reviewer 2: Univ.Prof Dr. **Jürgen Fleig**
Instituts für Chemische Technologien und Analytik
Technische Universität Wien
Getreidemarkt 9/164, 1040 Wien, Österreich

Human beings always do the most intelligent thing
... after they've tried every stupid alternative and none of them have worked.

- R. Buckminster Fuller



Die approbierte gedruckte Originalversion dieser Dissertation ist an der TU Wien Bibliothek verfügbar.
The approved original version of this doctoral thesis is available in print at TU Wien Bibliothek.

Abstract

Oil, coal and gas together account for the majority of global primary energy consumption and they are projected to remain the dominant energy source until at least 2050. These fuels, however, impose serious pollution and emissions that impose a growing strain on both our economy and environment. Therefore, we need alternative solutions that provide sustainable fuels from renewable energy sources. We also need better strategies to protect our environment, such as converting organic waste in air and water to harmless chemicals. Photocatalysis can provide a solution to both of these challenges; it promises an efficient purification of air and water as well as the production of hydrogen and solar fuels via light-assisted water splitting and conversion of organic compounds.

The aim of this thesis was to modify TiO₂-based photocatalysts and to investigate the mechanisms and deactivation kinetics during photocatalytic degradation of organic molecules and sacrificial hydrogen evolution. For this, I converted TiO₂ nanoparticles into core-shell nanostructures through the deposition of ultrathin layers of an insulating metal oxide (SiO₂) with tuneable thickness in the range of 0 to 1 nm. The film thickness and uniformity, interfacial and surface properties as well as charge separation dynamics and charge transfer properties and were studied with a range of state-of-the-art techniques.

In the first part, the deposition of SiO₂ has enabled the direct tuning of the kinetics and selectivity towards degradation of differently charged organic dyes, by modifying the adsorption characteristics and accessibility of active Lewis sites. It was also possible to extract the respective rate limiting processes for different thickness regimes.

In the second part, I investigated the early-stage deactivation phenomenon during hydrogen evolution reaction (HER) that was recently discovered for TiO₂ photocatalysts modified with Pt nanoparticles. I investigated the mechanism for different process conditions (type of sacrificial agent, Pt content, deposition method) and used the core-

shell strategy to uncover the origins for deactivation. The results show that the choice of deposition method plays a key role as it affects the dispersion and amount of the adsorbed Pt precursor, the Pt reduction kinetics and the initial size of the Pt nanoparticles, and – consequently – both the kinetics and the extent of deactivation. Moreover, I demonstrated that it is possible to minimize the deactivation with one monolayer of SiO₂ shell while retaining a high charge transfer efficiency to the adsorbed reactant molecules.

In the third part, I introduced nanocavities (< 1nm) into the SiO₂ shells on TiO₂. Preliminary studies showed that these cavities allowed for highly size-selective degradation of primary and secondary alcohols. Moreover, this strategy can be used to distinguish between a direct and indirect charge transfer-based oxidation mechanism of sacrificial agents during HER. Future studies are required to increase the activity for better results, to correlate reaction kinetics and selectivities with the number and topology of these nanocavities and to analyze intermediates for understanding the overall reaction mechanism.

Zusammenfassung

Öl, Kohle und Gas sind die Energieträger des weltweiten Primärenergieverbrauchs und werden voraussichtlich bis 2050 bleiben. Diese Energieträger verursachen jedoch ernsthafte Verschmutzungen, besonders CO₂ Emissionen, die die Umwelt nachhaltig belasten. Wir brauchen daher alternative Lösungen, die Energieträger aus erneuerbaren Quellen bereitstellen. Zusätzlich brauchen wir effizientere Strategien um organische Abfälle in Luft und Wasser in harmlose Chemikalien umzuwandeln. Photokatalyse bietet Lösungen für beide Herausforderungen; es verspricht eine effiziente Reinigung von Luft und Wasser sowie die Herstellung von Wasserstoff durch photo-unterstützte Wasserspaltung und Umwandlung organischer Stoffe.

Das Ziel dieser Arbeit war es, TiO₂-basierte Photokatalysatoren zu modifizieren und die Mechanismen und Deaktivierungs-Kinetiken während des photokatalytischen Abbaus organischer Moleküle und der Entwicklung von Wasserstoff zu untersuchen. Dazu habe ich TiO₂-Nanopartikel mit ultradünnen Schichten von SiO₂ mit einstellbarer Dicke zwischen 0 und 1 nm modifiziert, um sogenannte Kern-Schale-Nanopartikel zu erstellen. Die Filmdicke und Homogenität, Grenzflächen- und Oberflächeneigenschaften, sowie die Ladungstrennungsdynamik und Ladungsleitfähigkeit durch die Schicht wurden mit einer Reihe modernster Techniken untersucht.

Im ersten Teil konnte ich mit der SiO₂ Schicht die Kinetik und Selektivität während des photokatalytischen Abbaus geladener Farbstoffe bestimmen, indem die Adsorptionsgleichgewichte und Zugänglichkeit zu aktiven Lewis-Zentren beeinflusst wurden. Es war auch möglich die geschwindigkeitsbestimmenden Prozesse für verschiedene Schichtdicken zu bestimmen.

Im zweiten Teil untersuchte ich das Deaktivierungs-Phänomen, das im frühen Stadium der Wasserstoffentwicklung mit Pt-Nanopartikel modifizierten TiO₂ Photokatalysatoren entdeckt wurde. Ich habe den Mechanismus für verschiedene Prozessbedingungen (Art des Lochfängers, Pt-Gehalt, Pt-Abscheidungsmethode) untersucht und die Kern-

Schale-Partikel verwendet, um die Ursachen für die Deaktivierung aufzudecken. Die Ergebnisse zeigen, dass die Wahl der Abscheidungsmethode eine Schlüsselrolle spielt, da sie die Dispersion und Menge der adsorbierten Pt-Vorstufe, die Pt-Reduktionskinetik und die anfängliche Größe der Pt-Nanopartikel und – folglich – sowohl die Kinetik als auch das Ausmaß der Deaktivierung beeinflusst. Darüber hinaus habe ich gezeigt, dass es möglich ist, die Deaktivierung mit einer Monolage der SiO₂-Schale zu minimieren und gleichzeitig eine hohe Ladungstransfereffizienz auf die adsorbierten Reaktanden-Moleküle beizubehalten.

Im dritten Teil habe ich Nanolöcher (< 1nm) in die SiO₂-Schalen auf TiO₂ eingebaut. Vorläufige Studien zeigten, dass diese Löcher einen gröbenselektiven Abbau von primären und sekundären Alkoholen ermöglichten. Darüber hinaus kann diese Strategie verwendet werden, um zwischen einem direkten und einem indirekten Ladungstransferbasierten Oxidationsmechanismus von Lochfängern während der HER zu unterscheiden. Zukünftige Studien sind erforderlich, um die Aktivität für bessere Ergebnisse zu erhöhen, Reaktionskinetiken und Selektivitäten mit der Anzahl und Topologie dieser Nanolöcher zu korrelieren und Zwischenprodukte zu analysieren, um den Gesamtreaktionsmechanismus zu verstehen.

Contents

Abstract	iii
Zusammenfassung	v
Table of Contents	ix
Lists of Abbreviations, Figures and Tables	xi
1 Motivation	1
2 Introduction	3
2.1 Photocatalysis	3
2.1.1 Classification of devices and clarification of terms	3
2.1.2 The sun as an energy source	5
2.1.3 Combustion of harmful organic molecules	6
2.1.4 Hydrogen as renewable energy source	7
2.2 Materials requirements	9
2.2.1 Semiconductors as photocatalysts	10
2.2.2 TiO ₂ as photocatalyst	13
2.2.3 The co-catalyst Pt	14
2.3 Core-shell TiO ₂ – SiO ₂ particles	17
2.3.1 Core-shell particles in photocatalysis	17
2.3.2 TiO ₂ – SiO ₂ core-shell particles	18
2.3.3 Ultrathin layers of SiO ₂ on TiO ₂	19
2.3.4 Nanocavities in an SiO ₂ shell	22
3 Methodology	25
3.1 Synthesis and preparation	25
3.1.1 Synthesis of ultrathin shells	25

3.1.2	Synthesis of nanocavities	31
3.2	Used chemicals	33
3.3	Characterization	34
3.3.1	Transmission electron microscopy	34
3.3.2	Energy-dispersive X-ray spectroscopy	35
3.3.3	X-ray photoelectron spectroscopy	35
3.3.4	Total reflection X-ray fluorescence	36
3.3.5	Small angle X-ray scattering	37
3.3.6	Infrared spectroscopy	38
3.3.7	UV-vis spectroscopy	39
3.3.8	Zeta potential	41
3.3.9	Physisorption studies	43
3.3.10	Thermogravimetric analysis	44
3.4	Photocatalytic experiments	45
3.4.1	Organic dye degradation	45
3.4.2	Online HER experiments	47
3.4.3	Size selective hole scavenging	51
4	Preliminary studies	53
4.1	Characterization of core-shell nanoparticles	53
4.1.1	Shell thickness and surface properties	53
4.1.2	Nature of the interface and the electronic structure	65
4.2	Characterization of nanocavities samples	73
4.2.1	Quantifying the amount of calixarenes on the TiO ₂ surface	73
4.2.2	Spectroscopic measurements of calixarenes on the TiO ₂ surface	76
4.2.3	Characterization of the nanocavity containing core-shell TiO ₂ -SiO ₂ particles	77
4.3	Influence of parameters on HER	79
4.4	Oxygen evolution reaction	90
4.5	Reproducibility of the photocatalytic systems	92
5	Rate limiting steps of dye degradation	95
5.1	Introduction	95
5.2	Adsorption and degradation studies	97
5.3	Conclusion	103

6	Deactivation during HER	105
6.1	Introduction	105
6.1.1	Methanol oxidation mechanism	106
6.1.2	Strong Metal-Support Interaction	109
6.1.3	Nature of the Pt co-catalysts	112
6.1.4	Summary	115
6.2	Deactivation with Pt/TiO ₂ –SiO ₂	116
6.2.1	Reasons for the decrease in activity with the introduction of an SiO ₂ layer	120
6.2.2	Reasons for the decrease of the ESD with the introduction of an SiO ₂ layer	124
6.3	Conclusion & Outlook	152
7	Size selective hole scavenging	155
7.1	Size selection properties of the nanocavities	157
7.2	Size selection of sacrificial agents during HER	159
7.3	Conclusion and Outlook	162
	Bibliography	165
	Appendix	191
	Acknowledgements	203
	CV	205



Die approbierte gedruckte Originalversion dieser Dissertation ist an der TU Wien Bibliothek verfügbar.
The approved original version of this doctoral thesis is available in print at TU Wien Bibliothek.

List of Abbreviations

aCN	Acetonitrile
AHP	Alkaline Hydrogen Peroxide
Ana	Anatase
ATR(-FTIR)	Attenuated Total Reflection Fourier Transform Infrared Spectroscopy
a.U.	Arbitrary Units
BET	Brunauer-Emmer-Teller
BJH	Barret-Joyner-Halenda
DI	Deionized (water)
DRS	Diffuse Reflectance Spectroscopy
EDX	Energy-Dispersive X-ray Spectroscopy
EFTEM	Energy Filtered Transmission Electron Microscopy
EN	Electronegativity
ESD	Early-Stage Deactivation
GC	Gas Chromatography
HER	Hydrogen Evolution Reaction
IEP	Isoelectric Point
IR	Infrared
LED	Light Emitting Diode
MB	Methylene Blue
MF	Methyl Formate
MO	Methyl Orange
NP	Nanoparticle
OER	Oxygen Evolution Reaction
OTS	Octadecyltrichlorsilane
PC	Photocatalysis
PD	Photodeposition
PL	Photoluminescence Spectroscopy
SA	Sacrificial Agent

Contents

SSA	Specific Surface Area
SAM	Self-Assembled Molecule
SAXS	Small Angle X-Ray Scattering
SG	Sol-gel
SMSI	Strong Metal-Support Interaction
SP	Salt Precipitation
TA	Terephthalic Acid
TAOH	2-Hydroxyterephthalic Acid
TGA	Thermogravimetric Analysis
TEM	Transmission Electron Microscopy
TEOS	Tetraethoxysilane
TPS	Triple-Phase Boundary
TXRF	Total Reflection X-ray Fluorescence
XPS	X-Ray Photoelectron Spectroscopy
UV	Ultraviolet
US	Ultrasonication
Vis	Visible (light)
WI	Wetness Impregnation
QY	Quantum yield
ZP	Zeta Potential

List of Figures

2.1	Energetics of catalytic and synthetic reactions	4
2.2	Solar spectrum	6
2.3	Pourbaix diagram for water	8
2.4	Mechanistics steps in photocatalysis	10
2.5	Band potentials of semiconductors	11
2.6	Semiconductor doping and bandgap transitions	12
2.7	Anatase unit cell and HER on Pt/TiO ₂	13
2.8	Band bending	15
2.9	Layer growth models	19
2.10	Sol-gel and molecular self-assembly growth	21
2.11	Grafting of templates onto TiO ₂	23
3.1	X-ray measurement techniques	37
3.2	optical spectroscopy techniques	40
3.3	Zeta Potential	42
3.4	Setup of the organic dye degradation setup	46
3.5	Setup of the online HER setup	47
3.6	Setup of the size selective HER setup	51
4.1	TEM graphs of SP samples.	56
4.2	TEM images of SAM and SG samples.	57
4.3	TEM images of SG samples set 1	59
4.4	TEM images of SG samples set 2	62
4.5	Zeta Potential	64
4.6	Tauc plots	65
4.7	ATR-FTIR spectra	66
4.8	XPS of SG samples set 1	68
4.9	XPS of SG samples set 2	69

List of Figures

4.10	Photoluminescence lifetime studies	70
4.11	Photoluminescence studies	73
4.12	TGA: Calixarene coverage	74
4.13	TGA: Calixarene coverage	75
4.14	Spectroscopy: Calixarene coverage	76
4.15	TEM graphs of NC samples.	77
4.16	HER reproducibility: Methanol and Pt source and lamp controllers	79
4.17	HER reproducibility: Pt addition and ultrasonication	80
4.18	HER reproducibility: Water cooling temperature	81
4.19	HER: Amount of catalyst	82
4.20	HER: Longterm studies	83
4.21	HER reproducibility: Pt amount, ultrasonication, on anatase and rutile	84
4.22	TEM images of Rutile and Anatase with 0.2 and 1.0 wt.% Pt	86
4.23	HER of P25 and anatase:rutile 8:2	87
4.24	Oxygen evolution reaction	90
4.25	HER reproducibility: Two batches of anatase	92
4.26	Reproducibility of the size selective HER setup	94
5.1	Degradation mechanisms of MB and MO	96
5.2	Adsorption studies of MB and MO	98
5.3	PC degradation of MO	99
5.4	PC degradation of MB	101
5.5	Dye degradation conclusion	104
6.1	Longterm HER with 0.2 and 1.0 wt.% Pt on anatase	108
6.2	Strong metal-support interaction	109
6.3	Surface energies and work functions of transition metals	111
6.4	Pt stability on TiO ₂	114
6.5	HER of core-shell samples	118
6.6	TEM images of Pt/core-shell samples	120
6.7	Pt deposition on core-shell TiO ₂ – SiO ₂	121
6.8	HER of core-shell samples normalized to the Pt surface area	123
6.9	HER activity decrease conclusion	123
6.10	HER, CO ₂ and CO evolution of core-shell samples	124
6.11	HER, CO ₂ and CO evolution of core-shell samples with different SAs	125
6.12	Methanol oxidation mechanism conclusion	127

6.13	HER over core-shell samples with and without nanocavities	128
6.14	TEM of anatase and nanocavities containing samples after HER	129
6.15	Longterm HER with 0.2 and 1.0 wt.% on TS0 and TS2	131
6.16	TEM images of 0.2 wt.% Pt/TS0 and Pt/TS2 samples	132
6.17	TEM images of 1.0 wt.% Pt/TS0 and Pt/TS2 samples	133
6.18	SMSI and agglomeration conclusion	137
6.19	HER, CO ₂ and CO evolution of TS0 with different Pt deposition methods	139
6.20	TEM images of 0.2 wt.% on Pt/TS0 with WI	140
6.21	Pt deposition on TS0 conclusion	141
6.22	HER, CO ₂ and CO evolution of TS2 with different Pt deposition methods	142
6.23	TEM images of 0.2 wt.% on Pt/TS2 with WI	142
6.24	Pt deposition on TS2 conclusion	143
6.25	Electron affinity and work function of Pt	145
6.26	Pt deposition on TS2 conclusion	147
6.27	Pt deposition on TS2 conclusion	149
6.28	ESD conclusion	150
7.1	Nanocavities in a shell of a core-shell sample	156
7.2	FTIR spectra of nonanol	157
7.3	Conversion of nonanol	159
7.4	Conversion of nonanol	160
7.5	Size-selective HER with 5% SA and different amounts of H ₂ O	160
7.6	Size-selective HER with 1% and 5 mM of SA	161
A.1	TEM images of SG samples after upscaling	191
A.2	Photoluminescence emission spectra	192
A.3	Photoluminescence fit	192
A.4	EDX spectrum	193
A.5	XPS survey spectra set 1	195
A.6	XPS survey spectra of sample set 2	195
A.7	N ₂ physisorption isotherms and t-plots of sample set 1	197
A.8	N ₂ physisorption isotherms and t-plots of sample set 2	199
A.9	Spectroscopy: Original NC samples DRS UV-vis data	200
A.10	Spectroscopy: Original SG samples DRS UV-vis data	200



Die approbierte gedruckte Originalversion dieser Dissertation ist an der TU Wien Bibliothek verfügbar.
The approved original version of this doctoral thesis is available in print at TU Wien Bibliothek.

List of Tables

3.1	Sample list - Core-shell samples	30
3.2	Sample list - Calixarene samples	32
3.3	Sample list - Nanocavities samples	32
3.4	Used chemicals	33
4.1	Physical properties of SP, SAM and SG samples	56
4.2	Physical properties of SG samples set 1	58
4.3	Physical properties of SG samples after upscaling	61
4.4	Physical properties of SG samples set 2	63
4.5	Photoluminescence lifetimes	71
4.6	0.2 and 1.0 wt.% Pt NPs size after HER over rutile and anatase	86
4.7	HER activity of anatase, rutile, P25 and anatase:rutile 8:2	88
5.1	Physical properties of SG samples set 1	97
5.2	Rate constants of PC degradation of MO and MB	102
6.1	Physical properties of SG samples set 2	117
6.2	HER activities normalized to Pt	122
6.3	H ₂ , CO ₂ and CO with different SAs	126
6.4	Deactivation of in-situ PD 0.2 and 1.0 wt.% Pt over TS0 and TS2	134
6.5	Deactivation of 0.2 wt.% Pt deposited in-situ PD and WI over TS0 and TS2	144
A.1	XPS of SG samples set 2	194
A.2	Pt amount and surface area	201
A.3	HER activities of SG sample set 2	202
A.4	HER activities of SG sample set 2	202



Die approbierte gedruckte Originalversion dieser Dissertation ist an der TU Wien Bibliothek verfügbar.
The approved original version of this doctoral thesis is available in print at TU Wien Bibliothek.

1 Motivation

The onset of the industrial revolution in the early 1900s led to a broad range of pollution, i.e. the introduction of contaminants into the environment, which accumulate in the air, water, land and biological organisms.¹ Technological advancements and a growing consumption led to large scale production and an increase in long-distance transportation, which destroy natural habitats and emit unprecedented amounts of pollutants, such as greenhouse gases, synthetic chemicals, heavy metals and crude oil. The consequences are manifold and drastic; the loss of habitat and the accumulation of harmful substances has led to a catastrophic decline in wildlife population, while the emission of greenhouse gases led to a change in climate that has developed into a climate crisis.²⁻⁴

Technologies to reduce pollution, such as the use of renewable energy, sustainable building or waste reduction, are available; however, they are either not applied due to limitations in cost, geography, reliability or education; or their application is neither efficient nor sustainable enough to tackle the challenges set by several intergovernmental treaties and non-governmental organizations;⁵ such as the Paris agreement, that plans to limit the global temperature increase to 1.5°C; or the WWF calling for action to end the destruction of natural habitats and reforming our food production methods.^{4,6}

Scientific development is important to drive the efficiency, sustainability, reusability and applicability of technologies to reduce pollution from the energy and production demands of the rising human population. Especially photocatalysis is a promising approach that is often not yet efficient enough to be applied at a large-scale level. To eliminate these limitations, we work towards a better understanding of the underlying mechanisms and catalysts requirements, to apply more sustainable materials and systems.

Specifically, I research model systems to unravel the limitations in activity caused by the surface properties, charge carrier behavior, nature of the co-catalyst, and so on.

1 Motivation

By changing the surface of a model photocatalyst with the introduction of an ultrathin isolating SiO₂ shell, it is possible to investigate differences in the activity and correlate them to the characteristics of the catalyst, which were analyzed in with a plethora of methods. One motivation of this thesis was to unravel the rate limiting steps during combustion of toxic dyes, to design catalysts that increase the combustion efficiency. The second motivation was to investigate the cause for the unstable behavior of the model catalyst Pt/TiO₂ during H₂ evolution in certain photocatalytic systems. Specifically, I investigated several possible contributions, such as the sacrificial agent oxidation mechanism and the co-catalyst/catalyst interaction, which were influenced by the SiO₂ shell. Lastly, by creating shells with specific cavities, size selective photocatalysis can give further insights about oxidation mechanisms in direct contact with the catalyst.

2 Introduction

In this chapter I will give a motivation for the research projects, an introduction to photocatalysis and its applications, the requirements for photocatalysts, and the use and benefits of core-shell nanoparticles as photocatalysts, with a focus on TiO_2 as a core photocatalyst, SiO_2 as a shell, and Pt as a co-catalyst.

2.1 Photocatalysis

In the following section I will define the terms "photocatalysis" and "photosynthesis" and their differences. I will further explain the need and strategies of environmental applications for liquid photocatalysis, such as the combustion of pollutants and the generation of hydrogen from water.

2.1.1 Classification of devices and clarification of terms

Photocatalysis can be defined as the "change in the rate of a chemical reaction or its initiation under the action of ultraviolet, visible or infrared radiation in the presence of a substance - the photocatalyst - that absorbs light and is involved in the chemical transformation of the reaction partners".⁷ Photons themselves are not seen as the catalyst, as they are used up in the process. The distinction between photocatalysis and photolysis is that the former requires a catalytic material, which absorbs the light and initiates or accelerates the chemical reaction, while in the latter the molecule itself absorbs the light, which leads to the dissociation of a bond.⁸

There is a distinction between homogeneous and heterogeneous photocatalysis: In homogeneous photocatalysis the reactants and catalysts are in the same phase, while in heterogeneous photocatalysis they exist in separate phases, i.e. solid-gas or solid-

2 Introduction

liquid systems, where the catalyst is typically a solid semiconductor. In this thesis, I will only describe heterogeneous photocatalysis since it exclusively contains research in this field.

The research community uses the term "photocatalysis" not only to describe photocatalytic but also photosynthetic processes - which is technically incorrect. Per definition, catalysis and synthesis differ in their thermodynamics: "Catalysis" is the process of increasing the reaction rate of a thermodynamically downhill reaction by decreasing the activation barrier ($\Delta G < 0$, see Figure 2.1a), while "photosynthesis" is usually thermodynamically unfavorable ($\Delta G > 0$, see Figure 2.1b). Common definitions of photocatalysis include all excitonic chemical conversion systems; photocatalytic as well as photosynthetic systems.^{7,9} Therefore, photosynthetic processes are often termed "photocatalytic" in literature.

Nevertheless, photocatalytic and photosynthetic processes are very different. Their main difference lies in the stability of their products: Due to its exergonic nature, a back-reaction is hardly a problem in photocatalytic processes. In photosynthetic processes, however, one must take care to separate the products after their formation to suppress reverse reactions. This can be done either by separate compartments, charge-transfer selectivity or removal of the products from the reaction sites.⁹

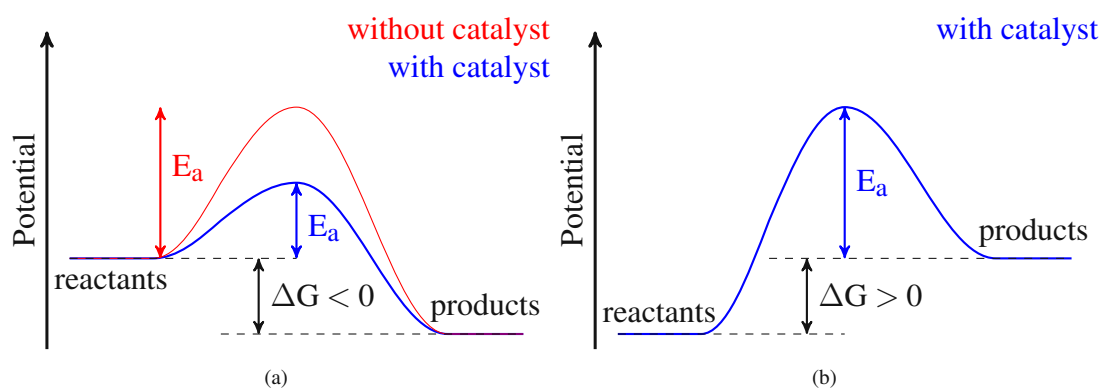


Figure 2.1: Energetics of downhill (photocatalytic) and uphill (photosynthetic) reactions. (a) Downhill reaction ($\Delta G < 0$) with and without a catalyst. With a catalyst the activation energy E_a is reduced. (b) Uphill reaction ($\Delta G > 0$) only occurs with a suitable catalyst.

An example for a true photocatalytic process is the oxidative degradation of organic compounds to molecular fragments or CO_2 - which is a downhill reaction that can be

initiated or accelerated by a photocatalyst. An example for a photosynthetic process is the production of hydrogen and oxygen from water, i.e. "water splitting" - an uphill reaction ($\text{H}_2\text{O} \rightarrow \text{H}_2 + \frac{1}{2}\text{O}_2$, $\Delta G^0 = 237.13 \text{ kJ mol}^{-1}$).¹⁰ The back reaction is known as "oxyhydrogen reaction" or "Knallgas reaction", a highly exothermal reaction known for its explosiveness.

Water splitting is challenging to realize, partly due to its unfavorable thermodynamics, but also because the oxygen evolution requires four photogenerated holes in proximity to the adsorbed reactant (O^{2-}), leading to slower kinetics of the reaction. Therefore, a lot of researchers use a sacrificial agent (SA), i.e. a hole scavenger - a substance that is easily oxidized. The use of SAs can enhance the hydrogen evolution reaction rate significantly ($\text{H}_2\text{O} + \text{Red} \rightarrow \text{H}_2 + \text{Ox}$).¹¹ The full reaction can be thermodynamically up- or downhill, depending on the chemical bias.⁹ In the case of methanol as an SA and a 1:1 molar ratio of $\text{CH}_3\text{OH}/\text{H}_2\text{O}$ the full reaction has a small, though positive change in Gibb's energy, and is therefore still regarded as photosynthesis ($\text{CH}_3\text{OH} + \text{H}_2\text{O} \rightarrow \text{CO}_2 + 6\text{H}_2$, $\Delta G^0 = 16.1 \text{ kJ mol}^{-1}$).¹² Importantly, studies found that for low H_2O :methanol ratios, a significant portion of protons stem from the sacrificial agent, rather than from water.^{11,13,14} Even though little or no O_2 is created in these systems, they are sometimes referred to as "photocatalytic water splitting" in literature. The system used in this work will be called "photocatalytic hydrogen evolution" or "hydrogen evolution reaction" (HER).

2.1.2 The sun as an energy source

Several energy sources are considered as renewable and as having the potential of replacing fossil fuels in the future. These are wind, geothermal, water, biomass and solar energy.¹⁷ The sun offers a large and steady source of energy: The average solar radiation arriving at the earth's surface per year is $\approx 1000 \text{ W m}^{-2}$.^{15,18}

The challenge is to convert this radiation to useful forms of energy. For this, photo-conversion materials need to absorb radiation and convert them into energy carriers, electricity or chemical energy, or into energy that can be used directly, such as heat.¹⁹ The sunlight consists of $\approx 4\%$ ultraviolet (UV) radiation ($\lambda < 400\text{nm}$), $\approx 53\%$ visible (vis) radiation ($\lambda = 400 - 800\text{nm}$) and $\approx 43\%$ infrared (IR) radiation ($\lambda > 800\text{nm}$).²⁰ Solar energy conversion requires systems that absorb radiation in these wavelength ranges and then efficiently convert the energy into useful forms. Solar cells, which

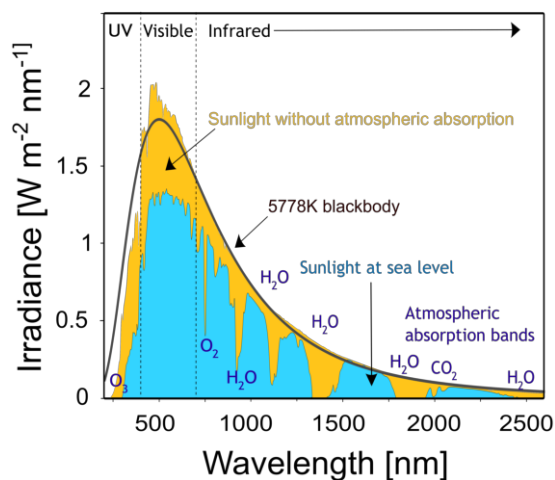


Figure 2.2: The solar light radiation spectrum at the top of the earth's atmosphere (orange) and at the sea level (blue). The sun produces light with a distribution similar to what would be expected from a 5778 K (5505°C) blackbody, which is approximately the sun's surface temperature. Absorption by gases with specific absorption bands in the atmosphere are marked. Regions of ultraviolet (UV), visible, and infrared (IR) light are labeled. These curves are based on the American Society for Testing and Materials (ASTM) Terrestrial Reference Spectra.^{15,16}

convert radiation into electricity, are known for efficiencies between 10 and 20%, because they only capture a fraction of the solar spectrum, and, in some solar cells, charge recombination further limits the conversion efficiency.¹⁹ This is also the case for photocatalytic conversion with semiconductors, which often requires radiation in the UV range. Therefore, increasing the efficiency of light absorption and conversion is one of the biggest challenges in solar energy conversion.

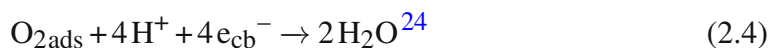
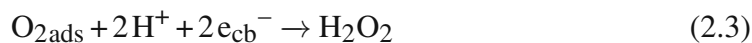
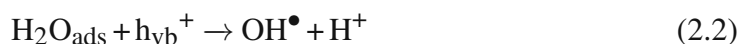
2.1.3 Combustion of harmful organic molecules

Organic pollutants, stemming from agricultural, pharmaceutical or industrial processes, are often deposited into the air and wastewater streams in amounts that are harmful for the environment, animals and humans. many of these pollutants are resistant to environmental degradation: If the wastewater or gas emissions are not treated to remove these substances they are distributed and bioaccumulate, i.e. gradually accumulate over time in biological organisms.²¹

An example for water-soluble organic pollutants are synthetic dyes. They can be toxic to aquatic life, affect natural photosynthesis due to reduced light penetration and some are carcinogenic to humans. Their structures are complex and aromatic, they are stable and not easily biodegraded.¹ Next to adsorption, ultrafiltration and coagulation, the

photocatalytic combustion of organic compounds with sunlight is a potentially green and inexpensive method to achieve their degradation. After complete combustion, they are broken down into harmless chemicals like CO₂ and water.²² The overall reaction has a negative Gibbs energy, is therefore exergonic and considered as "true photocatalysis".

The exact mechanism of the photocatalytic combustion of organic molecules in aqueous solutions is still under discussion. The adsorption of the molecules on the catalyst's surface plays an important role, and it depends on the charge and size of the organic molecule, their access to the catalyst's surface and the catalyst's properties. Upon adsorption, the organic molecules can be directly oxidized via transfer of an electron from the reactant to the catalyst. However, the state of the art is that many of the reactants are degraded indirectly via OH[•], which is generated by oxidation of adsorbed H₂O. OH[•] has an oxidation potential of ≈ 2.3V at pH 7. For comparison, photogenerated holes on TiO₂ have a potential of ≈ 2.5V:²³



Due to the generation of OH[•] photocatalytic degradation can take place at a distance up to 500 μm away from the TiO₂ surface.²³

2.1.4 Hydrogen as renewable energy source

Fossil fuels, as a limited resource, are consumed much faster than replenished and the combustion of fossil fuels is the main source for anthropogenic CO₂ emissions. Due to their link to climate change and its adverse effects on nature, there is need for alternative fuels, that are generated from renewable energy sources and do not emit any greenhouse gases upon combustion.^{3,26}

Hydrogen as a fuel is a promising alternative, as its combustion only yields water.

2 Introduction

Its usage as an energy source has been discussed since the oil crisis in 1970 and it offers many benefits: With 120 MJ kg^{-1} it has the highest specific energy density of all substances known and with 0.09 kg m^{-3} it has a very low density. It is the most abundant element on earth; most of it is bound in chemical compounds, such as water and hydrocarbons. As an energy carrier it can be used in internal combustion engines, which yields water, and in fuel cells, where chemical energy is converted to electricity with water and heat as a byproduct.²⁷ The advantages and possible applications led to the idea of a "hydrogen economy", where hydrogen is the most or exclusively used energy carrier.

Hydrogen storage and distribution are crucial issues regarding the development of a hydrogen economy, especially for mobile applications. The most established storage system is in the form of pressurized gas, often contained in high-pressure steel or aluminum vessels or underground salt caverns. However, due to extremely high pressures and the connected safety issues, gaseous storage systems face substantial hindrance. The storage as cryogenic liquid is also impractical, as it requires very low temperatures due to its boiling point of 20 K. Its current use in applications is limited to where it is consumed within a short time. However, promising approaches are researched, such as special solid materials, which can reversibly adsorb and desorb hydrogen; either via physisorption, e.g. on zeolites, or chemisorption, e.g. forming metal hydrides.²⁷

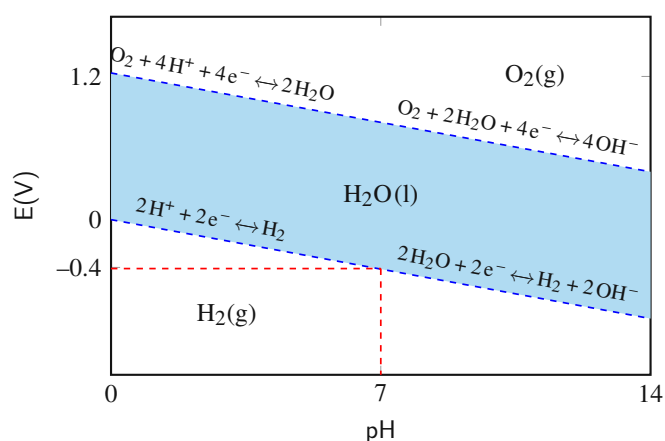


Figure 2.3: Pourbaix (E-pH) diagram for water. The blue area is the equilibrium region for water, above and below the equilibrium regions for oxygen and hydrogen, respectively. The vertical scale is the voltage potential relative to a SHE electrode, the horizontal scale is the pH of the aqueous solution. The red dashed line indicates the reduction potential of water at pH 7.

It is a secondary energy carrier, i.e. it is transformed from a primary energy source.²⁸ To be an attractive green fuel, it has to be generated with renewable energy sources and in a sustainable system. According to a statistic of 2001, hydrogen is mainly produced via conversion of natural gas (48%), heavy oils and naphtha (30%) and coal (18%).²⁶ The energy sources mentioned are non-renewable and do not fulfill the requirement of minimizing greenhouse gas emissions. Therefore, other technologies are in development, such as the production of hydrogen from hydro power, wind, solar, biomass and geothermal energy sources²⁷.

More specifically, renewable supply strategies that are researched include electrolysis and photoelectrochemical conversion of water, with the use of wind or solar-generated electricity, and the photocatalytic reduction of water via absorption of solar radiation. The latter require a photoelectrode or photocatalyst with suitable conduction band minima to reduce H^+ to H_2 . The reduction potential of H^+/H_2 is ≈ -0.4 V at pH 7.⁹ The Nernst equation and its graphical representation, the Pourbaix diagram (Figure 2.3), give an estimation of the reduction potential of an aqueous electrochemical system at a given pH value:

$$E_H = E^0 - \frac{RT}{nF} \ln \left(\frac{a_{red}}{a_{ox}} \right) \quad (2.6)$$

where E_H is the voltage potential with respect to the standard hydrogen potential (SHE), E^0 is the standard electrode potential at pH 0, R is the gas constant, T the temperature in Kelvin, n the amounts of electrons transferred in the reaction, F the Faraday constant and a_{red} and a_{ox} the activities of the reduced and oxidized species.

Specifically for hydrogen reduction from water the Nernst equation can be written as:

$$E_H = -\frac{RT}{nF} \ln(10) \text{ pH} \approx -0.059 \text{ pH} \quad (2.7)$$

2.2 Materials requirements

In the following section I will discuss material requirements for semiconductor and co-catalysts for their use in heterogeneous photocatalysis. The focus lies on the model photocatalyst TiO_2 and the commonly used co-catalysis Pt, which are the main catalysts used in this work.

2.2.1 Semiconductors as photocatalysts

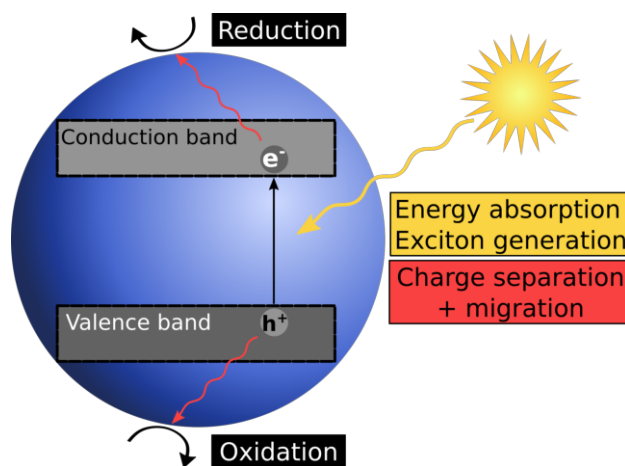


Figure 2.4: General mechanism of photocatalysis in a solid semiconductor.

In general, a photocatalyst converts photons into charge carriers, which can then react with a reactant that is adsorbed on the catalyst. The materials first requirement is therefore sufficient light absorption leading to charge excitation, i.e. the formation of electron-hole pairs. This qualification is met by some semiconducting metal oxides or sulfides. For the use of solar light as a renewable energy source the absorbed light energy needs to lie in the solar light spectrum, i.e. the band gap E_g of the semiconductor must not be too large. Further requirements for a heterogeneous photocatalyst are the separation of charge carriers, their transfer to the surface and their reaction with reactants on the surface (Figure 2.4).⁹

Another important requirement are appropriate band positions of the conduction and valence band. The suitability depends on the application, i.e. the reduction potentials of the reactants in the system. Hydrogen evolution from water, for example, requires a conduction band position of less than ≈ -0.4 V at pH 7 (Figure 2.5).⁹ Semiconductors with a large band gap ($E_G > 3\text{eV}$) often have a conduction band potential that is more negative than -0.4 V. However, only photons in the UV range can be absorbed by these semiconductors. Solar light consists of only $\approx 4\%$ of UV radiation ($< 400\text{nm}$). On the other hand, semiconductors with a small band gap ($E_G < 3\text{eV}$) often have inadequate conduction band potentials for many applications. It is therefore important to minimize the band gap of materials while keeping suitable band positions. Approaches to do this

include doping or photosensitization.²⁹

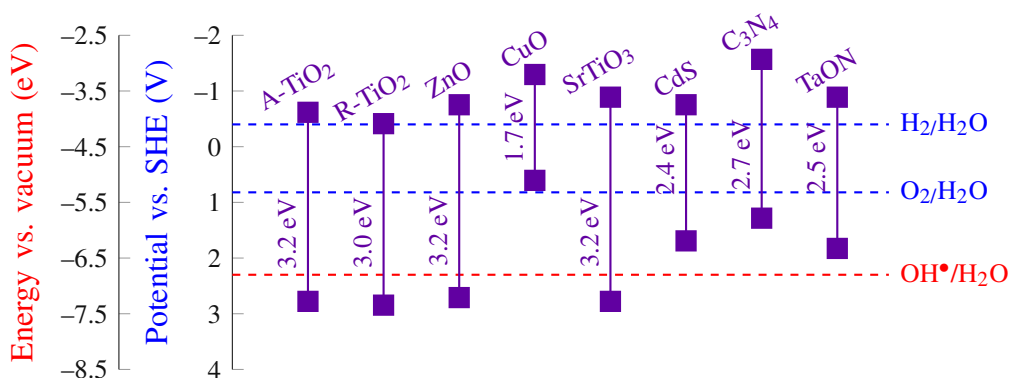


Figure 2.5: Conduction band, valence band potentials and band gap energies of common semiconductor photocatalysts relative to the redox potentials of water splitting and decomposition of organic molecules at pH 7. Redrawn from^{2,30}

Once an electron-hole pair is generated, the charge carriers need to stay separated until they reach the surface and react with reactants. Charge recombination is detrimental to the photocatalytic activity and must therefore be minimized. There are several strategies to decrease the material's recombination rate. One common approach is the use of nanomaterials to minimize the distance the charge carriers have to travel to the surface. Another approach is the modification of materials to decrease defects, which act as recombination centers; hybridization with nanocarbons; or the introduction of electron traps, often done via surface modifications.^{23,31}

The quantum yield (QY) of a photocatalytic system is a measure for the extend of recombination. It is defined as the efficiency of electron-hole pair usage, i.e. the ratio of the number of photons absorbed and the number of events occurring.³²

$$\text{QY} = \frac{\# \text{ of reacted electrons}}{\# \text{ of absorbed photons}} \quad (2.8)$$

Ideally, each photon reaching the semiconductor is absorbed, generating an electron-hole pair, which is separated and transferred onto the surface to react with reactants. The efficiency of absorption is lowered by scattering or absorption saturation, which are difficult to evaluate. Therefore, quantum yield determinations use the ratio of the number of incident photons transmitted onto the photocatalyst, calculated from the

2 Introduction

measured photon flux, to the number of reacted electrons, determined from the amount of products generated.

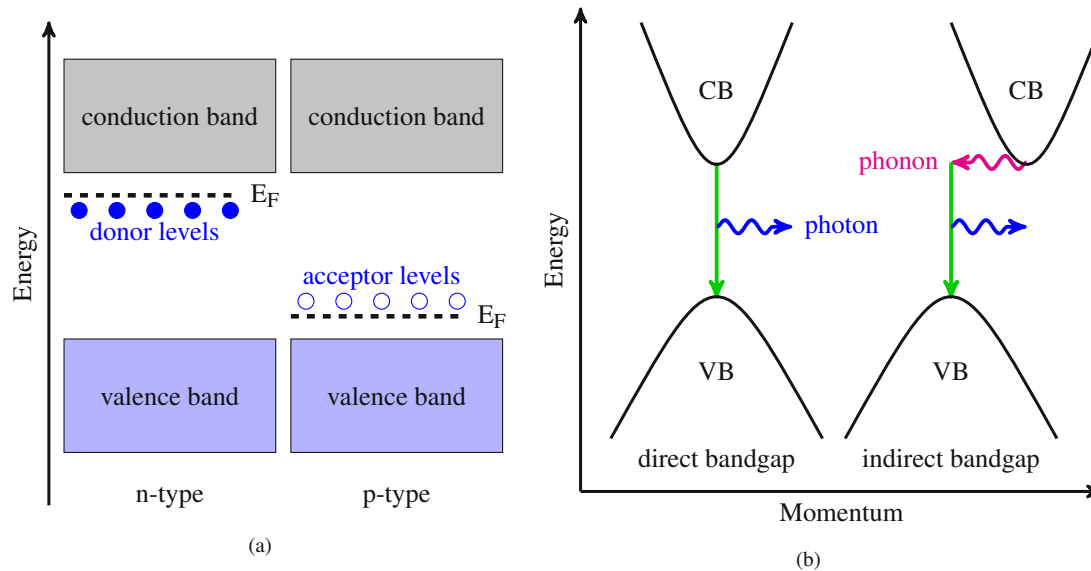


Figure 2.6: (a) Two types of semiconductor doping: n-type and p-type. (b) Direct and indirect bandgap transitions. Indirect bandgap transitions require a phonon transition.

The properties of semiconductors can be modified by doping, i.e. adding small amounts of impurities. Two kinds of doping are common: Negative type (n-type) doping leads to an excess of electrons, shifting the Fermi level closer to the conduction band. Positive type (p-type) doping leads to a deficiency of electrons and therefore the Fermi level shifts closer to the valence band (Figure 2.6a). Even without extrinsic doping, a semiconductor can have intrinsic doping due to defects in the crystal lattice, e.g. vacancies. An example for an intrinsically n-type doped semiconductor is TiO_2 .

The band gaps of semiconductors can be of two types: direct or indirect. The electron's crystal momentum, a quasimomentum associated with the wave vector \mathbf{k} , can be the same or different in the valence and conduction band. If it's the same, the electron can directly relax and emit a photon, leading to the term "direct band gap". If the \mathbf{k} vectors are different, the electron must transfer momentum to the crystal lattice to change its state (Figure 2.6b). Thus, the excited electrons cannot directly recombine with holes, which increases the photogenerated electron-hole lifetime. An example for an indirect band gap semiconductor is anatase, a phase of TiO_2 commonly used in

photocatalysis.³³

2.2.2 TiO₂ as photocatalyst

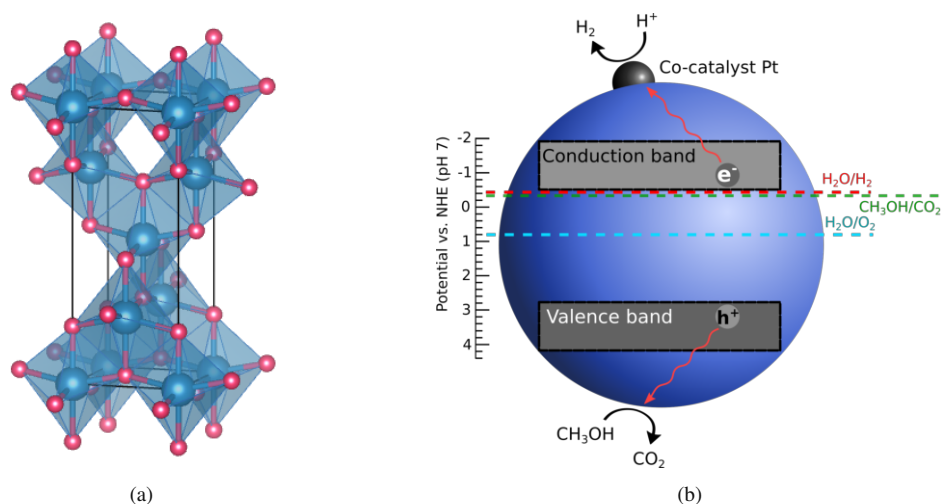


Figure 2.7: (a) Ball-stick model including polyhedra of the unit cell of anatase, a polymorph of TiO₂ often used in photocatalysis; (b) sacrificial hydrogen evolution on a Pt/TiO₂ nanocatalyst.

The most commonly used heterogeneous photocatalysts are large band gap materials, which means they only show efficient activity when irradiated with UV light. TiO₂ is a model photocatalyst, which has a band gap of 3.2 eV (anatase) or 3.0 eV (rutile).

The photocatalytic properties of TiO₂ are known since the 1960s. Research started with photoelectrochemical water splitting using TiO₂ and platinum as electrodes. Soon other applications became relevant. When TiO₂ powder is dispersed in a solution and irradiated, it leads to redox processes in its surroundings. It is also known for self-cleaning, anti-fogging properties and many other applications benefiting from its photo-induced hydrophilicity.²³

TiO₂ has three common polymorphs: anatase, rutile and brookite. Anatase is metastable, most often found as small crystals and transforms to the thermodynamically most stable phase, rutile, at temperatures above 600°C.³⁴ It crystallizes in the tetragonal crystal system, where it disposes a ditetragonal dipyramidal crystal form (Space group: I 4₁/amd, Figure 2.7a). Anatase and rutile have been studied extensively for

photocatalytic applications, where anatase has shown a higher photocatalytic activity than rutile, due to the following reasons:

- a higher electron mobility;³⁵
- a smaller particle size;³⁶
- a longer electron lifetime due to an indirect bandgap (whereas rutile has a direct bandgap);^{35,36}
- the formation of special surface active sites, due to the higher molar volume of the crystal structure.³⁶

Anatase has suitable band positions for many applications. The conduction band potential of anatase lies around -0.5V . Water is reduced to H_2 at $\approx -0.4\text{V}$ at pH 7, close to the conduction band potential of anatase, providing a small potential difference - the driving force for the reaction.³⁷ Due to its valence band position at $\approx 2.7\text{V}$, anatase is able to oxidize water which requires a potential of 0.8V at pH 7. However, this reaction requires four holes and two adsorbed H_2O in close proximity to each other, which hinders this reaction kinetically. On the other hand, the photocatalytic decomposition of sacrificial agents, such as CH_3OH , happens step-wise and only requires one hole each step. The overall reaction ($\text{CH}_3\text{OH} + \text{H}_2\text{O} \rightarrow \text{CO}_2 + 6\text{H}^+ + 6\text{e}^-$) has an oxidation potential of $\approx -0.38\text{V}$ at pH 7, and therefore a much higher driving force than the oxygen evolution. With low H_2O to CH_3OH ratios, the oxidation takes place directly at the surface. With very high H_2O to CH_3OH ratios, above 300, the indirect oxidation mechanism via OH^\bullet is dominant, which requires an oxidation potential of $\approx 2.3\text{V}$.^{12,23} The oxidative degradation of organic dyes happens either indirectly, via the generation of OH^\bullet , or directly, when the organic dye is adsorbed on the catalyst's surface.²³

2.2.3 The co-catalyst Pt

The hydrogen evolution efficiency from pure anatase is rather low. To increase the efficiency, co-catalysts have been introduced, which act as electron traps to reduce charge recombination and as active sites for the hydrogen reduction.^{38,39} Common co-catalysts are transition metals like Pt, Pd,⁴⁰ Rh,⁴¹ Au,^{42,43} Ag, Ir, Ni⁴⁴ and metal oxides like CuO .² A benchmark system in photocatalytic HER is Pt/ TiO_2 , a pair of cooperative catalysts that promote each others catalytic activity.

Pt is deposited as nanoparticles onto the TiO_2 surface, usually by wet impregnation or photodeposition from Pt complexes, such as H_2PtCl_6 or $(\text{NH}_3)_4\text{PtCl}_2$. Wet impregnation usually consists of adding the Pt precursor to a suspension, which is followed by stirring, drying and further oxidation, reduction and heat treatment, often under H_2 atmosphere at higher temperatures $> 200^\circ\text{C}$.^{45–47} A simple alternative is photodeposition, where the Pt ion is reduced on TiO_2 under UV illumination.⁴⁸ This can be done "in-situ", during the photocatalytic experiment or "ex-situ", which also involves post-synthetic treatment, such as oxidation and reduction, possibly at higher temperatures.⁴⁹ In the Eder research group, the most used method is in-situ photodeposition of Pt from H_2PtCl_6 in a TiO_2 H_2O :methanol slurry during the hydrogen evolution experiment.

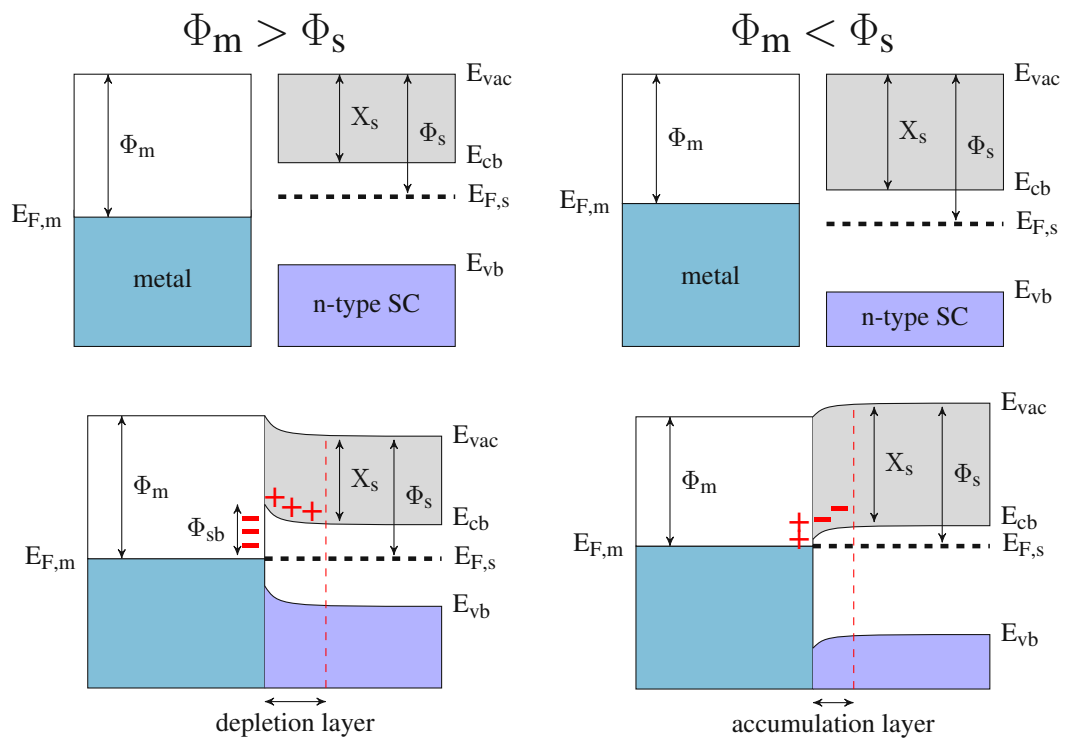


Figure 2.8: Energy band diagrams of metal with n-type semiconductor not in contact (above) and in contact under equilibrium (below). Φ_m , metal work function; Φ_s , semiconductor work function; X_s , electron affinity of the semiconductor; Φ_{sb} , schottky barrier height; E_F , Fermi level; E_{vac} , vacuum energy; E_{vb} , energy of valence band maximum; E_{cb} , energy of conduction band minimum. Redrawn from Zhang et al.⁵⁰

Band bending

When two materials are in close contact with each other, their energy bands adjust to align their Fermi levels - due to an electron flow from the higher to the lower Fermi level. This electrical junction will induce band bending on the interface, which allows for better charge separation, reduced recombination and therefore enhanced photocatalytic activity.

The band bending of a junction between a metal and an n-type semiconductor is shown in [Figure 2.8](#). If the metal's work function is greater than the semiconductor work function ($\Phi_m > \Phi_s$) then photogenerated electrons will move from the semiconductor to the metal and a Schottky barrier Φ_{sb} is formed at the interface. The electrons flow from the metal to the semiconductor, if the metal work function is smaller than the semiconductor work function ($\Phi_m < \Phi_s$). This electron transfer proceeds until the Fermi levels E_F are equal.⁵⁰

The work function of the co-catalyst/metal in relation to the semiconductor's work function is an important parameter. The work function is defined as the difference between the vacuum energy E_{vac} and the Fermi level E_F . The Fermi level depends on dopant concentrations and it is also affected by surface conditions: It can vary for different surface orientations and surface terminations. For example, the work function of oxidized anatase is $\Phi_s \approx 5.2$ eV and it decreases to $\Phi_s \approx 4.4$ eV upon water vapor adsorption.⁵¹ To facilitate transfer of the electrons from the semiconductor to the metal, the work function of the metal Φ_m needs to be greater than the work function of the semiconductor ($\Phi_m > \Phi_s$). The co-catalyst's work function depends not only on the kind of metal and surface orientation but also on the size of the nanoparticles. The size plays a role due to quantum confinement of very small particles: Bulk Pt has a work function of 5.65 eV but the electron affinity for a single Pt atom in the gas phase is only 2 eV.^{52,53} Pt nanoparticles deposited onto TiO_2 vary a lot in their diameter depending on the deposition method. The diameter of 1 nm was found to be optimal for photocatalytic HER.^{52,54} A reason for this could be the dispersion of the Pt on the surface, which also plays a crucial role for the activity. Good dispersion increases the access to triple-phase boundaries and active sites and decreases the path electrons have to travel in the semiconductor before they reach the co-catalyst. Up until now, these small Pt sizes have only been achieved with ex situ gas-phase deposition.⁵² Photodeposition of Pt onto TiO_2 , the technique used in this work for reasons stated

later, usually leads to Pt nanoparticle sizes greater than 1.5 nm.^{38,41,49}

Even though the band diagram formalism describes the situation for an intimate contact between metal and semiconductor, band bending still occurs when there is an ultrathin layer of an isolating material between them, which has been shown for metal-oxide-semiconductor field-effect transistors.⁵⁵ In my work, I used ultrathin SiO₂ layers between TiO₂ and Pt, which are transparent to electrons due to their atomic dimensions and allow electron transport and therefore band bending.

2.3 Core-shell TiO₂–SiO₂ particles

In this section, I will discuss the use and benefits of core-shell nanoparticles, especially TiO₂–SiO₂, in photocatalysis and introduce several synthesis approaches for the formation of ultrathin shells.

2.3.1 Core-shell particles in photocatalysis

A core-shell particle has an inner spherical material that is surrounded by a shell of a different material, each with dimensions at the nanoscale. They can combine multiple functionalities, such as adsorption capacity, dielectric properties, thermal stability and catalytic activity. This makes them suitable for many applications in the field of catalysis and energy storage.

The first core-shell catalysts were made out of porous shells with a cavity between core and shell. They are called "yolk shell" and they were developed to optimize the transport behavior of reactants. Due to a growing interest in core-shell structures, they have been developed further to materials where the shell fully or partially encapsulates the core by forming chemical bonds.⁵⁶

Depending on the materials, the catalytically active sites may be at the core, at the shell, or even at their interface. The triple-phase boundary of core, shell and liquid/gas phase may be beneficial for the conversion of reactants. The interface may also be capable of trapping electrons or holes, therefore increasing the charge carrier lifetime. Specifically, they have been studied for their impact on the catalytic activity, e.g. due to different diffusion or sorption properties or due to synergistic effects of the two (or

more) materials.^{34,57–59} Among the studied photocatalytic applications are the degradation of organic molecules and CO₂ reduction.^{56,60}

2.3.2 TiO₂–SiO₂ core-shell particles

Regarding TiO₂, a plethora of core-shell strategies have been applied to enhance the photocatalytic activity and investigate mechanistic details. Efficiencies and activities of catalysts depend on their phase, morphology, particle size and surface area. TiO₂ has been coated around insulators or metals to increase the effective surface area by minimizing aggregation, to optimize light harvesting, to increase the stability or to reduce charge carrier recombination.^{57,61–63} If coated around another semiconductor the composite can show favorable photocatalytic and optical properties, e.g. the extension of the light absorption range and better charge separation at the interface.^{30,56,64}

TiO₂ can also be used as a core. Benefits include a better interfacial charge separation, thermal stability and increased dispersion. It has been encapsulated by metals, nanocarbons, semiconductors and insulators.^{56,65} Specifically, an insulating SiO₂ layer in the nanometer range has been shown to increase the photocatalytic conversion by an interplay of several effects:

- Ti–O–Si bonds can act as active sites in several reactions.^{32,59,62,66–68}
- The SiO₂ surface is more acidic than the TiO₂ surface, therefore some reactants experience improved adsorption kinetics.^{69,70}
- SiO₂ is non-reducible and less oxygen vacancies are present than in TiO₂.⁷¹
- In TiO₂, d-orbitals are involved in bond formations, while the Si has no d-orbital available for bonding, leading to different bond strengths between metal co-catalysts and supports.⁷²
- The TiO₂–SiO₂ interface serves as a trap state for charge carriers, therefore decreasing their recombination.^{59,73,74}

The SiO₂ layer can also shield catalytically active sites or inhibit charge transfer from TiO₂ to the reactant, therefore decreasing the photocatalytic activity. The extend of these effects depend on the layer coverage and thickness.⁵⁷ It is therefore of great interest to produce ultrathin shells, which allow charge transfer via tunneling, and shells with cavities, which allow the reactant to diffuse to the TiO₂ surface or allow access to

interfacial sites.⁷⁵

2.3.3 Ultrathin layers of SiO₂ on TiO₂

Several strategies have been applied to achieve the deposition of ultrathin SiO₂ shells on TiO₂ or other metal oxides. Among those are salt precipitation, sol-gel synthesis, molecular self-assembly, atomic layer deposition (ALD), microemulsion, micelle formation and electrochemical synthesis.

Before going into some of those synthesis techniques, I want to explain how SiO₂ deposition on the TiO₂ support is beneficial for homogeneous coverage of the core with the shell.

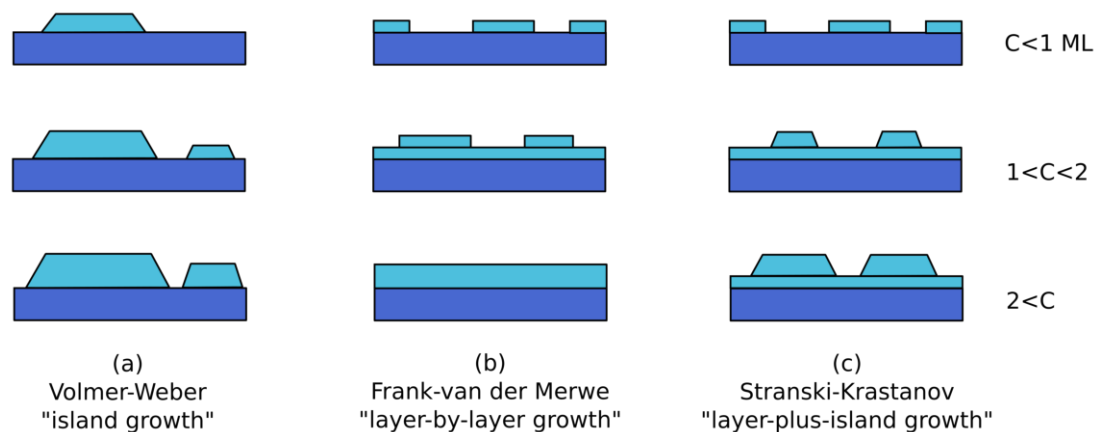


Figure 2.9: Three different layer growth models can be distinguished; (a) the Volmer-Weber model describes the growth of distinguishable islands; (b) the Frank-van der Merwe model describes complete film formation before the growth of subsequent layers; (c) the Stranki-Krastanov model describes the formation of a 2D layer before island form on top of it.

In general, three main different layer growth mechanisms can be distinguished:

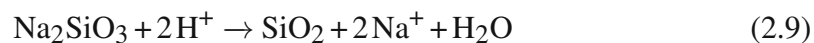
1. The Volmer-Weber growth model, also called "island growth", describes the growth of distinct 3D islands on the support that increase in size with the deposition time (see Figure 2.9a). This happens when the ad-atoms of the layer material are more strongly coupled with each other than with the support.
2. The Frank-van der Merwe growth model, also called "layer-by-layer growth",

describes the primary formation of a monolayer. After this layer fully covers the support the formation of more layers proceed on top of it (see [Figure 2.9b](#)). This happens, when the ad-atoms interaction with the support is stronger than with other ad-atoms.

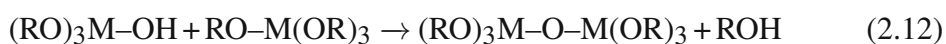
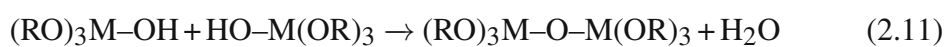
3. The Stranski-Krastanov growth model, also called "layer-plus-islands growth model", is an intermediary process with both 2D layer formation, followed by 3D island formation (see [Figure 2.9c](#)). The 3D island growth starts on a critical layer thickness, which is dependent on the materials properties, such as lattice parameters and surface energies.

SiO₂ precursors, such as tetraethoxysilane (TEOS), form silanols when hydrolyzed (see [Figure 2.10](#)). The silanol can then condense with other hydroxyl groups to form metal oxide polymers: It either reacts with hydroxyl groups of other silanols or of the TiO₂ surface, depending on the electronegativity (EN) of the metal. Titanium has a lower EN (1.54) than silicon (1.90), which leads to the preferential condensation of silanols on TiO₂ surfaces.⁷⁶ Therefore, I expect either a Frank-van der Merwe or a Stranski-Krastanov growth.

A simple wet chemical synthesis process is salt precipitation, e.g. of the precursor sodium silicate Na₂SiO₃. The salt forms SiO₂ according to [Equation 2.9](#). The sodium silicate solution is added drop-wise to the suspension while controlling its pH and temperature. After addition of the required amount, the suspension is aged, filtered, washed and calcined.



SiO₂ shells are also easily synthesized by sol-gel chemistry. Sol-gel processes require a metal alkoxide precursor which polymerizes to a metal oxide. First, the alkoxide group is hydrolyzed to an hydroxyl group ([Equation 2.10](#)) which then condenses with other hydroxyls ([Equation 2.11](#)) or alkoxide groups ([Equation 2.12](#)).



Catalysts, such as HCl or NH_3 , increase the hydrolysis and condensation rate. With progressing condensation, small particles form in the solution (sol) which then polymerize to an amorphous structure (gel). At this point, the gel still contains a lot of solvent molecules and requires drying and calcination. Depending on the calcination conditions - such as temperature and time - the metal oxide can stay amorphous or crystallize.

While sol-gel offers good control over porosity, morphology and thickness, it is tricky to achieve layer-by-layer growth in the ultrathin layer region. Therefore, step-wise layer growth techniques have been developed. One of those techniques is done in a water-free solvent and starts with the chemisorption of the alkoxides on the support - instead of hydrolyzation with water they react with the hydroxyl group of the metal oxide. Remaining alkoxides are removed by filtration and washing and only then is the chemisorbed alkoxide hydrolyzed with water, to interconnect the layer and to form new hydroxyl groups on the surface, onto which the next layer can be built. This is repeated to achieve the required amounts of layers.⁷⁷

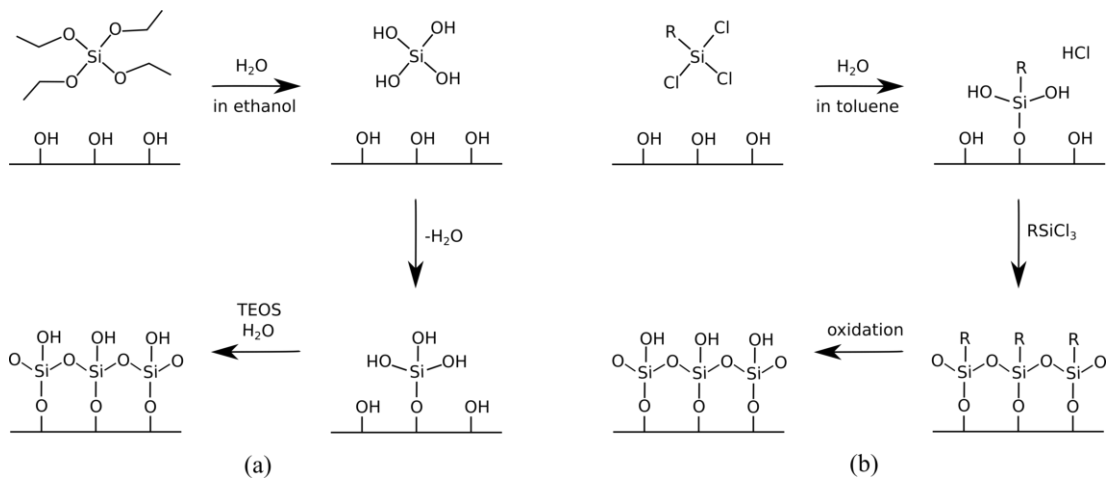


Figure 2.10: A single step of step-wise wet chemical layer growth techniques; (a) sol-gel: The step-wise addition of a calculated amount of the silica precursor tetraethoxysilane (TEOS) leads to a controlled layer growth on TiO_2 ; (b) molecular self-assembly: The alkyltrichlorosilane precursor leads to self-limiting growth of one layer due to the non-polar residue.

Another way of step-wise sol-gel layer deposition is done by adding the precursor in precise amounts to the suspension, enough to form only one layer. The amount of precursor is calculated considering the surface area or the OH-density of the support

material. The system is then stirred in a solvent containing water and a catalyst until the reaction is complete. This concludes one step. The step can be repeated until the required number of layers is formed, and only afterwards is the powder filtered and washed (see [Figure 2.10a](#)).⁷⁸

Another method that yields precise layer formation is molecular self-assembly. Here, the layer precursors have a highly reactive head group and a non-reactive, non-polar residue. The reactive side chemisorbs on the support material while the non-polar ending limits the layer growth. After deposition the material is filtered, washed and the non-polar endings have to be oxidized to hydroxyl groups. After that, the next layer can be formed (see [Figure 2.10b](#)).⁷⁹

A state-of-the-art method for precise control over the formation of monolayers or sub-monolayers is atomic layer deposition (ALD). Similar to chemical vapor deposition (CVD), the support is placed in a vacuum chamber and exposed to reactive precursor gases. Two or more precursors are introduced to react with each other and build a layer on the support. Unlike CVD, where the precursor gases flow simultaneously through the chamber, in ALD the precursors are introduced individually in alternating sequences. In between the sequences the remaining precursors or volatile by-products from the former sequence are removed with a gas purge. This ensures a controlled, self-limiting, layer-by-layer growth of sub-nanometer layers.^{61,80}

2.3.4 Nanocavities in an SiO₂ shell

Shells with pores allow reactants to access the core catalyst or the interfacial sites. Porous materials have also been applied to select between different reactants due to their sizes and diffusion properties. Other benefits of porous structures are a high reactant adsorption capacity in connection to their high surface area.

Among porous materials that have been used in heterogeneous catalysis are zeolites and mesostructured oxides. While mesoporous structures, which typically include silica and alumina, offer pore sizes in the range of 2 to 50 nm, zeolites have micropores below 1 nm diameter.⁸¹ Pores with high diameters, i.e. mesopores, often aren't selective enough regarding the size of reactants, while pores below 1 nm suffer from diffusion limitations. To select among reactants that are sized between 1-2 nm, pores have to be created with this specific size. Canlas et al. reported that cavity containing

oxide sieving layers with specific pore sizes have been deposited on TiO₂ nanoparticles by grafting bulky templates on the TiO₂ surface before growing a metal oxide layer around it. They created pore sizes between 1 and 2 nm which successfully select between differently sized alcohols.⁸²

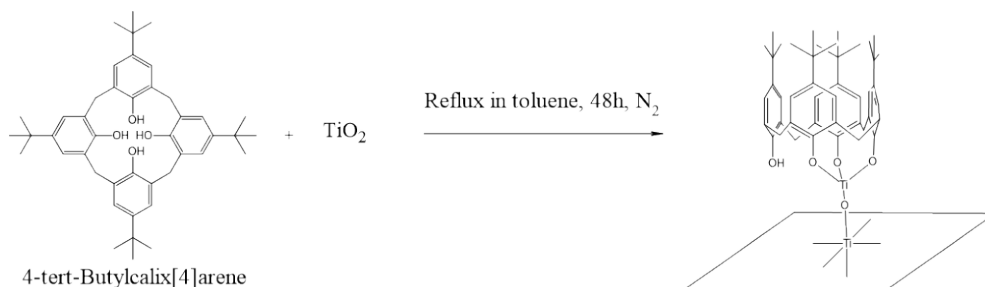


Figure 2.11: The synthesis of grafting 4-tert-butyl[4]calixarenes onto TiO₂.

Among those bulky templates, that are used to define the pores in shells, are calixarenes. Calixarenes are cyclic oligomers, where each building block contains a phenol ring which is connected to the next building block via a methylene groups in ortho position to the -OH group. It can be functionalized with different residues leading to a plethora of structures. Their name is derived from the greek "calix", meaning cup or crown, and "arene", which refers to the aromatic building block. 4-tert-Butyl[4]calixarene is composed of four building blocks and a 4-tert-butyl group is para position to the -OH group. This molecule serves as a bulky template which can be attached to the TiO₂ surface before depositing SiO₂ around it. When the template is removed in the final synthesis step, an insulating shell that contains nanocavities remains.

The calixarenes are grafted onto TiO₂ with a straight-forward and easy synthesis: An excess of calixarenes is dissolved in toluene and the TiO₂ nanoparticles are suspended in the mixture. The suspension is refluxed under an inert atmosphere until the reaction is completed. The -OH groups of the calixarenes coordinate around a Ti⁴⁺ surface ion, creating an orange colored complex (see Figure 2.11).^{82,83}

The surface is then covered with SiO₂ with a step-wise sol-gel approach as introduced in the former section, covering every part of the surface except for the parts where the calixarenes are grafted. The calixarenes are then removed by either thermal or ozone treatment.



Die approbierte gedruckte Originalversion dieser Dissertation ist an der TU Wien Bibliothek verfügbar.
The approved original version of this doctoral thesis is available in print at TU Wien Bibliothek.

3 Methodology

In this chapter I will give a description of the synthesis methods, characterization techniques and photocatalytic setups and calculations that are important for this thesis. This includes an overview over the chemicals used for synthesis and photocatalysis and a detailed sample list of the most relevant samples of this project.

3.1 Synthesis and preparation

In this section, I will explain different synthesis attempts to generate homogeneous ultrathin shells, with and without nanocavities, around titania nanoparticles (NPs). These include the salt precipitation synthesis (SP), molecular self-assembly (SAM) and stepwise sol-gel synthesis (SG). This section describes the synthesis of the samples but sometimes refers to the characterization, to explain which synthesis methods were successful. The details of the characterizations of these samples will be described in [section 4.1](#).

3.1.1 Synthesis of ultrathin shells

The term "ultrathin" is not clearly defined. While some understand ultrathin layers to have thicknesses below 100 nm, in the field of "ultrathin 2D materials", and often in catalysis, it is understood as a monolayer up to a few atomic layers - less than 5 nm.^{58,84–88} I will use the same definition, but the ultrathin shells I created are most often less than 1 nm in thickness.

Salt precipitation synthesis

The first synthesis method to generate ultrathin layers of SiO₂ on anatase is the "salt precipitation synthesis" (SP), which is inspired by Hu et al.⁵⁹ It is done by adding sodium metasilicate Na₂SiO₃ at a constant basic pH. 1 g of TiO₂ anatase with a measured BET surface area of 92 m²g⁻¹, in this work referred to as Ana₉₂, was suspended in 10 ml of de-ionized water and ultrasonicated for 30 minutes in a three-neck flask. It was heated to 75°C and stirred while the pH was set to 10 with 0.1 M NaOH solution. A 0.5 M solution of Na₂SiO₃ in water was prepared and added dropwise while measuring the pH and keeping at 10 ± 0.5 by adding 0.1 M H₂SO₄. After the addition of 2.5 ml of the Na₂SiO₃ solution, or 1.25 mmol, half of the suspension was removed from the flask and aged, i.e. stirred for 3 hours, in a separate vial. This sample will be referred to as **T₉₂S1_{10%}^{SP}**: The SP denotes the salt precipitation synthesis method, the 10% is the expected ratio of SiO₂ to TiO₂, and 92 m²g⁻¹ is the measured surface area of the anatase support.

Another 1.25 ml of the Na₂SiO₃ solution was added to the remaining suspension, leading to the total addition of 1.25 mmol to 0.5 g of anatase, and then aged for three hours. The second sample should therefore have twice times as much SiO₂ in the suspension than the first sample, and it will be referred to as **T₉₂S2_{20%}^{SP}**.

Self assembled monolayer synthesis

The second synthesis method I tried was inspired by Vallant et al.⁷⁹ It's the molecular self assembly of a monolayer by using a precursor that limits further growth itself. The used precursor was octadecyltrichlorsilane C₁₈H₃₇Cl₃Si (OTS). The polar head group SiCl₃⁻ is very reactive and chemisorbs on the TiO₂ surface, while the non-polar residue hinders further layer growth. After the synthesis of one layer, the residue needs to be oxidized to form a hydroxyl group - to which the next OTS molecule can bind.

The synthesis was performed in toluene, with a measured water content of 11.22 mM, under an argon box with a fresh bottle of OTS. 2 g of Ana₉₂ was suspended in 100 ml of deionized water and ultrasonicated for 15 min. A 70 mM solution of OTS in toluene was prepared and aged for 10 minutes. The anatase suspension was added to the OTS solution and the mixture was stirred for 2 hours. The powder was then

filtered, washed with toluene and acetone and calcined at 500°C for 30 minutes with a 10 K/min ramp. This sample will be referred to as $T_{92}S1_{7\%}^{SAM}$ - 1 step of self assembly monolayer (SAM) synthesis, which should lead to 7% of SiO₂ to anatase, that has a surface area of 92 m²g⁻¹. The expected amount of silica was set to 7% because this constitutes to one monolayer.

Step wise sol-gel synthesis

The first sol-gel synthesis method is inspired by Ichinose et al.⁷⁷ Metal alkoxide sol-gel precursors usually react with water to form metal hydroxides which then condense together to form metal oxide polymers. In this synthesis, water was not added to the suspension of the support and precursor solution, so the metal alkoxide can only react with surface hydroxyl groups on the support, and only after chemisorption will the remaining alkoxide residues be hydrolyzed with water. This synthesis method will further be referred to as sol-gel synthesis 1, or **SG1**.

1 g of anatase Ana₉₂ was suspended in 50 ml of ethanol abs., ultrasonicated for 5 minutes and flushed with argon gas for 30 minutes. Then 1.12 ml tetraethyl orthosilicate (TEOS) was added dropwise, leading to a 100 mM solution of TEOS in ethanol. The mixture was stirred for 10 min. The powder was then filtered and washed with ethanol abs. under argon, to remove all unreacted TEOS. The powder was then hydrolyzed with water and dried at air. This constitutes one step of SG1 synthesis. 0.1 g of the powder was taken out, and the sol-gel synthesis was repeated on the remaining powder, with aliquot amounts of precursor. Up to 7 steps were performed.

The maximum coverage from one step was approximated to be 1/4 of the available hydroxyl groups on anatase, which were measured to be 7.3 OH nm⁻² with a TGA method by Mueller et. al.⁸⁹ The diameter of a chemisorbed TEOS on anatase before hydrolysis was calculated to be 0.9 nm. A maximum of 1.6 molecules per nm² can chemisorb onto the surface. The 1-step sample will be referred to as $T_{92}S1_{2\%}^{SG1}$. For characterization I chose the 4-step and 7-step samples, which will be referred to as $T_{92}S4_{7\%}^{SG1}$ and $T_{92}S7_{12\%}^{SG1}$.

This method did not lead to the expected results: In TEM no deposited layer was visible, which could be because of the low reactivity of the precursor. It is either necessary to increase the concentration of TEOS in the solution or to use a catalyst,

3 Methodology

such as HCl or NH₃. Due to their gaseous nature they are commonly dissolved in water, which is avoided in this synthesis method. The goal was to find an easy wet chemical synthesis to deposit ultra-thin layers. Therefore, other methods of step-wise sol-gel shell growth were investigated. In the following methods, the powder was not filtered after each step, but a specific amount of precursor was added in each step to control the growth of the shell.

The next sol-gel synthesis method (**SG2**) was inspired by Bo et al.⁹⁰ 0.1 g of anatase Ana₉₂ was dispersed in 18 ml ethanol abs. and 2.7 ml NH₄OH (33 wt.%) and ultrasonicated for 30 minutes. Then, 0.019 ml (84 μmol) of TEOS, ideally leading to 0.27 nm of shell per step, were added and the suspension was stirred for one hour. The steps of sonication and TEOS addition were carried out a total of 4 times. After the final step the powder was filtered and calcined with 3.5 K/min to 325°C, which was held for one hour. This sample is referred to as **T₉₂S₄^{SG2}_{21%}**.

The next method (**SG3**) is inspired by the same group.⁹¹ 0.1 g of anatase Ana₉₂ was dispersed in 13 ml ethanol abs. and ultrasonicated for 30 minutes. The main difference to the former method is that one step constitutes the addition of 84 μmol TEOS and 1.28 ml of NH₄OH and no additional ultrasonication. The steps were carried out a total of 4 times and the calcination procedure was the same as in SG2. This sample will be referred to as **T₉₂S₄^{SG3}_{21%}**.

The fourth SG synthesis method (**SG4**) is inspired by Ardagh et al.⁷⁸ Here, the amount of precursor added is not calculated in reference to the surface area of the support and the desired thickness, but referring to the amount of hydroxyl groups on the support. 0.1 g of anatase Ana₉₂ were dispersed in 4 ml ethanol abs. and 0.6 ml NH₄OH and ultrasonicated for 30 minutes. Then, 0.012 ml (54 μmol) of TEOS (one TEOS molecule per 2 hydroxyl groups) were added and the suspension was stirred for one hour. The steps of ultrasonication and TEOS addition were carried out a total of 4 times. The calcination procedure was the same as for SG2 and SG3. This sample will be referred to as **T₉₂S₄^{SG4}_{15%}**.

The combination of SG2, SG3 and SG4 led to the next synthesis methods in this work, SG5 and SG6. In **SG5**, each step constitutes of ultrasonication for 30 minutes, and the addition of 0.030 ml (134 μmol) TEOS and 8.2 ml NH₄OH to 0.25 g of anatase Ana₉₂ in 32 ml of ethanol abs.. This led to a sample series with up to 5 steps of TEOS addition. The single step sample is referred to as **T₉₂S₁^{SG5}_{4%}**, 2-step as **T₉₂S₂^{SG5}_{8%}** and so

on. For the full list, see [Table 3.1](#).

After this synthesis, I wanted to see if I could simply upscale the method to achieve a higher yield. Also, I ran out of the Ana₉₂ batch and switched to a new one, Ana₇₀. This led to a sample series with inhomogeneous layer thicknesses, and I decided to change the synthesis method. The ultrasonication time in each step was decreased to 10 minutes, to be able to add a 6th step in the course of one day, since stirring over night led to permanent agglomeration of the core-shell particles. The TEOS precursor was diluted 1:10 in ethanol abs. before addition to the suspension to achieve better dispersion of the precursor before deposition of the supports surface. The added TEOS amount for each step was decreased. Furthermore, all solutions were stirred until the last sample was done. This synthesis method **SG6** led to the next sample series: 1 g of anatase Ana₇₀ was dispersed in 128 ml ethanol abs. and ultrasonicated for 10 minutes. Then 0.9 ml of a 1:10 TEOS solution ((401 μmol)) and 5.7 ml NH₄OH were added and the suspension was stirred for 1 hour. This constitutes one step. The samples will be referred to as **T₇₀S1_{3%}^{SG6}**, **T₇₀S2_{6%}^{SG6}** and so on. For the full list, see [Table 3.1](#).

3 Methodology

Table 3.1: List of all relevant core-shell samples (without nanocavities) of this work.

Name	Method	Support [mmol]	Steps	Precursor/step [mmol]	Set
T₉₂S1^{SP}_{10%}	SP	6.25 Ana ₉₂	1	0.625 Na ₂ SiO ₃	-
T₉₂S2^{SP}_{20%}	SP	6.25 Ana ₉₂	2	0.625 Na ₂ SiO ₃	-
T₉₂S1^{SAM}_{7%}	SAM	25.0 Ana ₉₂	1	excess OTS	-
T₉₂S4^{SG1}_{7%}	SG1	1.25 Ana ₉₂	4	excess TEOS	-
T₉₂S7^{SG1}_{12%}	SG1	1.25 Ana ₉₂	7	excess TEOS	-
T₉₂S4^{SG2}_{21%}	SG2	1.25 Ana ₉₂	4	0.084 TEOS	-
T₉₂S4^{SG3}_{21%}	SG3	1.25 Ana ₉₂	4	0.084 TEOS	-
T₉₂S4^{SG4}_{15%}	SG4	1.25 Ana ₉₂	4	0.054 TEOS	-
T₉₂S0^{SG5}_{0%}	SG5	3.13 Ana ₉₂	0	-	1
T₉₂S1^{SG5}_{4%}	SG5	3.13 Ana ₉₂	1	0.134 TEOS	1
T₉₂S2^{SG5}_{8%}	SG5	3.13 Ana ₉₂	2	0.134 TEOS	1
T₉₂S3^{SG5}_{11%}	SG5	3.13 Ana ₉₂	3	0.134 TEOS	1
T₉₂S4^{SG5}_{15%}	SG5	3.13 Ana ₉₂	4	0.134 TEOS	1
T₉₂S5^{SG5}_{18%}	SG5	3.13 Ana ₉₂	5	0.134 TEOS	1
T₉₂S8^{SG5}_{26%}	SG5	3.13 Ana ₉₂	8	0.134 TEOS	-
^{2nd} T₉₂S2^{SG5}_{8%}	SG5	6.26 Ana ₉₂	2	0.268 TEOS	-
^{2nd} T₉₂S4^{SG5}_{15%}	SG5	6.26 Ana ₉₂	4	0.268 TEOS	-
T₇₀S1^{SG5}_{3%}	SG5	12.5 Ana ₇₀	1	0.407 TEOS	-
T₇₀S2^{SG5}_{6%}	SG5	12.5 Ana ₇₀	2	0.407 TEOS	-
T₇₀S3^{SG5}_{9%}	SG5	12.5 Ana ₇₀	3	0.407 TEOS	-
T₇₀S4^{SG5}_{12%}	SG5	12.5 Ana ₇₀	4	0.407 TEOS	-
T₇₀S5^{SG5}_{14%}	SG5	12.5 Ana ₇₀	5	0.407 TEOS	-
T₇₀S0^{SG6}_{0%}	SG6	12.5 Ana ₇₀	0	-	2
T₇₀S1^{SG6}_{3%}	SG6	12.5 Ana ₇₀	1	0.401 TEOS	2
T₇₀S2^{SG6}_{6%}	SG6	12.5 Ana ₇₀	2	0.401 TEOS	2
T₇₀S3^{SG6}_{9%}	SG6	12.5 Ana ₇₀	3	0.401 TEOS	2
T₇₀S4^{SG6}_{11%}	SG6	12.5 Ana ₇₀	4	0.401 TEOS	2
T₇₀S5^{SG6}_{14%}	SG6	12.5 Ana ₇₀	5	0.401 TEOS	2
T₇₀S6^{SG6}_{16%}	SG6	12.5 Ana ₇₀	6	0.401 TEOS	2

3.1.2 Synthesis of nanocavities

The synthesis of ultrathin SiO₂ shells containing nanocavities on TiO₂ was done by first grafting a bulky template onto the TiO₂ surface, followed by the deposition of an ultrathin SiO₂ shell around the templates and finally removal of those templates.

The template of choice was 4-tert-butyl[4]calixarene, a bulky molecule that is shaped like a crown (see Figure 2.11). In a standard grafting synthesis 300 mg of a TiO₂ nanopowder were dispersed in 150 ml of toluene abs. and 100 mg (excess) of 4-tert-butylcalix[4]arene were added to the suspension. The mixture was refluxed under inert atmosphere (N₂) for 48 hours and then filtered, yielding a brownish orange powder. This powder was dried for 24 hours at 120°C. This led to the sample $T_{P25}C_{667}^{48h}$, where 48 is the duration of refluxing the synthesis suspension in hours, 667 is the concentration of calixarenes in mg · l⁻¹ and P25 is the modification of TiO₂ used in this synthesis.

Several variations were applied to this standard synthesis. First, the duration of refluxing was reduced to 4 hours to see if the reaction is complete after a shorter synthesis, which led to the sample $T_{P25}C_{667}^{4h}$. Then the modification of the TiO₂ support was varied: I used P25 = T_{P25}, anatase = Ana₉₂/T_{ana} and rutile = T-rut, which led to $T_{P25}C_{667}^{48h}$, $T_{ana}C_{667}^{48h}$ and $T_{rut}C_{667}^{48h}$, respectively.

Two approaches were pursued to gain control over the amount of calixarenes on the TiO₂ surface. First, the amount of calixarene was reduced to 50, 25 and 12.5 mg, which led to $T_{ana}C_{333}^{48h}$, $T_{ana}C_{167}^{48h}$, and $T_{ana}C_{83}^{48h}$. When this did not lead to sufficient results, the amount of hydroxyl groups on the TiO₂ surface was changed with two methods: To increase the -OH groups an alkaline hydrogen peroxide (AHP) treatment was applied to TiO₂ by mixing 900 mg of anatase with 50 ml of an 8 M NaOH an 100 mM H₂O₂ solution and stirring it for 24 hours. It was then filtered and dried for 4 hours at 120°C, yielding a slightly yellow powder. To reduce the hydroxyl groups on the surface of TiO₂ the powder was calcined at 500°C for 4 hours (10 Kmin⁻¹). The powders were then used in a standard grafting synthesis, which led to the samples $T_{AHP}C_{667}^{48h}$ and $T_{calc}C_{667}^{48h}$.

Additional to the powders upon which calixarenes were grafted, several reference samples were made: 300 mg of the TiO₂ powder was refluxed or just stirred in pure toluene (abs.) for 4 hours, then filtered and dried according to the standard synthesis, which

3 Methodology

led to the samples $T_{P25}C_{refl}^{4h}$ and $T_{P25}C_{stir}^{0h}$.

The following samples were used for the synthesis of nanocavities: $T_{ana}C_{667}^{48h}$ and $^{2nd}T_{ana}C_{667}^{48h}$. 0.2 g of the calixarene samples were used as a support for the sol-gel synthesis method SG5. The amount of TEOS was downscaled according to the determined calixarene coverage of the surface to achieve comparable SiO_2 shell thicknesses. Other than that, the same procedure was used as described above. The calcination temperature of $325^\circ C$ is sufficient to remove the calixarene templates (see [subsection 4.2.1](#)).⁸²

Table 3.2: List of all relevant calixarene samples of this work.

Name	Calix. amount [mg/150ml]	Calix. conc. [mg/l]	Reflux [h]	Support [300 mg]
$T_{P25}C_{667}^{48h}$	100	667	48	T_{P25}
$T_{P25}C_{667}^{4h}$	100	667	4	T_{P25}
$T_{P25}C_{refl}^{4h}$	0	0	4	T_{P25}
$T_{P25}C_{stir}^{0h}$	0	0	0	T_{P25}
$T_{ana}C_{667}^{48h}$	100	667	48	Ana_{92}
$^{2nd}T_{ana}C_{667}^{48h}$	100	667	48	Ana_{92}
$T_{rut}C_{667}^{48h}$	100	667	48	T_{rut}
$T_{ana}C_{333}^{48h}$	50	333	48	Ana_{92}
$T_{ana}C_{167}^{48h}$	25	167	48	Ana_{92}
$T_{ana}C_{83}^{48h}$	12.5	83	48	Ana_{92}
$T_{AHP}C_{667}^{48h}$	100	667	48	Ana_{AHP}
$T_{calc}C_{667}^{48h}$	100	667	48	Ana_{calc}

Table 3.3: List of all relevant core-shell samples containing nanocavities of this work.

Name	Method	Support [mmol]	Steps	Precursor/step [mmol]
$T_{92}S4^{NC}$	SG5	$2.5 T_{ana}C_{667}^{48h}$	4	0.058 TEOS
$T_{92}S6^{NC}$	SG5	$2.5 ^{2nd}T_{ana}C_{667}^{48h}$	6	0.058 TEOS

3.2 Used chemicals

Table 3.4: List of chemicals used in this work.

Substance	Composition	CAS	Purity	Supplier
Ethanol (EtOH)	C ₂ H ₆ O	64-17-5	99.9% abs.	Acrox organics
Methanol (MeOH)	CH ₄ O	67-56-1	HPLC grade	VWR
Formaldehyde	CH ₂ O	50-00-0	37% in water	Roth
Formic acid	CH ₂ O	64-18-6	99%	VWR
Methyl formate	C ₂ H ₄ O ₂	107-31-3	>97%	Merck
Methylene Blue	C ₁₆ H ₁₈ ClN ₃ S	122965-43-9	”pure”	Merck
Methyl Orange	C ₁₄ H ₁₄ N ₃ NaO ₃ S	547-58-0	-	Merck
1-Nonanol	C ₉ H ₂₀ O	143-08-8	95%	Merck
5-Nonanol	C ₉ H ₂₀ O	623-93-8	>95%	Merck
Acetonitrile	C ₂ H ₃ N	75-05-8	99.9%	VWR
Toluene	C ₇ H ₈	108-88-3	abs.	VWR
Hydrogen peroxide	H ₂ O ₂	7722-84-1	35%	AppliChem
4-tert-butylcalix[4]arene	C ₄₄ H ₅₆ O ₄	60705-62-6	95%	Merck
Hexachloroplatinic acid	H ₂ PtCl ₆	18497-13-7	8 wt.% in H ₂ O	Merck
Anatase	TiO ₂	1317-70-0	99.7%	Merck
P25	TiO ₂	13463-67-7	99.8%	Degussa
Rutile	TiO ₂	1317-80-2	99.5%	Merck

3.3 Characterization

This section will give a description of the different methods I used for characterization of my core-shell catalysts. Electron microscopy is used for morphological and structural analysis at the nanoscale. In particular, transmission electron microscopy (TEM) with energy-dispersive X-ray spectroscopy (EDX) is a critical tool for the characterization of shell thickness and homogeneity. I will furthermore describe X-ray fluorescence (XRF) and X-ray scattering. A section on spectroscopy covers UV-vis diffuse reflectance (DRS), infrared (FTIR), photoluminescence (PL) and X-ray photoelectron spectroscopy (XPS). Surface characteristics are determined with physisorption studies (BET, BJH), zeta potential (ZP) and thermogravimetric analysis (TGA).

3.3.1 Transmission electron microscopy

Electron microscopy, in general, is based on the interaction of electrons with matter to obtain high-resolution images of structures at the nanoscale. Visible light microscopy has limitations regarding its resolution, which is, according to Abbe's law (Equation 3.2), limited by the wavelength of light. High-energy electron beams have de Broglie wavelengths which are in the range of picometers, as seen in the following equation including a relativistic correction:

$$\lambda = \frac{h}{m \cdot v} = \frac{h}{\sqrt{2m_0 \cdot eU_A(1 + \frac{eU_A}{2m_0c^2})}} = 2.51 \text{ pm} \quad (3.1)$$

where λ is the de Broglie wavelength, U_A is the acceleration voltage, here 200 kV, e is the elementary charge, m_0 is the mass of the electron, c is the speed of light, and h is the Planck's constant.

$$d = 0.61 \cdot \frac{\lambda}{\text{NM}} \quad (3.2)$$

According to Abbe's law, the resolution d is dependent on the wavelength and the numerical aperture (NM) of the optical system.

The incident electron beam is generated by an electron source (field emission gun, W filament), accelerated and focused with electromagnetic lenses onto the sample, where it interacts with the materials in various ways. For the electrons to reach the sample without collision with gases, ultra-high vacuum (UHV) is needed. In transmis-

sion electron microscopy (TEM) the electrons transmit through a thin sample and are imaged by a phosphorous screen or a CCD camera.

In this work, bright-field (BF) imaging mode was used, which images the part of the beam that is not diffracted or absorbed by the material, though it is also possible to obtain dark-field (DF) images and diffraction patterns. The contrast is due to the thickness or density of the sample, the atomic number, crystal structure or orientation, electron losses and more. With TEM it is possible to investigate the crystallinity and size of nanoparticles, though many other analysis techniques are often attached to the microscope to perform elemental analysis, e.g. energy-dispersive X-ray analysis (EDX) and electron energy loss spectroscopy (EELS).

For this work, the samples were measured on a FEI Tecnai G20 and a FEI Tecnai F20 (Thermo Fischer Scientific, Waltham, USA) with an acceleration voltage of 200 keV and a resolution of 0.24 nm. The powdered samples were dispersed in EtOH by stirring or ultra-sonication or taken out of a photocatalytic reactor containing water and methanol. The solution was dropped onto a copper grid, which are coated with a holey carbon film (200 mesh, Science Services GmbH, München) and then dried in ambient conditions.

3.3.2 Energy-dispersive X-ray spectroscopy

During TEM measurements, high energy electrons interact with the sample by removing an electron from their inner shell of the atoms. The orbital is then filled with an electron from a higher shell, leading to the release of energy, some of which is in the form of X-rays of a characteristic energy. The energy of the X-rays is determined in a silicon drift detector (EDAX Apollo XLTW SDD) with a resolution of <129 eV.

3.3.3 X-ray photoelectron spectroscopy

X-ray photoelectron spectroscopy is based on the photoelectric effect, i.e. the emission of electrons upon irradiation with photons, in this case, high energy X-ray photons which lead to emission of the core electrons of the sample. The binding energy (BE) of the emitted electrons is characteristic for the elements, and the chemical environment can be determined from the shifts in the BE of the electrons. The BE is determined

from the energy of the incoming photons (e.g. Al-K α , 1486.6 eV), the kinetic energy of the emitted electrons detected in the hemispherical analyzer and the work function of the detector. Due to the detection of electrons, the method is surface sensitive - the analysis depth ranges from 1 - 10 nm depending on the inelastic mean free path of the electrons in the materials and the angle between sample surface and detector.

The instrument used in this work is a custom-built SPECS XPS spectrometer with a Al-k α source (μ Focus 350, 1486.6 eV, beam energy and spot size: 70 W and 400 μ m, angle 51° to sample surface normal, base pressure: $5 \cdot 10^{-10}$ mbar, measurement pressure: $2 \cdot 10^{-9}$ mbar) and a hemispherical Phoibos WAL-150 analyzer (acceptable angle: 60°). The samples are mounted onto the sample holder with double sided carbon tape. Pass energies of 100 /30 eV and energy resolutions of 1 eV/100 meV are used for survey/detail spectra, respectively.

The data analysis was done with CASA XPS software, employing transmission corrections (as per instruments vendor's specifications), Shirley and Shirley Tougaard backgrounds and Scofield factors.⁹²⁻⁹⁴ The BE calibration was done by taking adventitious carbon (C-C) as a reference signal at 284.8 eV. The detection limits are in the range of 0.1-1 at.%, the accuracy is around 10-20%.

3.3.4 Total reflection X-ray fluorescence

Total reflection X-ray fluorescence (TXRF) is based on the emission of characteristic X-rays after a core electron has been removed by incoming high energy photons (X-rays) and an electron from an upper orbital has filled the empty orbital. The difference between EDX, XPS and this technique is that the first has an incoming electron beam and outgoing photons, the second has photons coming in and photoelectrons going out and the last one, XRF, has photons incoming and outgoing.

The incident angle of the incoming beam is below the critical angle of total reflection for the reflector (below a few mrad for a quartz reflector), which limits excitation to the outer layer of the sample, which is dispersed on the reflector. An energy-dispersive X-ray detector is placed above the substrate. It is used for trace analysis due to its detection limits in the pg range for excitation with X-ray tubes.

For this work an ATOMIKA 8030C X-ray fluorescence analyzer was used. It has a Mo X-ray tube (monochromatized K α : 17.5 keV, 50 kV and 47 mA for 100 s for X-ray

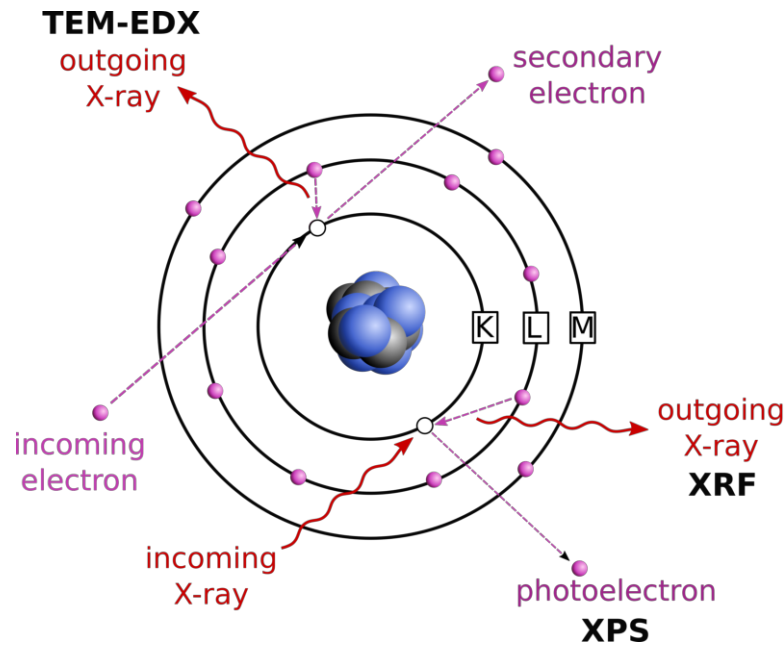


Figure 3.1: X-ray measurement techniques: TEM-EDX; an incoming electron removes a core electron, which gets filled by an electron from a higher orbital. The characteristic energy difference between the two orbitals is released as radiative energy and detected by an EDX detector. XPS; an incoming X-ray removes a core electron (photoelectron) which gets detected to determine the binding energy. XRF; an incoming X-ray removes a core electron, the hole is filled by a higher energy electron, and the characteristic energy difference between the orbitals is detected.

generation and an energy-dispersive Si(Li) detector. 1 mg of sample was fixed onto the reflector with a polyvinyl alcohol solution (5 μ l, 1%), which was dried before the measurement.

3.3.5 Small angle X-ray scattering

Small angle X-ray scattering is based on the elastic scattering (typically $0.1 - 10^\circ$) of electromagnetic waves at high energies when traveling through a material. It is non-destructive and quantifies density differences leading to structural information, e.g. particle shapes and sizes in the nanometer range.

The instrument used in this work was a Bruker AXS Nanostar with an Image Plate (Fujifilm) detector and Fuji FLA7000 to scan the image. A capillary was filled with the dry nanopowder or with a suspension in DI water before measurement. The data was radially averaged and evaluated via Fit2D, a free software by ESRF.

3.3.6 Infrared spectroscopy

Infrared (IR) spectroscopy is based on the transition of vibrational and rotational levels of materials upon interaction with electromagnetic waves in the infrared range. Far IR ($\tilde{\nu} = 400\text{-}10\text{ cm}^{-1}$, $\lambda = 25\text{-}1000\text{ }\mu\text{m}$) induces mainly rotation in molecules, mid IR ($\tilde{\nu} = 4000\text{-}400\text{ cm}^{-1}$, $\lambda = 2.5\text{-}25\text{ }\mu\text{m}$) and near IR ($\tilde{\nu} = 12500\text{-}4000\text{ cm}^{-1}$, $\lambda = 0.8\text{-}2.5\text{ }\mu\text{m}$) results in the vibration of molecular bonds.

The energy which is absorbed is characteristic for the type and strength of the bond (k) and the reduced mass (μ) of the molecule:

$$\tilde{\nu} = \frac{1}{2\pi c} \sqrt{\frac{k}{\mu}} \quad (3.3)$$

For a bond/vibrational mode to be IR active, its transition must include a change in the dipole moment of the molecule, and the selection rule, $\Delta v_i = \pm 1$, must be fulfilled.

Fourier Transform Infrared Spectroscopy

Fourier Transform Infrared Spectroscopy (FTIR) is a special kind of IR spectrometer, where the spectrum is not recorded by scanning through the wavelengths but calculated via Fourier Transformation (FT) from a measured interferogram. This is done in a Michelson interferometer, where a coherent light beam is split into two beams with a beam splitter. While one part reflects on a fixed mirror, the other part reflects on a moving mirror, back to the beam splitter where they recombine and superimpose. This results in an interferogram, which displays the intensity vs. the position of the moving mirror, which is then transformed to an IR spectrum with FT. The advantages are a faster analysis time, better signal-to-noise ratio and a higher optical throughput. FTIR analysis has therefore become a standard measuring technique.

Attenuated Total Reflection

Attenuated total reflection (ATR) is an IR sampling technique that is commonly used for the analysis of solids or opaque liquids. The incoming IR beam enters a prism of a high refractive index material (ATR crystal) under specific conditions (critical angle for total reflection) under which it undergoes total reflection multiple times. The

internal reflectance creates an evanescent field which extends beyond the surface of the ATR crystal, where it can interact with the sample. If IR frequencies are absorbed by vibrational modes of the sample, the evanescent wave will be attenuated. The depth of penetration of the evanescent wave, which is in the order of micrometers, is dependent on the wavelength, the refractive index of the ATR crystal and the sample and the incident angle. It is a qualitative analysis technique rather than a quantitative one and the spectra are not directly comparable to transmission FTIR spectra. Both limitations are due to the dependence of the penetration depth on the wavelength as well as on the extinction coefficients of the vibrational modes in the sample.⁹⁵

In this work, two ATR-FTIR machines were used: A PerkinElmer FTIR Spectral UATR-TWO with a spectrum Two Universal ATR (Single Reflection Diamond) crystal was used to characterize the core-shell samples of set 1; a Bruker IR Tensor 27 with a diamond ATR crystal was used to characterize core-shell samples of set 2 and the grafting of calixarenes during the synthesis of nanocavities.

3.3.7 UV-vis spectroscopy

In UV-vis spectroscopy visible and UV light is absorbed by matter by exciting valence electrons into higher energy levels, and can be emitted in radiative relaxation of excited electrons. The energy needed for the excitation is characteristic for a substance, e.g. molecule or compound, the method is non-destructive, it does not require physical contact with the sample and it can be used for transmission and reflectance spectroscopy. Therefore, UV-vis spectroscopy is a common method for qualitative and quantitative chemical analysis.

Diffuse reflectance spectroscopy

In diffuse reflectance spectroscopy (DRS) the UV-vis light is transmitted on a solid surface. Photons can penetrate the materials into a certain depth and interact with the matter through multiple reflections and absorptions. Additionally to specular reflection, some photons are diffusely scattered into different directions.

During the DRS measurement, a monochromator with a dispersive element scans through the desired wavelength range. The incoming light is transmitted onto the sam-

3 Methodology

ple surface and the reflected light is collected in an integrating sphere (Ulbricht sphere) where a representative portion is transferred to the detector.

In semiconductors, this method is often used to determine the bandgap. While a typical UV-vis spectrometer displays the information in a Reflectance [%] vs. wavelength [nm] for the determination of the bandgap, the information is transformed to display $(\alpha E)^{1/\gamma}$ vs. E [eV], where α is the absorption coefficient and γ is a factor that depends on the nature of the electron transition, e.g. it is 1/2 for direct and 2 for indirect transitions.⁹⁶ This α is often approximated with the Kubelka-Munk formula:⁹⁷

$$F(R_{\infty}) = \frac{(1 - R_{\infty})^2}{2R_{\infty}} = \frac{K}{S} \quad (3.4)$$

This $(F(R_{\infty})E)^{1/\gamma}$ vs. E plot is often referred to as Tauc plot, and used to determine the Tauc bandgap via intersection of a linear fit of this steep increase of the data with the x-axis. Strictly speaking, this method is only valid for amorphous, nanostructured and mixed-phase poly-crystalline materials.⁹⁷

In this work, DRS of powders was done with a Jasco V-670 UVvis photospectrometer with an Ulbricht-sphere inside a diffuse reflectance unit. The sample was positioned in a solid sample holder with a diameter of 3 mm.

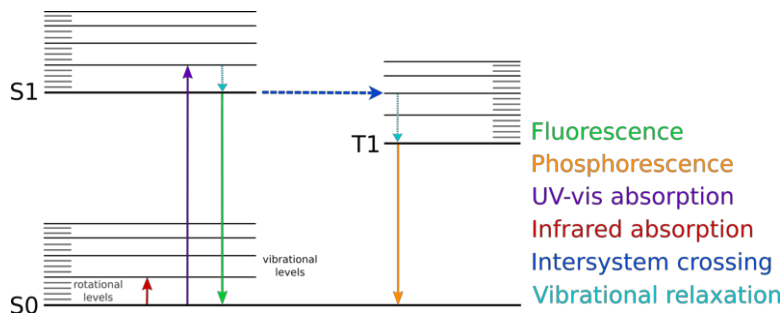


Figure 3.2: Optical spectroscopy techniques: Spectroscopy techniques involving UV-vis light include: Infrared absorption, leading to mainly vibrational transitions; UV-vis absorption leading to mainly electronic transitions; UV-vis absorption to a higher electronic and vibrational state followed by vibrational relaxation can lead to fluorescence, or, if intersystem crossing occurs, phosphorescence. S0 is the electronic ground state (singlet), S1 the excited singlet state and T1 the excited triplet state.

Photoluminescence spectroscopy

In photoluminescence spectroscopy, the material absorbs a photon from the UV-vis region to an excited vibrational level of an excited electronic level. It then undergoes vibrational relaxation, non-radiative. It then either relaxes electronically, which leads to fluorescence, or undergoes intersystem crossing, a forbidden transition involving a spin change of the electron, which leads to a much slower relaxation called phosphorescence. Some of the characteristic red-shifted energy released during relaxation is in the form of radiative energy, which is usually detected in an angle which excludes detection of the reflected or transmitted excitation beam.

The term fluorescence spectroscopy is used for a standard analysis technique for fluorescent molecules, including many biostructures such as proteins. It is often used in biochemical, medical and chemical analysis. Photoluminescence spectroscopy is often applied for semiconducting materials in materials science, to analyze electronic transitions, charge transfer mechanisms and defect types and concentrations.

Photoluminescence studies can be performed in several ways: In excitation spectroscopy the best wavelength for absorption of a materials can be determined and in emission spectroscopy the radiative recombination of electrons and holes can be quantified. Emission spectroscopy can be done in a time-resolved measurement, which determines the lifetime of excited state which can lead to fluorescence (typically 10^{-9} to 10^{-6} s) or phosphorescence (typically 10^{-3} to 10^2 s).⁹⁸

In this work, a photoluminescence spectrometer by Picoquant (FluoTime 300), with two double monochromators for emission and detection, an Xe lamp to scan in the wavelength range of 250 to 800 nm and a laser source at 378 nm, which is coupled to the detector with a state-of-the-art time-correlated single photon counting (TCSPC) system to detect the first photoluminescent photon that arrives at the detector after the sample has been excited with a picosecond laser pulse.

3.3.8 Zeta potential

The Zeta Potential is the electric potential (Coulomb potential) at the shear surface or slipping plane of a mobile particle in a suspension. Outside of the particle several planes can be described: The Stern plane, which contains the Helmholtz double layer

of tightly bound ions, and the shear plane, which contains loosely bound ions. These ions balance the particle's surface charge and the suspended particle and its solvation layer becomes neutral.

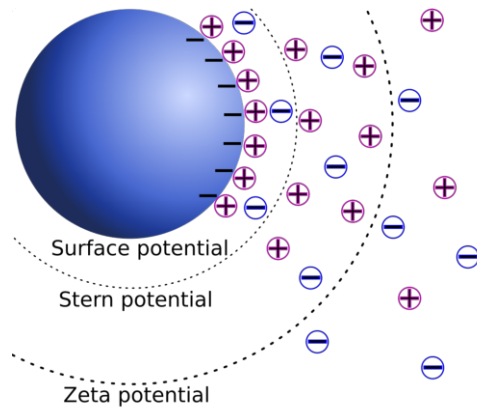


Figure 3.3: The Zeta Potential of a negatively charged particle in suspension.

If the particle moves through the liquid, some ions of the diffuse layer are removed through friction and the particle regains some of its potential. This potential is called Zeta Potential (ZP). Its charge polarity is the same as the surface potential, though the ZP generally has a lower value.

By applying an electric field to the suspension the charged particles are set into movement. A laser beam, that is transferred through the solution, is scattered on the moved particles which leads to a Doppler shift. This

doppler shift is measured and then used to determine the electrophoretic mobility. Different models can be used to convert the electrophoretic mobility to the ZP; the choice is dependent on the particle size and thickness of the electric double layer. Nanoparticles in low electrolyte concentration suspensions can be treated with the Hückel equation:

$$\mu_e = \frac{2\varepsilon\zeta}{3\eta} \quad (3.5)$$

where μ_e is the electrophoretic mobility, ε is the permittivity of the solution, ζ is the Zeta Potential and η is the viscosity.

By varying the pH of the suspension, a Zeta Potential curve can be determined, where the intercept of the curve with the x-axis is used to determine the isoelectric point (IEP) of a metal oxide. This is the pH where the surface charge of the particle is zero, which means that the particles do not rebel each other and agglomerate strongly.^{99,100} If the pH of a suspension is lower (higher) than the IEP of a metal oxide, then the surface is negatively (positively) charged. A Zeta Potential above 30 mV (or below -30 mV) means that the particles are sufficiently charged to repel each other and they are well dispersed in the suspension. Between 0 and 30 mV they are weakly agglomerated.

In this work a ZetaPlus (Brookhaven Instruments Corporation) Zeta Potential Analyzer was used. Sample preparation was done by weighing 10 mg of the metal oxide, filling

it up with 10 ml of HPLC water and ultrasonicing it for 5 minutes. It was then stirred for 24 hours (aging) before it was diluted further 1:500, by dispersing 0.2 ml in 10 ml of HPLC water. The pH was then adjusted with HCl and NaOH to 1, 3, 5, 7 and 9, which was determined with a glass electrode. The measurements were done in a plastic cuvette, which was flushed with the suspension before measurement. Each measurement was repeated three times. The Hückel model was used to convert the mobility data in Zeta Potential values.

3.3.9 Physisorption studies

Physisorption measurements are done at low temperatures ($T = 77\text{ K}$) by dosing small amounts of an inert gas, such as N_2 and Argon, which adsorbs on the sample surface due to non-covalent attractive forces, and then decreasing the amount of adsorbed gas in the sample room, which leads to desorption. Via measuring and evaluating the amount of adsorbed and desorbed gas molecules and the adsorptive pressure, which are illustrated in isotherms, the specific surface area and pore characteristics of the sample can be unraveled.

In this work, Brunauer-Emmet-Teller (BET), deBoer t-plot methods and Barret-Joyner-Halenda (BJH) were used to evaluate the gas adsorption data. BET is a common method that is based on multilayer adsorption theory, an expansion of the Langmuir adsorption theory. The Langmuir theory is based on the monolayer formation of adsorbates on a surface in idealized conditions from which the Langmuir equation is derived, which describes the fractional coverage ϑ_A of the surface:

$$\vartheta_A = \frac{[A_{\text{ad}}]}{[S_0]} = \frac{K_{\text{eq}}^A \cdot p_A}{1 + K_{\text{eq}}^A \cdot p_A} \quad (3.6)$$

where $[A_{\text{ad}}]$ is the surface concentration of the adsorbate A [m^{-2}], S_0 is the total number of surface adsorption sites, K_{eq}^A is the equilibrium adsorption constant and p_A is the partial pressure of A.

The BET theory incorporates the possibility of multilayer formation during adsorption, and is based on the assumptions that the Langmuir theory can be applied to each layer, the adsorbents only interact with adjacent layers and the enthalpy of the first layer is greater than of the second and higher layer. This leads to the BET equation and the

surface coverage ϑ_{BET} :

$$\vartheta_{\text{BET}} = \frac{n_{\text{ads}}}{n_{\text{m}}} = \frac{C \cdot p}{(p_0 - p) \left(1 + (C - 1) \left(\frac{p}{p_0}\right)\right)} \quad (3.7)$$

where n_{ads} is the amount of adsorbate, n_{m} is the monolayer equivalent, p and p_0 are the equilibrium and saturation pressure of the adsorbates and C is the BET C -constant:

$$C \approx e^{\frac{q_1 - q_2}{RT}} \quad (3.8)$$

BJH is used to determine the pore characteristics, such as pore diameter, pore volume and pore size distribution of mesopores and small macropores. It is based on the Kelvin model of pore filling.

The DeBoer t-plot method is used to determine the micropore volume of microporous materials and, by subtracting from the BET surface area, determine the external surface area. This is done by comparing with standard isotherms of a non-porous reference.¹⁰¹

N_2 physisorption measurements were done at 77 K on an ASAP 2010 and ASAP 2020 instrument by Micromeritics GmbH (Aachen, Germany). Prior to the measurements, the samples (≈ 250 mg) were heated up to 80 - 150°C in vacuum for several hours.

3.3.10 Thermogravimetric analysis

Thermogravimetric analysis (TGA) is a thermal analysis method which measures the changes in mass when a sample is heated in a specific atmosphere. Mass losses can be due to several processes, such as desorption of physisorbed water on the surface, hydrolysis of surface hydroxyl groups, combustion of organic substances, oxidation of metals of reduction in reductive atmospheres.

TGA measurements were done with a TGA 8000 (Perkin Elmer). The heating rate was either 5 or 10 K/min and a gas flow of 20 ml/min of synthetic air was used. 5 mg of the sample was used as a starting mass. Before the measurement, the sample was held at 120-200°C for 2 hours to remove physisorbed water.

3.4 Photocatalytic experiments

Photocatalytic hydrogen evolution and dye degradation experiments were performed in three different closed reactors which were designed for their specific purposes. All reactors were water cooled and the reaction solution was illuminated by an Thorlabs LED with a maximum at 365 nm (± 10 nm). Further details about the experiments, such as detection methods, rate calculations, etc. can be found in the following subsections.

3.4.1 Organic dye degradation

To evaluate the photocatalytic activity towards combustion of organic molecules, 10 mg of the catalyst powder was ultrasonicated for 10 min in 50 ml of an aqueous solution of methyl orange (MO, $C_{14}H_{14}N_3SO_3-Na^+$, 8 mg/l) or methylene blue (MB, $C_{16}H_{18}N_3S^+Cl^-$, 8 mg/l). The amount of catalyst and the dye concentration were optimized to lead to a 20-60% decolorization for the uncoated reference Ana₉₂ catalyst, to make sure differences in conversion are apparent. The chosen dye concentration ensures an optimum in UV-vis absorption, yet leaves the solution diluted enough to apply a simplified Langmuir-Hinshelwood model.

First, the suspension was stirred in the dark in a closed, water cooled reactor for 2 h, where a portion of 2.5 ml was collected and filtered through a syringe filter (Polypropylene, 0.45 μ m) every 60 minutes for adsorption studies (Figure 3.4). The amount of adsorbed dye was calculated by using the following equation:

$$q_t [g \cdot m^{-2}] = \frac{(c_b - c_t) [g \cdot l^{-1}] \cdot V [l]}{m [g] \cdot SSA [m^2 \cdot g^{-1}]} \quad (3.9)$$

where c_t is the concentration of the dye in the suspension after 2 hours, c_b is the concentration of the solution without a catalyst after 2 hours, V is the volume of the suspension, m is the catalysts mass (mg) and SSA is the selective surface area of the catalyst.

After adsorption studies have been performed, the suspension was illuminated with maximum intensity. The average distance between the light source and the suspension was 14 cm and the photon flux at this height was $6.7 \cdot 10^{20} s^{-1}$, calculated according to

3 Methodology

the following equation:

$$\Phi [\text{m}^{-2} \cdot \text{s}^{-1}] = \frac{P [\text{W}] \cdot \lambda [\text{m}]}{(h [\text{J} \cdot \text{s}] \cdot c [\text{m} \cdot \text{s}^{-1}] \cdot A [\text{m}^2])} \quad (3.10)$$

where Φ is the photon flux, P is the power measured with a power meter with an effective area $A = 0.31 \cdot 10^{-3} \text{ m}^2$, N_A is the Avogadro constant, h is Planck's constant and c is the speed of light in vacuum.

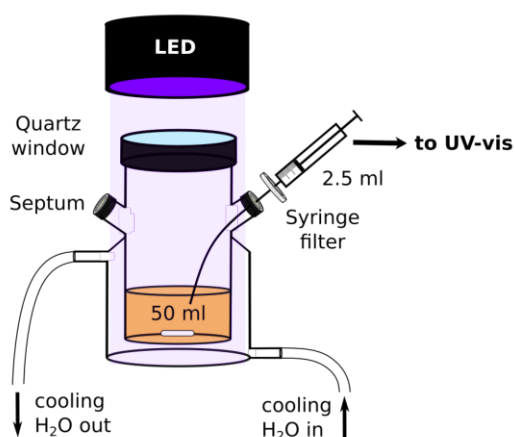


Figure 3.4: Setup of the organic dye degradation setup. A photocatalyst is suspended in 50 ml of an aqueous dye solution, which is stirred, cooled and illuminated with an LED lamp at 365 nm. A portion of 2.5 ml is collected at specific time intervals to be analyzed via UV-vis spectroscopy.

Portions of 2.5 ml were removed from the solution after intervals of irradiation. The decolorization of the solutions was analyzed in UV-vis spectroscopy and the peak areas (340-600 nm for MO, 420-800 nm for MB) were evaluated to compare the photocatalytic activity of the samples.

Apparent rate constants of the first 30 minutes of photocatalytic decolorization were determined with a simplified Langmuir-Hinshelwood scheme for low concentrations resembling a first-order rate law:

$$c = c_0 \cdot e^{-k \cdot t} \quad (3.11)$$

where c_0 is the initial concentration after reaching adsorption equilibrium, k is the

apparent first order rate constant and t is the time in seconds.^{102,103}

3.4.2 Online HER experiments

Online HER experiments were done in a custom-made flow reactor, through which a carrier gas (argon 5.0) flows through the solution with 30 ml min^{-1} (mass flow controller by Q-Flow 140 Series, MCC Instruments), then goes through a CaCl_2 trap and a water trap (model WT 20.5 N, SUN-Control-Analytik GmbH) before it goes to an online analyzer (X-Stream, Emerson) which quantifies H_2 with a thermal conductivity detector (TCD), and CO_2 and CO with a photometric non-dispersive infrared (IR) gas sensor. The water cooling temperature is controlled with a cryostat at 15°C for most of the experiments shown in this work. Earlier experiments were cooled with an in-house water cooling system without a specified temperature. The suspension in the reactor (100 ml) was illuminated with an LED lamp at 365 nm from the top through a quartz glass.

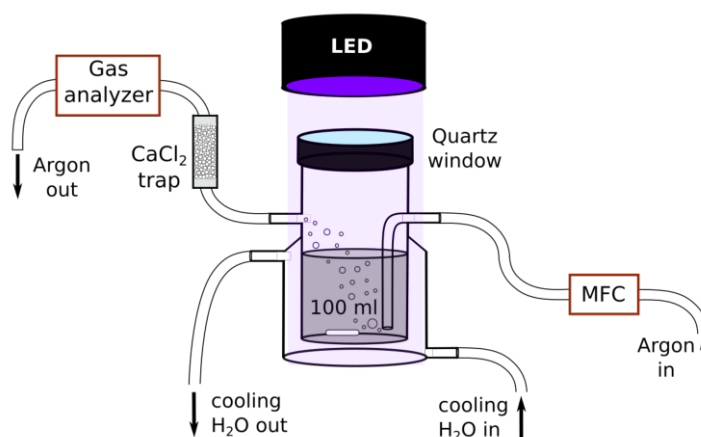


Figure 3.5: Setup of the online HER setup: An Argon gas stream of 30 ml/min is transferred through 100 ml of a stirred, cooled suspension of the catalyst in a 1:1 H_2O :methanol solution containing specific amounts of the Pt co-catalyst precursor. The suspension is illuminated with maximum intensity at 365 nm . The gas mixture is transferred through a water trap to the gas analyzer, which detects H_2 , O_2 , CO_2 and CO .

The experiments were performed with in-situ photodeposition of the co-catalyst Pt. 20 mg of the catalyst (TiO_2 anatase or core-shell samples) was ultrasonicated in a 1:1 $\text{MeOH}:\text{H}_2\text{O}$ solution for 60 seconds. After placing the suspension in the reactor,

3 Methodology

it was cooled and flushed with argon. Then, 50 μl of a prepared hexachloroplatinic acid (H_2PtCl_6) stock solution was added to the suspension. In many experiments, this addition was done in the dark, as visible light reduces some of the Pt^{4+} .

Calculation of the activity

The signal output of the gas analyzer is in ppm, which needs to be converted to absolute values using the ideal gas law:

$$pV = nRT \quad (3.12)$$

The activity is then calculated according to:

$$\begin{aligned} \text{activity } [\mu\text{mol} \cdot \text{h}^{-1}] &= \frac{\text{activity } [\text{ppm}]}{10^6 \text{ ppm}} \cdot \text{flowrate } [\text{ml} \cdot \text{min}^{-1}] \cdot \frac{\text{m}^3}{10^6 \text{ ml}} \\ &\cdot \frac{60 \text{ min}}{\text{h}} \cdot \frac{p \text{ [Pa]}}{T \text{ [K]} \cdot R \text{ [m}^3 \cdot \text{Pa} \cdot \text{mol}^{-1} \cdot \text{K}^{-1}]} \cdot \frac{10^6 \mu\text{mol}}{\text{mol}} \quad (3.13) \\ &= \frac{\text{activity } [\text{ppm}] \cdot \text{flowrate } [\text{ml} \cdot \text{min}^{-1}]}{407.5 \text{ [ppm} \cdot \text{ml} \cdot \text{h} \cdot \text{min}^{-1} \cdot \mu\text{mol}]} \end{aligned}$$

The average distance from the lamp to the suspension was 10 cm and the estimated photon flux was $\Phi = 2.5 \cdot 10^{21} \text{ m}^{-2} \text{ s}^{-1}$ (Equation 3.10).

With the illuminated area of the reactor, $A_{\text{reactor}} = 2.8 \cdot 10^{-3} \text{ m}^2$, it is possible to determine the number of incident photons per second (Equation 3.14).

$$\# \text{ of incident photons } [\text{s}^{-1}] = \Phi \text{ [m}^{-2} \text{ s}^{-1}] \cdot A_{\text{reactor}} \text{ [m}^2] \quad (3.14)$$

The number of H_2 molecules produced per second can be determined via Equation 3.15:

$$\# \text{ of H}_2 \text{ molecules } [\text{s}^{-1}] = \frac{\text{activity } [\mu\text{mol} \cdot \text{h}^{-1}] \cdot N_{\text{A}} \text{ [N} \cdot \text{mol}^{-1}]}{3600 \text{ [s} \cdot \text{h}^{-1}] \cdot 10^6 \text{ [\mu mol} \cdot \text{mol}^{-1}]} \quad (3.15)$$

Finally, the quantum yield or photonic efficiency can be calculated according to:

$$\text{Quantum yield } [\%] = \frac{\# \text{ of H}_2 \text{ molecules } [\text{s}^{-1}] \cdot 2}{\# \text{ of incident photons } [\text{s}^{-1}]} \cdot 100 \quad (3.16)$$

Calculation of the co-catalyst amount

For this stock solution, 200 μl of a concentrated H_2PtCl_6 solution by Merck (8% in H_2O , $\rho(\text{Pt}) = 40 \text{ g l}^{-1}$) was diluted to 10 ml ($4.1 \cdot 10^{-3} \text{ mol} \cdot \text{l}^{-1}$) which contains 8 mg of Pt. To calculate the volume to be added to the suspension, we assume a total reduction of Pt^{4+} to Pt^0 :

$$c_{\text{stock}} = \frac{c_{\text{H}_2\text{PtCl}_6} [\text{wt.}\%] \cdot V_{\text{pipette}} [\text{ml}] \cdot \rho_{\text{H}_2\text{PtCl}_6} [\text{g} \cdot \text{ml}^{-1}]}{M_{\text{H}_2\text{PtCl}_6} [\text{g} \cdot \text{mol}^{-1}] \cdot V_{\text{flask}} [\text{ml}]} \quad (3.17)$$

$$= \frac{0.8 \cdot 0.2 \cdot 1.05}{409.81 \cdot 0.010} = 4.1 \cdot 10^{-3} \text{ mol} \cdot \text{l}^{-1}$$

$$V_{\text{stock}} = \frac{m_{\text{catalyst}} [\text{g}] \cdot c_{\text{co-catalyst}} [\text{wt.}\%]}{M_{\text{H}_2\text{PtCl}_6} [\text{g} \cdot \text{mol}^{-1}] \cdot c_{\text{stock}} [\text{mol} \cdot \text{l}^{-1}]} = \quad (3.18)$$

$$= \frac{0.02 \cdot 0.2}{195.084 \cdot 4.1 \cdot 10^{-3}} = 50 \mu\text{l}$$

The error of this stock solution was calculated according to gaussian error propagation with the uncertainties of the eppendorf pipettes and volumetric flasks provided by the company:

$$\rho(\text{Pt})_{\text{stock}} = \rho(\text{Pt})_{\text{H}_2\text{PtCl}_6} [\text{g} \cdot \text{l}^{-1}] \cdot \frac{V_{\text{pipette}} [\mu\text{l}]}{V_{\text{flask}} [\mu\text{l}]} \quad (3.19)$$

$$= 40 \cdot \frac{200 \pm 2.5}{10000 \pm 25} = 0.8 \text{ g} \cdot \text{l}^{-1} \pm 1.3\%$$

$$m(\text{Pt})_{\text{reactor}} = \rho(\text{Stock}) [\text{g} \cdot \text{l}^{-1}] \cdot V_{\text{pipette}} [\mu\text{l}] \quad (3.20)$$

$$= 0.8 \pm 0.95\% \cdot 50 \pm 2.5 = 40 \mu\text{g} \pm 5.2\%$$

As can be seen, the preparation of the stock solution only has a small error, provided that the operator did not make any additional errors. However, the addition of the stock solution to the reactor solution shows a bigger error (5%), coming from the error of the eppendorf pipette. After addition, the reactor was closed and the baseline was stable in the online analyzer after 60 minutes. The suspension was then illuminated for 30, 150 or 1080 minutes (short-, mid- and longterm experiments). The baseline values before and after the illumination were used to correct the drift by subtracting a straight line from the data points.

Calculation of the co-catalyst surface area

The Pt surface area was calculated according to the following reactions. Due to the different wetting behaviors of Pt on the TiO₂ and SiO₂ surface, we assumed the particles to have a hemispheric form and calculated the accessible surface area of the round part only.⁴⁴ All dimensions are SI base units.

The upper surface area (A) and the volume of a single hemisphere, A_{hs} and V_{hs} , respectively, were calculated according to:

$$A_{\text{hs}} = 2 \cdot \pi \cdot r^2 \quad (3.21)$$

$$V_{\text{hs}} = 2 \cdot \pi \cdot r^3 \quad (3.22)$$

where r is the radius taken from the diameter measured via TEM (see [Table 6.2](#)).

The measured relative mass of Pt was multiplied by the catalysts mass used in an HER experiment to determine the absolute Pt mass m . The amount of hemispheric nanoparticles N were determined via

$$N = \frac{m}{\rho \cdot V_{\text{hs}}} \quad (3.23)$$

where $\rho = 21.45 \text{ g} \cdot \text{cm}^{-3}$ is the density of Pt.

Multiplying N with the surface area of one particle SA_{hs} can be simplified to total surface area accessible

$$A_{\text{tot}} = A_{\text{hs}} \cdot N = \frac{m}{\rho \cdot r} \quad (3.24)$$

3.4.3 Size selective hole scavenging

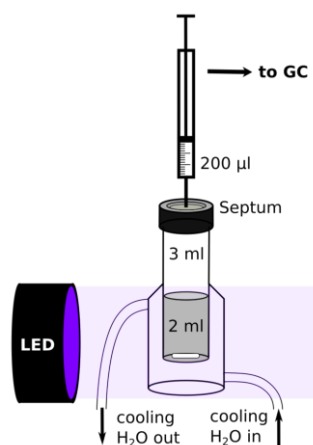


Figure 3.6: Setup of the size selective HER setup

Size selective hole scavenging was done with TiO_2 – SiO_2 core-shell nanoparticles described in the former sections, but the SiO_2 shell has cavities of ≈ 1 nm in diameter, giving access to some sacrificial agents (SAs) while discriminating others. The hydrogen evolution experiments (HER) done with size-selective catalysts were done without a co-catalyst, as the co-catalyst nanoparticles would fill the nanocavities, blocking the access of the SAs to the TiO_2 surface.

Due to the low activity of pure TiO_2 in photocatalytic HER, the detection was done by sampling a small gas amount from the head space from the reactor which was analyzed with a gas chromatograph (GC). To achieve detectable concentrations, a small reactor was chosen for these experiments, which also reduced the amount of solvent and catalyst.

The reactor of choice contains a volume of 3 ml in total, of which 2 ml were filled with the solvent, leaving 1 ml of gaseous head space. Of this head space 200 μ l were sampled every 30 minutes to be analyzed with a Shimadzu GC-2030, containing a 2m Shincarbon column and a BID detector. The GC was calibrated for H_2 , CO and CO_2 and the results are presented in ppm. The temperature of the reactor was kept constant with water cooling at 15°C . 5 mg of the catalyst was suspended in 2 ml of water, SA and acetonitrile, ultrasonicated for 60 second and the transferred to the reactor, which was closed gas-tight with a cap containing a septum. The reactor, which consists of

3 Methodology

quartz, was illuminated from the side. Total illumination lasted three hours.

4 Preliminary studies

In this chapter I will give a detailed description of the preliminary characterizations of the core-shell and nanocavities samples. I will also describe how several parameters influence the activity and early-stage deactivation (ESD) during photocatalytic HER and reproducibility of all photocatalytic (PC) experimental setups used in this project.

4.1 Characterization of core-shell nanoparticles

In this section I will discuss the results of preliminary characterizations of the core-shell samples. These include the analysis of the shell thickness and structure with microscopic, spectroscopic and physisorption methods. I will further show the analysis of the interfaces and the shells influence on physical and chemical properties with spectroscopic and electrokinetic analysis methods.

4.1.1 Shell thickness and surface properties

Introduction

There are several options to determine the layer thickness of a compound. Examples are ellipsometry, some electrochemical measurements, optical scattering and several microscopy techniques.^{79,99,104} Some of those techniques are only applicable for 2D materials and others have an insufficient detection limit for nanoparticles, where characterization is only valid if the shell exceeds a threshold thickness.¹⁰⁵ When dealing with ultrathin shells - below one nanometer - the characterization of the shell thickness becomes more challenging.

In this project, several ultrathin shell thickness characterizations were tested and com-

pared. First, I measured the particle diameters with Small Angle X-Ray Scattering (SAXS). The shell thickness can be determined from the differences in particle sizes. Two modes of sample preparation were applied; in an aqueous suspension and as a dry powder. While SAXS has a lot of potential in measuring the particle sizes and shapes, it was difficult to evaluate the measured data due to the formation of agglomerates - which is characteristic for TiO₂ nanoparticles. We achieved better results with the complementary techniques Transmission Electron Microscopy (TEM) and Energy Dispersive X-Ray Spectroscopy (EDX), by comparing the determined shell thickness from both methods. In TEM images, a visible amorphous shell was measured at different spots. With EDX, the ratio of Si to Ti was determined and the shell thickness of SiO₂ was calculated from the ratio, assuming that the shell coverage was uniform and homogeneous:

$$d = \frac{M_{\text{shell}} \cdot r_{\text{aSi}}}{A \cdot \rho \cdot M_{\text{bulk}} \cdot r_{\text{aTi}}} \cdot 10^3 \text{ [nm]} \quad (4.1)$$

where M_{shell} is the molecular mass of SiO₂, M_{bulk} is the molecular mass of TiO₂, r_{aSi} and r_{aTi} are the ratios of Si and Ti from EDX, A is the surface area of 1 g TiO₂ and the density of amorphous SiO₂ was taken as $\rho = 2 \text{ g} \cdot \text{cm}^{-3}$.

Before the thickness calculation, I corrected with a factor containing the differences between a rectangular layer box and a spherical shell ("curvature factor"):

$$V_{\text{ss}} = \frac{\frac{4}{3} \cdot \pi (R^3 - r^3)}{d \cdot 4 \cdot \pi \cdot r^2} \quad (4.2)$$

The numerator holds the volume of a spherical shell. The average inner radius "r" from TEM measurements was $r = 8.5 \text{ nm}$ and outer radius "R" was "r" plus the desired thickness, respectively. The denominator holds the volume of a rectangular box with the surface area of a shell as a base. The calculated thickness from [Equation 4.1](#) was divided by this curvature factor of the spherical shell V_{ss} to get a more accurate thickness value.

When TiO₂ is covered with an SiO₂ shell, the surface characteristics change significantly. When dispersed in water, different metal oxides have different effects on the pH of the suspension, depending on the density of surface hydroxyl groups and the likelihood of their protons to dissociate. Proton dissociation changes the surface charge,

which is a characteristic value for a metal oxide. The change of surface charge was determined for different shell thickness by measuring the Zeta Potential (ZP). The ZP can be used to calculate the apparent surface coverage of core-shell particles but the results were not conclusive.⁵⁷ This method does not seem to work for ultrathin shells, which could be due to a "subsurface effect": The surface charge is influenced by the underlying bulk TiO₂ until the shell reaches a critical thickness, and only then does the surface charge have similar values as pure SiO₂. The surface coverage was therefore determined with TEM and correlates with the calculated thicknesses from the TEM-EDX results (Equation 4.1).

To determine the specific surface area (SSA) and porosity of the shell, N₂ physisorption at 77 K was measured for the most relevant samples and the results were analyzed via BET. The BET surface area includes all the surface area that N₂ can access, i.e. on which it can adsorb and desorb. To get information about the porosity the t-plot method was used to determine the microporous volumes of the samples and their contribution to the BET SSA. With the difference in micropore SSA and BET SSA, the external SSA, i.e. the externally accessible SAA for reactants which are too large to fit into micropores, was determined.¹⁰¹

Salt precipitation samples

The TEM images of the salt precipitation samples show that T₉₂S_{20%}^{SP} has a homogeneous shell thickness of 3.05 ± 0.87 nm, while the shell of T₉₂S_{10%}^{SP} was not visible (see Figure 4.1b and c). EDX analysis revealed a shell thickness for T₉₂S_{20%}^{SP} of 0.27 ± 0.06 nm and for T₉₂S_{10%}^{SP} of 0.05 nm (see Table 4.1). The big difference of the shell thickness for T₉₂S_{20%}^{SP} determined via TEM and EDX is possibly due to an agglomeration of the nanoparticles during the synthesis - during formation of the silica shell the particles grew together and formed a larger agglomerate. Good dispersion during the synthesis is crucial for a homogeneous coverage of the nanoparticles.

In SAXS measurements of the aqueous suspensions, the diameter of pure TiO₂ nanoparticles was determined to be 13 nm, while the T₉₂S_{20%}^{SP} sample had a diameter of 14.2 nm. According to this, the shell thickness is 0.6 nm. The SAXS measurement of the dry, powdered samples resulted in a diameter of 7.6 ± 3.4 nm for TiO₂ and 9.4 ± 2.6 nm for T₉₂S_{20%}^{SP}. This leads to a shell thickness of 0.9 ± 4.2 nm. Both measurement methods, as a dry powder and in a suspension, led to different results, with a standard

4 Preliminary studies

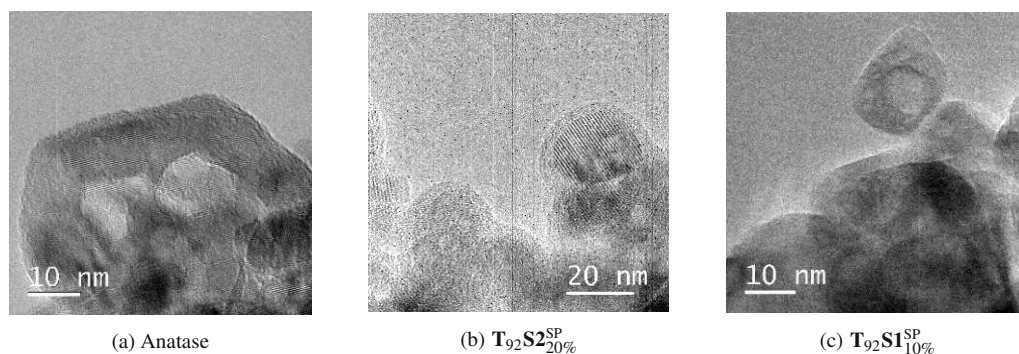


Figure 4.1: Transmission electron microscopy (TEM) images of salt precipitation TiO_2-SiO_2 core-shell nanoparticles. (a) is pure anatase Ana_{92} ; (b) $T_{92}S_{20\%}^{SP}$ has a 2-3 nm thick visible layer; (c) $T_{92}S_{10\%}^{SP}$ has no visible layer.

deviation that is higher than the determined shell thickness.

Self-assembled monolayers

The TEM image of the molecular self assembly core-shell sample $T_{92}S_{7\%}^{SAM}$ shows a very thin, inhomogeneous, barely visible layer of approximately 0.5 nm (see Figure 4.2a). EDX analysis revealed a shell thickness of 0.14 ± 0.02 nm, but this value assumes a homogeneous coverage, while the TEM images show that only some areas are covered with an ultrathin layer of SiO_2 . It was therefore concluded, that this method does not lead to a homogeneous monolayer.

Table 4.1: Physical properties of core-shell TiO_2-SiO_2 nanoparticles: Calculated thickness as expected from the synthesis, SiO_2 shell thicknesses determined from the average of 10 elemental ratios measured by EDX and 10 thickness measurements from TEM images. *Shells are too thin to be detected.

Sample		Shell thickness [nm]		
Name	steps	calc.	EDX	TEM
$T_{92}S_{0\%}^{SG5}$	0	0	0.03 ± 0.03	0
$T_{92}S_{10\%}^{SP}$	1	0.38	0.05 ± 0.04	*
$T_{92}S_{20\%}^{SP}$	2	0.86	0.27 ± 0.06	3.05 ± 0.87
$T_{92}S_{7\%}^{SAM}$	1	0.30	0.14 ± 0.02	≈ 0.5
$T_{92}S_{7\%}^{SG1}$	4	1.2	0.03 ± 0.04	*
$T_{92}S_{12\%}^{SG1}$	7	2.1	0.06 ± 0.01	*

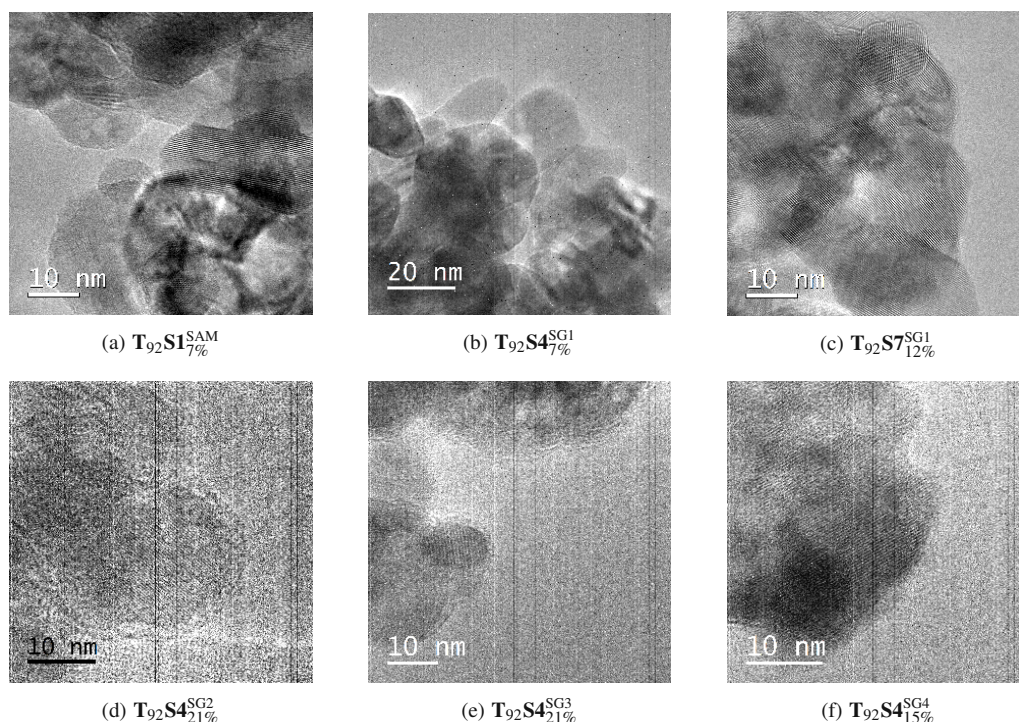


Figure 4.2: Transmission electron microscopy (TEM) images of molecular self assembly and sol-gel TiO_2 - SiO_2 core-shell nanoparticles. (a) $\text{T}_{92}\text{S1}_{7\%}^{\text{SAM}}$ has a thin, visible layer; (b) $\text{T}_{92}\text{S4}_{7\%}^{\text{SG1}}$ and (c) $\text{T}_{92}\text{S7}_{12\%}^{\text{SG1}}$ have no visible layer; (d) $\text{T}_{92}\text{S4}_{21\%}^{\text{SG2}}$ has a thin, visible layer; (e) $\text{T}_{92}\text{S4}_{21\%}^{\text{SG3}}$ has a 1.2 nm thick layer and (f) $\text{T}_{92}\text{S4}_{15\%}^{\text{SG4}}$ has a thin, inhomogeneous layer.

Sol-gel samples

There are many sol-gel samples in this project that have been characterized and I want to go through them chronologically. My first attempt in stepwise sol-gel synthesis was to filter and hydrolyze after each step of TEOS addition, which led to the samples $\text{T}_{92}\text{S4}_{7\%}^{\text{SG1}}$ and $\text{T}_{92}\text{S7}_{12\%}^{\text{SG1}}$ - 4 steps and 7 steps of TEOS addition, ideally leading to 4 and 7 monolayers of SiO_2 on the surface, respectively. The TEM images of these samples are shown in Figure 4.2b and c. No shell is visible in these samples. EDX analysis of $\text{T}_{92}\text{S7}_{12\%}^{\text{SG1}}$ revealed a Si/Ti ratio that leads to a 0.06 ± 0.01 nm thick shell, much thinner than the expected 2.1 nm. According to SAXS, the shell on $\text{T}_{92}\text{S4}_{7\%}^{\text{SG1}}$ is 0.7 nm thick, but there was no layer visible in TEM. In conclusion, this synthesis method SG1 did not lead to the expected results.

The next set of sol-gel core-shell samples were prepared with an ammonia catalyst and ultrasonication either once before or before each TEOS addition step, depending on the synthesis. This led to the samples $\text{T}_{92}\text{S4}_{21\%}^{\text{SG2}}$, $\text{T}_{92}\text{S4}_{21\%}^{\text{SG3}}$ and $\text{T}_{92}\text{S4}_{15\%}^{\text{SG4}}$. $\text{T}_{92}\text{S4}_{21\%}^{\text{SG2}}$ has

4 Preliminary studies

a very thin layer visible in TEM and a 0.55 ± 0.05 nm thick layer according to EDX, which is significantly lower than the expected 0.96 nm. After calcination this powder showed a lot of residual carbon. $T_{92}S4_{21\%}^{SG3}$ has a 1.2 ± 0.2 nm thick layer in TEM and a 0.7 ± 0.07 nm thick layer according to EDX, which is lower than the expected 0.93 nm. The difference in the thickness from TEM and EDX could be because of a permanent agglomeration of the NPs during the synthesis - this sample was only ultrasonicated before the synthesis. $T_{92}S4_{15\%}^{SG4}$, where the amount of added TEOS was calculated according to the amount of surface hydroxyl groups, shows a thin, inhomogeneous layer and according to EDX the layer thickness is 0.35 ± 0.02 nm, half of the expected 0.7 nm (see Table 4.2).

In conclusion, the synthesis that led to $T_{92}S4_{15\%}^{SG4}$ works best, and the repetition of ultrasonication before each TEOS addition seems to be important for the inhibition of a permanent agglomeration of the particles and therefore for a homogeneous layer deposition. Additionally, I decided to add the catalyst NH_3 in each step, and to calculate the amount of TEOS addition according to the surface area, rather than according to the amount of surface hydroxyl groups.

Table 4.2: Physical properties of core-shell TiO_2-SiO_2 nanoparticles, "step-wise SG set 1": Calculated thickness as expected from the synthesis, SiO_2 shell thicknesses determined from the average of 10 elemental ratios measured by EDX and 15 thickness measurements from TEM images. Specific surface area (SSA) was determined via N_2 physisorption as has an error of $\pm 2 \text{ m}^2\text{g}^{-1}$. *Shells are too thin to be detected. **This value was not measured for this sample.

Sample		Shell thickness [nm]			SSA [m^2g^{-1}]		
Name	steps	calc.	EDX	TEM	BET	micropores	ext.
$T_{92}S0_{0\%}^{SG5}$	0	0	0.03 ± 0.03	0	92	0	92
$T_{92}S4_{21\%}^{SG2}$	4	1.03	0.55 ± 0.05	*	**	**	**
$T_{92}S4_{21\%}^{SG3}$	4	1.03	0.70 ± 0.07	1.20 ± 0.20	**	**	**
$T_{92}S4_{15\%}^{SG4}$	4	0.68	0.35 ± 0.02	*	**	**	**
$T_{92}S1_{4\%}^{SG5}$	1	0.17	0.10 ± 0.01	*	88	2	86
$T_{92}S2_{8\%}^{SG5}$	2	0.34	0.30 ± 0.02	*	80	12	68
$T_{92}S3_{11\%}^{SG5}$	3	0.51	0.61 ± 0.03	0.63 ± 0.13	81	11	70
$T_{92}S4_{15\%}^{SG5}$	4	0.68	0.81 ± 0.04	0.83 ± 0.18	54	11	43
$T_{92}S5_{18\%}^{SG5}$	5	0.85	0.91 ± 0.09	0.97 ± 0.13	74	22	52
$T_{92}S8_{26\%}^{SG5}$	8	1.37	1.49 ± 0.33	3.64 ± 1.00	**	**	**

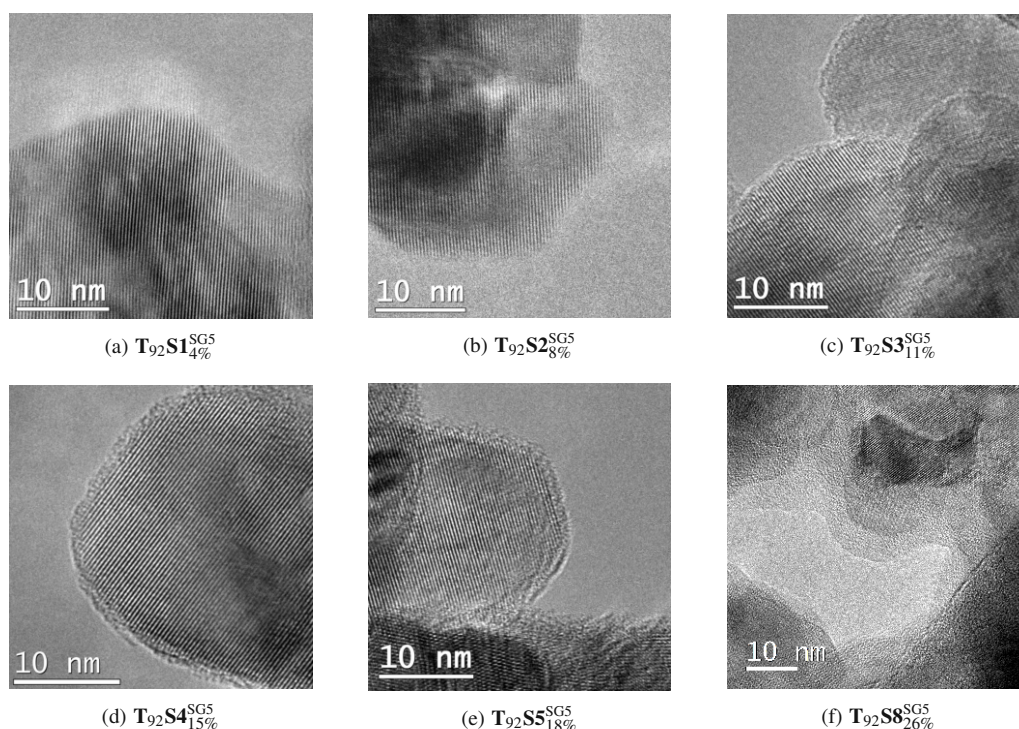


Figure 4.3: Transmission electron microscopy (TEM) images of sol-gel TiO_2 – SiO_2 core-shell nanoparticles set 1. (a) 1-step sample $\text{T}_{92}\text{S1}_{4\%}^{\text{SG5}}$ and (b) 2-step sample $\text{T}_{92}\text{S2}_{8\%}^{\text{SG5}}$ have no visible layer; (c) 3-step $\text{T}_{92}\text{S3}_{11\%}^{\text{SG5}}$ has a visible, inhomogeneous layer; (d) 4-step $\text{T}_{92}\text{S4}_{15\%}^{\text{SG5}}$ and (e) 5-step $\text{T}_{92}\text{S5}_{18\%}^{\text{SG5}}$ have a homogeneous layer; (f) 8-step $\text{T}_{92}\text{S8}_{26\%}^{\text{SG5}}$ has a thick layer.

Sol-gel samples set 1

The combination of best parts of the three different step-wise sol-gel synthesis that led to $\text{T}_{92}\text{S4}_{21\%}^{\text{SG2}}$, $\text{T}_{92}\text{S4}_{21\%}^{\text{SG3}}$ and $\text{T}_{92}\text{S4}_{15\%}^{\text{SG4}}$, i.e. a combination of ultrasonication, addition of the NH_3 catalyst and TEOS in each step, led to the sol-gel method 5 (SG5) and first set of step-wise sol-gel samples, referred to as "step-wise SG set 1".

TEM-EDX

TEM images of these samples are shown in Figure 4.3. $\text{T}_{92}\text{S1}_{4\%}^{\text{SG5}}$ (1 step) has no visible layer in TEM, but according to EDX the shell is 0.1 ± 0.01 nm thick on average. Since a monolayer of amorphous SiO_2 has a thickness of ≈ 0.3 nm, one third of the surface of the $\text{T}_{92}\text{S1}_{4\%}^{\text{SG5}}$ sample is covered with islands of SiO_2 .^{106,107} $\text{T}_{92}\text{S2}_{8\%}^{\text{SG5}}$ (2 step) is covered with one monolayer of SiO_2 according to EDX; 0.30 ± 0.02 nm, which is too thin to be visible in the TEM images. For higher step samples, the shell is visible in TEM: At least 10 positions were measured in the TEM images for visible layers. For $\text{T}_{92}\text{S3}_{11\%}^{\text{SG5}}$ this leads to an average thickness of 0.63 ± 0.13 nm, which fits

with the thickness determined with EDX: 0.61 ± 0.03 nm, but it is than the calculated thickness, i.e. the projected thickness calculated during the synthesis, of 0.51 nm. This could be because of an agglomeration of the anatase particles in the former steps, which leads to less surface area available for the precursor to form the next SiO₂ layer. The determined external surface areas shown in [Table 4.2](#) verify this assumption: The higher the synthesis step number, the lower the surface area of the samples. With less surface area to access, the following SiO₂ layers are going to be thicker than calculated.

T₉₂S4^{SG5}_{15%} (4 step) shows a homogeneous layer in TEM, leading to a thickness of 0.83 ± 0.18 nm which is also close to the thickness according to EDX; 0.81 ± 0.04 nm. Again, both values are higher than the calculated thickness of 0.68 nm. The five step sample **T₉₂S5^{SG5}_{18%}** has a homogeneous layer in TEM that was measured to be 0.97 ± 0.13 nm. According to EDX it is 0.91 ± 0.09 nm. The 8 step sample **T₉₂S8^{SG5}_{26%}** has a thick layer in TEM; 3.64 ± 1 nm and a lower thickness according to EDX; 1.49 ± 0.22 nm. It is clearly visible that the layer has grown around an agglomerate of anatase particles (see [Figure 4.3f](#)). Due to the overall duration of the synthesis, this sample was stirred overnight after the first four steps, where the particles may have agglomerated permanently during the sol-gel condensation, before performing the last four steps. Due to the non-linearity of the thickness with number of steps it is also possible that one hour of stirring might not be enough for the conversion of TEOS to SiO₂ to be finished. The calculated thickness from the deposition amount of TEOS should lead to 0.17 nm per step. In the 1-step sample **T₉₂S1^{SG5}_{4%}** the thickness is only 0.1 nm and the thickness seems to "catch up" in samples that are stirred longer. The comparison of the calculated and measured thickness for each sample can be seen in [Table 4.2](#).

N₂-physisorption

[Table 4.2](#) shows the changes of the specific surface area (SSA) for samples with different synthesis steps. The total SSA according to BET (SSA_{BET}) decreases with increasing number of steps. Analysis from the t-plot of the N₂ physisorption reveals that part of the SSA (SSA_{micropores}) is composed of the inner surface area within micropores (pores with a diameter < 2 nm).¹⁰⁸ Micropores in the amorphous silica shells are formed during sol-gel processes if the temperature is low (< 40 C°) and if silica nuclei are formed before attaching to the core-shell particles.¹⁰⁸ It is plausible that the contribution of micropores to the total surface area increases with increasing step number. This also explains why the thickness determined via TEM is larger than the one determined via EDX for higher step samples.

4.1 Characterization of core-shell nanoparticles

I calculated the difference between the SSA_{BET} and $SSA_{\text{micropores}}$ as the active, external surface area ($SSA_{\text{ext.}}$). The $SSA_{\text{ext.}}$ decreases considerably with increasing step number, which I attribute to the increasing tendency of these core-shell structures to form agglomerates during sol-gel condensation¹⁰⁹. Even half an hour of ultrasonication during each step did not sufficiently inhibit the formation of permanent agglomerates.

Table 4.3: Physical properties of core-shell TiO_2 - SiO_2 nanoparticles, after an attempt to upscale the synthesis: Calculated thickness as expected from the synthesis, SiO_2 shell thicknesses determined from the average of 10 elemental ratios measured by EDX and 15 thickness measurements from TEM images. Specific surface areas (SSA), t-plot external area and t-plot micropore area from N_2 physisorption. *Shells are too thin to be detected or were not measured for other reasons. **No N_2 physisorption measured for these samples.

Sample		Shell thickness [nm]			SSA [m^2g^{-1}]		
Name	steps	calc.	EDX	TEM	BET	micropores	ext.
$^{2nd}\text{T}_{92}\text{S}_2\text{SG}_{8\%}^5$	2	0.34	0.43 ± 0.08	*	78	6	72
$^{2nd}\text{T}_{92}\text{S}_4\text{SG}_{15\%}^5$	4	0.68	0.87 ± 0.11	0.73 ± 0.15	70	14	56
$\text{T}_{70}\text{S}_1\text{SG}_{3\%}^5$	1	0.17	0.03 ± 0.01	*	**	**	**
$\text{T}_{70}\text{S}_2\text{SG}_{6\%}^5$	2	0.34	0.25 ± 0.03	*	**	**	**
$\text{T}_{70}\text{S}_3\text{SG}_{9\%}^5$	3	0.51	0.56 ± 0.11	*	**	**	**
$\text{T}_{70}\text{S}_4\text{SG}_{12\%}^5$	4	0.68	0.73 ± 0.05	*	**	**	**
$\text{T}_{70}\text{S}_5\text{SG}_{14\%}^5$	5	0.86	0.85 ± 0.09	*	**	**	**

Scaling up the synthesis

Due to the low amount of sample from the first set of step-wise SG samples - only 250 mg each, which were used for the dye degradation studies - an up-scaling of the synthesis was attempted, first to 0.5 g and then to 1 g. TEM images of these samples can be seen in the appendix, and their determined thicknesses from TEM and EDX compared to the calculated thickness can be seen in Table 4.3. $^{2nd}\text{T}_{92}\text{S}_2\text{SG}_{8\%}^5$ has a thicker shell than $\text{T}_{92}\text{S}_2\text{SG}_{8\%}^5$ and the standard deviation of the measurements is higher. Up-scaling it to 1 g led to the samples $\text{T}_{70}\text{S}_1\text{SG}_{3\%}^5$ (1 step) and $\text{T}_{70}\text{S}_2\text{SG}_{6\%}^5$ (2 step), which have a much lower measured amount than expected. However, samples with a higher step number led to measured thicknesses close to the expected values. This could be due to the less effective distribution of the precursor in the higher solvent volume right after addition - longer synthesis times or more NH_3 in the higher step samples gives

the precursor enough time to form the layer. It should also be mentioned that right before this synthesis the batch of anatase was changed. While the calculation of the precursor amount included the surface area of anatase, the amount of nanopores and their distribution might still be different for each batch.

Sol-gel samples set 2

To increase the homogeneous distribution of the precursor in the solvent prior to deposition, the precursor was diluted 1:10 in abs. ethanol right before the addition and added dropwise. The addition of the amount of TEOS was changed to attempt 0.15 nm of shell thickness deposited per step - half a monolayer. This finally led to the "step-wise SG set 2", as seen in Figure 4.4. This method yielded better results which can be seen in Table 4.3.

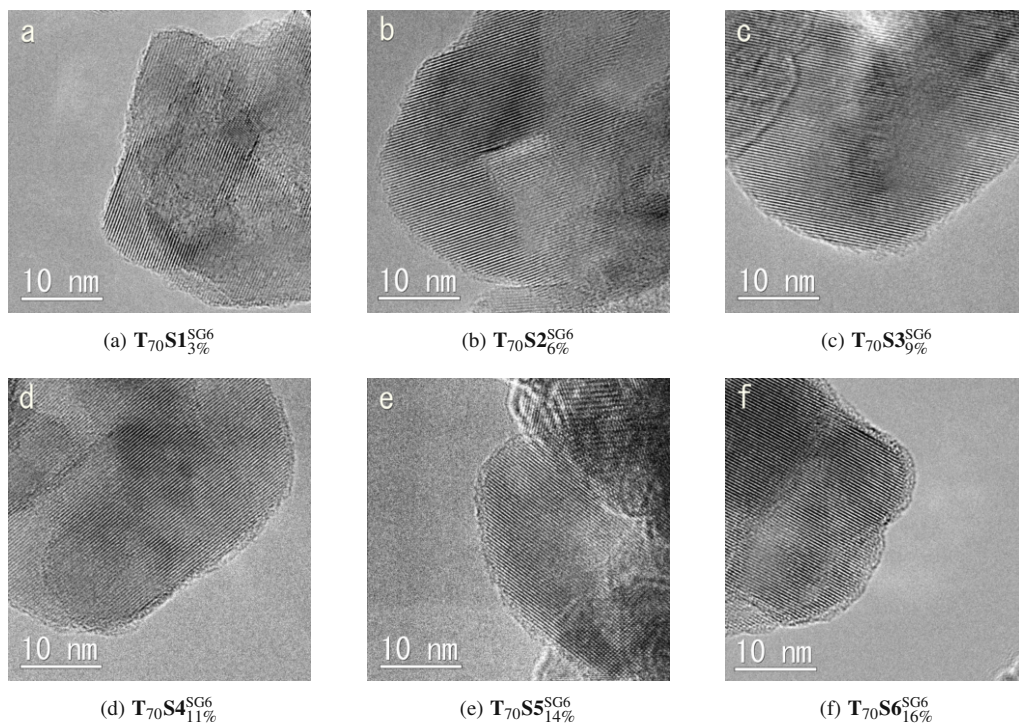


Figure 4.4: Transmission electron microscopy (TEM) images of sol-gel TiO_2 - SiO_2 core-shell nanoparticles set 2. (a) 1-step sample $\text{T}_{70}\text{S1}_{3\%}^{\text{SG6}}$ has thin patches of SiO_2 ; (b) 2-step $\text{T}_{70}\text{S2}_{6\%}^{\text{SG6}}$ and (c) 3-step $\text{T}_{70}\text{S3}_{9\%}^{\text{SG6}}$ have a more homogeneous layer; (d) 4-step $\text{T}_{70}\text{S4}_{11\%}^{\text{SG6}}$, (e) 5-step $\text{T}_{70}\text{S5}_{14\%}^{\text{SG6}}$ and (f) 6-step $\text{T}_{70}\text{S6}_{16\%}^{\text{SG6}}$ have a very homogeneous layer.

TEM-EDX

TEM images of these samples are shown in Figure 4.4. $T_{70}S1_{3\%}^{SG6}$ (1 step) has visible patches of SiO_2 on the surface. According to EDX the shell is 0.16 ± 0.07 nm thick. Since the monolayer of amorphous SiO_2 has 0.3 nm, half of the surface of this sample is covered with islands of SiO_2 . $T_{70}S2_{6\%}^{SG6}$ (2 step) has a more homogenous amorphous shell visible in TEM and according to EDX the sample is covered with one monolayer of SiO_2 ; 0.31 ± 0.05 nm. $T_{70}S3_{9\%}^{SG6}$ has islands on a homogeneous layer in TEM with a measured thickness of 0.49 ± 0.13 nm, which fits with the thickness determined via EDX: 0.46 ± 0.08 nm, and it is a bit lower than the calculated thickness. $T_{70}S4_{11\%}^{SG6}$ (4 step) to $T_{70}S6_{16\%}^{SG6}$ (6 step) samples shows a homogeneous layer, and the thicknesses determined via TEM and EDX correlate well, though they are lower than the calculated thicknesses, which might be due to an incomplete reaction time for higher step samples.

Table 4.4: Physical properties of core-shell TiO_2-SiO_2 nanoparticles, "step-wise SG set 2": Calculated SiO_2 shell thickness as expected from the synthesis, thicknesses determined from the average of 10 elemental ratios measured by EDX and 15 thickness measurements from TEM images. Specific surface area (SSA) was determined via N_2 physisorption as has an error of ± 2 m^2g^{-1} . *Shells are too thin to be detected.

Sample		Shell thickness [nm]			SSA [m^2g^{-1}]		
Name	steps	calc.	EDX	TEM	BET	micropores	ext.
Ana ₇₀	0	0	0.01 ± 0.00	-	67	0	67
$T_{70}S0_{0\%}^{SG6}$	0	0	0.01 ± 0.00	-	67	0	67
$T_{70}S1_{3\%}^{SG6}$	1	0.17	0.17 ± 0.07	*	67	4	63
$T_{70}S2_{6\%}^{SG6}$	2	0.34	0.33 ± 0.05	*	56	8	48
$T_{70}S3_{9\%}^{SG6}$	3	0.51	0.49 ± 0.08	0.49 ± 0.13	60	7	53
$T_{70}S4_{11\%}^{SG6}$	4	0.67	0.63 ± 0.08	0.64 ± 0.11	58	10	48
$T_{70}S5_{14\%}^{SG6}$	5	0.84	0.78 ± 0.11	0.78 ± 0.14	63	14	49
$T_{70}S6_{16\%}^{SG6}$	6	1.01	0.97 ± 0.09	0.93 ± 0.18	56	16	40

N_2 -physisorption

As observed in sample set 1, there is a decrease of the SSA_{BET} and SSA_{ext} surface area for higher step numbers due to permanent agglomeration of the nanoparticles during the sol-gel condensation. The amount of micropores increases with the step number,

which is also consistent with the results from sample set 1 (Table 4.4). Therefore, the up-scaling of the synthesis method has led to comparable results.

Zeta Potential

With TEM, EDX and N_2 -physisorption I determined the thickness and porosity of the shells. ZP was used to investigate the changes in the surface chemistry with the shell thickness. Figure 4.5a shows the ZP at different pH values for sample set 1. The results are similar for set 2 (Figure 4.5b).

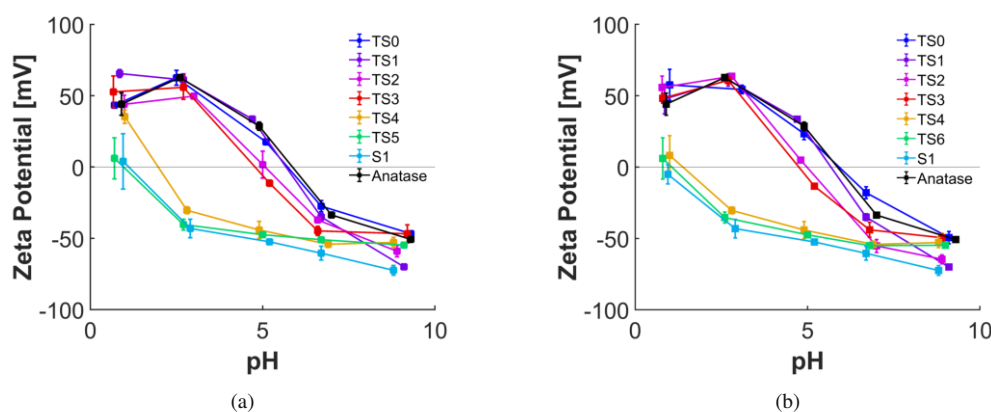


Figure 4.5: Variations of the Zeta Potential with the pH of reference anatase, synthesized silica and core-shell samples with various step numbers for (a) sample set 1 and (b) sample set 2.

It can be seen that the ZP changes gradually towards the pure silica ZP with increasing synthesis steps, indicating that the surface coverage increases with the number of steps.⁹⁹ The isoelectric point (IEP), i. e. the intercept of the ZP curve with the x-axis, is the pH at which the shear plane around the particle carries no electric charge. The IEP can be linked to the point of zero surface charge.^{105,110–112} This means that at pH 7 the surface of anatase, which has an IEP of 6, is slightly negatively charged due to deprotonation of surface hydroxyl groups.¹¹⁰ The reference sample $T_{92}S_{0}^{SG5}$, which simulates the synthesis conditions in absence of TEOS, shows a similar curve as the anatase, indicating that the reaction environment itself did not significantly change the surface properties of anatase. The addition of silica affected the IEP considerably: the thicker the silica shell, the closer the IEP of the samples are to the IEP of pure silica (S1), which has a value of ≈ 1 , where a lot of surface OH groups are dissociated. According to the results from TEM-EDX, the surface of anatase is covered with

a monolayer of SiO₂ in the T₉₂S₂^{SG5} sample, but the ZP is closer to anatase than it is to SiO₂. This is explained with the subsurface effect, where the surface charge of ultrathin layers of SiO₂ is influenced by the underlying bulk TiO₂: As soon as the shell reaches a critical thickness, which according to my results is 2-3 atomic layers, the surface charge has similar values as bare SiO₂.

Therefore, the ZP results cannot be used to determine the surface coverage, but they show that the shell thickness increases gradually with the synthesis step number, which can be correlated with the TEM and EDX results.

4.1.2 Nature of the interface and the electronic structure

To investigate the nature of the Ti-O-Si bonds and changes in the light absorption and charge carrier behavior upon deposition of a shell, I characterized the most relevant samples, e.g. core-shell SG set 1 and set 2, with spectroscopic techniques, such as infrared-, UV-vis-, photoluminescence- and X-Ray photoelectron spectroscopy.

DRS UV-vis

Diffuse reflectance UV-vis spectra were recorded for both sets and transformed into tauc plots, from which the optical band gaps were calculated via the intercept of the extrapolation of the tangent on the photon energy axis (the details are explained in [section 3.3.7](#)).

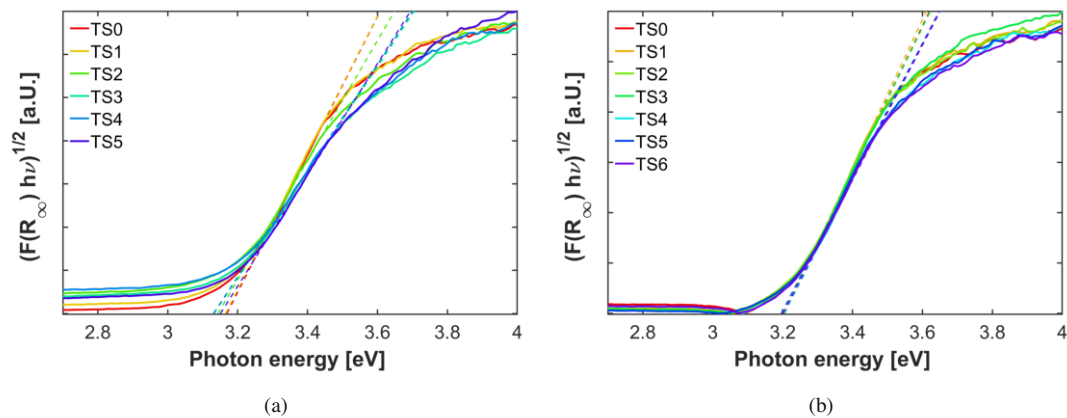


Figure 4.6: Band gap plots of sol-gel core-shell samples; (a) set 1; (b) set 2.

4 Preliminary studies

The band gaps of the coated samples show a difference of maximum 0.04 eV and 0.01 eV to the reference samples, which have bandgaps of 3.17 eV and 3.2 eV for $T_{92}S0^{SG5}_{0\%}$ and $T_{70}S0^{SG6}_{0\%}$, respectively. This indicates that the optical absorption behavior did not change upon the introduction of an SiO_2 shell.

ATR-FTIR

ATR-FTIR spectra of the coated samples and reference samples and pure silica can be seen in Figure 4.7. Please note that these are qualitative results, and a quantitative evaluation can only be done within a sample set and not between sets.

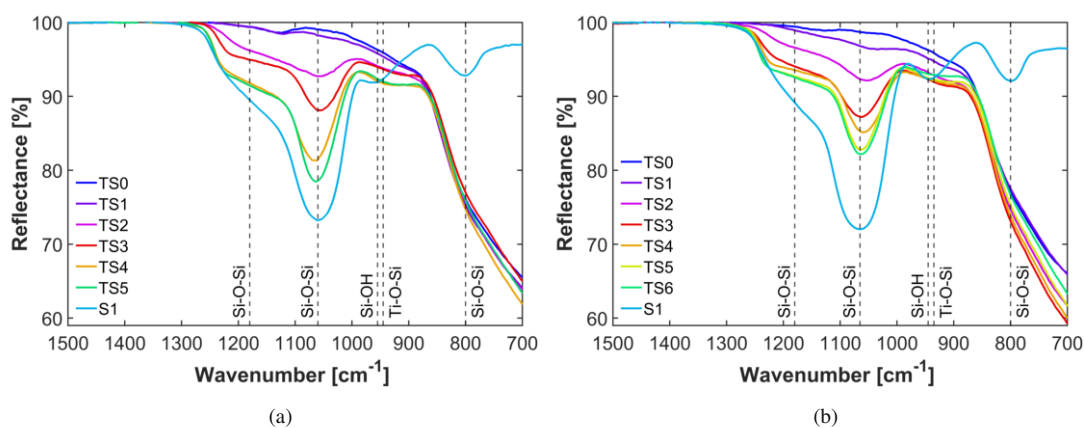


Figure 4.7: ATR-FTIR spectra of SiO_2 , S1 and core-shell samples with increasing shell thickness; (a) set 1; (b) set 2.

The two peaks 1060 and 1180 cm^{-1} , visible for the samples with a shell thickness of at least one monolayer and the plain silica sample (S1), belong to the in-phase and out-of-phase asymmetric vibration of Si-O-Si, respectively.^{66,113,114} The peak height increases with increasing shell thickness. The peak maximum position shifts from 1055 to 1065 cm^{-1} and from 1035 to 1065 cm^{-1} with increasing shell thickness, for set 1 and set 2, respectively. This shift indicates the formation of stronger Si-O-Si bonds with thicker shells. The symmetric stretching vibration (in phase) of Si-O-Si at 790 cm^{-1} is only visible for the plain silica because it is overlaid by the broad Ti-O-Ti vibration.¹¹⁵ The characteristic stretching vibration of Ti-O-Si at 940 cm^{-1} is visible for the coated samples and its intensity rises with increasing shell thickness until $T_{92}S4^{SG5}_{15\%}$ and $T_{70}S3^{SG6}_{9\%}$, respectively.^{116,117} These results indicate the number of synthesis steps needed to completely cover the surface with silica. However, the Ti-

O-Si vibration is close to the vibration of Si-OH at $\approx 945 \text{ cm}^{-1}$, visible for the silica sample S1, which makes this conclusion debatable.^{113,114}

XPS

X-Ray Photoelectron Spectroscopy was measured for selected samples from both sets. The results of selected samples of set 1, which includes the reference sample $\text{T}_{92}\text{S0}_{0\%}^{\text{SG5}}$, 2-step $\text{T}_{92}\text{S2}_{8\%}^{\text{SG5}}$, 4-step $\text{T}_{92}\text{S4}_{15\%}^{\text{SG5}}$ and 8-step $\text{T}_{92}\text{S8}_{26\%}^{\text{SG5}}$, can be seen in Figure 4.8. The survey spectra can be found in the appendix (Figure A.5).

The binding energy B.E. of the oxygen O 1s signal shifts upward with increasing Si content, indicating the decreasing negative charge around the oxygen due to the more electronegative Si atoms. Several peaks can be fitted to the spectra: For $\text{T}_{92}\text{S0}_{0\%}^{\text{SG5}}$, the major peak at 529.8 eV (purple peak) corresponds to the Ti-O-Ti bond while smaller peaks were attributed to surface hydroxyl groups and carbon-oxygen bonds of adventitious carbon structures.¹¹⁸ For $\text{T}_{92}\text{S2}_{8\%}^{\text{SG5}}$ and $\text{T}_{92}\text{S4}_{15\%}^{\text{SG5}}$, peaks located around 531.8 eV and 532.8 eV increase in height. They were attributed to the Ti-O-Si (blue peak) and Si-O-Si (green peak) bonds, respectively. With increasing shell thickness the Ti-O-Ti signal decreases. This is due to the surface nature of XPS: As the SiO_2 shell thickness increases less of the O 1s signal from TiO_2 is detected. Additional peaks at higher B.E. can be attributed to Si-OH, adsorbed water and carbon oxygen bonds of adventitious carbon structures, now adsorbed on the SiO_2 shell and having higher B.E..^{68,74,116,119,120} $\text{T}_{92}\text{S8}_{26\%}^{\text{SG5}}$ has a thick layer larger than 3 nm as a shell. Due to charging of the sample, the signal is distorted and no peaks were fitted to the signal.

This Ti-O-Si bond formation can also be verified by the Si 2p core region of the XPS spectra. For $\text{T}_{92}\text{S2}_{8\%}^{\text{SG5}}$, only one peak can be fitted at 102.6 eV, while the $\text{T}_{92}\text{S4}_{15\%}^{\text{SG5}}$ sample shows a broader signal, to which 2 peaks at 103 eV and 105.2 eV can be fitted. Due to a decrease of electron density around Si in the Si-O-Si bond the B.E. shifts to higher values compared to the Si in Ti-O-Si, indicating that at the $\text{T}_{92}\text{S2}_{8\%}^{\text{SG5}}$ sample most Si-O bonds are close to the TiO_2 surface, e.g. forming Ti-O-Si bonds. With thicker shells a distinct Si-O-Si peak can be observed.⁵⁷

With increasing SiO_2 coverage, the two Ti peaks of the XPS data, Ti 2p_{1/2} and Ti 2p_{3/2} at 464.3 and 458.6 eV, respectively, shift towards higher BE, because of the increasing amount of Ti-O-Si bonds, which reduce the electron density around the Ti atom.⁶⁸ For the $\text{T}_{92}\text{S2}_{8\%}^{\text{SG5}}$ sample, the relative intensity of Ti-O-Ti seems to be too high for a Ti-O-Si peak to be visible, while for thicker layers, at the $\text{T}_{92}\text{S4}_{15\%}^{\text{SG5}}$ sample,

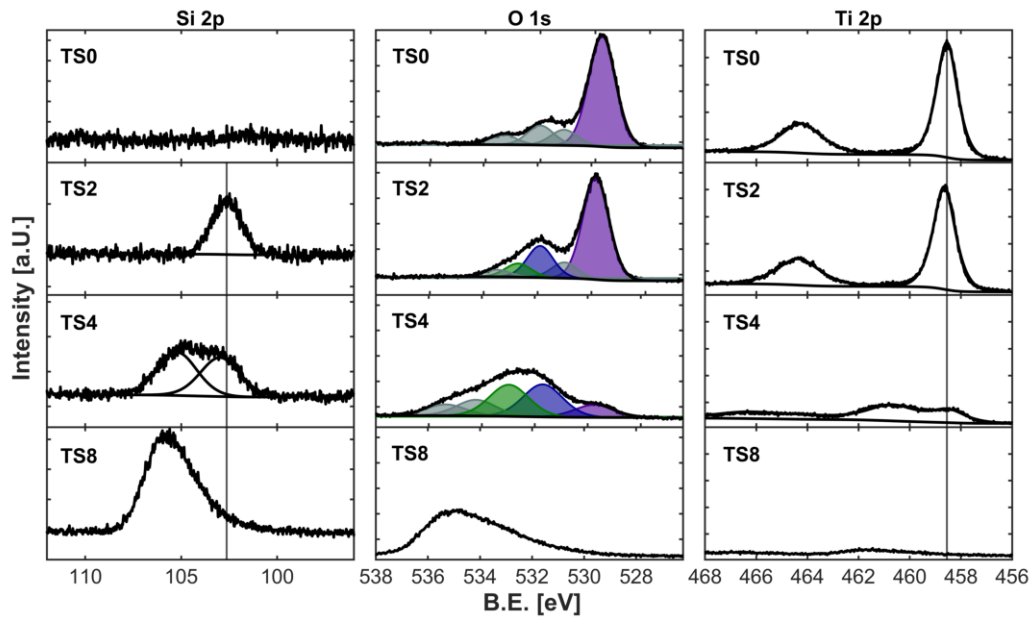


Figure 4.8: X-ray photoelectron spectroscopy (XPS) of the core-shell SG set 1. Shown here are detailed measurements of the signals Si 2s, O 1s and Ti 2p. For a detailed analysis of the peaks please refer to the text.

four peaks are visible. The total intensity of the Ti signal is reduced because the XPS analysis is surface sensitive.

There are several differences between the XPS spectra taken for SG sample set 1 and set 2. Please note that for the sample set 2 the shell was deposited on a different batch of anatase, a significant time passed between the two measurements and they were measured by different researchers, though on the same machine and with the same measurement parameters.

The spectra of the selected samples from set 2, 1-step $T_{70}S1_{3\%}^{SG6}$, 2-step $T_{70}S2_{6\%}^{SG6}$, 4-step $T_{70}S4_{11\%}^{SG6}$ and 6-step $T_{70}S6_{16\%}^{SG6}$, are shown in Figure 4.9. The Si 2p spectra reveal an increase of the Si amount with increasing shell thickness. There is little Si detectable for the $T_{70}S1_{3\%}^{SG6}$ sample, but the signal becomes stronger for thicker shells. The gradual chemical shift to higher binding energies from 102.3 eV to 103.3 eV for $T_{70}S1_{3\%}^{SG6}$ and $T_{70}S6_{16\%}^{SG6}$, respectively, reveals an electronic interaction between TiO_2 and SiO_2 . Furthermore, the full width at half maximum (FWHM) of the peaks, shown in the appendix (Table A.1), increases from 0.84 to 1.63 eV for $T_{70}S1_{3\%}^{SG6}$ and $T_{70}S6_{16\%}^{SG6}$, respectively, which indicates an interaction between the core and the shell. The survey spectra can also be found in the appendix (Figure A.6).

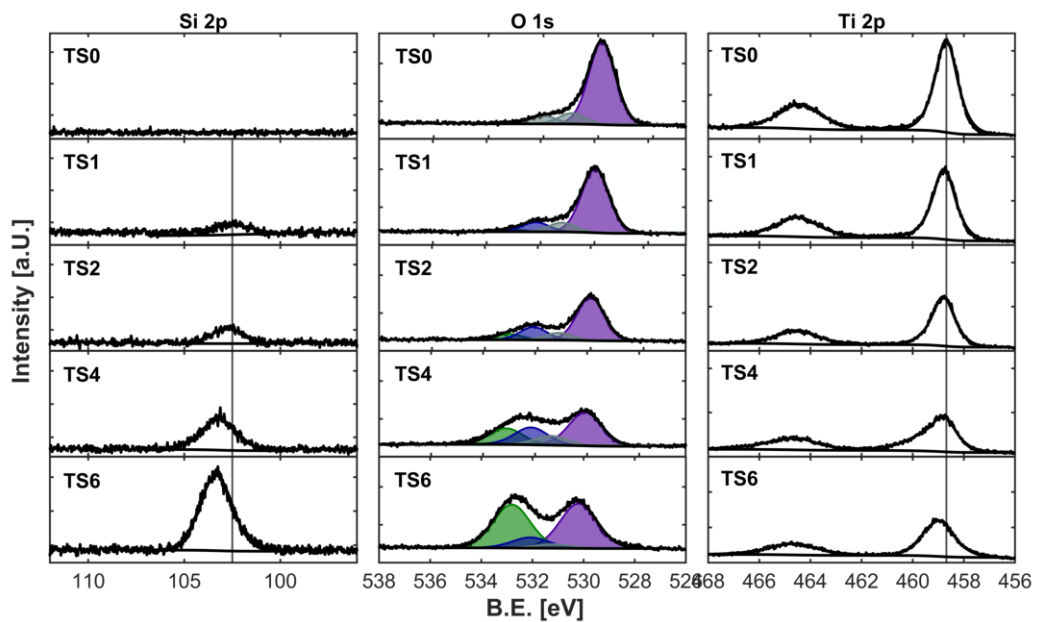


Figure 4.9: X-ray photoelectron spectroscopy (XPS) of the core-shell SG set 2. Shown here are detailed measurements of the signals Si 2s, O 1s and Ti 2p. For a detailed analysis of the peaks please refer to the text.

The O 1s spectra for the reference sample $T_{70}S0_{0\%}^{SG6}$ shows the Ti–O–Ti O 1s signal at 529.9 eV. The signal was fitted with several peaks, which were attributed to adventitious carbon oxygen species, adsorbed water and the O 1s signals corresponding to Ti–O–Ti at 529.9 eV (purple peak).¹¹⁸ With the increase of shell coverage and thickness a peak around 532.5 eV appears, which corresponds to the Si–O–Si bond (green peak) and increases while the Ti–O–Ti signal decreases. For $T_{70}S2_{6\%}^{SG6}$ and $T_{70}S4_{11\%}^{SG6}$ a small peak around 532.1 eV, right between the Ti–O–Ti and Si–O–Si peak, can be fitted to the signal, which is attributed to the Ti–O–Si bond (blue peak).^{68,74,116,119,120}

The Ti 2p 3/2 signal, corresponding to Ti–O–Ti, is positioned at 458.2 eV for $T_{70}S0_{0\%}^{SG6}$ and shifts to higher binding energies up to 459.1 eV for $T_{70}S6_{16\%}^{SG6}$. The FWHM of the peak increases from 1.03 to 1.37 eV for Ana₇₀ and $T_{70}S6_{16\%}^{SG6}$, respectively (see Table A.1). This is due to a decrease in electron density around Ti upon the formation of a Ti–O–Si bond. The relative decrease of the Ti–O–Ti signal with increasing shell thickness is smaller than in sample set 1. This different behavior could be due to the change of the anatase batch or a change in the shell synthesis, i.e. a different inelastic mean free paths of the electrons in the materials.

In conclusion, during synthesis Si–O first binds to the TiO₂ surface, creating a mono-

layer and inducing a shift to higher binding energies. After full coverage of the TiO_2 surface more Si–O–Si bonds are created, leading to the increase in shell thickness and broadening of the signal.^{76,121} The combined characterization with TEM, FTIR and XPS thus suggests a layer-by-layer growth via the van-der-Merwe or the Krastanov growth model (see Figure 2.9).

Photoluminescence lifetime

Transient photoluminescence spectroscopy can be used to study the recombination of excitons in the core-shell structures. Upon electron-hole recombination photons are emitted, and the photoluminescence (PL) emission intensity and lifetimes can be used to quantify the recombination.

Electron and hole traps, which are associated with defects in TiO_2 , have been found to lead to a broad photoluminescence signal in the visible range. In anatase, a PL peak at ≈ 530 nm (green PL) has been assigned to the recombination of mobile electrons from the conduction band with trapped holes in the valence band, which are associated with oxygen vacancies. Another peak between 600 and 650 nm (red PL) comes from a recombination of trapped electrons in the conduction band with mobile valence band holes from the valence band (Figure 4.10a).¹²² In my studies, I found that the contribution of the red photoluminescence is much smaller than the green emission peak, as can be seen in the appendix (Figure A.2).

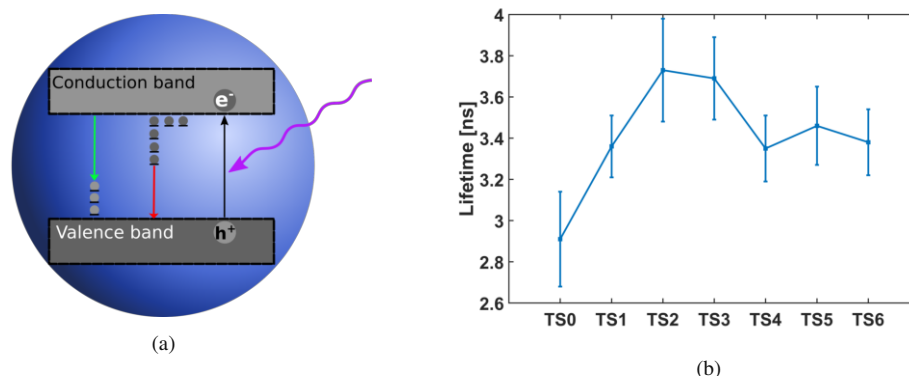


Figure 4.10: (a) Trap states due to electron or hole defects in TiO_2 leading to a broadband photoluminescence in the visible range; green emission comes from recombination of electrons with trapped holes, red emission from trapped electrons with VB holes; redrawn from Mercado et al.¹²²; (b) photoluminescence lifetimes $\tau_{\text{Av,Int}}$ with standard deviation determined with a two-term exponential fit. Note that the measurements were performed on samples before Pt deposition.

In literature, several reports describe the increase of the lifetime of excitons upon introduction of a SiO₂ phase close to TiO₂.^{59,73,74} I measured the reference and core-shell powders in a suspension of deionized water at a concentration of 2 g · l⁻¹, with an excitation wavelength of 378 nm, to take emission spectra and analyze the lifetime at the maximum of the emission peak (550 nm). I did not observe any changes in the intensity of the PL signal or new trap states upon introduction of an SiO₂ shell (Figure A.2). The exciton lifetimes $\tau_{Av,Int}$ showed distinct changes with shell thickness, as seen in Figure 4.10b and in Table 4.5. The lifetimes increase from 2.9 to 3.7 ns from Ana₇₀ to T₇₀S₂^{SG6}_{6%} and T₇₀S₃^{SG6}_{9%} and then decrease slightly for thicker shells.

Table 4.5: The determined lifetimes fitted via a two-term exponential fit. Shown are both lifetimes and the average lifetimes weighted by the intensities.

Sample	τ_1 [ns]	τ_2 [ns]	$\tau_{Av,Int}$ [ns]
T ₇₀ S ₀ ^{SG6} _{0%}	4.48 ± 0.50	0.71 ± 0.15	2.91 ± 0.23
T ₇₀ S ₁ ^{SG6} _{3%}	4.76 ± 0.28	0.80 ± 0.05	3.36 ± 0.15
T ₇₀ S ₂ ^{SG6} _{6%}	5.20 ± 0.49	0.89 ± 0.12	3.73 ± 0.25
T ₇₀ S ₃ ^{SG6} _{9%}	5.14 ± 0.34	0.88 ± 0.06	3.69 ± 0.20
T ₇₀ S ₄ ^{SG6} _{11%}	4.64 ± 0.26	0.79 ± 0.05	3.35 ± 0.16
T ₇₀ S ₅ ^{SG6} _{14%}	4.71 ± 0.32	0.84 ± 0.13	3.46 ± 0.19
T ₇₀ S ₆ ^{SG6} _{16%}	4.90 ± 0.29	0.77 ± 0.05	3.38 ± 0.16

The following explanations for the increase in lifetime upon SiO₂ introduction to TiO₂ are found in literature.

- Yang et al. stated that new electronic states are created by SiO₂ species on the surface above the top of the valence band of anatase. They supported this statement with a peak fitting of the PL signals, which were red-shifted upon introduction of an SiO₂ shell, and a peak fitting showed an additional peak at 600 nm.¹²³
- Miyashita et al. explain the increase in lifetime with band bending and charge separation at the interface of TiO₂ and SiO₂. However, this effect was described for SiO₂ layers thicker than 10 nm, where the layer thickness is insulating enough to keep the charge carriers at the interface;⁷³ layers thinner than 3

nm generally allow electron tunneling and transfer through the shell..^{44,88,124}

- The introduction of SiO₂ on the TiO₂ surface leads to interfacial Ti-O-Si bonds that serve as trap states in which charge carriers are caught, thus leading to lower recombination. An optimal amount coating for maximum lifetime increase was found to be $\approx 5\%$ of SiO₂ on P25 by Yuan et al. while it decreases for thicker shells.⁷⁴

The best peak fit I achieved in my emission spectra leads to two fitted peaks, at 630 and 557 nm (see Appendix, [Figure A.3](#)). I did not observe any changes in the emission signal upon SiO₂ introduction, neither in the peak position, FWHM, nor in the intensity (see Appendix, [Figure A.2a](#)). I can therefore not confirm the creation of new electronic states that were found by Yang et al.. Due to the low thickness of the shell (<1 nm) I can also not explain the lifetime increase with the band bending at the TiO₂-SiO₂ interface, as Miyashita et al. did. The increase in lifetime is therefore explained with the creation of trap states at the Ti-O-Si bonds. A monolayer of SiO₂ seems to lead to the longest lifetime of the electron-hole pairs.

Charge transfer investigations

A hypothesis for the lifetime decrease with thicker shells could be less efficient charge separation due to the insulating layer. In order to ensure an efficient charge separation, the charge carriers need to transfer through the insulating shell and into the water. This provides the driving force for further charge separation at the TiO₂-SiO₂ interface. If the SiO₂ shell becomes too thick, then this process may become limited because the charge carriers cannot transfer through the shell but rather accumulate at the interface, which means that charge carriers recombine faster, thus reducing the lifetime.

To test if the SiO₂ shell hinders the charge transfer from TiO₂ to the solution, I illuminated the catalysts in a terephthalic acid (TA) solution with a 365 nm LED lamp for 10 minutes. TA acts as an OH radical catcher: If the charge transfer is hindered, less OH radicals are produced, leading to a decreased concentration of the oxidized product 2-hydroxyterephthalic acid (TAOH) ([Figure 4.11a](#)). TAOH can be quantified by measuring its fluorescence at 425 nm (see appendix [Figure A.2b](#)).¹²⁵

I determined the charge transfer efficiency by comparing the peak areas of the emission peaks ([Figure 4.11b](#)). There was no significant decrease of the emission with the increase of the shell thickness. The charge transfer is barely inhibited by the shell, which

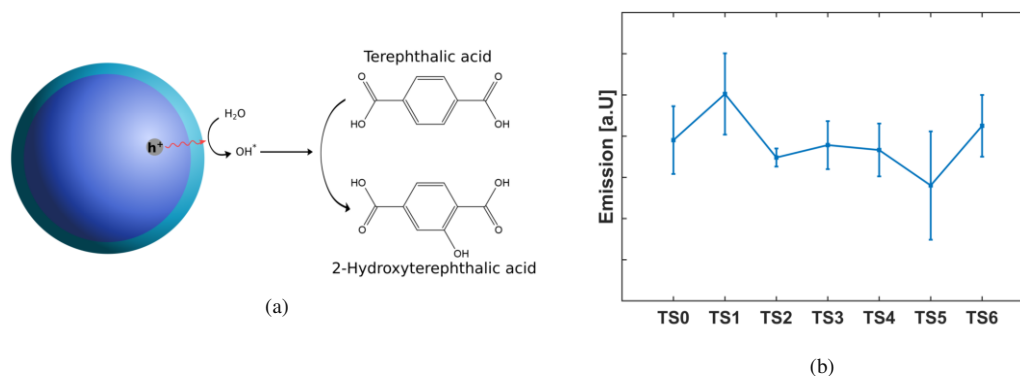


Figure 4.11: (a) Photoluminescence lifetimes $\tau_{Av,Int}$ with standard deviation determined with a two-term exponential fit; (b) Determination of reactive oxygen species (ROS) via fluorescence of OH-TA (average of 3 replicates). Note that the measurements were performed on samples before Pt deposition.

is compliant to former charge transfer studies through ultrathin insulating layers.⁷⁵ Below a shell thickness of 3 nm electron tunneling is possible.^{44,88,124} Therefore, the decrease in lifetime for thicker layers cannot be due to charge accumulation at the core-shell interface.

Therefore, it remains unclear as to why the fluorescence lifetime should decrease for shells thicker than a monolayer. Since the difference is close to the standard deviation of the exponential curve fit, it will not be investigated further (Figure 4.10b).

4.2 Characterization of nanocavities samples

In this section I will discuss the results concerning the synthesis of core-shell samples containing nanocavities in their shells. First, I will describe the characterization of templates which were grafted onto TiO_2 before SiO_2 deposition, where I will focus on quantifying the amount of the templates. I will also show spectroscopic characterizations and finally a few results concerning the nanocavities after shell deposition.

4.2.1 Quantifying the amount of calixarenes on the TiO_2 surface

To quantify the amount of calixarenes on the TiO_2 powders, TGA was used to measure the mass loss and calculate the surface coverage.

4 Preliminary studies

The following method was used for the TGA measurements displayed in Figure 4.12: 5 mg of the powder was heated to 195°C and held at this temperature to remove adsorbed H₂O until the weighted mass was stable ($\Delta m < 0.01\%$ over 3 min). The sample was then heated further with 5 K · min⁻¹ until 900°C. The combustion temperature of 4-tert-butyl-calix[4]arene is 325°C.⁸²

Figure 4.12a shows the mass loss of calixarenes of P25 with two different synthesis lengths, 4 and 48 hours of refluxing, and two potential reference samples, which were created by refluxing or stirring P25 in toluene (abs.). Unfortunately, the reference samples show a mass loss due to the combustion of unknown substance with an onset temperature at 450°C. For this reason, untreated P25 was used as a reference substance for the calculation of the surface coverage with calixarenes. It is clearly visible that the duration of synthesis does not lead to a significantly different calixarene coverage: Both samples show a mass loss of $\approx 1.8\%$.

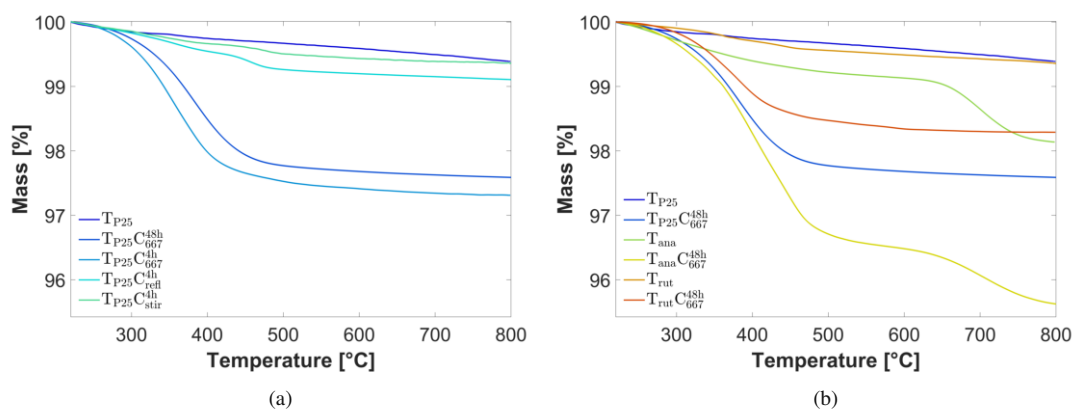


Figure 4.12: The mass loss in TGA measurements due to combustion of calixarenes on TiO₂ nanoparticles (a) The reference samples and different synthesis length of calixarenes on P25; (b) the calixarene standard synthesis on different phases of TiO₂.

The maximum surface coverage was calculated the following way: Assuming the most dense circle packing, which leads to a surface coverage of 90.69%, a surface area of 55 m² · g⁻¹ of P25 and an upper area of 4-tert-butyl-calix[4]arenes of 1.5 · 10⁻¹⁸ m², the maximum mass loss in the TGA would be 3.9%. Therefore the surface coverage on P25 is $\approx 46\%$.⁸³

Figure 4.12b shows the mass loss of calixarenes with the standard synthesis of 48

hours on different modifications of TiO₂: P25, anatase and rutile. While rutile shows a smaller relative mass loss than P25, anatase shows a significant higher mass loss, which is due to the higher surface area of anatase.

A monolayer of calixarenes on anatase (SSA = 92 m²) would amount to a mass loss of 6.4%. The measure mass loss of 2.7% therefore leads to a surface coverage of 42%, which is similar to the P25 sample. Both anatase samples showed similar results; $T_{\text{ana}}C_{667}^{48\text{h}}$ and $^{2\text{nd}}T_{\text{ana}}C_{667}^{48\text{h}}$ (not shown here).

Since the immersion time during synthesis does not seem to affect the coverage significantly (Figure 4.12a), which indicates that the saturation is reached quickly, I varied the amount of hydroxyl groups on the anatase surface to increase the calixarene surface coverage. To quantify the hydroxyl groups on the surface, a TGA method reported by Mueller et al. was used: The powder was heated up 120°C and held at this temperature to remove adsorbed H₂O until the weighted mass was stable ($\Delta m < 0.01\%$ over 3 min). It was then heated to 500°C and the mass loss, assumed amount of hydroxyl groups at 500°C and a calibration factor were used to calculate the amount of hydroxyl groups on the anatase surface.⁸⁹ According to this, untreated anatase has a hydroxyl density of $6.3 \cdot 10^{18} \text{ OH} \cdot \text{m}^{-2}$, calcined anatase has $3.6 \cdot 10^{18} \text{ OH} \cdot \text{m}^{-2}$ and anatase treated with AHP has a density of $7.1 \cdot 10^{18} \text{ OH} \cdot \text{m}^{-2}$. TGA plots can be seen in Figure 4.13a.

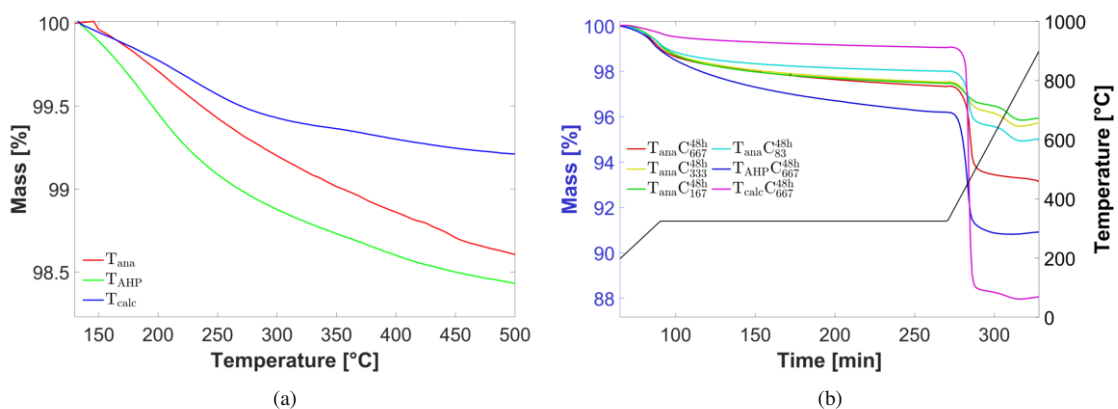


Figure 4.13: TGA analysis on pure titania T_{ana} to (a) quantify the amount of OH groups on the surface after oxidation and calcination pretreatment; to (b) quantify the amount of calixarenes chemisorbed on the surface of Ana₉₂ after different synthesis methods.

To quantify the calixarenes on the surface of anatase (calixarene calibration), the TGA method was optimized: After the isothermal step at 195°C, the sample was heated up to 325°C and held for 120 minutes. It was then heated up further to 900°C. The results, after subtracting the respective reference measurements, can be seen in Figure 4.13b. It can be seen that $T_{\text{ana}}C_{667}^{48h}$, $T_{\text{ana}}C_{333}^{48h}$ and $T_{\text{ana}}C_{167}^{48h}$ all have approximately the same mass loss, while $T_{\text{ana}}C_{83}^{48h}$ has a lower mass loss, which results in a surface coverage of 31% - in reference to the maximum possible surface coverage.

The AHP treated and calcined samples show a much higher and lower mass loss, respectively, which leads to a calculated surface coverage of 60% and 15%, respectively. This method is therefore a good approach to tune the amount of calixarenes chemisorbed on the TiO_2 surface.

4.2.2 Spectroscopic measurements of calixarenes on the TiO_2 surface

The calixarene calibration samples were also analyzed via spectroscopic methods, to see if any signals can be used to quantify the amount of calixarenes on the surface.

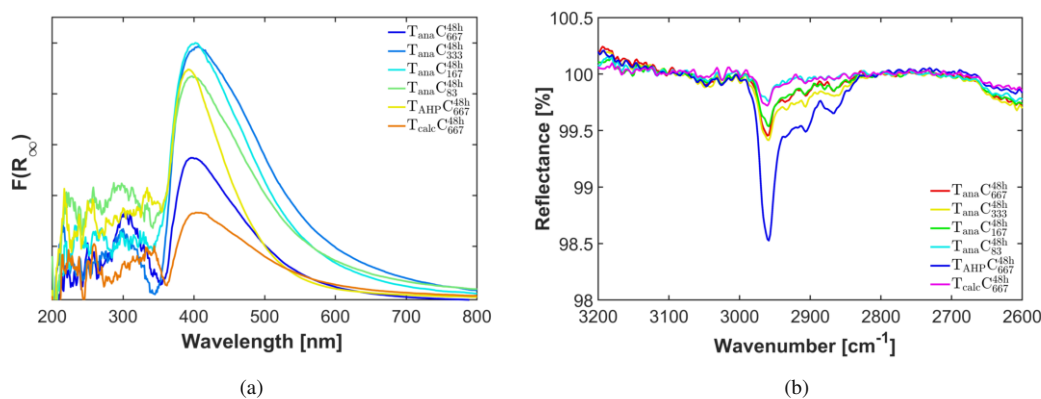


Figure 4.14: Spectroscopic analysis to quantify the amount of calixarenes chemisorbed on the surface of Ana_{92} after different synthesis methods.

The Kubelka-Munk (KM) plots can be seen in Figure 4.14a. Please note that the background of these measurements was pure Ana_{92} , so this spectrum shows only the absorption peak of the Ti-O-C bond at 410 nm, i.e. the measured signal comes from

the chemisorption of calixarene on TiO_2 (orange complex).⁸³ The original reflectance data can be seen in the appendix (Figure A.9). The peak intensity does not scale with the amount of calixarenes determined in TGA measurements: While the peak height of $\mathbf{T}_{\text{ana}}\mathbf{C}_{667}^{48\text{h}}$ is between the peaks intensities of the higher calixarene amount $\mathbf{T}_{\text{AHP}}\mathbf{C}_{667}^{48\text{h}}$ and the lower amount $\mathbf{T}_{\text{calc}}\mathbf{C}_{667}^{48\text{h}}$, the peaks for $\mathbf{T}_{\text{ana}}\mathbf{C}_{333}^{48\text{h}}$, $\mathbf{T}_{\text{ana}}\mathbf{C}_{167}^{48\text{h}}$ and $\mathbf{T}_{\text{ana}}\mathbf{C}_{83}^{48\text{h}}$ are about the same height as the $\mathbf{T}_{\text{AHP}}\mathbf{C}_{667}^{48\text{h}}$ peak, even though their calixarene content is lower. Therefore, KM plots cannot be used to quantify the amount of calixarenes.

Figure 4.14b shows the ATR spectra of the calibration samples. Here, the focus lies on the calixarene signals between 2800 and 3000 cm^{-1} . The intensity of the most intense peak at 2960 cm^{-1} increases with the amount of calixarenes determined in the TGA measurements: The $\mathbf{T}_{\text{AHP}}\mathbf{C}_{667}^{48\text{h}}$ peak is highest, while the samples with the lowest calixarene concentration, $\mathbf{T}_{\text{calc}}\mathbf{C}_{667}^{48\text{h}}$ and $\mathbf{T}_{\text{ana}}\mathbf{C}_{83}^{48\text{h}}$, are the smallest and hardly quantifiable due to the low signal-to-noise ratio. The peaks of $\mathbf{T}_{\text{ana}}\mathbf{C}_{667}^{48\text{h}}$, $\mathbf{T}_{\text{ana}}\mathbf{C}_{333}^{48\text{h}}$ and $\mathbf{T}_{\text{ana}}\mathbf{C}_{167}^{48\text{h}}$ show a similar peak height, in accordance with the amounts determined in TGA. Due to the low signal intensity, ATR-FTIR is not a good method to quantify the calixarene coverage on TiO_2 .

4.2.3 Characterization of the nanocavity containing core-shell TiO_2 - SiO_2 particles

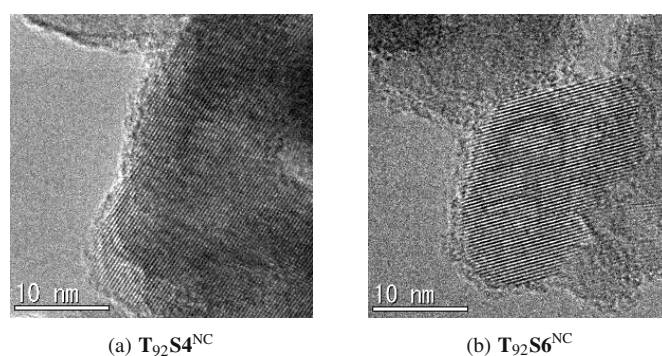


Figure 4.15: Transmission electron microscopy (TEM) images of nanocavity containing TiO_2 - SiO_2 core-shell nanoparticles. (a) $\mathbf{T}_{92}\mathbf{S4}^{\text{NC}}$ show an inhomogeneous layer due to nanocavities with an average layer thickness of $0.8 \pm 0.3\text{ nm}$; (b) $\mathbf{T}_{92}\mathbf{S6}^{\text{NC}}$ shows a layer as inhomogeneous, but the layer is thicker ($1 \pm 0.5\text{ nm}$).

Figure 4.15 shows typical TEM images of the nanocavity containing core-shell particles after removal of the calixarene templates. Due to the 3D nature of the particles, it is not possible to view the 1 nm sized nanocavities, but the TEM images clearly show an inhomogeneity in layer thickness, which suggests a nanoporous layer. $T_{92}S6^{NC}$, which has 6 steps of SiO_2 sol-gel deposition clearly shows a thicker layer (1 ± 0.5 nm) than $T_{92}S4^{NC}$, which only has 4 steps of deposition (0.8 ± 0.3 nm).

4.3 Influence of parameters on HER

In this section I will discuss the different parameters that influence the photocatalytic activity during hydrogen evolution reaction (HER), such as the sources of the sacrificial agent methanol and the Pt precursor, the conditions of the addition of platinum, ultrasonication, UV lamp control, the TiO₂ phase, the amount of the co-catalyst platinum, and the cooling water temperature. I will further compare different systems toward the early-stage deactivation (ESD) during HER.

Influence of parameters on the activity

In the following subsection, several parameters will be changed during HER with 0.2 wt.% Pt on anatase (Ana₉₂) in 50 ml H₂O and 50 ml methanol to investigate the influences on the photocatalytic activity and to maximize the reproducibility. The co-catalyst Pt was deposited in-situ during illumination of the photocatalyst TiO₂. This was done by adding specific amounts of the Pt precursor H₂PtCl₆ to the reaction mixture before closing the reactor and illuminating it.

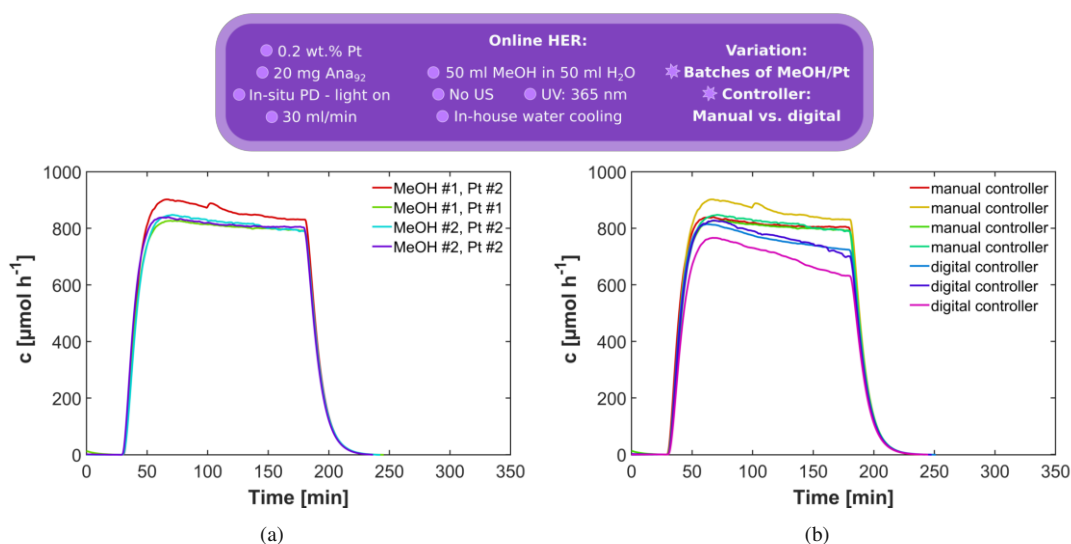


Figure 4.16: Hydrogen evolution reaction over time (a) while varying the sources of methanol and Pt, using the manual controller and applying no ultrasonication and (b) varying the controller, also without ultrasonication.

Methanol and Pt batch

To exclude influences of different commercial batches of the sacrificial agent methanol and the co-catalyst precursor H_2PtCl_6 , different batches of those purchased chemicals were varied during HER experiments. Figure 4.16a shows that changing the methanol and H_2PtCl_6 source do not impact the activity during HER. This indicates that there is no significant effect by the batches of the precursor or sacrificial agent.

LED lamp controllers

The LED lamps can be either controlled by a manual or a digital controller, which, according to power meter measurements, lead to slightly different power outputs over time. Figure 4.16b shows that they seem to have a slight impact on the activity over time; the use of the manual controller leads to a stable activity over time; while using the digital controller leads to a small deactivation that is assigned to the controller rather than to the inherent early-stage deactivation that has been observed in our system.

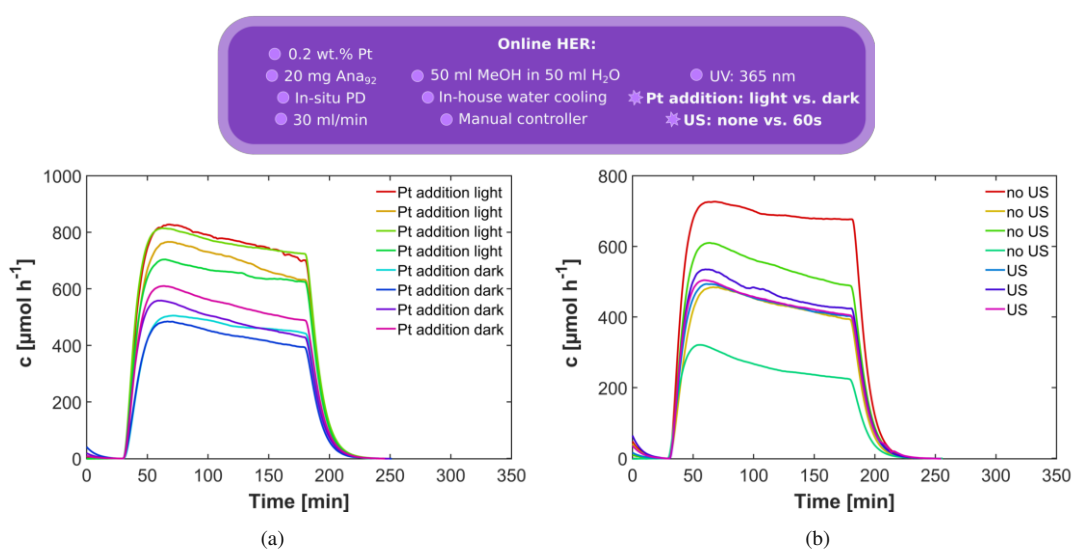


Figure 4.17: Hydrogen evolution reaction over time (a) comparing the addition of the Pt precursor with the room light on and in the dark and (b) with and without 60 seconds of ultrasonication prior illumination, using the digital controller and applying no ultrasonication and Pt precursor addition in the dark.

Addition of the Pt precursor

The Pt precursor was originally added while the room light was turned on, but according to L. Deilmann some of the Pt is already deposited when under illumination of visible light.¹²⁶ Therefore, I compared the impact of the Pt addition on the activity and ESD with the room light on and off. It can be seen in Figure 4.17a that, while the reproducibility was not increased, the activity was obviously influenced by the Pt addition in the dark.

Ultrasonication

To increase the dispersion of the TiO₂ catalyst, the suspension was ultrasonicated (US) for 60 seconds before degassing with Ar and before Pt addition. As can be seen in Figure 4.17b there is a big increase in reproducibility when US is applied. This indicates that ultrasonication offers control over the dispersion that is important for comparable results.

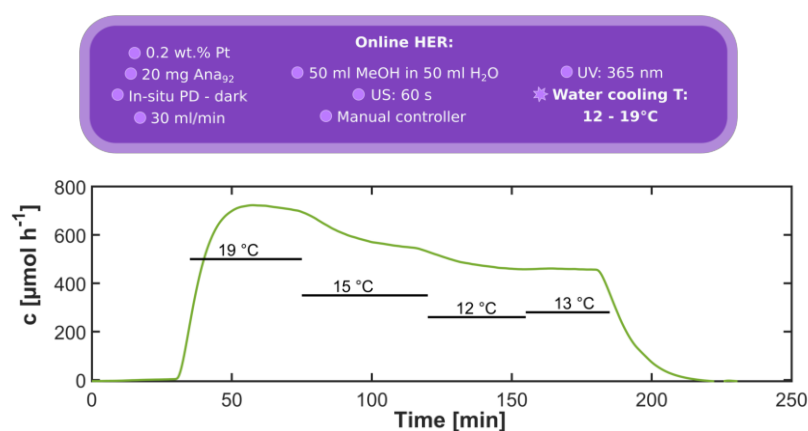


Figure 4.18: Hydrogen evolution reaction over time while changing the temperature of the water cooling system.

Water cooling temperature

Another crucial parameter is the temperature of the cooling water. The effect of this parameter may not be very distinctive at first and it only reveals itself over a long time: In the course of a few days the temperature of the in-house cooling water, which may be influenced by the outside temperature does not change much. However, if the experiments are repeated after a few weeks the activity changes significantly. Figure 4.18

4 Preliminary studies

shows the effects of changing the cooling water temperature during an experiment. Crucially, a decrease of 5°C can decrease the activity by more than 25%. In the end, the installation of a cryostat, which set the temperature to 15°C, helped to increase the reproducibility significantly.

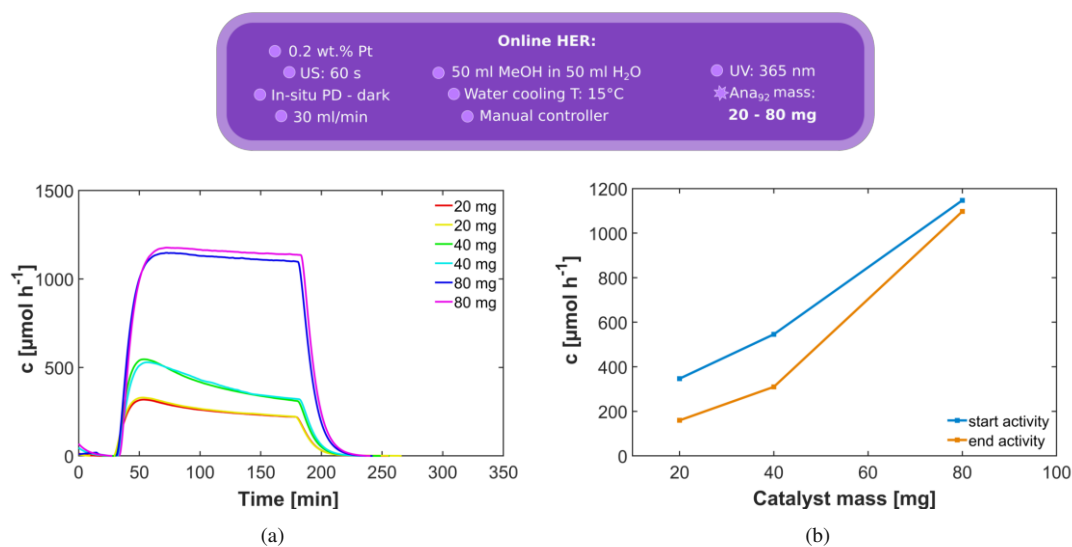


Figure 4.19: Hydrogen evolution reaction over time with different amount of catalyst; (a) shows time-dependent HER plots; (b) shows the start activity, which is the maximum activity, and the end activity plotted against the catalyst mass.

Variation of the catalyst amount

To see if the amount of mass in the system is rate limiting, I increased the mass to see how much the activity increases. Originally, 20 mg of catalyst was used in an HER experiment, which leads to a suspension concentration of 0.2 g/l. The amount was increased to 40 mg and 80 mg. As seen in Figure 4.19 the maximum activity increases almost linearly with the catalyst mass, while the ESD is strongest for lower amounts and minimized for the highest concentration of catalyst. The fact that there is no saturation plateau visible in Figure 4.19b indicates that the catalyst amount used in this work is not rate limiting.

Longterm studies and early-stage deactivation

The early-stage deactivation (ESD) describes a strong (multi-)exponential decay of the activity after a maximum is reached after ≈ 50 minutes of illumination. It has been

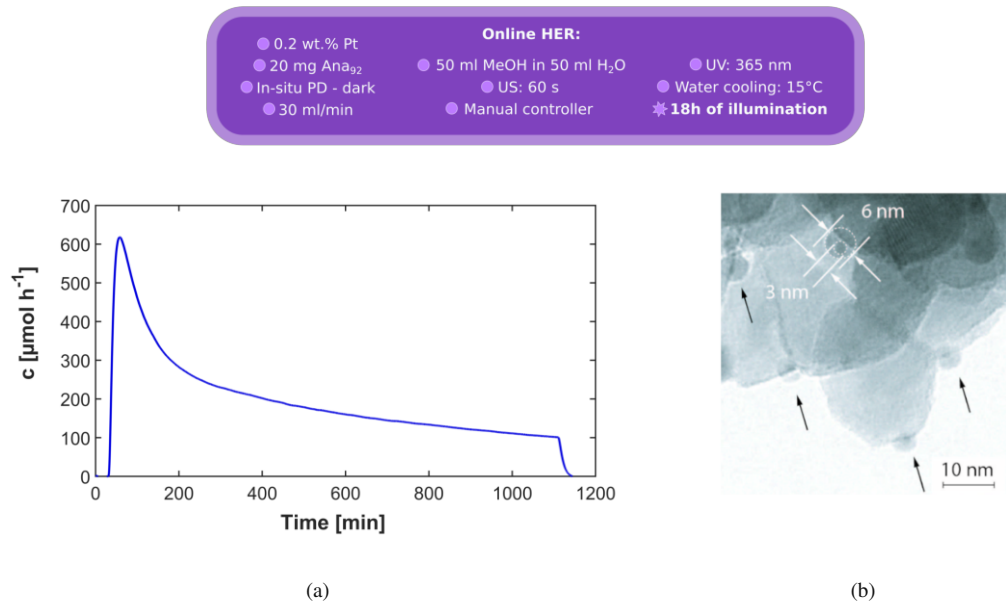


Figure 4.20: (a) Hydrogen evolution reaction over time with illumination over 18 hours shows the ESD in this system; (b) TEM image of an HER experiment conducted on P25 that shows the encapsulation of the co-catalyst Pt.¹²⁷

observed in several HER systems in Eder's research group; G. Haselmann found that it is connected with the ratio of oxygen vacancies and amount of Pt, and a possible explanation is the decoration of Pt with suboxide TiO_x species, as can be seen in Figure 4.20b.¹²⁷ Further investigating the causes for ESD is an important part of this work. To determine the saturation rate after ESD, the illumination was extended to 18 hours. Figure 4.20a shows the longterm study of anatase, where the activity is decreased to 16% its original activity.

Influence of parameters on the early-stage deactivation

In the following subsection, the amount of Pt and the effect of ultrasonication on the early-stage deactivation (ESD) will be investigated over several phases of TiO_2 in a 50ml H_2O and 50 ml methanol system.

The first parameter varied was the phase of TiO_2 , e.g. anatase, rutile, and the popular combination of the two; commercially obtained Evonik P25 (formerly Degussa) - which, according to Evonik, consists of 80% anatase and 20% rutile. P25 was further compared to a self-made mixture of the two phases in the same ratio (8:2 anatase:rutile mixture). With this comparison the influence of the interface between anatase and rutile can be investigated; since Evonik synthesizes P25 via flame-spray pyrolysis, which creates particles that comprise both phases sharing intimate contact with each other; while the 8:2 mix is made by simply mixing the pure phases together. Other parameters varied were the amount of Pt photodeposited on the support and ultrasonication of the suspensions before HER.

Please keep in mind that these experiments were performed before the system's reproducibility was optimized (see [section 4.5](#)). The comparison of photocatalytic activity is therefore not reliable, so I will only focus on the impact of the parameters on the percentage of ESD.

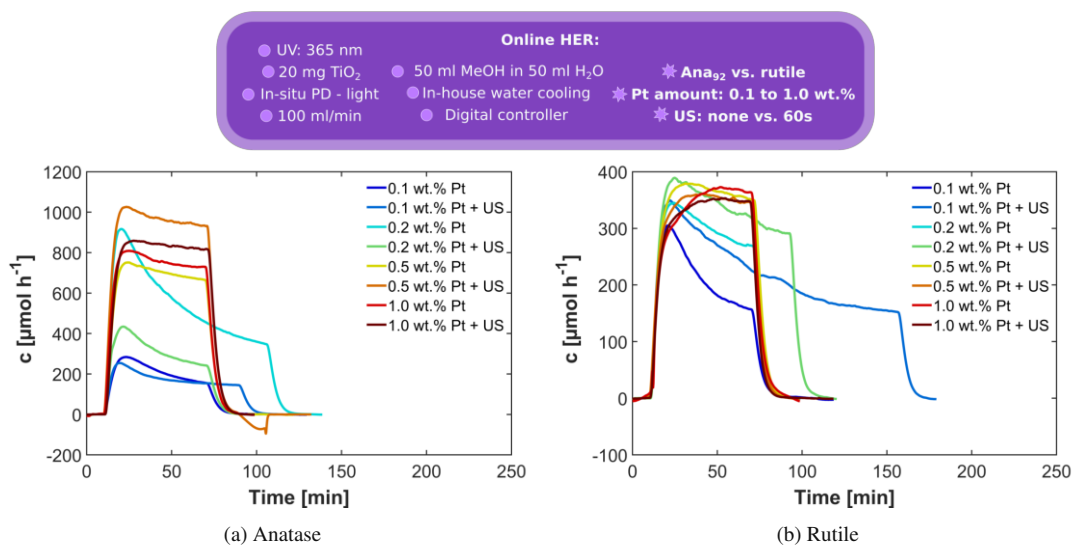


Figure 4.21: Hydrogen evolution reaction over time with different Pt co-catalysts amounts and ultrasonication for the phases (a) anatase and (b) rutile.

Anatase and rutile

First, the TiO₂ phases, anatase and rutile, were kept the same while the amount of Pt was varied with and without ultrasonications. From the combined results shown in [Figure 4.21](#) the following conclusions can be drawn:

- Over anatase the ESD is strongest for 0.2 wt.% of Pt ([Figure 4.21a](#)).
- Ultrasonication (US) the anatase suspension before illumination seems to have no impact on the ESD.
- The impact of US on the activity over anatase is inconclusive: For the 0.2 wt.% sample the US lowers the activity while for higher Pt loading it increases the activity slightly.
- The amount of Pt has a strong impact on the activity over anatase, which is because Pt acts as the active sites for the HER.
- Interestingly, the Pt amount does not seem to have an impact on the HER activity over rutile, as seen in [Figure 4.21b](#).
- Over rutile, 0.1 wt.% shows a similar deactivation behavior as over anatase, while it is much lower for 0.2 wt.% Pt.
- The ESD behavior is lowest for Pt amounts over 0.5 wt.% for both phases.

These results are congruent with literature: Anatase is reported as the phase with the highest photocatalytic activity for hydrogen reduction, owing to its higher conduction band position, smaller particle size, longer lifetime and faster migration of photoexcited electrons and holes. On the other hand, rutile is considered to be superior in photocatalytic oxygen evolution - which is not relevant in my studies due to the addition of the sacrificial agent methanol, which is easily oxidized by both phases.^{33,36}

Other studies showed that the photocatalytic activity rises with the Pt amount from 0.1 to 1.0 wt.% over anatase while it does not increase over rutile.^{128,129} While these reports are agreeing with the HER results displayed above, they do not explain the reason for these different activities. A possible explanation might lie in the platinum deposition on the two phases, leading to differently dispersed or sized Pt nanoparticles on the TiO₂ surfaces.

To investigate this, TEM images were taken after 50 minutes of HER over 0.2 and 1.0 wt.% Pt + US of both phases (see [Figure 4.22](#)). The size distribution was determined by measuring the diameters of 15 particles. As seen in [Table 4.6](#), the NPs are initially

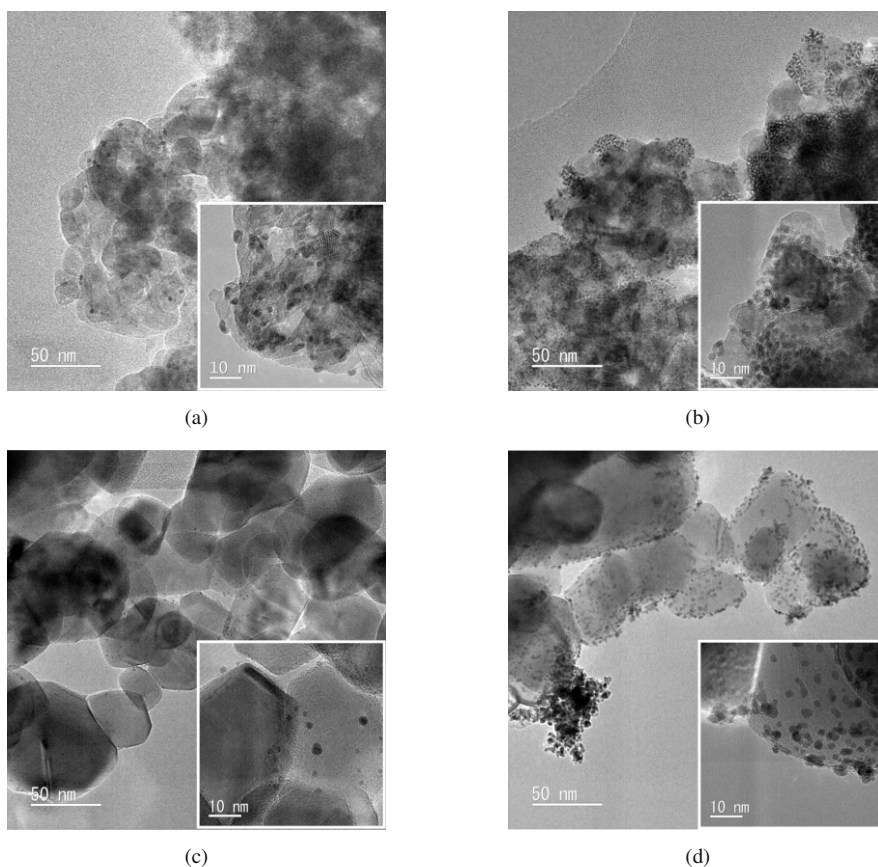


Figure 4.22: Transmission electron microscopy (TEM) images of Anatase with (a) 0.2, (b) 1.0 wt.% Pt and Rutile with (c) 0.2 and (d) 1.0 wt.% Pt

Table 4.6: The average Pt size for 0.2 and 1.0 wt.% Pt after 50 minutes of HER over rutile and anatase.

Phase	Pt amount [wt. %]	Pt size [nm]	Phase	Pt amount [wt. %]	Pt size [nm]
Anatase	0.2	1.9 ± 0.5 nm	Rutile	0.2	2.2 ± 0.7 nm
	1.0	1.9 ± 0.5 nm		1.0	2.8 ± 1.2 nm

bigger on rutile, their size also increases more with the Pt amount and the size distribution of the particles is bigger. A higher Pt amount leads to higher agglomeration on both phases, while the Pt NPs are well distributed for the 0.2 wt.% loadings.

P25 and 8:2 mix

Figure 4.23 shows the comparison of HER for P25 and the self-made mixture of anatase:rutile (8:2 mix). With higher Pt amounts (> 0.5 wt.%) over P25 very high activities can be achieved. While anatase and the 8:2 mix show ESD up to 0.2 wt.% Pt and rutile only for 0.1 wt.% Pt, P25 shows strong ESD up to 0.5 wt.% Pt. The

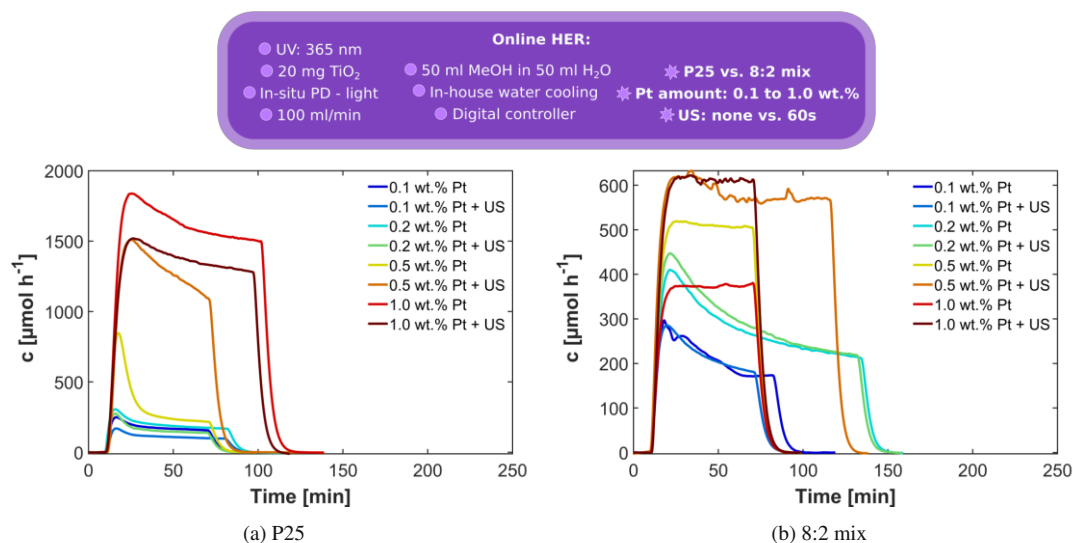


Figure 4.23: Hydrogen evolution reaction over time with different Pt co-catalysts amounts and ultrasonication for (a) commercial P25 and (b) self-made mixture of anatase:rutile 8:2.

increases in activity and ESD might be due to synergistic effects in P25, e.g. charge separation at the anatase/rutile interface. Additionally, ultrasonication decreases the ESD over 0.5 wt.% Pt on P25, while it has almost much lower effects over other systems (Figure 4.23a). The 8:2 mix generally shows both lower activities and low ESD for Pt amounts above 0.5 wt.%, but its behavior for lower Pt amounts is similar to P25. Overall, the 8:2 mix behaves similar to anatase, which the mixture is mainly composed of.

Conclusion

The combined results of the ESD in each system can be seen in Table 4.7.

1. The ESD is strongest for low Pt amounts (< 0.5 wt.%), particularly with P25, while higher amounts show a much lower ESD.
2. The impact of ultrasonication on the ESD is insignificant in most systems, contrary to previous results.¹²⁷
3. With the exception of rutile, higher Pt amounts lead to higher overall activities.

According to the results in this section the following setup was chosen; The use of manual controller, to minimize changes in the activity due to a decrease in illumination intensity; ultrasonication for 60 seconds prior to the HER to increase reproducibility; and addition of the Pt precursor in the dark, to exclude photodeposition before data

4 Preliminary studies

Table 4.7: Hydrogen evolution reaction activity after 70 minutes of illumination compared to maximum activity in percent for different TiO₂ phases and varying Pt co-catalyst amount. Deactivating samples with more than 25% loss of activity after 60 min of illumination are bold. For anatase, both the 0.1 and 0.2 wt.% Pt lead to ESD, which is not affected by US. The 8:2 mix behaves similarly. Rutile only shows ESD for 0.1 wt.% Pt, which is decreased with US. P25 shows ESD up to 0.5 wt.%, which is decreased with US only for 0.5 wt.% Pt.

Phase	US [60 s]	Pt [wt.%]	Deactivation [%]	Phase	US [60 s]	Pt [wt.%]	Deactivation [%]
Anatase	no	0.1	45	Rutile	no	0.1	48
		0.2	50			0.2	22
		0.5	12			0.5	8
		1.0	10			1.0	0
	yes	0.1	39		yes	0.1	36
		0.2	45			0.2	19
		0.5	10			0.5	3
		1.0	5			1.0	0
P25	no	0.1	37	8:2 mix	no	0.1	42
		0.2	43			0.2	36
		0.5	74			0.5	3
		1.0	15			1.0	0
	yes	0.1	41		yes	0.1	36
		0.2	50			0.2	37
		0.5	27			0.5	9
		1.0	12			1.0	1

acquisition. The water cooling temperature was set to 15°C in all experiments, as this parameter is crucial for a high reproducibility. The 0.2 wt.% Pt anatase system was chosen for further experiments; because it shows strong ESD; it is a pure phase, which makes analysis of the mechanism more straightforward; and the ESD seems to be not strongly dependent on ultrasonication, which can create additional oxygen vacancies that have been connected to the ESD in former studies.¹²⁷ I decided to apply ultrasonication before each experiment, simply because better dispersion of the catalysts will likely increase the reproducibility of the system. Henceforth, the 0.2 wt.% Pt loading on anatase catalyst will be referred to as Pt/TiO₂.

Summary of parameters influencing the ESD

The combination of the findings of this work and former works of my colleagues, Haselmann and Deilmann, let me reach the conclusion that the ESD during photocatalytic HER with Pt/TiO₂ is dependent on the following parameters:

- The source of illumination; UV light leads to ESD while visible light illumination does not. The ESD increases with increasing illumination intensity.^{126,127}
- Contrary to Haselmann's results, the findings here suggest that ultrasonication of the catalyst before the photocatalytic experiment does not increase the ESD.¹²⁷
- Calcination of the catalyst before HER reduces the ESD.¹²⁷
- Lower Pt concentrations (< 0.5 wt.% Pt) lead to increased ESD (see [Table 4.7](#)).
- The phase of TiO₂ is relevant: P25 shows significant ESD up to 0.5 wt.% Pt, Anatase up to 0.2 wt.% Pt and Rutile only for 0.1 wt.% Pt (see [Table 4.7](#)).
- ESD was only observed up to a threshold concentration of the catalyst in the reaction solution, which is below 80 mg of the catalyst in 100 ml of a methanol/water solution (see [Figure 4.20](#)).

The creation of oxygen vacancies is facilitated by UV illumination and ultrasonication, while it is healed through calcination.^{44,130,131} The results therefore indicate that the amount of Pt and oxygen vacancies has a central influence on the ESD. The reasons will be further explored in [section 6.1](#).

4.4 Oxygen evolution reaction

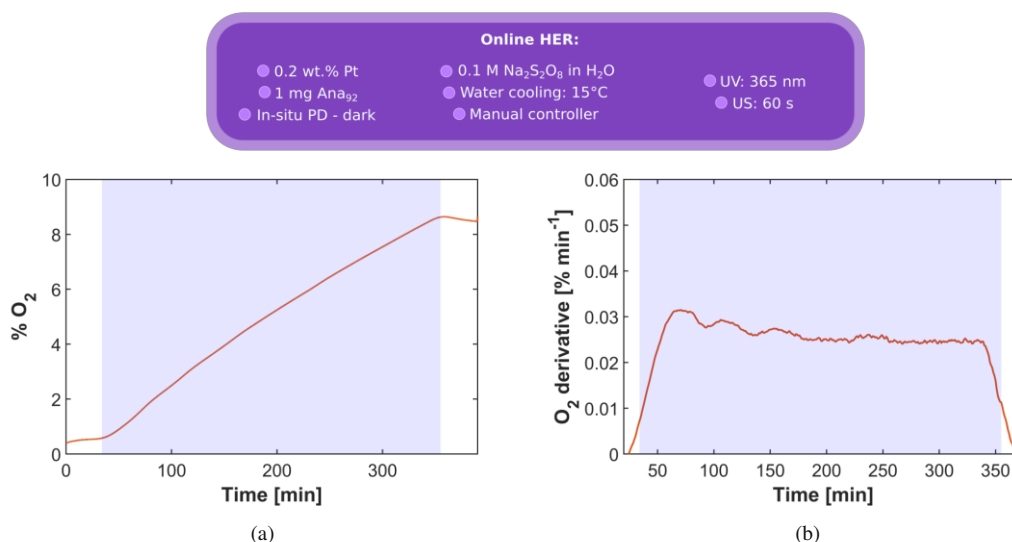


Figure 4.24: (a) Exemplary time dependence plot of the oxygen content in % over pure TiO₂ loaded with 0.2 wt.% Pt in a 0.1 M Na₂S₂O₈ solution. Upon illumination the O₂ content rises with nearly constant gradient; (b) the derivative of the rising oxygen content in the reactor. The data was smoothing with a moving average algorithm. The light purple area indicates illumination with UV light (365 nm).

To investigate if the complementary water-splitting reaction does also show early-stage deactivation, an oxygen evolution experiment (OER) was performed with Pt/TiO₂. Due to the relative minute amount of O₂ created in the system, a highly sensitive oxygen sensor was used in a new system that has been developed by the Eder group.

1 mg of catalyst powder was suspended in 2.5 ml of an 0.1 M Na₂S₂O₈ solution in distilled water by ultrasonating it for one minute. The experiment was done in a reactor (1.5 cm diameter) with a UV LED lamp illuminating from the side. Before closing the reactor specific amounts of an aqueous H₂PtCl₆ solution were added to the suspension in the dark. Pt species deposit on the metal oxide surface and reduce during illumination leading to 0.2 wt.% Pt of the catalysts mass. The reactor was sealed gas tight with a septum on top through which a retractable needle-type O₂ sensor (Pyroscience) was punctured. Before illumination, the gas room in the reactor was flushed with argon until the O₂ sensor showed a stable baseline. The suspension was stirred at 500 rpm and exposed to UV irradiation from an LED lamp (Thorlabs SOLIS-365C) with an emission maximum at 365 nm. The duration of illumination was 6 hours

to observe possible changes in the activity.

As seen in [Figure 4.24](#), upon illumination the O₂ content rises with nearly constant rate - no significant ESD of the oxygen evolution is observable. Unlike the HER, which takes place on the Pt surface, the OER evolves directly on the TiO₂ surface.¹³² The investigation of OER in the context of ESD has been done for the first time in this work; the results show that the ESD is connected to the co-catalyst Pt.

4.5 Reproducibility of the photocatalytic systems

In this section I will show the reproducibility and error of the photocatalytic systems; the online HER, the dye degradation and the size selective HER system.

Reproducibility of the HER systems

The reproducibility of the HER system is reported for the following parameters: 20 mg of catalyst powder in 50 ml of HPLC methanol and 50 ml DI water was ultrasonicated for 60 seconds and then transferred to a reactor. The suspension was flushed with argon before the Pt co-catalyst precursor H_2PtCl_6 was added in the dark, e.g. with the room lights turned off and window shades closed. The cooling water temperature was set to $15 \pm 0.5^\circ\text{C}$.

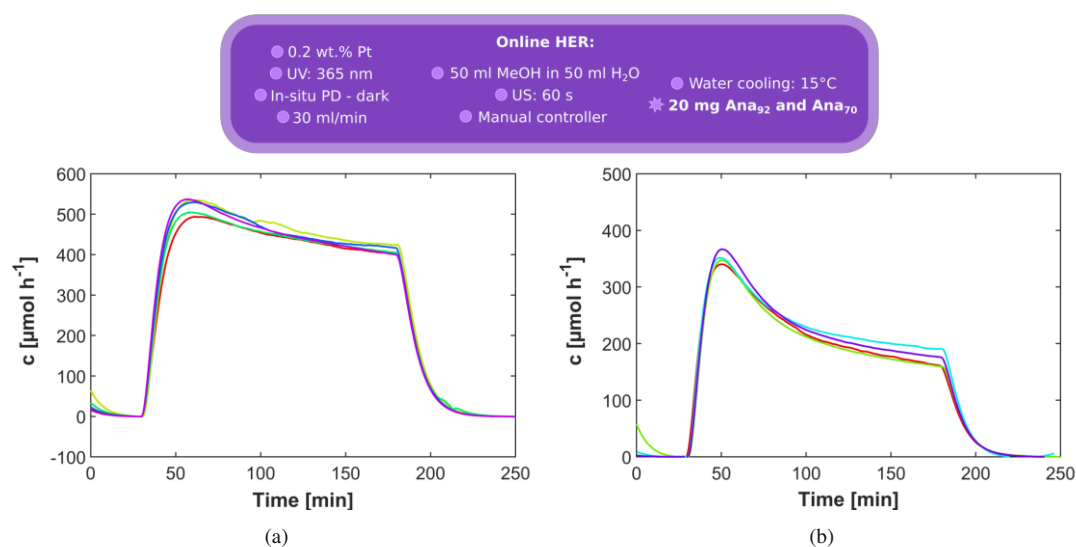


Figure 4.25: Reproducibility of the hydrogen evolution reactions over time with (a) Ana₉₂ and with (b) Ana₇₀.

For Ana₉₂, the mean and standard deviation of the starting activity was found to be $520 \pm 20 \mu\text{mol} \cdot \text{h}^{-1}$. For the end activity, after 150 minutes of illumination, they were found to be $410 \pm 11 \mu\text{mol} \cdot \text{h}^{-1}$. In percentage, these errors are less than 5%. The average deactivation was $79 \pm 2.7\%$. The values were calculated for 5 measurements which can be seen in Figure 4.25a.

For Ana₇₀, the mean and standard deviation of the starting activity was $365 \pm 37 \mu\text{mol} \cdot \text{h}^{-1}$, at the end it was $170 \pm 17 \mu\text{mol} \cdot \text{h}^{-1}$. In percentage, these errors are about 10%. The average deactivation was $46 \pm 0.4\%$. The values were calculated for 3 measurements which can be seen in [Figure 4.25b](#).

Reproducibility of the dye degradation system

The dye degradation system was tested for its reproducibility by measuring the photocatalytic degradation of each dye over the reference Ana₉₂ three times. For methyl orange (MO) the mean and standard deviation of the conversion were $29 \pm 2.9\%$ after 30 minutes and $79 \pm 7.8\%$ after 120 minutes. For methylene blue (MB) the mean and standard deviation were $18 \pm 2\%$ after 30 minutes and $60 \pm 9.4\%$ after 120 minutes. The results can be seen in [Figure 4.26a](#).

Reproducibility and LOQ of the size selective hole scavenging system

The system for size selective hole scavenging was tested for its reproducibility with 5% of 5-nonanol as a sacrificial agent in a 10% H₂O in acetonitrile (aCN) solution. This was done by repeating one set of measurements, that is Ana₉₂ and T₉₂S6^{NC}, 3 times and calculating the mean and the standard deviation. The maximum standard deviation after 3 hours of illumination was found to be $0.09 \mu\text{mol} \cdot \text{g}^{-1}$. The results of the set of measurement can be seen in [Figure 4.26b](#).

The limit of quantification (LOQ) is not clearly defined by IUPAC, it is most often referred to as 10 times the standard deviation of the blank. This value, 10 times σ is sometimes seen as arbitrary and conventions differ from laboratory to laboratory. According to EURACHEM's guide to analytical chemistry, the "limit of quantitation is the lowest concentration of analyte that can be determined with an acceptable level of uncertainty. It should be established using an appropriate measurement standard or sample, i.e. it is usually the lowest point on the calibration curve (excluding the blank). It should not be determined by extrapolation. Various conventions take the limit to be 5, 6 or 10 standard deviations of the blank measurement."^{133–135} 5-10 times this value would require to a minimum activity of $0.5\text{-}1 \mu\text{mol} \cdot \text{g}^{-1}$ after 3 hours,

4 Preliminary studies

which is not achieved with nonanol as a sacrificial agent in HER.

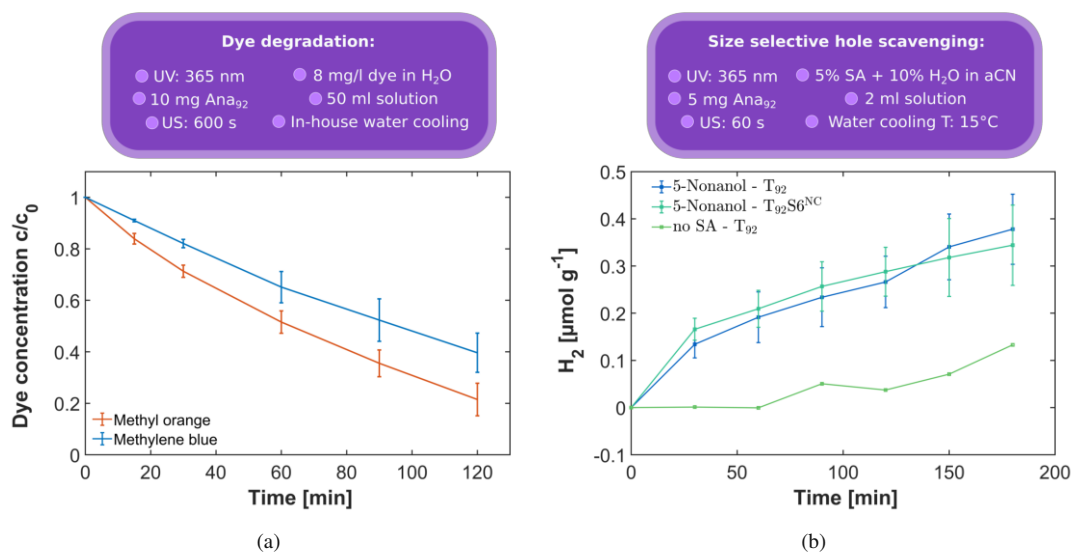


Figure 4.26: Reproducibility of the (a) dye degradation and (b) size selective HER setup.

5 Rate limiting steps of dye degradation

5.1 Introduction

TiO₂, as a catalysts, is often used as a model system for fundamental and applied photocatalytic studies. The combustion of organic dyes, as reactants, is considered a model application for photocatalysis. Commonly used dyes are methylene blue and methyl orange.^{59,62,103,136,137} The efficiency of heterogeneous catalysts depends on the catalyst's surface characteristics, such as the surface area, polarity and surface charge, and charge carrier dynamics, such as recombination and their transfer to the surface. The reactant can converse indirectly via the reaction with OH radicals, which are formed on the catalysts surface and can travel up to 500 μm, but they are conversed more easily if they interact with the catalyst's surface, where they are adsorbed closely to the charge carriers created in the semiconductor.

Core-shell structures with ultrathin shells offer a tunable system for functional and mechanistic investigations in heterogeneous catalysis. By varying the shell's thickness the interaction and therefore the adsorption and degradation of the reactant will be influenced. Coating of photocatalysts with ultrathin SiO₂ shells can have several additional advantages. It can lead to reduced recombination of electron-hole pairs and less agglomeration of nanoparticles, therefore a better quantum yield and a higher accessible surface area.^{59,62,67,74,108}

TiO₂ – SiO₂ core-shell structures have been investigated for different applications in photocatalysis, with shells mostly limited to thick (several nm) and/or mesoporous coatings.^{57,67,138–141} As expected, coatings of several nm thickness diminish the photocatalytic activity, often to zero, due to an inhibition of charge transfer.^{34,142} According to my preliminary results, ultrathin shells below 1 nm of thickness, do not have

5 Rate limiting steps of dye degradation

a significant influence on the charge transfer to the surface (Figure 4.11(b)). Only a few groups have investigated the effects of SiO₂ coatings thinner than 2 nm, often with irregular thickness and morphology.^{58,107,108,143}

To investigate the contributions of possible charge transfer inhibition, charge recombination, adsorption efficiency and photocatalytic degradation efficiency in core-shell samples with nonporous shells of different thicknesses between 0 and 1 nm, I performed dye degradation studies of a positively and negatively charged dyes and compared their results.

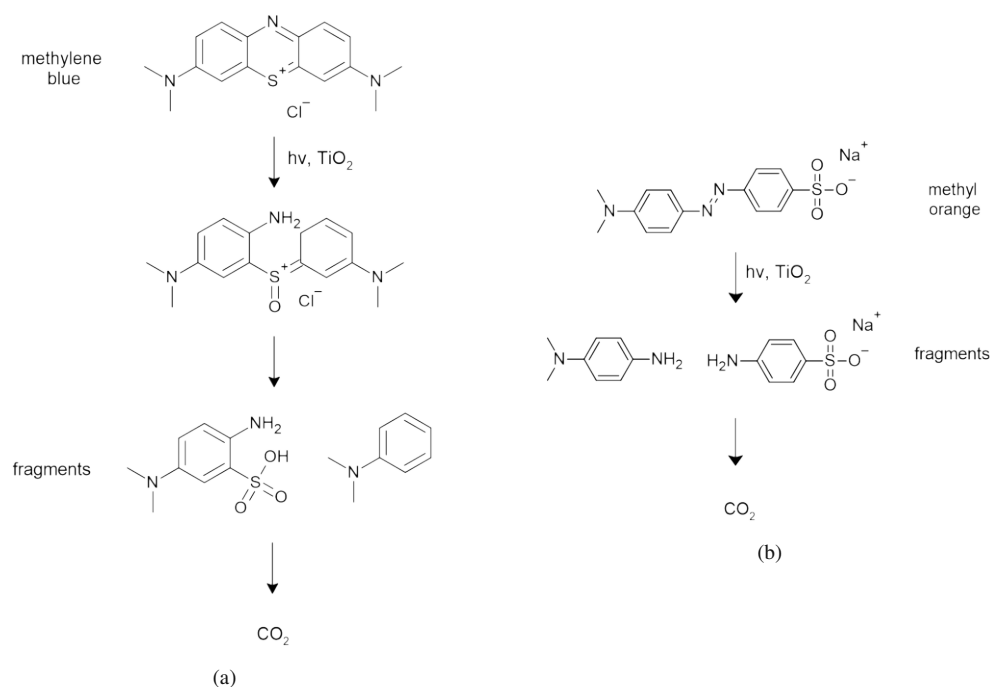


Figure 5.1: Possible degradation mechanisms of (a) methylene blue (MB) and (b) methyl orange (MO).^{144,145}

In particular, I chose methyl orange (MO) and methylene blue (MB). Methyl orange is a negatively charged, water-soluble, organic azo dye. SiO₂ suspended in water has a negatively charged surface, on which MO will be adsorbed less and an SiO₂ coating is therefore expected to decrease the photocatalytic activity. This has been verified in literature, unless the coating was incomplete or mesoporous; then, it was found that

the introduction of SiO₂ even increases the degradation kinetics and extend.^{67,146} The hypothesis is that the SiO₂ shell decreases the extend of agglomeration of the catalyst NPs, which consequently leads to a higher yield of OH[•] radicals, which fuels the degradation. A certain threshold thickness was observed, at which the degradation efficiency decreases. Methylene blue (MB) is a positively charged, water-soluble organic dye used in the textile and paper industry. Literature has shown that TiO₂ coated with SiO₂ are more efficient in degrading MB photocatalytically. This is explained with an increased adsorption of the positively charged dye on the negative silica surface and reduced recombination rates of generated excitons.^{59,141} None of these studies have compared the effects of different shell thicknesses.

Table 5.1: Relevant characteristics sample set 1 which was used for dye degradation studies: SiO₂ shell thicknesses measured by TEM and EDX, specific surface areas (SSA), t-plot external area and t-plot micropore area from BET.

Sample	Shell thickness [nm]			SSA [m ² g ⁻¹]	
	TEM	EDX	BET	micropores	external
TS0	-	0.03 ± 0.03	92	-	92
TS1	-	0.10 ± 0.02	88	2	86
TS2	-	0.30 ± 0.02	80	12	68
TS3	0.63 ± 0.13	0.61 ± 0.03	81	11	70
TS4	0.84 ± 0.18	0.81 ± 0.04	54	11	43
TS5	0.97 ± 0.13	0.91 ± 0.1	74	22	52

5.2 Adsorption and degradation studies

The sample set used in this section was sample set 1, consisting of **T₉₂S0^{SG5}_{0%}**, **T₉₂S1^{SG5}_{4%}**, **T₉₂S2^{SG5}_{8%}**, and so on. To increase the readability I will refer to them as TS0, TS1, TS2, and so on. For details about the preliminary characterizations, please refer to [section 4.1](#). A summary of the most relevant results for this chapter can be seen in [Table 5.1](#).

I investigated the effects of silica shell thickness on the photocatalytic degradation of differently charged reactants via UV irradiation. To monitor their degradation I ana-

5 Rate limiting steps of dye degradation

lyzed their decolorization via UV-vis, which is usually the first stage of the molecule's decomposition.^{147–149} Proposed degradation mechanisms can be seen in Figure 5.1.

I prepared solutions of each dye with a concentration of 8 mg l^{-1} . To test the reproducibility, the experiments were done three times with pure An_{92} (see section 4.5). Blind measurements without a catalyst were also performed to determine the degradation by illumination alone. 10 mg of the powder were dispersed in 50 ml of the dye solution with ultrasonication. The suspension was then transferred to a photoreactor (subsection 3.4.1), placed into a dark box underneath an LED lamp with a maximum emission at 365 nm. The amount of catalyst and the dye concentration were optimized in the bachelor project of a student to lead to a 20-60% decolorization for the uncoated reference An_{92} catalyst, to make sure differences in conversion after the introduction of an SiO_2 shell are apparent.¹⁵⁰

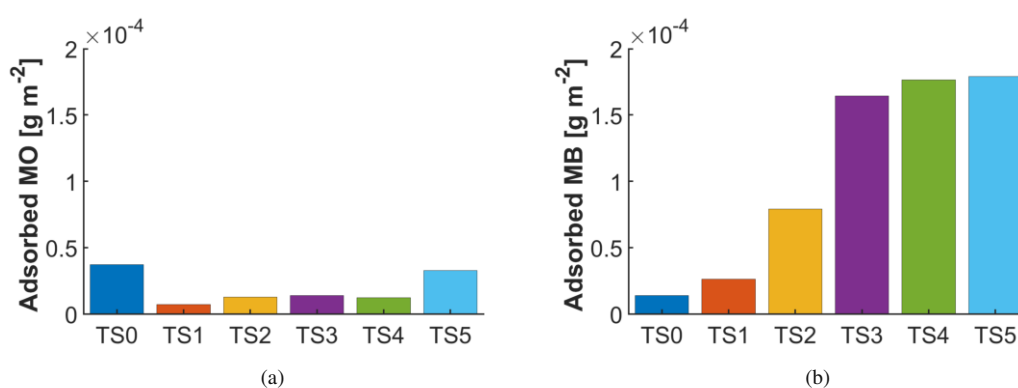


Figure 5.2: Adsorption studies in the dark of a blind and different core-shell samples of (a) methyl orange (MO) and (b) methylene blue (MB).

The measured pH values of the catalyst suspended in dye solution were 4.4 and 4.3 for MB and MO, respectively. The titania surface is therefore slightly positively charged, while the silica surface has a negative charge. As shown in Figure 4.5, the core-shell structures exhibit IEPs that lie between the respected values of both pure oxide references. According to this, it is expected that methylene blue, as a positively charged reactant, will adsorb more strongly on the core-shell structures within increasing silica thickness, while the adsorption of methyl orange will decrease.

Adsorption studies

First, I determined the adsorption equilibrium by stirring the suspension in the dark for 2 hours. I correlated the adsorbed amount with the respective SSA_{BET} (Table 5.1) and further compared it to the value of the blind measurement. The graphs show that the negatively charged reactant (Figure 5.2a) is indeed adsorbed to a higher extent on the positively charged TS0 than the positively charged reactant (Figure 5.2b). It also shows that the adsorption capacity of the positive reactant increases with increasing shell thickness of a negatively charged SiO_2 layer, up to TS4, which has a layer thickness of 0.81 nm. The negative reactant, while initially showing a decrease in adsorption when the shell is introduced, shows an increase in adsorption for the sample TS5. Considering that the adsorbed amounts were measured after two hours, and thus at equilibrium (see Figure 5.3a), the increased adsorption can be attributed to filling of micropores, which have been determined to be double as high for TS5 as for thinner layers.

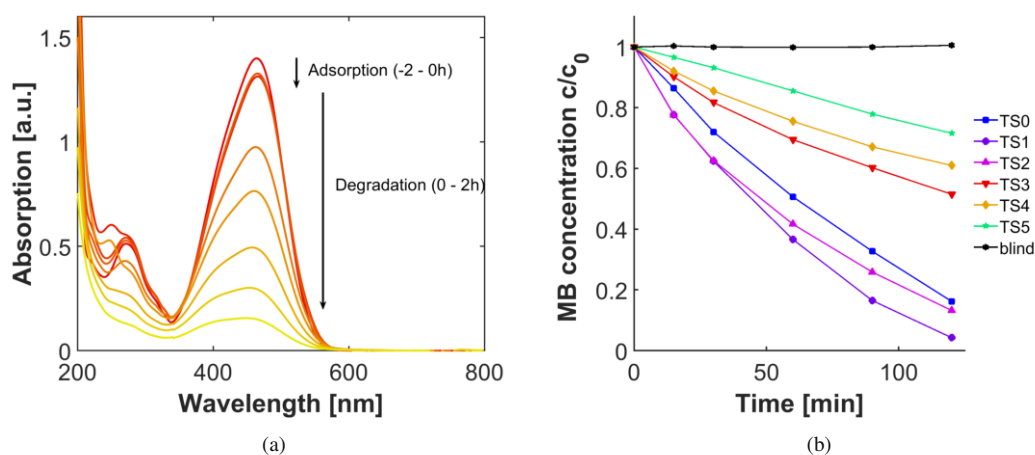


Figure 5.3: (a) Selected spectra shown for the adsorption (.2 to 0 hours) and degradation (0 to 2 hours) of methyl orange (MO) on TS2; (b) photocatalytic degradation of MO over no catalyst (blind), reference TS0 and different core-shell samples (TS1-TS5).

Degradation of MO

Figure 5.3a shows the selected UV-vis absorption spectra of the MO adsorption and degradation experiment done with the most effective sample, TS2. The highest peak is the absorption from the original solution before adding the catalyst, and the next three spectra were taken from the supernatant solution after the addition of the catalyst: One

immediately after ultrasonication of the catalyst in the solution for one minute, and two more after stirring in the dark for up to two hours. As can be seen, the adsorption in the dark is small and the equilibrium is achieved quickly - it was achieved after ultrasonication, for all samples.

Figure 5.3b shows the degradation in MO dye concentration upon illumination with UV light. TS1 and TS2 show a slightly increased photocatalytic performance compared to the reference TS0, while the activity gradually decreases with thicker shells (TS3 to TS5) to values below the reference values (see Table 5.2). The higher activity of TS1 and TS2, compared with the reference sample TS0, is surprising, especially if we consider that the adsorption capacity of MO on these catalysts was lower than on TS0 (Figure 5.2).

Concluding from these results, the adsorption is not the rate limiting step in this system. A possible explanation for the activity increase is a better dispersion of the nanoparticle catalysts due to the negatively charged silica surface. This explanation is often found in literature^{107,146}. While it is true that the IEP of the coated samples, which is around pH 5, would favor dispersion of the catalysts in neutral solutions, it is unlikely that the dispersion is favored at the measured pH of 4.4 (MB) and 4.3 (MO).

The increase could also be due to reduced recombination of electron-hole pairs upon charge trapping at the silica-titania interface as discussed by Hu et al⁵⁹. We did not observe such changes, e.g. by solid-state photoluminescence spectroscopy, in this sample set. We did, however, measure an increased lifetime of charge carriers in suspension of sample set 2 (see Figure 4.10). According to this, the introduction of an SiO₂ shell fuels the photocatalytic activity by reducing electron-hole recombination in the catalyst.

Another explanation is that the formation of Ti-O-Si sites can foster the photocatalytic activity: In TiO₂-rich TiO₂-SiO₂ mixed samples these interfacial sites act as aprotic Lewis acidic sites, contrary to protic Bronsted sites, as the charge difference in the differently coordinated metals (the coordination number is 6 for Ti⁴⁺ and 4 for Si⁴⁺) leads to a positive charge imbalance, which activates the oxidation of negatively organic dyes.^{68,151} Furthermore, it has been proposed that the Ti-O-Si bonds exhibit higher O₂ adsorption and could promote the formation of active oxygen species and increase the mobility of lattice oxygen, enhancing the catalytic activity.¹⁵²

I observed an increase in the number of Ti-O-Si bonds in ATR-FTIR (Figure 4.7) with

increasing step number. It is likely that these bonds become inaccessible beyond a monolayer of silica (i.e. > TS2). Therefore, the activity does not increase further in the thicker core-shell structures T3 to T5, but decreases significantly. Beyond that, the adsorption is unfavored and the Ti-O-Si sites do not accelerate the photocatalytic conversion.

Degradation of MB

Figure 5.4a shows the selected UV-vis absorption spectra of the MB adsorption and degradation experiment done with TS2. As in Figure 5.3a, the highest peak is from the solution before adding the catalyst, and three more spectra were taken after ultrasonication for one minute and stirring in the dark. As with MO, the adsorption equilibrium is achieved after ultrasonication.

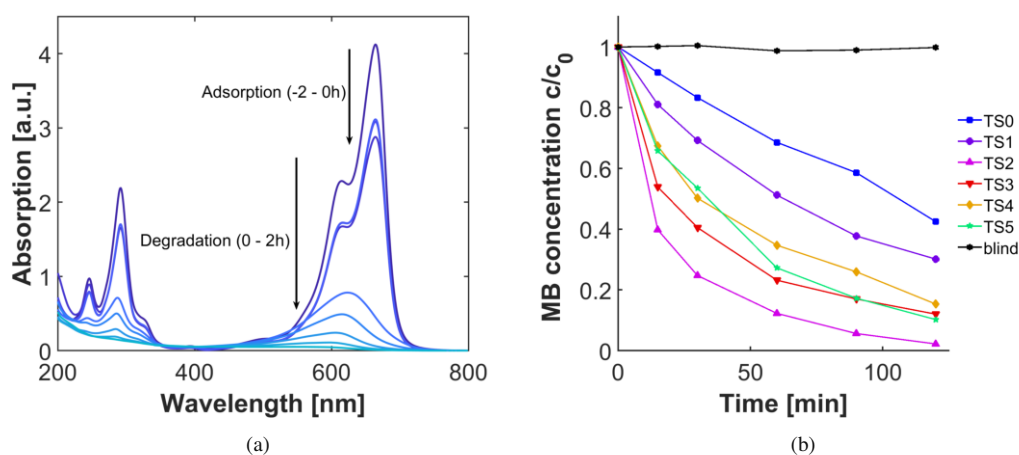


Figure 5.4: (a) Selected spectra shown for the adsorption (.2 to 0 hours) and degradation (0 to 2 hours) of methylene blue (MB) on TS2; (b) photocatalytic degradation of MO over no catalyst (blind), reference TS0 and different core-shell samples (TS1-TS5).

As soon as illumination starts, a decrease of the peak at 664 nm can be seen, while the peak at 615 nm decreases much slower. One explanation for this is, that the peak at 665 nm corresponds to the monomer of methylene blue, while the peak at 615 nm corresponds to the dimer - which gets degraded much slower.¹⁵³ Another possible explanation is, that the peak at 664 nm corresponds to methylene blue as is, while the successive demethylation leads to absorption at lower wavelengths.¹⁵⁴ The two peaks in the UV region correspond to the aromatic rings, and their decrease shows the

5 Rate limiting steps of dye degradation

degradation of the molecule to smaller fragments.¹⁴⁵ The peak shift was found to be the same over all measured catalysts.

The photocatalytic activity enhances until TS2, beyond which it decreases again, while showing an activity larger than the reference sample TS0 (Figure 5.4b, Table 5.2). TS2 shows only half of the adsorption efficiency of thicker shell samples, while still showing the highest photocatalytic activity. This is explained by several processes. On the one hand, the increase in adsorption capacity and the reduction of electron-hole pair recombination benefits the degradation process for all core-shell samples. So does the acceleration of the catalytic activity by accessible Ti-O-Si sites, which accelerate the conversion up to TS2, explaining its high conversion compared to its adsorption efficiency. Beyond that (TS3 - TS5), the conversion shows a similar trend as the adsorption efficiency, suggesting that in this thickness regime the reactant adsorption becomes rate dominating.

Table 5.2: SSA_{ext} normalized apparent rate constants of the first 30 minutes of methyl orange (MO) degradation and methylene blue (MB) degradation of different core-shell samples.

Sample	Rate constant $\cdot 10^{-4}$ [$s^{-1} m^{-2}$]			
	MO	R ²	MB	R ²
TS0	1.95	0.99	1.09	0.99
TS1	3.21	0.99	2.59	0.98
TS2	4.01	0.99	13.1	0.99
TS3	1.59	0.99	8.18	0.97
TS4	2.03	0.99	9.21	0.99
TS5	0.75	0.99	7.15	0.97

The apparent rate constants of the first 30 minutes of the degradation studies were determined with a pseudo-first order rate law and normalized with the SSA_{ext} calculated from BET (Table 5.2). I used the external surface area SSA_{ext} to correlate the data because micropores and small mesopores impose kinetic limitations for pore diffusion of large reactant molecules, such as MB and MO, which is hindering dynamic processes in liquid phase.^{32,155–157}

From TS1 to TS2, e.g. up to 0.3 nm shell thickness, the degradation rates for MO and

MB increase. The rate contributing factors are; the adsorption, which is determined by the surface charge and thus decreases for MO and increases for MB; the reduction of the charge recombination, which decreases up to TS2; and the access to acidic Ti-O-Si sites, which are also most prominent on the TS2 sample. Beyond a thickness of 0.3 nm, the degradation rates for both dyes decrease; for MO the rate constants reach similar values as over TS0, while for MB the rate constants are much higher than over the catalyst without a shell. The access to the Ti-O-Si sites is hindered, as is its contribution to the degradation. The charge recombination is constant over each shell thickness, but its contribution does not play a dominating role for the degradation rate; for MO it is not higher over shell thicknesses beyond a monolayer than over TS0. The adsorption in this thickness regime is as low for MO as it is over TS2, while it further increases for MB.

For TS0, the rate dominating factor is the adsorption of the reactant, which is favored for MO. The degradation of both MO and MB is most efficient over the sample TS2, and decreases for only one of them for thicker layers. This indicates that the access to Ti-O-Si sites is the rate dominating factor for layers up to 0.3 nm (TS1 and TS2). For thicker layers, the adsorption seems to play the dominating factor to the degradation rate, as it decreases the rate for MO and increases it for MB.

Note, that the charge transfer is not rate limiting in this thickness regime, as has been determined in preliminary studies. It will, however, be rate limiting for much thicker shells (> 3 nm), which suppress the transfer of charge carriers from the core to the adsorbed reactants.^{67,74} A reduction in catalyst NPs agglomeration has also not been proposed as dominating the degradation rate, as the agglomeration of the NPs is not expected to be significantly decreased in the determined pH.

5.3 Conclusion

In this project I showed how the deposition of ultra-thin layers of SiO₂ on TiO₂ nanoparticles with different thicknesses in the range between 0 and 1 nm can unravel contributing factors in photocatalytic combustion of organic dyes. Importantly, tests with both, positively-charged and negatively-charged dyes, allowed a direct comparison of photocatalytic performance and the identification of rate dominating factors in this ultra-thin thickness regime.

5 Rate limiting steps of dye degradation

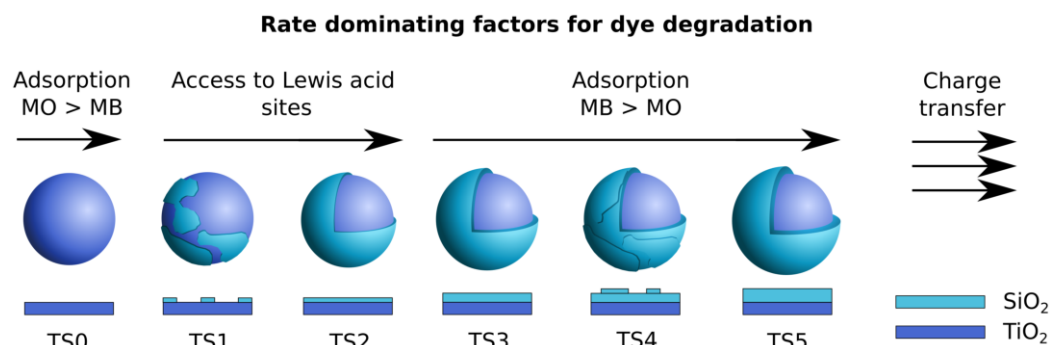


Figure 5.5: Concluding remarks of dye degradation studies: For TS0 the adsorption of the dye, which is more efficient for MO than for MB, is the dominating factor for the degradation rate. Up to one monolayer coverage the accessibility of Lewis acid sites is rate dominating. After full coverage, Lewis acid sites are not accessible anymore and the effect of adsorption becomes dominating, which is beneficial for MB and detrimental for MO.

Accessible Ti-O-Si bonds in samples TS1 (islands of SiO₂) and TS2 (monolayer of SiO₂) act as active Lewis sites and are likely responsible for the observed increase in activity for both dyes. In this thickness regime (<0.3 nm) the accessibility of these acidic sites is the rate dominating factor. When the shell is thicker than a monolayer (TS3-TS5), these sites are not available anymore. Instead, the effect of adsorption becomes dominating; this leads to a favor of the degradation activity for the positively charged MB and disfavors the degradation of the negative MO.

This work demonstrates that the performance of a photocatalyst can be tuned through the deposition of ultra-thin shells, with the performance being defined by the reduction of the charge recombination, the adsorption and the accessibility of interfacial sites.

6 Deactivation during HER

6.1 Introduction

When composited with platinum nanoparticles as a co-catalyst, TiO_2 is one of the most active photocatalyst for hydrogen evolution reactions (HER).^{39,158–160} There are two different ways to achieve Pt deposition on photocatalyst supports: Ex-situ, e.g. by wet impregnation or photodeposition with subsequent oxidation and reduction treatments at elevated temperatures, and in-situ, e.g. by in-situ photodeposition.^{41,45,46,49} The advantages of photodeposition are that Pt^{4+} will preferentially deposit on sites where photogenerated electrons are likely to reach the surface of the catalyst, thereby ensuring that electrons reach the co-catalyst during photocatalysis which increases the activity.¹⁶¹ Although Pt/ TiO_2 is considered a benchmark for HER, the reported reaction rates vary considerably, as these values depend on temperature, light intensity, reactor design and amount and type of sacrificial agents.^{162,163}

The research group of Prof Eder recently observed a deactivation during the early stages of photocatalytic hydrogen evolution, i.e. during the first three hours, in a system that uses in-situ photodeposition of Pt.¹⁶⁴ This effect has been investigated by varying several parameters, such as Pt amount, catalyst pretreatments, methanol concentration, dispersion, illumination source wavelength and intensity. It was found that the early-stage deactivation (ESD) is prominent under specific conditions: With low Pt concentrations (≤ 0.5 wt.%) and methanol concentrations $\geq 25\%$. It was enhanced under high UV intensities and with ultrasonication (US) pretreatment, and strongly reduced after calcination pretreatment in air. Though there is still a lack of understanding about the origin of the effect, it is likely connected to the amount of oxygen vacancies, which are introduced through UV illumination and US, they can be and they are healed through calcination (see [section 4.3](#)).^{44,130,131}

Several processes can affect the kinetics and the extend of ESD during photocatalytic

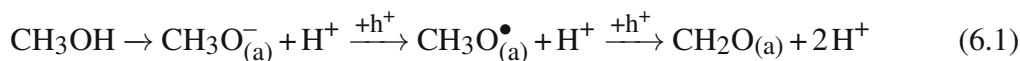
HER with methanol as a sacrificial agent. The hypotheses thus are:

1. A change in the **methanol oxidation mechanism**, possibly leading to the formation of CO - a known Pt catalyst poison.³⁸
2. A **strong metal-support interaction** between Pt and TiO₂ leading to either a change in the geometric effect, i.e. encapsulation of the Pt NP with sub-stoichiometric TiO_{2-x}, or a change in bifunctional effects.^{164,165}
3. A change in the **size, agglomeration and chemical state** of the Pt NPs during the photocatalysis.¹⁶⁶

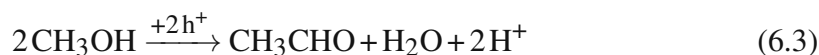
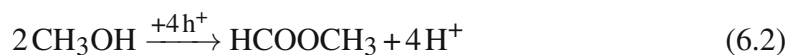
6.1.1 Methanol oxidation mechanism

Methanol is often used as a sacrificial agent in photocatalytic HER, because it is easily oxidized and, as a benchmark reference system, the reaction pathways have been studied by several groups and are summarized below.^{167–169} Please keep in mind, that some of these conclusions stem from gas-phase studies, while our experiments are conducted in the liquid phase.

The first step of methanol oxidation on TiO₂ is the chemisorption of a methoxy group, for which oxygen vacancies are the preferred adsorption sites.^{38,170–172} According to time-resolved IR spectroscopy, photogenerated holes are captured by methoxy in the course of a few nanoseconds, hundred times faster than the capture by surface hydroxyl groups, and a few thousand times faster than the reduction of protons on Pt.^{172,173} In the direct methanol oxidation pathway, the capture of a hole leads to a methoxy radical, the consumption of another hole and deprotonation leads to formaldehyde (Equation 6.1).^{170,172}

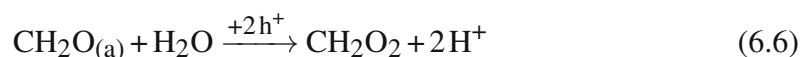
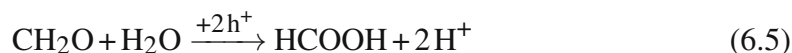


Bimolecular side reactions of methanol can lead to methyl formate, ethanal and dimethylether.¹⁶⁷

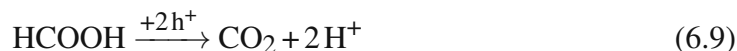
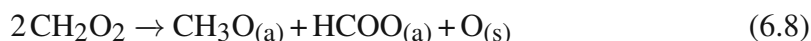




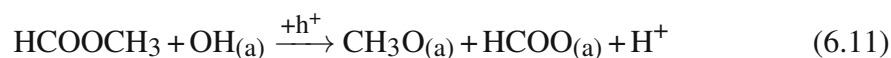
The formaldehyde generated in Equation 6.1 can capture two more holes and oxidize to either formic acid, dioxomethylene (DOM) or CO. ^{167,168}



Products can further lead to Canizzaro disproportionation of DOM (Equation 6.6) to adsorbed methoxy and formate at low temperatures. Formic acid (Equation 6.5) either oxidizes to CO₂ or dehydrates to CO, while the latter has shown to be more likely in gaseous studies. ^{167,168}



Methyl formate (MF) disproportionates to methoxy and formate. The latter dehydrates similar to Equation 6.10. According to Schubert et al. MF leads to larger amounts of CO than from formic acid but the kinetics are slower ¹⁶⁹



According to the proposed mechanisms, several pathways can lead to the generation of CO. The formation of CO is crucial, as it is a known Pt catalyst poison that strongly adsorbs on the active sites, blocking the hydrogen evolution. ¹⁷⁴ In a study by Huang et al., HCOOH and HCHO were also identified as poisonous to Pt and both Pt and TiO₂, respectively. ¹⁷⁵

In order to better understand whether the ESD is connected to a change in the CO/CO₂ formation mechanism, I monitored both gases simultaneously with H₂ during the first hours of photocatalytic HER. It appears that for low Pt concentrations (< 0.5 wt.%)

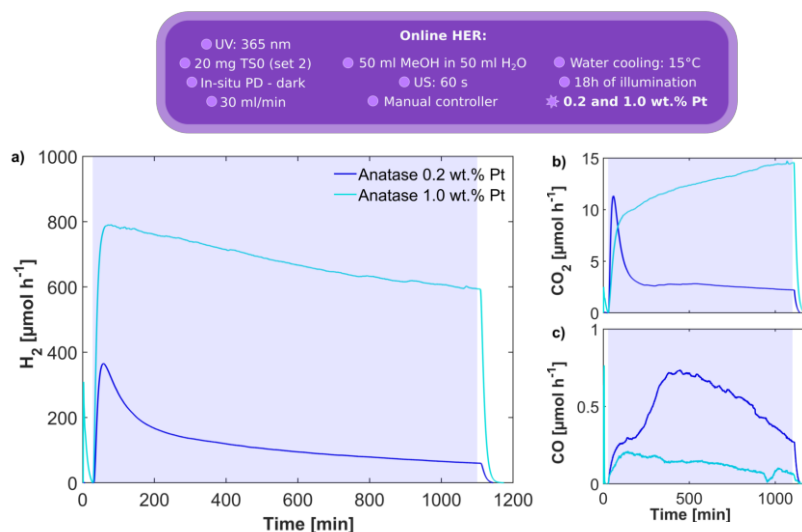


Figure 6.1: Anatase with 0.2 and 1.0 wt.% Pt in a longterm photocatalytic hydrogen evolution experiment. a) is the hydrogen evolution, which deactivates for lower Pt amounts; b) shows the CO₂ generation, which, in the 0.2 wt.% Pt sample decreases with the H₂ decrease, but it rises over time in the 1.0 wt.% Pt sample; c) shows the CO generation, which rises with the deactivation for the 0.2 wt.% Pt sample and is comparatively low for the 1.0 wt.% Pt sample.

Pt) the CO₂ evolution correlates well with the H₂ evolution. In contrast, CO shows a strong increase with the ESD and the decrease in CO₂ evolution. This indicates a change in the methanol oxidation mechanism that is related to the H₂ deactivation (see Figure 6.1). For higher Pt concentrations (> 1.0 wt.% Pt) no ESD and much less CO generation was observed. This result is among the first CO/CO₂ generation studies in the liquid phase and it is consistent with gas phase studies, where a higher Pt content led to a higher selectivity towards CO₂ and lower selectivity towards CO formation.¹⁶⁷ Pt NPs or atoms occupy the preferred adsorption sites for methanol, i.e. oxygen vacancies, which can lead to different methanol oxidation mechanisms.^{171,172} Indeed, we recently observed with in-situ ATR that at lower Pt concentrations bimolecular side reactions are dominant: For 0.7 wt.% Pt an oxidation pathway via methyl formate prevailed for the first 15 minutes, followed by a direct pathway as soon as Pt growth was completed after 30 minutes. Oxidation on TiO₂ with 2.7 wt.% Pt solely followed the direct pathway.³⁸

CO can act as a poison for Pt when enough CO is generated to adsorb on a significant amount of available Pt sites. As can be seen in Figure 6.1c, the average rate of CO is around 0.5 μmol · h⁻¹ after the ESD of H₂. A full coverage of the Pt surface with CO requires one CO molecule per surface Pt site.¹⁷⁶ The diameter of a Pt nanoparticle is around 1.7 nm for 0.2 wt.% Pt/TiO₂, which amounts to a dispersion of 0.66, i.e. 66%

of the Pt atoms are surface atoms.¹⁷⁷ The amount of Pt surface atoms is therefore 0.1 μmol , which is well below the average amount of generated CO per hour.

In summary, the amount of Pt is connected to the ESD as well as to the amount of generated CO. Both, methanol as well as the Pt precursor, preferably adsorb on surface oxygen vacancies. There seems to be a competition for those adsorption sites which apparently changes the methanol oxidation mechanism. This change in mechanism leads to either intermediates that act poisonous to the catalyst or to the generation of CO - a known Pt poison - which is related to the H₂ deactivation.

6.1.2 Strong Metal-Support Interaction

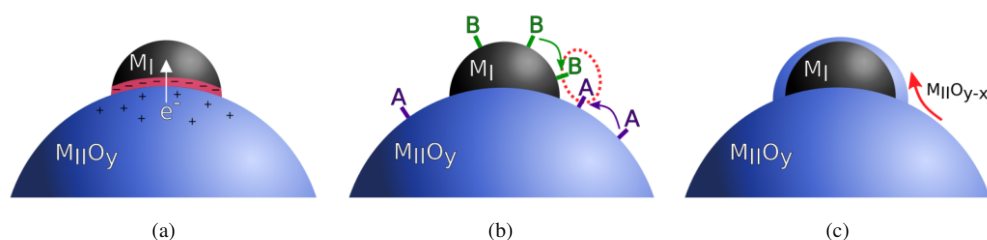


Figure 6.2: Strong metal-support interaction; (a) electronic effect; (b) bifunctional effect and (c) geometric effect.

The agglomeration and size of the co-catalysts NPs on the TiO₂ support influences the photocatalytic performance, as they determine the amount of active sites for HER - which are on the Pt surface - and the amount of electrons transferred to the co-catalyst - as the electron density is inversely proportional to the metal NPs size.^{50,72,178,179} These characteristics are determined by the strength of the metal-support interaction. "Strong metal-support interaction" (SMSI) is intensively studied in heterogeneous catalysis. It was first described by Tauster et al., who described the suppression of H₂ and CO chemisorption capacity on metal clusters on TiO₂ after it has been reduced chemically at high temperatures.^{178,180} Three factors have since then been described which contribute to the strength of metal-support interaction:⁴⁴

- An **electronic factor**, describing the charge transfer between the metal and the support, leading to changes of the electronic structure in the metal (see Fig-

ure 6.2a).

- A **bifunctional factor**, describing new reaction sites at the boundary between metal and support, which leads to separate yet synergistic reaction sites improving the photocatalytic performance (see Figure 6.2b).
- A **geometric factor**, where the metal cluster is decorated or encapsulated by mobile sub-oxide species, such as TiO_{2-x} , blocking active sites on the co-catalyst (see Figure 6.2c). This phenomenon is known to occur on reducible metal oxides such as TiO_2 .

The metal-support interactions are defined by interfacial phenomena, including chemical reactions, transport phenomena and charge redistribution during interface formation. Depending on the strength of the metal-support interaction, new phases can form between metal and support. For weak interactions the electronic structure is almost unchanged. Non-transition metal oxides, where the cation has no d-orbital available for bonding, the transition metal weakly interacts with the oxide anion. Supports like this, examples are SiO_2 and MgO , do not provide good nucleation centers for metal clusters, and the clusters are prone to migrate even at low temperatures. On transition metal oxides, the co-catalyst can interact with the d-orbitals of the cation. The metal is closest to the cation when surface anion vacancies are available as nucleation centers. This interaction between metal and cation was found to be mainly ionic, stemming from the electron transfer from the reduced cation to the metal, known as the **electronic effect** of SMSI.⁷²

The **bifunctional effect** describes how the support can participate in the creation of catalytically active centers at the triple-phase boundary (TPB), also called "dual site" reaction system. Reactant A is adsorbed on the support while reactant B is adsorbed on the metal. The mobile reactants move to the metal-support perimeter where they react with each other (Figure 6.2b). Therefore, the density of those TPBs, increased by low agglomeration and small particle sizes, as well as the amount of surface oxygen vacancies close to the co-catalyst can influence the photocatalytic activity.⁷²

The **geometric effect**, leading to the partial or total encapsulation of the co-catalyst, involves the transfer of sub-stoichiometric TiO_x species onto the metal. This is energetically favorable when the metal's surface energy (γ) is larger than the oxide surface's surface energy. Especially metals with a surface energy higher than $\gamma > 2.0 \text{ J/cm}^{-2}$ are prone to encapsulation. Pt, Ir, and Os have a surface energy higher than 2.0 J/cm^{-2}

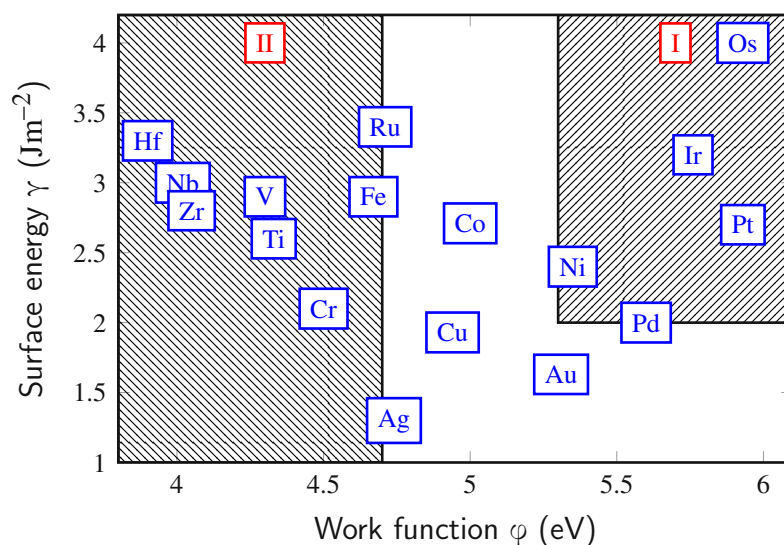


Figure 6.3: Surface energies γ and work functions ϕ of different transition metals. For the work functions, ϕ (111) values were taken for fcc metals, (100) values for bcc metals, if available. Otherwise polycrystalline values were taken.¹⁸¹ Surface energy γ values were taken from calculations by Mezey and Giber.¹⁸² Two regions are drawn, concerning their behaviour on TiO₂: Region I, where encapsulation is expected ($\phi > 5.3$ eV and $\gamma > 2$ Jm⁻²) and region II, where oxidation of metals on TiO₂ is possible ($\phi < 4.7$ eV). This graph was redrawn from Fu et al., but some values were updated.¹⁸³

while Au, Ag and Cu have a low surface energy. Metal oxides with a low surface energy are, for example, TiO₂ and V₂O₅, while SiO₂ and Al₂O₃ have a higher surface energy.^{72,184} It has also been shown that encapsulation occurs for metals with large work functions on reducible n-type oxides, such as defective TiO_x, where the Fermi level E_F of the metal is below the E_F of the support.⁴⁴ For work functions and surface energies of common metals commonly used as co-catalysts see Figure 6.3.

However, SMSI and the connected effects were originally described for catalysts which were treated with high temperatures under highly reductive atmospheres.^{185,186} The question emerges if the observations can be transmitted to in-situ photodeposited Pt during low temperature photocatalysis. Some groups have reported the decoration of noble metals by Ti-suboxide or -hydroxide species after in-situ photodeposition.^{42,164,187} Encapsulation requires the generation of oxygen vacancies in reducible metal oxides, which can be introduced through a highly reductive atmosphere (H₂) at high temperatures (> 300°C), through ultrasonication treatment or through illumination with UV light.^{44,130,131} Indeed, US treatment increases the ESD while healing the oxygen vacancies through calcination in air strongly reduces it.¹²⁷ While it is not clear if US treatment and UV illumination induce enough oxygen vacancies in TiO₂ to promote significant SMSI related effects, there is a clear indication that the deactivation is

connected to a critical number of oxygen vacancies.

In summary, SMSI and its related effects are strongly connected to the catalytic activity: The electronic and bifunctional effects can increase the activity, while the geometric effect lowers it due to the blocking of active sites on the Pt surface. As has been described in [section 4.3](#), the ESD highly depends on the ratio of Pt to the surface oxygen vacancies V_O , i.e. a low Pt/ V_O ratio in a catalyst shows strong ESD while a high ratio shows only long-time linear deactivation. The amount of surface oxygen vacancies in connection to the strength of metal-support interaction has been investigated before: Pt binds more strongly to the support when adsorbed on an oxygen vacancy, which influences the electronic effect.¹⁸⁸ Furthermore, some reaction mechanisms are influenced by oxygen vacancies in proximity to the co-catalyst, which is related to the bifunctional effect.¹⁸⁹ Oxygen vacancies also promote the mobility of sub-stoichiometric oxide species TiO_x , leading to the encapsulation of Pt and blocking its active sites which then inhibits H_2 generation, according to the geometric effect.¹⁹⁰ My hypothesis, therefore, is that the initial amount and further generation of surface oxygen vacancies during photocatalysis influence the strength of the metal-support interaction; which can facilitate the encapsulation of the co-catalyst, thereby decreasing accessible active sites; or it leads to changes in the bifunctional effect and therefore changes in the activity.

6.1.3 Nature of the Pt co-catalysts

The dispersion, morphology and oxidation state of Pt on TiO_2 will also affect the activity during HER. Some studies have investigated the the oxidation state during photoreduction and analyzed the size, shape, loading and dispersion of the Pt co-catalysts after illumination.

Kozlova et al. noticed that most of the photodeposited Pt had a oxidation state of 2+, and the catalyst deactivated after 400 minutes due to agglomeration of the Pt NPs.¹⁶⁶ Yang et al. observed that the photoreduction of Pt^{4+} to Pt^{2+} and finally Pt^0 takes several hours until Pt^0 is the dominant species, while Vorontsov et al. found that the initial oxidation state during photoreduction is only higher than 0 in basic solutions.^{191,192} Murcia et al. also noticed an increase in the size with increased illumination time, possible reoxidation of Pt^0 or desorption by OH^* species present in the illuminated aqueous solution and a decrease in dispersion with the deposition time. They observed

an increase in activity up to 120 minutes during photocatalytic phenol oxidation, where a maximum of Pt^0 was observed.¹⁶¹ These studies mainly describe how the activity during photocatalytic oxidation of organic molecules decreases after a few hours due to changes in the co-catalyst. None of them describes the deactivation kinetics during the early stages of HER that has been observed in our research group.

It was also found that the Pt reduction rate is influenced by the concentration of Pt^{4+} in the solution. In the concentration range relevant for this project the rate increases linearly with the concentration, which can explain why the Pt loading affects the ESD.¹⁹³ The deposited NPs are also expected to have a higher diameter when deposited from higher concentrated solutions: The electron density in the already deposited Pt NPs hinders the creation of new nucleation sites, and the Pt precursor will preferentially reduce over already adsorbed Pt than on the TiO_2 surface.^{161,194}

The dynamic nature of Pt on TiO_2 is definitely complex and several contributions are summarized:¹⁶⁵

- Nanoparticle growth^{161,166}
- Migration/Ostwald ripening leading to agglomeration¹⁶⁶
- Dissolution to Pt^{n+} ^{47,161}
- Slow reduction by illumination^{191,192}
- Oxidation of Pt to PtO_x ¹⁹⁵
- The concentration of Pt^{4+} in the solution determines the reduction rate and size of the NPs^{193,194}

There is also some confusion about the different terms concerning the migration of Pt-species on the TiO_2 surface:

- Ostwald ripening: Smaller particles are less stable than larger particles, and single atoms will detach from small particles, migrate across the surface and reattach to other particles.^{196,197}
- Particle migration: Nanoparticles diffuse over the surface and sinter/coalesce or agglomerate with other nanoparticles.^{197,198}
- Dissolution to higher oxidation states and reduction at other sites on the support's

surface.⁴⁷

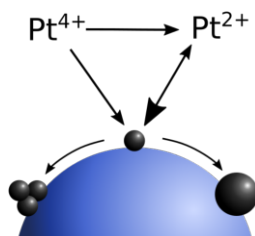


Figure 6.4: The stability of Pt nanoparticles on TiO₂: Shows an equilibrium between Pt⁴⁺, Pt²⁺ and adsorbed Pt⁰ nanoparticles on the surface, which possibly migrate over the surface to form agglomerates or increase in size.

The size increase and agglomeration can have detrimental effects on the photocatalytic activity: On larger NPs less surface atoms are available for reactants to adsorb and react. Furthermore, the electron density transferred from the support to the metal NP is inversely proportional to its size.¹⁷⁹ Agglomeration of the NPs leads to an increased travel path of photogenerated electrons, which means that less electrons reach the co-catalyst to react with adsorbed reactants, leading to a lower quantum yield.

Surface defects, such as oxygen vacancies, play a great role in the nucleation and stabilization of metal NPs on the support's surface. The increased concentration of electrons in surface oxygen vacancies and the proximity to Tiⁿ⁺ is the reason these defects serve as nucleation centers, where the Pt^{x+} reduces.¹⁹⁹ As explained above, transition metal co-catalysts are more stable on reducible metal oxide supports than on non-reducible metal oxides, due to covalent mixing between d-orbitals.^{44,200} The mobility of the Pt particles is reduced with increasing metal-support interaction. It is therefore expected that the migration and agglomeration during photocatalysis is less pronounced on TiO₂ than on core-shell TiO₂-SiO₂ catalysts. However, SMSI may only be induced with pretreatment of the Pt/TiO₂ at higher temperatures under reductive atmospheres.

In summary, the Pt size and agglomeration can change during photocatalysis, and the reduction of Pt may be slow and only fully reduced after hours of UV illumination, especially when Pt was photodeposited in-situ, without any pretreatment. My hypothesis is that these changes decrease the photocatalytic activity, because the amount of accessible surface Pt atoms, its electron density and the overall quantum yield is deter-

mined by the size and agglomeration of the NPs. It is thereby of interest to compare the activity and stability of the photocatalytic conversions over untreated Pt/TiO₂ with Pt/TiO₂ pretreated at high temperatures under reductive atmospheres, which likely induces stabilizing SMSI effects.

6.1.4 Summary

Several possible reasons for the ESD were explained in this section:

1. The **methanol oxidation mechanism**: It is likely connected to the amount of available surface oxygen vacancies on which methoxy adsorbs as a first mechanistic step. The course of the mechanism can lead to different CO/CO₂ ratios during the photocatalysis, where a higher CO/CO₂ ratio could be detrimental to the photocatalytic activity as CO acts as a potent poison for the Pt co-catalyst.
2. The strength of the metal-support interaction:
 - a) The **bifunctional effect**, which is influenced by the amount of oxygen vacancies in proximity to the co-catalyst.
 - b) The **geometric effect**, where the generation of oxygen vacancies can lead to mobile TiO_x, which can encapsulate the co-catalyst.
3. The **stability of Pt** during photocatalysis: The size and agglomeration of the NPs can change during photocatalysis which decreases the number of active sites and the quantum yield of the catalyst. This behavior is influenced by the nature of the support.
4. The **oxidation state of Pt**: Without reductive pretreatment of the co-catalyst, the photoreduction was found to be rather slow in higher concentrated samples, according to literature. This leads to a change in available co-catalysts mass and a change in the co-catalysts size during photocatalysis.

6.2 Deactivation with Pt/TiO₂–SiO₂

In order to better understand the phenomenon of early-stage deactivation (ESD) and to investigate the possible contributions explained in the former section, which are connected to the nature of the support and the number of surface oxygen vacancies, I developed the idea of using core-shell structures of TiO₂ with an ultrathin shell of a non-reducible metal oxide, such as SiO₂, as a photocatalyst for HER. It is well known that SiO₂ has a lower density of oxygen vacancies, a higher surface energy and a more negative surface charge than TiO₂.^{71,72} There are several ways in which an SiO₂ shell can affect the ESD:

- SiO₂ has less oxygen vacancies on which methoxy species can adsorb and it will affect the **methanol oxidation mechanism**, which could be related to the deactivation.
- SiO₂ is less mobile than TiO₂ and therefore and less prone to **encapsulate** the Pt co-catalyst.
- If the **bifunctional effect** is connected to the deactivation, a different behavior concerning product formation will be expected when then Pt co-catalyst is attached to SiO₂ instead of TiO₂.
- The **shape and mobility of Pt NPs** will be affected by the nature of the support, which can affect the quantum yield.
- The photoreduction mechanism and kinetics of Pt depends on the amount of precursor adsorption and nucleation sites, i.e. oxygen vacancies, which are lower on SiO₂.

In order to compare the two systems, i.e. Pt/TiO₂ and Pt/TiO₂–SiO₂, the SiO₂ shell needs to be homogeneous and ultrathin to allow charge transfer from the catalyst to the co-catalyst, i.e. electrons need to be able to travel uninhibited from TiO₂ to the SiO₂ surface.

So far, only very few works have studied TiO₂–SiO₂ core-shell structures for photocatalytic water splitting; those who have, used comparatively thicker shells. For example, Gong et al. used shells of 10 nm and more and observed that the H₂ production is negligible in this layer thickness region.⁶⁷ The decrease in activity is most likely attributable to the comparatively large thickness of the shells, which seem to

suppress the transfer of charge carriers from the core to the adsorbed reactants. To verify the charge transfer in the thickness regime between 0.3 and 1 nm, I performed charge transfer photoluminescence studies, which show that the electron transfer is not inhibited by an SiO₂ layer in this thickness regime, and hence fulfill the requirement mentioned above (see Figure 4.11b).

I investigated the effect of an SiO₂ layer with different thicknesses on the hydrogen evolution reaction using in-situ platinum photodeposition, to determine the influence of the SiO₂ shell, with variable thickness, on the photocatalytic activity, ESD and Pt size, dispersion and stability. In each run, 20 mg of catalyst powder was suspended in 100 ml of 50:50 deionized water:methanol (HPLC grade) by ultrasonicing it for one minute. Before illumination, specific amounts of an aqueous H₂PtCl₆ solution were added to the suspension in the dark, leading to a nominal concentration of 0.2 wt.% Pt (± 0.01 wt.%). Pt species deposit on the metal oxide surface and reduce during illumination.³⁸ The suspension was stirred at 500 rpm and exposed to UV irradiation from an LED lamp (Thorlabs SOLIS-365C) with an emission maximum at 365 ± 10 nm. The HER rate was monitored for an illumination period of 2.5 hours in order to follow the ESD behavior.

The experiments were done at least three times to assure the reproducibility of the system. The standard deviation after 2.5 hours of illumination was found to be less than $20 \mu\text{mol h}^{-1}$.

Table 6.1: Physical properties of SG sample set 2: SiO₂ shell thicknesses determined from the average of 10 elemental ratios measured by EDX and 15 thickness measurements from TEM images. Specific surface area (SSA) was determined via N₂ physisorption as has an error of $\pm 2 \text{ m}^2\text{g}^{-1}$. *Shells are too thin to be detected.

Sample	Shell thickness [nm]			SSA [m^2g^{-1}]	
	EDX	TEM	BET	micropores	external
TS0	0.01 ± 0.00	*	67	0	67
TS1	0.17 ± 0.07	*	67	3	64
TS2	0.33 ± 0.05	*	55	7	48
TS3	0.49 ± 0.09	0.49 ± 0.13	60	6	54
TS4	0.63 ± 0.09	0.64 ± 0.11	58	10	48
TS5	0.78 ± 0.11	0.78 ± 0.14	62	13	49
TS6	0.97 ± 0.09	0.93 ± 0.18	56	16	40

6 Deactivation during HER

The samples used in this part of the work were from the sample set 2, consisting of $T_{70}S0_{0\%}^{SG6}$, $T_{70}S1_{3\%}^{SG6}$, $T_{70}S2_{6\%}^{SG6}$, and so on. To increase the readability of this chapter, I will use the short names for the samples, e.g. $T_{70}S0_{0\%}^{SG6}$ will be **TS0**, $T_{70}S1_{3\%}^{SG6}$ will be **TS1**, $T_{70}S2_{6\%}^{SG6}$ will be **TS2**, and so on. For details about the preliminary characterizations, please refer to [section 4.1](#). A summary of the most relevant results for this chapter can be seen in [Table 6.1](#)

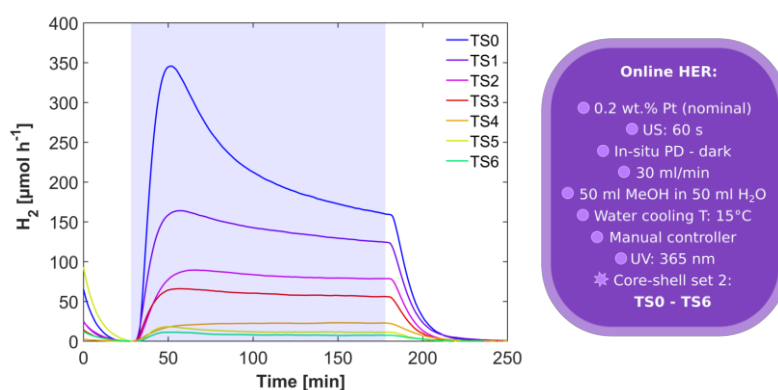


Figure 6.5: Exemplary time dependence plots of the hydrogen evolution rate over pure TiO₂ and core-shell samples SG set 2 loaded with 0.2 wt.% Pt in 50 vol.% methanol solution with US treatment. The light purple area indicates illumination with UV light (365 nm). Note that the plots shown here are typical examples. The average values of all measurements can be seen in [Table A.3](#).

The time-dependent HER behavior with the reference sample and different SiO₂ shell thicknesses can be seen in [Figure 6.5](#). The reference sample, pure TiO₂ (TS0), showed the highest maximum rates, yet also the strongest ESD. The rate reached an average maximum of 360 $\mu\text{mol} \cdot \text{h}^{-1}$ after about 20 min of illumination, then it dropped to a value of 160 $\mu\text{mol} \cdot \text{h}^{-1}$ after 2.5 hours without reaching saturation.

The introduction of SiO₂ has greatly impeded the deactivation of Pt for HER. The ESD is decreased for all core-shell samples; the sample TS1 shows only half of the ESD of TS0 (26 vs. 53%) and upon introduction of a monolayer of SiO₂ (TS2), it was reduced to about 15%, i.e. the end activity was 85% of the highest activity, ([Table 6.2](#)). The deactivation increases again for thicker layer samples, such as TS5 and TS6.

The SiO₂ layer also decreased the overall photocatalytic activity: TS2 shows only half the activity of TS0 after 2.5 hours of illumination, and the activity decreases gradually for thicker shells. Since the layers in this thickness regime are thin enough to facilitate

electron transfer from TiO₂ to Pt, the decrease in activity is not likely caused by the insulating properties of the layer (see [Figure 4.11](#)).

However, the decrease in catalytic performance could very well be because of differences in the metal-support interaction, such as; a change in the bifunctional effect, i.e. a different phase in the TPB; or a change in the electronic effect, i.e. the interfacial interaction or bonding mechanism between Pt and support. The interaction and bond properties determine the electron transfer to the metal, the adsorption properties and Pt photoreduction mechanism, which influence the Pt size, dispersion and stability on the support.²⁰¹

The reasons for the decrease in activity will be investigated in the next section.

6.2.1 Reasons for the decrease in activity with the introduction of an SiO₂ layer

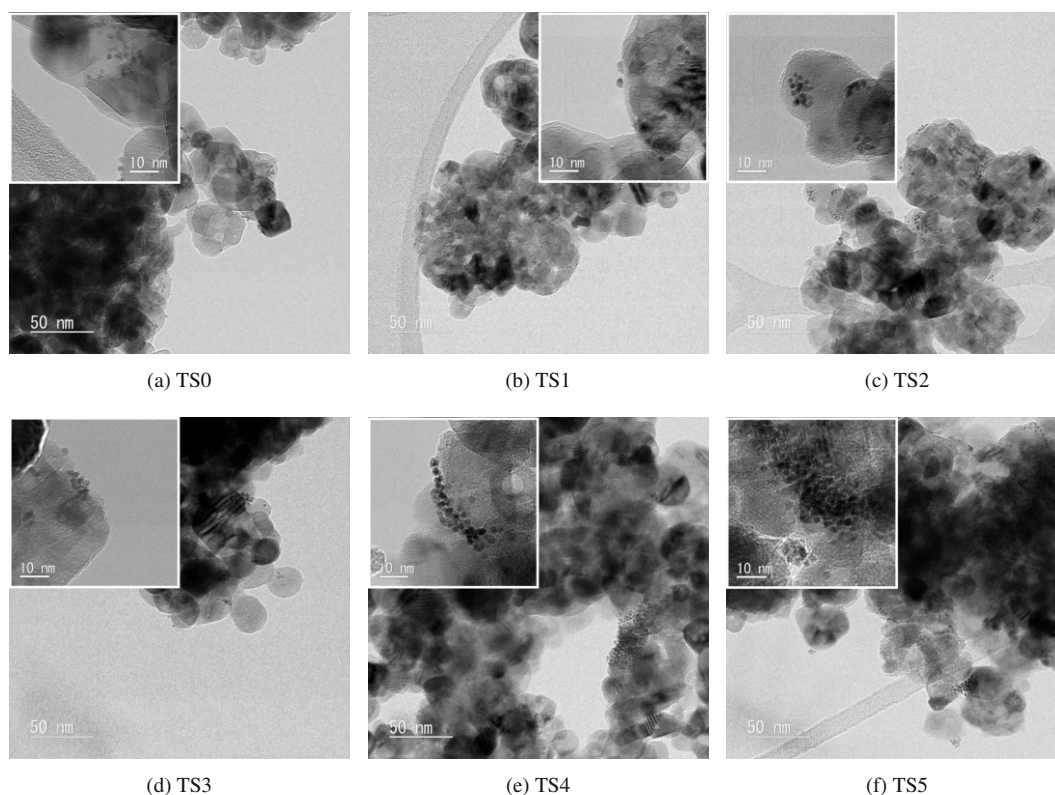


Figure 6.6: Typical transmission electron microscopy (TEM) images of TiO₂–SiO₂ core-shell nanoparticles with increasing shell thickness. (a) TS0 and (b) TS1 have no shell and layers of SiO₂, respectively. The Pt nanoparticles are well dispersed; (c) TS2, (d) TS3, (e) TS4 and (f) TS5 have thicker shell thicknesses. Thicker layers lead to higher Pt nanoparticle agglomeration.

To investigate the cause for the decreased activity I filtered the catalysts after HER, washed it with methanol and dried it in air to characterize it with TEM and TXRF. A closer look at TEM images of the Pt/TiO₂–SiO₂ core-shell samples reveals significant differences in the dispersion and location of Pt nanoparticles (Figure 6.6):

- Firstly, TEM reveals that the Pt nanoparticles (NPs) show an increasing tendency for **agglomeration** with increasing shell thickness. This observation is in line with the work of Bo et al., who reported that metal particles tend to agglomerate on SiO₂ more than on TiO₂.⁹⁰

- Secondly, the TEM images show that the average **size of the Pt NPs** increased from 1.7 to 3 nm for TS0 to TS6, respectively. This leads to a lower dispersion of Pt particles and thus a smaller catalytic surface, therefore reducing the amount of active sites/TPBs.
- Thirdly, the **amount of Pt** deposited on the catalyst deviates from the nominal loading of 0.2 wt.%, as determined by Total Reflection X-Ray Fluorescence (TXRF). Table 6.2 shows that the actual Pt loading decreased from 0.2 wt.% to almost half that value after a monolayer was introduced. Either 1) some of the Pt was still dissolved and not deposited on the supports surface, or 2) the Pt NPs were attached weakly to the support and detached after deposition.

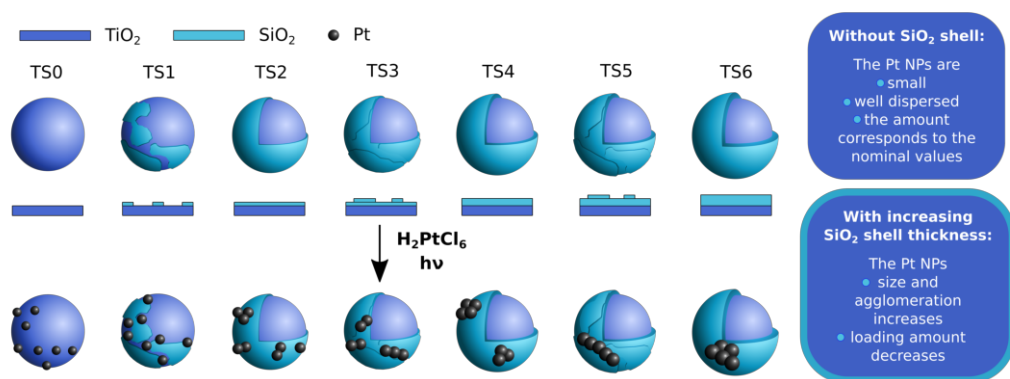


Figure 6.7: Reasons for the decreased activity of H₂ evolution with the introduction of a SiO₂ shell. The deposition of Pt nanoparticles on core-shell TiO₂–SiO₂ samples changes with the thickness: With thicker shells, the agglomeration and size of the nanoparticles increases, while the amount of deposited Pt on the surface decreases.

The results confirm that the platinum deposition works better on a TiO₂ surface than on SiO₂. This can be due to two factors:

1. Contrary to TiO₂, where Pt binds to an empty d-orbital, on SiO₂ only the oxygen anion is available for bonding. This leads to weaker bonds, possibly migration at low temperatures and easy removal through a filtering and washing process of the catalyst, as has been done prior to TXRF measurements.^{72,90}
2. The number of oxygen vacancies, which can serve as nucleation sites for Pt, is significant lower on SiO₂ than on TiO₂. Additionally, the negative surface charge increases gradually with the shell thickness, which decreases the initial

6 Deactivation during HER

approach of the precursor, PtL_6^{-2} , to the surface, and can lead to lower or differently dispersed precursor adsorption.¹⁹³ Fewer Pt nucleation sites and less precursor adsorption can lead to; a different photodeposition mechanism of the Pt precursor (see page 136, specifically Equation 6.15), which leads to less Pt^0 deposited on the catalyst's surface and a higher initial size and agglomeration of Pt NPs; and slower reduction kinetics.

Table 6.2: The platinum amount determined via Total Reflection X-Ray Fluorescence (TXRF). The Pt size was determined from TEM images (15 particles). The photocatalytic activity after 2.5 hours of illumination was normalized and correlated to the calculated Pt surface area (see Table A.2). The deactivation was determined by comparing the highest activity to the activity after 2.5 hours of illumination.

Sample	Pt amount [wt. %]	Size [nm]	Norm. activity [%]	Deact. [%]
Pt/TS0	0.20 ± 0.02	1.7 ± 0.3	100 ± 3	53 ± 0.4
Pt/TS1	0.22 ± 0.02	2.0 ± 0.5	80 ± 5	26 ± 2.0
Pt/TS2	0.12 ± 0.01	2.1 ± 0.4	96 ± 5	15 ± 6.9
Pt/TS3	0.16 ± 0.02	2.3 ± 0.7	56 ± 3	17 ± 3.3
Pt/TS4	0.10 ± 0.01	2.7 ± 0.7	45 ± 2	11 ± 13
Pt/TS5	0.10 ± 0.01	2.6 ± 0.6	22 ± 2	31 ± 12
Pt/TS6	0.11 ± 0.01	3.0 ± 0.9	20 ± 2	37 ± 4.8

The determined lower platinum loading and higher particle size are the cause for the lower photocatalytic activity during HER, since the surface area of the co-catalyst, i.e. number of active sites, directly correlates with the activity. They are major factors for the decrease in HER with the increase of shell thickness. I normalized the HER rates to the estimated changes in Pt surface area that is exposed to the reaction solution (the calculation of the surface area can be found in section 3.4.2 and Table A.2).

Figure 6.8 shows the normalized activity of HER, and the end activity (after 2.5 hours of illumination) is only slightly lower over the TS2 sample. TS1 shows 80% of the activity and the samples TS3 to TS6 show a gradual and significant decrease down to 20% of the activity without a shell (Table 6.2).

Since the charge transfer is not significantly inhibited in this shell thickness region the decrease of the end activity is attributed to the remaining ESD of 26% over TS1 and to the increase of agglomeration with increasing shell thickness for thicker shells

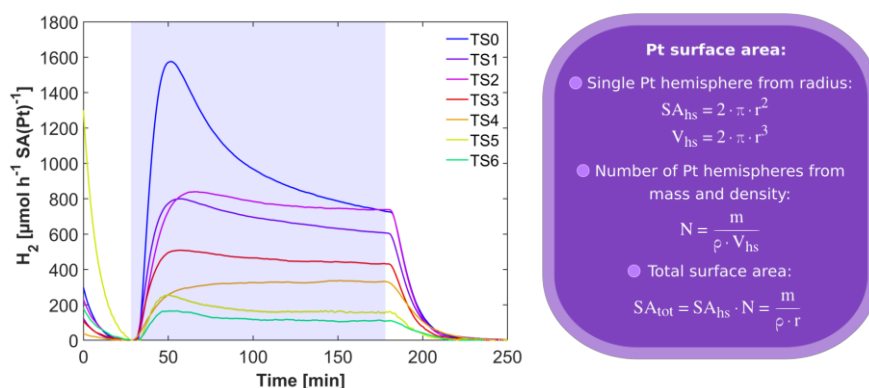


Figure 6.8: Exemplary time dependence plots of the hydrogen evolution rate over pure TiO₂ and core-shell samples SG set 2 loaded with 0.2 wt.% Pt in 50 vol.% methanol solution with US treatment. The data shown here is the same as in Figure 6.5, but the rate is correlated to the calculated Pt surface area determined from the nanoparticle size and amount of Pt (Table 6.2). The calculation of the Pt surface area is shown in the box to the right and in the appendix (Equation A.1). The light purple area indicates illumination with UV light (365 nm).

(TS3-TS6). Agglomeration has a diminishing effect; by a) increasing the average travel distance of photoelectrons from their origin of generation to the Pt electron sink, therefore increasing the probability for recombination; and by b) decreasing the number of accessible active sites or TPBs.^{72,202}

The difference in the starting activity (after 20-50 minutes of illumination) is attributed to different interaction between the reactants or Pt with the catalyst and is connected to the cause for the early-stage deactivation, which will be investigated in the next section.

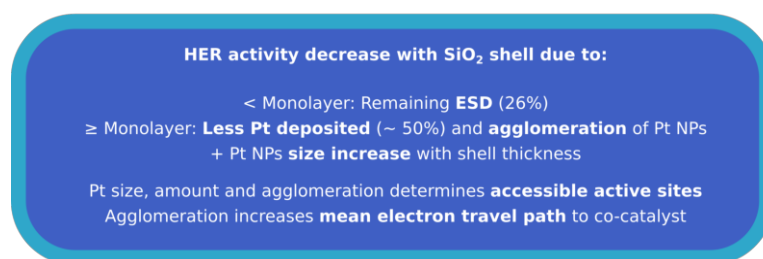


Figure 6.9: Concluding remarks concerning the HER activity decrease with introduction of an SiO₂ shell. After normalizing the activity to the Pt size and amount, the agglomeration causes further decreases in the activity.

6.2.2 Reasons for the decrease of the ESD with the introduction of an SiO₂ layer

As stated at the beginning of this chapter, different reasons could explain the ESD during HER with Pt/TS0 catalysts: A change in methanol oxidation mechanism leading to the catalyst poison CO; SMSI related effects, i.e. a bifunctional or geometric effect; a change in size and agglomeration of the co-catalyst; or slow reduction of Pt during in-situ photodeposition.¹⁷⁴

Changes in the methanol oxidation mechanism

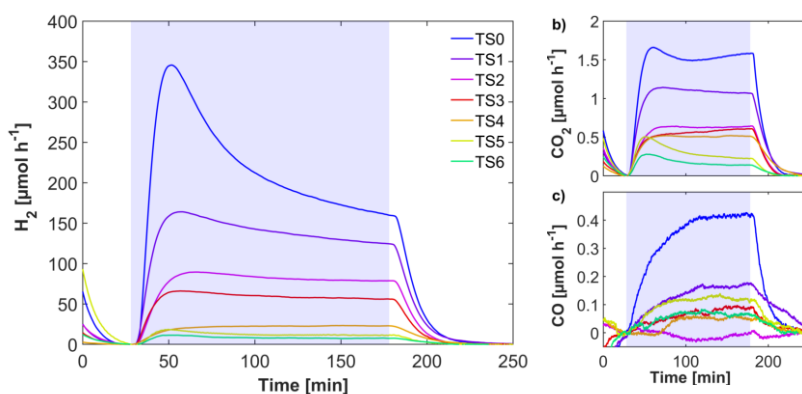


Figure 6.10: Exemplary time dependence plots of the **a)** H₂, as in Figure 6.5; **b)** CO₂ and **c)** CO evolution rate over pure anatase and core-shell samples loaded with 0.2 wt.% Pt in 50 vol.% methanol solution with US treatment. The light purple area indicates illumination with UV light (365 nm).

The methanol oxidation mechanism can be investigated by monitoring the generation of CO₂ and CO. As can be seen in Figure 6.10, the CO₂ rate decreases after an initial maximum and increases again after 60 minutes of illumination. In contrast, the CO rate rises with the H₂ deactivation, indicating a possible connection between the H₂ decrease and the CO increase. Most intriguingly: The sample with the lowest deactivation, TS2, also shows the lowest CO generation. This disagrees with the Mars van Krevelen (MvK) mechanism, which states that CO interacts with lattice oxygen, reduces the metal oxide and forms CO₂ and an oxygen vacancy.²⁰³ This mechanism should be inhibited on non-reducible metal oxides, such as SiO₂. This suggests that the cause for the different CO/H₂ selectivity has to be found at an earlier step in the

methanol oxidation pathway. According to the methanol oxidation mechanisms proposed in the beginning of the chapter, three intermediates are likely responsible for the generation of CO: formic acid, methyl formate (MF) and formaldehyde.

Naito et al. used these intermediates to study the mechanism of methanol reforming over several catalyst, and they found that formic acid had the lowest selectivity for CO over Pt-Ru/SiO₂ catalysts and much higher selectivity for CO over Pt-Ru/TiO₂, while methyl formate and formaldehyde showed similar selectivities over both catalysts.

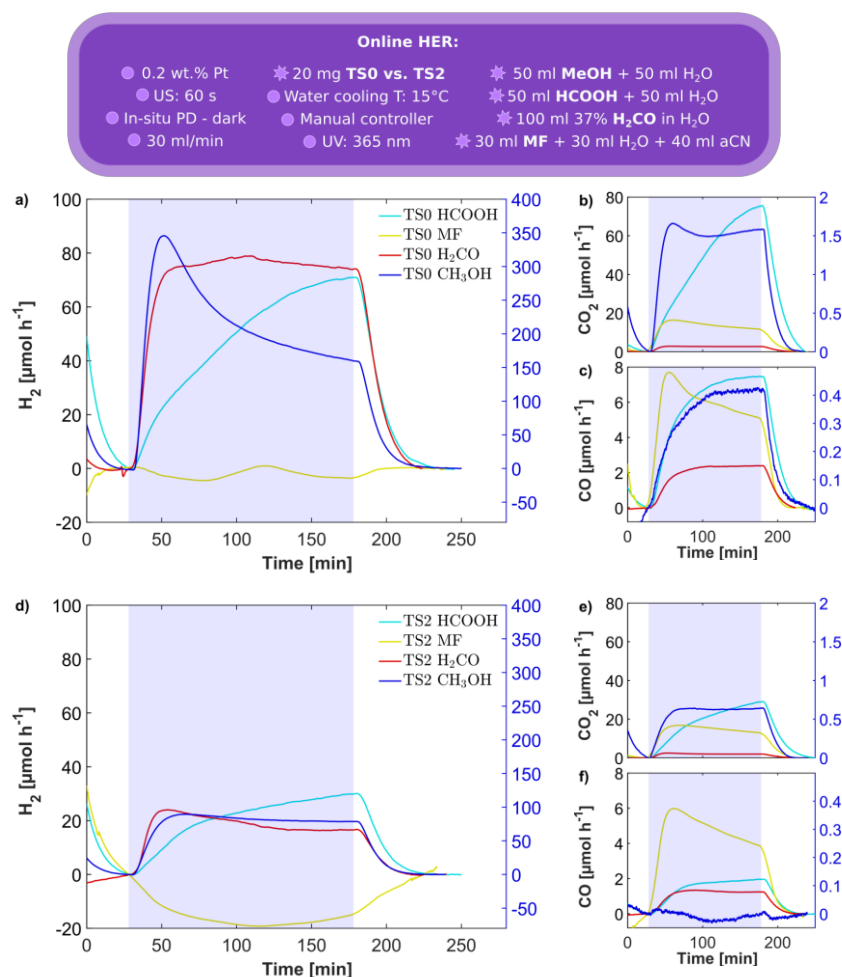


Figure 6.11: Exemplary time dependence plots of the **a)** H₂; **b)** CO₂ and **c)** CO evolution rate over pure TS0 and **d)** H₂; **e)** CO₂ and **f)** CO evolution rate over TS2 loaded with 0.2 wt.% Pt with different sacrificial agents; formic acid, methyl formate (MF), formaldehyde (left y-axis) and methanol (right y-axis). The light purple area indicates illumination with UV light (365 nm).

6 Deactivation during HER

Table 6.3: The activities of H₂ after 2.5 hours of illumination, the relative H₂ activity after 2.5 hours compared to the starting activity after 20-50 minutes, the CO/H₂ selectivity and the ratio of CO/CO₂ after 2.5 hours for the reference TS0 and the core-shell sample TS2 for different sacrificial agents (SA) are displayed in this table. The plots can be seen in [Figure 6.11](#).

Sample	SA	H ₂ [$\mu\text{mol} \cdot \text{h}^{-1}$]	Δ activity [%]	CO/H ₂ [%]	CO/CO ₂ [%]
Pt/TS0	MeOH	159	46	0.26	27
Pt/TS2	MeOH	79	89	0.01	1
Pt/TS0	HCOOH	71	246	11	10
Pt/TS2	HCOOH	30	211	7	7
Pt/TS0	MF	-3	-	-	43
Pt/TS2	MF	-14	-	-	30
Pt/TS0	H ₂ CO	74	99	3	88
Pt/TS2	H ₂ CO	17	69	7	64

These three intermediates were used as sacrificial agents (SAs) instead of methanol for the samples with the highest and lowest deactivation, TS0 and TS2, to see if there is any significant change in the CO selectivity. The results can be seen in [Figure 6.11](#). I calculated the CO/CO₂ ratios and CO/H₂ selectivities by dividing the CO rate after 2.5 hours of illumination with the respective CO₂ or H₂ rate for each experiment. The ratios, selectivities, the activity after 2.5 hours in reference to the starting activity and the measured H₂ rates after 2.5 hours for each experiment can be seen in [Table 6.3](#).

The observations are summarized here:

- There was no H₂ generation when MF was used as an SA.
- With the introduction of a SiO₂ shell the CO/CO₂ ratio decreases. The decrease of this ratio is very similar for formic acid (6.7 vs. 9.9%), methyl formate (30 vs. 43%) and formaldehyde (64 vs. 88%).
- The effect of SiO₂ on the CO/CO₂ ratio is much more pronounced when methanol is used as an SA (1 vs. 27%)
- When comparing the CO/H₂ selectivities, then formic acid has a lower and formaldehyde has a higher selectivity for CO (and CO₂) when a SiO₂ shell is introduced.
- None of the experiments with intermediate SAs show deactivation behavior in the H₂ generation.

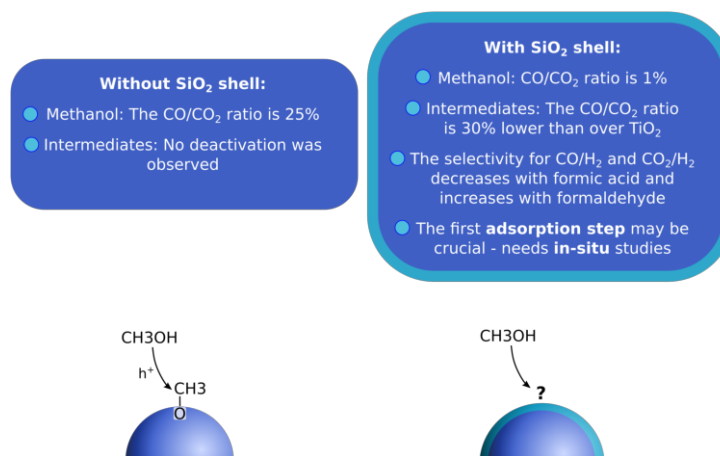


Figure 6.12: Concluding remarks of methanol oxidation mechanism studies: The crucial mechanistic step may be the adsorption of methanol on surface oxygen vacancies, which are numerous in TiO₂ but barely present in SiO₂

So far, these results do not explain why there is no CO generation over TS2 when methanol is used as an SA. As no ESD was observed with other SAs over Pt/TS0, it is possibly connected to the formation of the first methanol oxidation intermediate: Methoxy. Methanol forms methoxy preferably on an oxygen vacancy, of which much fewer are present on SiO₂. The proximity of adsorption sites, and therefore of reactants, defines the reaction mechanism, e.g. direct oxidation or bimolecular side reactions. The first few crucial steps in the methanol oxidation mechanism could therefore differ strongly over Pt/TS0 and Pt/TS2.³⁸

Summary of the methanol oxidation mechanism experiments

My experiments suggest that differences in the methanol oxidation mechanism exist and that likely the first step is key and determines the early-stage deactivation. To unravel the differences in the first crucial steps of the mechanism over Pt/TS0 and Pt/TiO₂–SiO₂ in-situ studies are needed.

SMSI effects and Pt agglomeration

Next, I investigated the effect of the ultrathin SiO₂ shells on potential SMSI effects that can be related to the change in activity, such as the bifunctional and the geometric effect.

Changes in the electronic effect of SMSI during HER have not been proposed as a hypothesis for ESD. The absence of relation has also been confirmed by my studies: As described above, the introduction of the SiO₂ shell significantly decreases the ESD. The deactivation is decreased by $\approx 50\%$ in the TS1 sample, where islands of SiO₂ cover half of the TiO₂ surface. During photodeposition, Pt will more likely deposit on the TiO₂ surfaces or at the TiO₂–SiO₂ edges than on the SiO₂ shell.⁹⁰ Since the deactivation is strongly affected in this sample even though electronic effect is not inhibited, it is not majorly related to the ESD.

The bifunctional effect

The bifunctional effect describes how dual active sites at the TPB of metal and support significantly influence the catalytic activity, which could change with the amount of surface oxygen vacancies close to the co-catalyst. While the reduction of protons mainly happens on the Pt surface, the dissociation of water is accelerated by surface oxygen vacancies, ideally close to the co-catalyst. The methanol oxidation mechanism, such as side and back reactions, can be influenced by the cooperation of metal oxide surface defects with the metal sites.²⁰⁴

To investigate if the bifunctional effect is the cause for the deactivation, I used a core-

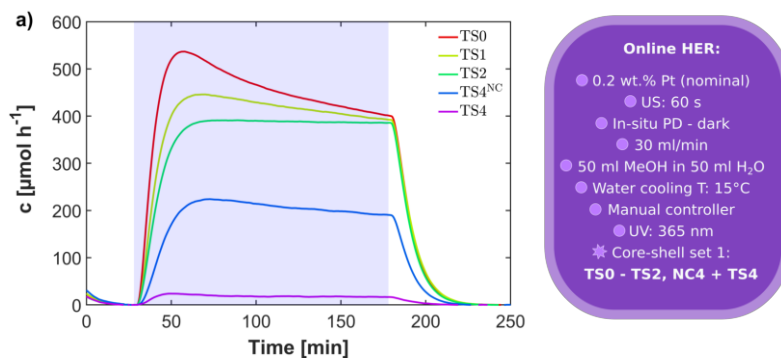


Figure 6.13: Time-dependent HER plots over the reference sample, core-shell samples of the sample set 1 and nanocavities containing core-shell samples. The light purple area indicates illumination with UV light (365 nm).

shell sample with nanocavities in the shell for HER experiments ($T_{92}S4^{NC}$, four steps of SiO₂ deposition). The Pt will rather deposit inside the nanocavities than on SiO₂ and the TPB will be defined by Pt and the surrounding SiO₂, contrary to $T_{92}S1_{4\%}^{SG5}$ where Pt NPs are at least partly surrounded by TiO₂. The results can be seen in Figure 6.13. Please keep in mind that the samples used for this experiment series is from sample set 1, which shows an overall lower ESD. The ESD behavior of the $T_{92}S4^{NC}$ sample strongly resembles the $T_{92}S1_{4\%}^{SG5}$ sample, even though the overall activity is decreased.

The HER activity lies between the activity of a monolayer of SiO₂ (TS2) and 0.9 nm of SiO₂ without nanocavities (TS4). While the electronic effect is not hindered in the $T_{92}S4^{NC}$ sample, and therefore not connected to the decrease in activity, the bifunctional effect may be. The TPB could play an important part to the photocatalytic activity, and the thick, surrounding SiO₂ layer could strongly inhibit the bifunctional effect, i.e. decreasing the HER activity. Furthermore, the decrease in activity can be partly attributed to the Pt NPs sizes, which are 1.8 ± 0.4 nm for pure Ana₉₂ and 2.3 ± 0.5 nm on $T_{92}S4^{NC}$.

TEM images of the catalysts after HER can be seen in Figure 6.14. Due to the similar deactivation behavior over $T_{92}S1_{4\%}^{SG5}$, where Pt is partly surrounded by TiO₂, and $T_{92}S4^{NC}$, where it is surrounded by SiO₂, the bifunctional effect, though possibly responsible to the overall activity decrease, is not the major cause for the ESD.

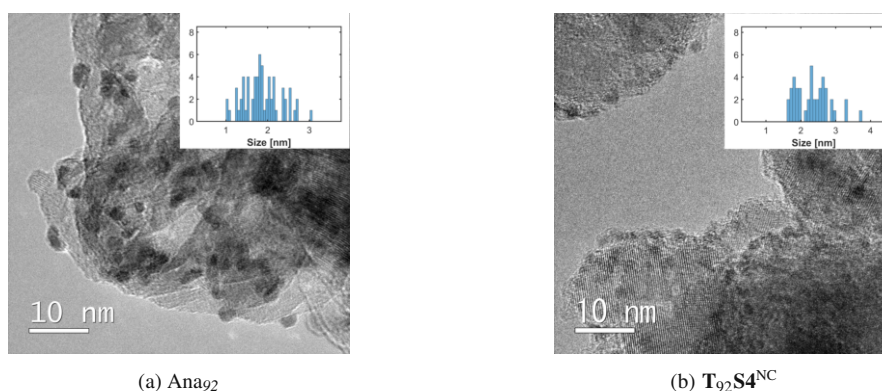


Figure 6.14: Typical transmission electron microscopy (TEM) images of Pt on a) anatase and b) $T_{92}S4^{NC}$, a nanocavities containing sample after HER.

The geometric effect

The geometric effect describes the encapsulation with sub-stoichiometric TiO_x during photocatalysis, which could inhibit the H_2 generation. To investigate this, my first strategy was to filter the catalysts after HER experiments, dry them in an air flow and analyze them via TEM. There was no encapsulation layer indicating a possible SMSI encapsulation effect visible for the sample exhibiting deactivation (Figure 6.6a). Since there is a possible reversibility of the encapsulation effect when the catalyst is exposed to air, I used a different sample preparation strategy: I performed long-term HER experiments (18 hours of illumination) and kept the sample under Argon until shortly before the TEM measurement.¹⁸⁶ Still, no encapsulation was observed in these samples, and the geometric effect was not found to be a major cause for the ESD.

However, another intriguing change concerning the Pt NPs was observed: The Pt particles strongly agglomerated (see Figure 6.16). This observation has been reported by few other groups, who investigated the deactivation over Pt/ TiO_2 during different photocatalytic applications, but it has not yet been observed for the ESD during HER.^{127,166,205–207}

During TEM measurements, I made another interesting observation: Some Pt NPs were not attached to the metal oxide but rested on the amorphous carbon film. It is possible that in-situ Pt photodeposition does not lead to a strong attachment of the Pt NPs to the support.

Pt nanoparticle agglomeration

The photocatalytic activity of Pt/ TiO_2 systems is strongly dependent on the size and dispersion of the Pt NPs, and the ESD could be explained with the agglomeration of the NPs during HER. To test this hypothesis, I prepared TEM samples after 30, 150 and 1080 minutes of UV illumination of in-situ photodeposited Pt on TS0 and TS2, the samples which show the highest and lowest deactivation, respectively, to see if the SiO_2 layer has an influence on the agglomeration.

I prepared samples with 0.2 and 1.0 wt.% Pt to investigate if the Pt size increase and agglomeration is dependent on the Pt concentration. The time-dependent HER rates can be seen in Figure 6.15: Over 1.0 wt.% Pt/TS0, the long-term deactivation is only 25% and correlates almost linearly with time compared to the ESD over 0.2 wt.% Pt/TS0, which shows an exponential decay, and leads to a decrease in activity of 85%

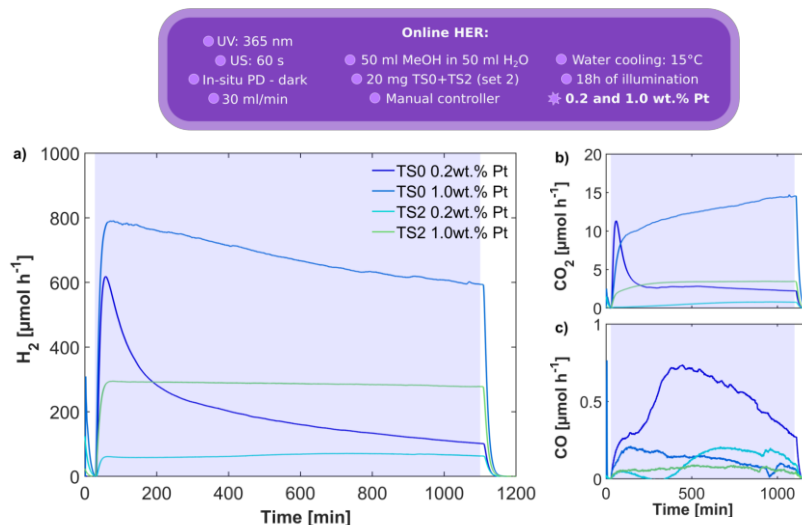


Figure 6.15: TS0 and TS2 with 0.2 and 1.0 wt.% Pt in a long-term photocatalytic hydrogen evolution experiment. **a)** is the H₂ evolution, which deactivates for lower Pt amounts; **b)** shows the CO₂ generation, which, in the 0.2 wt.% Pt sample decreases with the H₂ decrease, but it rises over time in the 1.0 wt.% Pt samples; **c)** shows the CO generation, which rises with the deactivation for the 0.2 wt.% Pt sample and is comparatively low for the other sample.

after 1080 minutes of illumination. Incidentally, the maximum activity of 1.0 wt.% Pt/TS0 is only one third higher than the maximum activity of 0.2 wt.% Pt/TS0.

Core-shell samples show stable, but lower activities than over the same Pt concentrations on TS0. The CO₂ and CO rates behave according to my former findings: With the ESD the CO₂ rate decreases and the CO rate rises, while for non-deactivating samples the CO₂ rate rises with time and the CO rate is negligible. This fits with previous observations that the CO formation correlates with the deactivation.

0.2 wt.% Pt

The TEM images of 0.2 wt.% Pt on TS0 and TS2 can be seen in [Figure 6.16](#). After 30 minutes of illumination, at the start of ESD, some of the Pt particles on TS0 are agglomerated. The agglomeration strongly increases over time. After 1080 minutes large agglomerates have formed and no single Pt NPs can be seen anymore.

It has been found before, that Pt incidentally shows higher Pt NPs sizes and agglomeration over an SiO₂ shell, especially with thicker shells ([Table 6.2](#)). This was attributed to an decreased dispersion of the Pt precursor on the SiO₂ surface, due to less nucleation sites, i.e. oxygen vacancies, and consequently a different photodeposition mechanism (see end of this section, specifically [Equation 6.15](#)). While the initial agglomeration

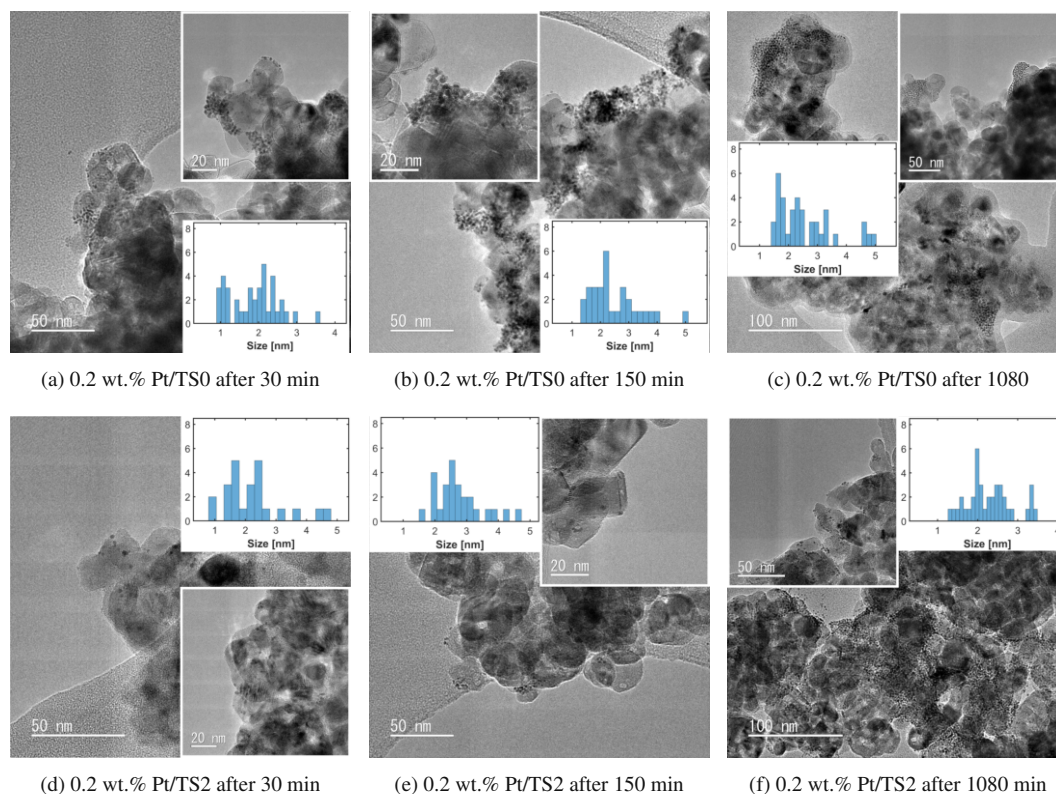


Figure 6.16: Typical transmission electron microscopy (TEM) images of Pt/TS0 and Pt/TS2 core-shell nanoparticles with 0.2 wt.% Pt when taken directly from the reactor solution after HER. The anatase reference TS0 after (a) 30; (b) 150 and (c) 1080 minutes of UV illumination and the core-shell sample TS2 after (d) 30; (e) 150 and (f) 1080 minutes of illumination.

is not strongly pronounced over the monolayer of SiO_2 , the Pt sizes are higher than over bare TiO_2 . The agglomeration also increases over time, but more Pt NPs share an interface with the support on TS2 than on TS0, where many of the NPs are lying on top of each other. Therefore, the agglomeration on TS2 is less pronounced. Additionally, the NPs size is much more stable over time on TS2 than on TS0.

1.0 wt.% Pt

The TEM images of the 1.0 wt.% Pt samples before and after HER are shown in [Figure 6.17](#).

No ESD was observed over these samples and the initial agglomeration is indeed much lower than on the 0.2 wt.% Pt samples, while the initial Pt size is higher (2.9 vs. 1.9 nm). The agglomeration and size of the Pt NPs on the TS0 sample changes slightly over time (2.9 to 3.3 nm), which could be connected to the small and almost linear de-

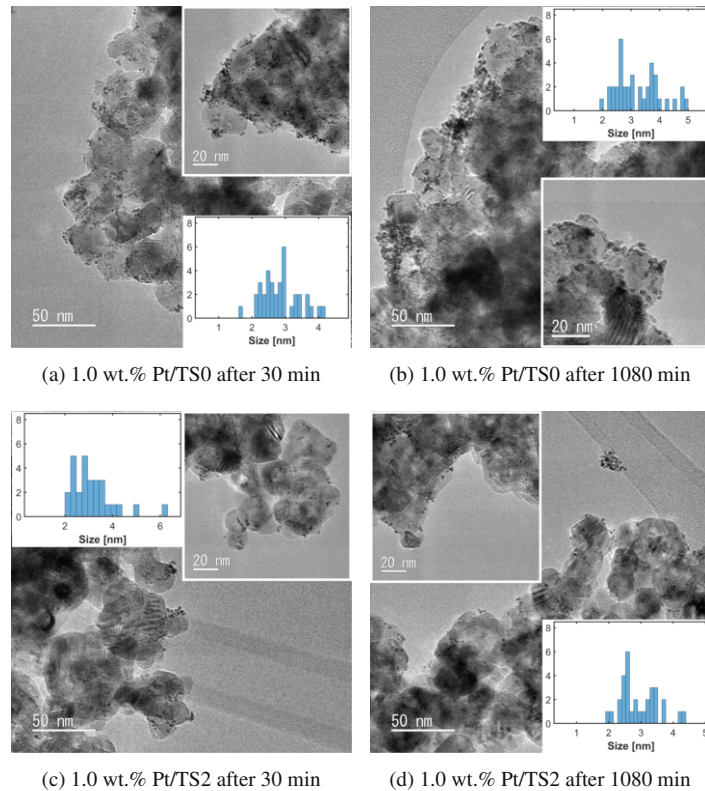


Figure 6.17: Typical transmission electron microscopy (TEM) images of Pt/TS0 and Pt/TS2 core-shell nanoparticles with 1.0 wt.% Pt when taken directly from the reactor solution after HER. The anatase reference TS0 after (a) 30 and (b) 1080 minutes of UV illumination and the core-shell sample TS2 after (c) 30 and (d) 1080 minutes of illumination.

activation. Compared to TS0, the TS2 sample with 1.0 wt.% Pt shows the same initial Pt size (2.9 nm), no deactivation during HER and no changes in the agglomeration or size of the NPs. Again, the TS2 sample shows lower but more stable HER rates and a higher Pt stability.

Discussion of the Pt size and agglomeration studies

The results of the Pt sizes, deactivation behavior and HER activities are summarized in Table 6.4. It shows that a strong agglomeration and size increase is observed for early-stage deactivating samples, some size increase and some agglomeration for almost linear deactivations, while stable sizes were observed in samples showing stable HER rates. The HER stability increases with a higher concentration and the introduction of an SiO₂ shell.

a) Pt mobility

The different deactivation behavior and Pt NPs stability over 0.2 and 1.0 wt.% Pt on TS0 could be explained with the difference in concentration: The NP size increase and agglomeration due to diffusion of NPs or due to Ostwald ripening over the supports surface is dependent on the Pt concentration and surface coverage.²⁰⁸

Table 6.4: The deactivation, activity after 1080 minutes of illumination, Pt size development and agglomeration over long-term HER experiments with 0.2 and 1.0 wt.% Pt over reference sample TS0 and core-shell sample TS2 are shown in this table. Deactivating samples with more than 50% loss of activity after 1080 min of illumination are bold.

	Sample Pt [wt. %]	Deact. [%]	Activity [$\mu\text{mol} \cdot \text{h}^{-1}$]	Pt size [nm]			Agglomeration
				after 30	150	1080 min	
TS0	0.2	84	620	1.9 ± 0.6	2.5 ± 0.9	2.6 ± 1.0	yes
	1.0	25	790	2.9 ± 0.6		3.3 ± 0.8	some
TS2	0.2	0	60	2.3 ± 1.0	2.7 ± 0.7	2.4 ± 0.6	some
	1.0	5	294	2.8 ± 0.6		2.7 ± 0.7	no

b) Reduction kinetics

Interestingly, the activity of 1.0 wt.% Pt/TS0 is only slightly higher than over 0.2 wt.% Pt/TS0 after 30 minutes of illumination. Calculating the surface area of Pt in both catalysts with the Pt NP diameters after 30 minutes of illumination and the nominal Pt loading, 0.2 and 1.0 wt.%, respectively, leads to $2 \cdot 10^{-3} \text{ m}^2$ for 0.2 wt.% and $6.4 \cdot 10^{-3} \text{ m}^2$ for 1.0 wt.% Pt (for the calculation refer to [section 3.4.2](#)). According to this, the activity over 1.0 wt.% is expected to be 3 times as high as over 0.2 wt.% Pt/TS0.

The nonlinear increase in HER rate with the Pt loading could also be explained with the difference in concentration, as it determines the reduction kinetics. In the relevant concentration ranges of this project, the photodeposition rate is linearly dependent on the concentration and on the constant of adsorption:¹⁹³

$$r = k\vartheta \approx kKc \quad (6.12)$$

where r is the reaction rate, ϑ is the occupancy ratio of the adsorption sites, k is the rate constant, K is the constant of adsorption and c is the concentration.

Therefore, the reduction rates are different for 0.2 and 1.0 wt.% Pt precursor concentrations, which leads to different activities and possible lower deactivation over time. With 1.0 wt.% the Pt on TS0 is reduced fast and initially forms larger particles, while with 0.2 wt.% the reduction on TS0 is slow and smaller particles, with a higher activity, are formed. The NPs grow while the reduction advances - and the activity decreases.

c) Photoreduction mechanism

Compared to 0.2 wt.% Pt/TS2, the activity over 1.0 wt.% Pt/TS2 is 5 times higher. The determined surface area of Pt is $1.6 \cdot 10^{-3} \text{ m}^2$ for 0.2 and $6.7 \cdot 10^{-3} \text{ m}^2$ for 1.0 wt.%, which is four times as high and nearly fits the difference in activity over these two samples. The initial Pt NPs sizes for 0.2 and 1.0 wt.% Pt show less differences on TS2 than they do on TS0 ($\Delta d=0.5 \text{ nm}$ vs. $\Delta d=1.0 \text{ nm}$). Compared to TS0, the HER rates are smaller, which has formerly been attributed to the higher Pt size, agglomeration and a lower deposited Pt amount.

Generally, the Pt NPs on SiO₂ show a higher initial size than on TiO₂, due to a less effective precursor adsorption and photodeposition mechanism; and less changes in the size and agglomeration with time and therefore more stable HER rates.

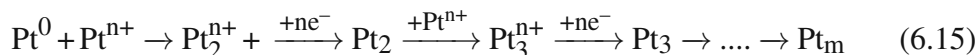
It has been proposed above that the negatively charged surface of SiO₂ lead to less adsorption of the Pt precursor PtCl₆⁻² and therefore slower reduction to Pt⁰. At first, this seems contradictory to the explanation above, where a higher Pt precursor concentration leads to faster reduction and therefore lower HER rates, which would conclude that a slower reduction on SiO₂ leads to higher initial HER rates. However, the crucial factor is the initial size of the Pt NPs. They can become initially larger with higher Pt concentrations, due to the faster reduction and NPs size growth; on SiO₂ due to fewer nucleation sites, which determine the photoreduction mechanism.

Two different photodeposition mechanisms have been proposed: ¹⁹³

1. Either all Pt⁴⁺ cations are adsorbed on the catalyst's surface before illumination and get reduced to Pt⁰ by photoelectrons generated in TiO₂ ($E^0 = 1.44 \text{ V}$ vs. SHE), which then form NPs by agglomeration. Due to the amount of oxygen vacancies on TiO₂, this mechanism is more likely to happen on the reference sample TS0.



2. Or, initially, only some Pt^{4+} cations get reduced on the surface and further Pt^{4+} cations adsorb on those metallic nuclei, where they get reduced cathodic-like to form clusters, which then grow in size through continued reduction of following Pt^{4+} . Due to the lack of surface oxygen vacancies on SiO_2 , this mechanism is more likely to happen on the core-shell sample TS2.



On the SiO_2 shell, where little of the precursor is adsorbed, some of the Pt reduces on nucleation sites, and following precursor ions adsorb on the Pt^0 rather than on the SiO_2 surface. This mechanism explains the initially larger NPs even though the reduction is slower than on TS0, and less Pt is deposited overall.

Summary of the SMSI and Pt agglomeration experiments

Neither the electronic, bifunctional nor the geometric effect of SMSI were found to be the major causes for ESD. However, during these investigations, I found that TEM measurements show a strong agglomeration and size increase of Pt NPs during HER in early-stage deactivating samples, i.e. in 0.2 wt.% Pt/ TiO_2 ; while they show stable sizes and less agglomeration in samples with a stable activity, i.e. when an SiO_2 layer is introduced or when the Pt concentration is increased (Table 6.4). It was suggested that the minimization of the deactivation in these samples is connected to an initial higher size and agglomeration of the Pt NPs, which are due to different precursor adsorption, photodeposition mechanisms and reduction kinetics. The observations and suggested reasons are illustrated in Figure 6.18.

I therefore deduced that the ESD on 0.2 wt.% Pt/TS0 is connected to the Pt mobility on the support, which includes a size increase and agglomeration; and a slow reduction of the Pt precursor, which initially forms small Pt NPs that increase in size when the reduction advances. Similar connections have been described in studies concerning photocatalytic oxidation of organic molecules over catalysts with a higher Pt loading (0.5 - 2.0 wt.%), where a linear deactivation was observed after several hours.^{161,166,205} However, it has not been investigated regarding the strong and nonlinear deactivation during the early-stages of photocatalytic HER, i.e. in the first hour of illumination.

The effect of increasing the stability of the Pt size and dispersion on the HER activity and ESD will be investigated in the next section.

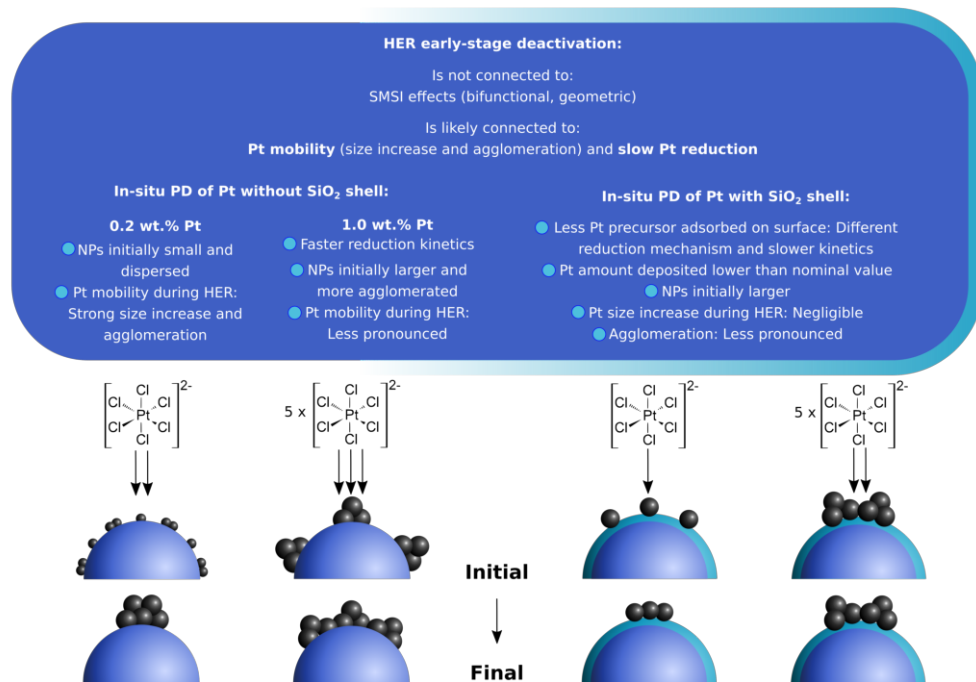


Figure 6.18: Concluding remarks concerning the SMSI and Pt agglomeration studies. The ESD in 0.2 wt.% Pt/TiO₂ is not caused by SMSI effects, but by the Pt size increase and agglomeration due to its mobility and its slow reduction. With higher Pt concentrations on TSO, the NPs are initially larger due to faster reduction kinetics, and less Pt mobility, i.e. negligible size increase and less agglomeration, was observed. With an SiO₂ shell, the NPs are initially larger due to a different photoreduction mechanism, no size increase was observed and the agglomeration was overall less pronounced than on TSO; there was some agglomeration with lower, but none with higher Pt concentrations. A higher initial Pt size and agglomeration correlate with lower, but more stable HER rates, and less changes in Pt size and agglomeration.

Dependence on the Pt deposition method

To further investigate the connection between Pt stability, i.e. changes in agglomeration and size, and ESD during HER I changed the Pt deposition method.

In-situ photodeposition has several advantages for photocatalysis: The reduction of Pt^{4+} requires electrons so the Pt atoms will preferentially deposit on sites where photo-generated electrons reach the surface, ensuring that following electrons can reach the co-catalyst, which increases the electron density in the Pt and therefore the photocatalytic activity.¹⁶¹ The combined results of the time-dependent HER and TEM images before and after the HER leads to the hypothesis that the Pt NPs are not attached well to the support leading to instabilities in their position, size and, consequently, their ability to collect electrons. Besides photodeposition, a common Pt deposition method is wetness impregnation, often followed by thermal and reductive treatments.

The high temperature reductive treatments strengthen the attachment between Pt and TiO_2 by not only reducing the Pt but also the TiO_2 . Reduced TiO_2 has more oxygen vacancies on which Pt adsorbs and form a strong Pt-Ti bond, while Pt can only form a weak bond with the oxygen anion on stoichiometric TiO_2 .²⁰⁹

G. Haselmann showed that pretreatments, which lead to more oxygen vacancies, facilitate ESD, while calcined TiO_2 , which has less oxygen vacancies, shows more stable H_2 evolution rates.¹²⁷ According to these results, the reduction of TiO_2 does not increase the stability of the H_2 rates. Nevertheless, the reduction of Pt may be more effective when Pt/TS0 catalysts are reduced in a pretreatment before HER rather than via in-situ photodeposition.^{161,166}

The following deposition methods were compared to in-situ photodeposition: Wetness impregnation (WI) was done in an aqueous suspension of TS0 and TS2 ($100 \text{ mg} \cdot \text{ml}^{-1}$) by adding the Pt precursor and stirring it for 2 hours, followed by drying it at 90°C for 24 hours. Half of the powder was calcined at 325°C in air for 3 hours and reduced with a flow of 2% H_2 in argon at 325°C for 2 hours. As a side note, 325°C was the set temperature for the oven and the sample temperature is $20\text{-}30^\circ\text{C}$ lower than the oven temperature ($\approx 300^\circ\text{C}$). This temperature is a compromise of the ideal reduction temperatures for the investigated systems: H_2PtCl_6 on TiO_2 is reduced at $\approx 145^\circ\text{C}$, while on SiO_2 it is reduced at higher temperatures, from 240°C up to 330°C .^{48,209,210} 300°C was set as the maximum sample temperature, because the reduction of TiO_2 in the presence of Pt starts above 300°C .²⁰⁹ The deposition routes employed in this work

are summarized here:

- In-situ photodeposition (in-situ PD)
- Wetness impregnation without H₂ treatment (WI - no H₂)
- Wetness impregnation with H₂ treatment (WI + H₂)

With this, I want to investigate if the reductive treatment stabilizes the NPs by strengthening the metal-support interaction, therefore decreasing the mobility, and by fully reducing Pt⁴⁺.¹⁶⁶

Pt deposition methods on bare TiO₂

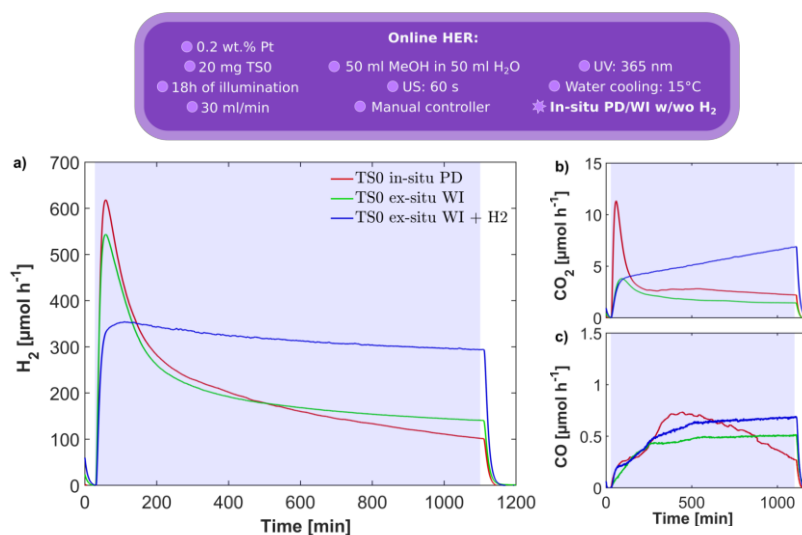


Figure 6.19: Exemplary time dependence plots of the **a)** H₂; **b)** CO₂ and **c)** CO evolution rate over the reference sample TS0 loaded with 0.2 wt.% Pt with different deposition methods and post-treatments. The light purple area indicates illumination with UV light (365 nm).

Longterm HER plots of Pt deposited on TS0 with different methods can be seen in Figure 6.19. The WI + H₂ sample shows no early-stage but a small linear deactivation - similar to 1 wt.% Pt/TS0 (see Figure 6.15). The WI - no H₂ sample shows the same deactivation behavior as the *in-situ PD* sample - the reductive pretreatment is thus key and plays a more critical role than the type of deposition (WI vs. PD). The CO₂ curve shows a higher maximum over the *in-situ PD* sample, over the WI - no H₂ sample it shows a lower maximum but similar values after 18 hours. For the WI + H₂ sample the CO₂ rises over time. The generation of CO during these experiments shows the same

increase over time for all samples, those with and without ESD. This is in disagreement to my former hypothesis - that the ESD of H_2 is connected to the methanol oxidation mechanism and the increase in CO generation.

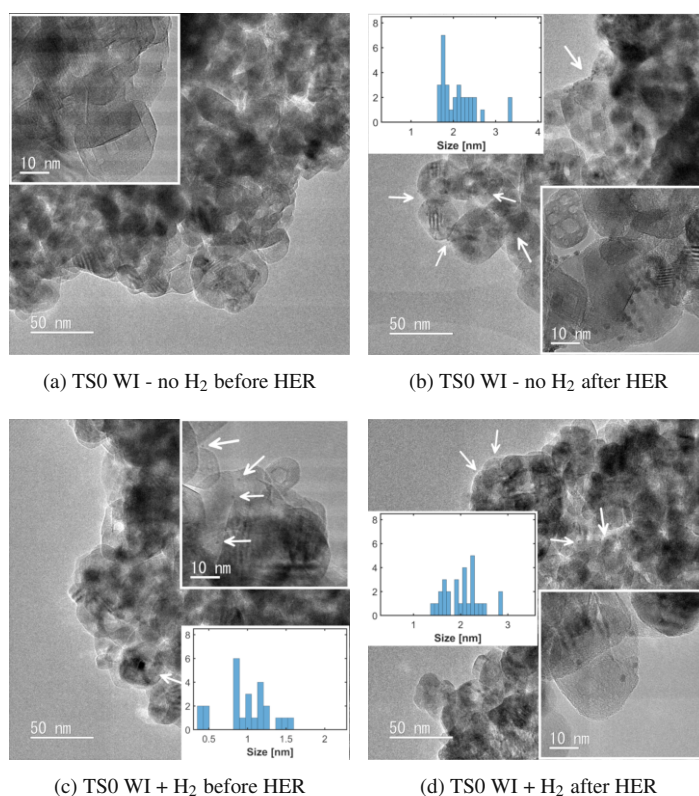


Figure 6.20: Typical transmission electron microscopy (TEM) images of Pt/TSO with 0.2 wt.% Pt deposited with ex-situ wetness impregnation (WI) without H_2 reduction (a) before and (b) after long-term HER and with H_2 reduction (c) before and (d) after long-term HER (1080 minutes of illumination).

Figure 6.20a shows the *WI - no H_2* catalyst before HER. Pt particles are barely visible and are smaller than 0.5 nm. After HER the Pt particles increased to ≈ 2 nm in size (Graph b). Agglomeration is barely visible for this sample, which is different to the *in-situ PD* sample (Figure 6.16c), even though the deactivation behavior for those two samples was very similar. The size increase, due to the mobility or slow reduction of Pt, is therefore more crucial for the ESD than the agglomeration.

When the catalyst was pretreated with H_2 (*WI + H_2*), some small Pt particles ≈ 1 nm can be seen before HER, and after HER the TEM graphs show several well dispersed Pt particles and their size increased to ≈ 2 nm (see Figure 6.20c, d). There was no ESD

during HER, but the Pt NPs still changed their size by about 1 nm. The stability of the Pt has increased with the reductive treatment, but changes in the size during HER and a small, almost linear deactivation was still observed. The size increase is not attributed to the advancing reduction, because Pt is reduced before HER, but rather to a mobility of the deposited Pt, which causes a slow, almost linear deactivation.



Figure 6.21: Summarized observations concerning the Pt deposition methods on TS0. It was found that the reduction in a pretreatment still leads to some size increase and a small deactivation, and that the main reason for the ESD is the size increase due to a slow photoreduction in samples where Pt is reduced by illumination.

In summary, the reductive pretreatment with H₂ at elevated temperatures ($\approx 300^\circ\text{C}$) stabilizes the Pt NPs on the TiO₂ and reduces the size increase, which consequently minimizes ESD. In these observations, the size increase correlates more with the ESD than the agglomeration. It was suggested that the Pt mobility after deposition plays a less important role to the ESD than the size increase due to the slow photoreduction.

Pt deposition methods with an SiO₂ shell

Longterm HER plots of TS2 can be seen in [Figure 6.22](#). The *in-situ PD* sample shows no deactivation during HER and only a small increase in the CO₂ and CO generation over time. Surprisingly, the *WI - no H₂* sample shows an ESD, even though a monolayer of SiO₂ minimized the deactivation in my former results. However, the deactivation here is slower than over TS0. The CO₂ rates shows similar deactivation while the CO rates increased over time, which is consistent with other ESD experiments. The *WI + H₂* sample shows stable HER and CO₂ rates and negligible amounts of CO. Interestingly, both WI samples show a much higher activity than the *in-situ PD* sample. While there are differences in the HER behavior over *in-situ PD* TS0 and TS2 samples, the WI Pt deposition on TS0 and TS2 leads to very similar HER behavior.

[Figure 6.23](#) shows TEM images of the TS2 samples before and after HER. The Pt size

6 Deactivation during HER

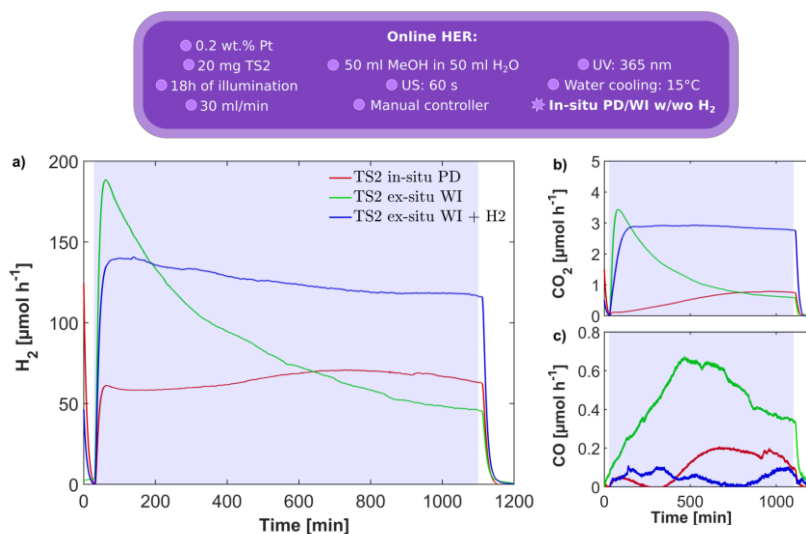


Figure 6.22: Exemplary time dependence plots of the **a)** H₂; **b)** CO₂ and **c)** CO evolution rate over the TiO₂–SiO₂ core-shell sample TS2 loaded with 0.2 wt.% Pt with different deposition methods and post-treatments. The light purple area indicates illumination with UV light (365 nm).

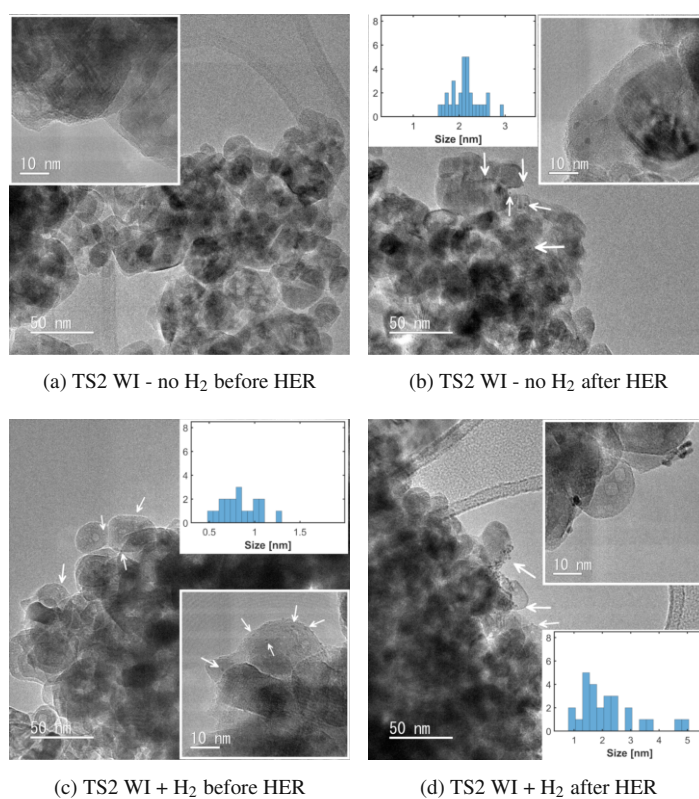


Figure 6.23: Typical transmission electron microscopy (TEM) images of Pt/TS2 with 0.2 wt.% Pt deposited with ex-situ wetness impregnation (WI) without H₂ reduction (a) before and (b) after longterm HER and with H₂ reduction (c) before and (d) after longterm HER (1080 minutes of illumination).

and size increase shows similar trends as on the TS0 catalysts: The Pt particles show a change in size of around 1 nm when the deactivation is low, while the size increase is > 1.5 nm when the ESD is > 50%. The size distribution was very narrow in most of the samples.

The higher end activity of the WI + H₂ sample could be because of the comparatively small Pt NPs (1.9 nm). But the Pt size difference between the in-situ PD (2.4 nm) and WI - no H₂ (2.1 nm) should also lead to differences in the HER activity, which was not observed. Therefore, the Pt sizes do not correlate with the end activity. Another explanation for the higher activity is the more complete deposition of Pt during the reductive pretreatment. It has been shown in former studies, that the photodeposition of Pt on an SiO₂ shell is significantly decreased compared to the photodeposition on bare TiO₂.

In summary, the stability during HER of the WI deposited Pt samples is similar on TS0 and on TS2. This suggests that the prereducive treatment is more essential for stable HER rates than the introduction of an SiO₂ shell. It was also found that the WI samples lead to a higher HER activity as the *in-situ PD* sample, which may be because of a more complete deposition of Pt.

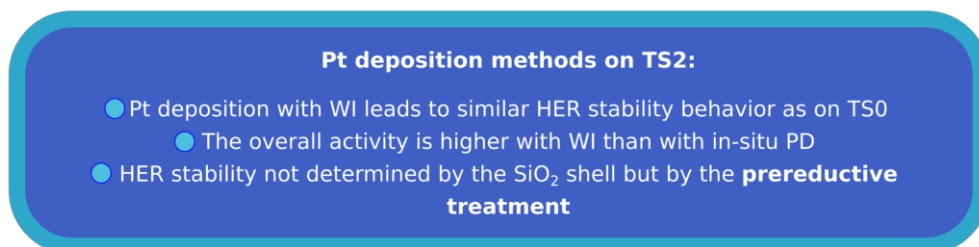


Figure 6.24: Summarized observations concerning the Pt deposition methods on TS2. They suggest, that the activity is higher with WI due to a more complete Pt deposition, and that the SiO₂ shell has less essential for the HER stability than the prereducive treatment.

Summary and discussion of the Pt deposition experiments

The results of the longterm experiments with different Pt deposition methods are summarized in Table 6.5. It shows the deactivation after 1080 minutes in percent, though not all loss of activity follows the exponential decay typical for ESD. It also shows the maximum activity after 20-50 minutes, the Pt NPs sizes before and after HER determined via TEM and if changes in the Pt NPs agglomeration are visible in TEM.

Table 6.5: The deactivation after 1080 minutes of illumination, the maximum activity after 20-50 minutes, Pt size development and agglomeration over long-term HER experiments with 0.2 wt.% Pt deposited via in-situ PD and WI over reference sample TS0 and core-shell sample TS2 are shown in this table. Deactivating samples with more than 50% loss of activity after 1080 min of illumination are bold.

	Sample	H ₂ red.	Deact.	Activity	Pt size [nm]		Agglomeration
			[%]	[$\mu\text{mol} \cdot \text{h}^{-1}$]	before	after HER	
TS0	in-situ PD	no	84	620	-	2.6 ± 1.0	strongly
	ex-situ WI	no	74	600	$\ll 0.5$	2.1 ± 0.5	no
		yes	15	350	1 ± 0.3	2 ± 0.4	no
TS2	in-situ PD	no	0	60	-	2.4 ± 0.6	some
	ex-situ WI	no	76	190	$\ll 0.5$	2.1 ± 0.3	no
		yes	16	140	0.8 ± 0.2	1.9 ± 0.8	no

1. Samples which were not pretreated in reductive atmospheres:

- **On TS0:** Generally show the same HER behavior, i.e ESD, as over in-situ PD Pt/TS0, which may be due to
 - Pt NPs size increase (>1.5 nm over 18 hours)
 - Slow reduction of Pt
- **On TS2:** Surprisingly show the same ESD behavior as over TS0 when WI was used, contrary to in-situ PD Pt/TS2. The Pt deposition method influences the adsorption and dispersion of the precursor on the TiO₂ and SiO₂ surfaces before photoreduction, which determines
 - the photodeposition mechanism
 - the reduction kinetics

Agglomeration of the Pt NPs was only observed in some samples showing ESD.

a) Effect of the Pt particle size on the accessibility of sites

The Pt size increase plays a more important role than the agglomeration, as agglomeration was not observed in all early-stage deactivating samples. While the agglomeration is difficult to quantify, the decrease of surface atoms due to the size increase can be estimated. Let's assume that the mobility of reduced Pt is the main contributor to ESD; that all Pt⁴⁺ cations are adsorbed on the catalyst's surface before illumination; that they are reduced to Pt⁰ by photoelectrons as soon as illumination starts; and that the single Pt atoms already acts as a co-catalyst for TiO₂ during HER, then:

The calculated surface area of all Pt single atom half spheres (radius of Pt⁰ = 130 pm, 10¹⁷ atoms) on TiO₂ leads to a total Pt surface area of ≈145 cm² and the relative amount of surface atoms is 100% (details on the calculation can be found in the appendix, Equation A.1). They then migrate and form nanoparticles with a diameter of 2 nm, exposing a surface area of 19 cm², which is a decrease of 87% - close to the decrease in activity in typical ESD samples. Additionally, the amount of kinks and steps and the relative amount of surface atoms decreases, only 50% of the atoms are on the surface.²¹¹ This decrease in accessible active sites contributes to the decrease in activity.

It needs to be pointed out, though, that the electron affinity of a single Pt atom is lower than the conduction band potential of TiO₂ (see Figure 6.25).⁵³ According to this, single Pt atoms do not act as co-catalysts, as only Pt clusters containing a threshold amount of Pt can trap electrons from the conduction band of anatase. It has been reported, that the optimum Pt NPs size for a high photocatalytic HER activity is ≈1 nm.^{52,54} Therefore, the relation between activity and surface area is valid only for Pt sizes above a certain threshold.

It was also found that the Pt NPs size is already higher than 1 nm at the maximum activity in in-situ PD measurements. The decrease in surface area was calculated to

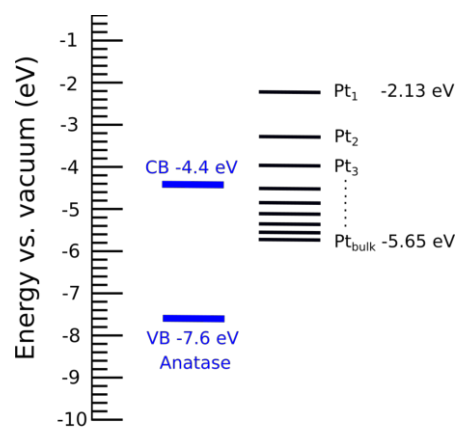


Figure 6.25: The electron affinity of a single Pt atom in the gas phase and work function of bulk Pt compared to the band levels of anatase. Redrawn from Sadeghi et al.⁵³

be 27% (from 1.9 to 2.6 nm Pt diameter, see [Table 6.4](#)), which is much smaller than the 84% decrease in activity. It is possible, though, that much smaller NPs are present, which have not been detected via TEM measurements.

While the surface area affects the photocatalytic activity, the determined sizes do not always correlate with the measured HER rate. Therefore, the size increase alone is not responsible for the ESD.

b) Reduction kinetics of Pt during HER

The early-stage deactivating behavior seems to be related to the reduction kinetics of Pt during HER, which is affected by the concentration of the Pt precursor and by the catalyst's surface properties. The kinetics determine the amount of Pt deposited, the Pt NPs size and the Pt oxidation state at different times during HER, all of which influence the photocatalytic activity.²⁰⁷ The combined results of this work suggest, that the mobility of Pt is not the only factor causing the deactivation behavior during HER. Several groups have found rather slow reduction rates and different Pt oxidation states during in-situ PD of Pt over TiO₂, together with changes in size and agglomeration.^{161,166,191,206,212} Their studies focused on higher Pt concentrations, between 0.5 and 2.0 wt.%, which made investigations of the Pt oxidation state feasible. The ESD in this project has been observed for Pt concentrations below 0.5 wt.%. Earlier studies showed, that the oxidation states in this low concentration regime are difficult to investigate due to low signal strengths.¹²⁷ To investigate Pt in the different stages of deposition, leaching experiments are currently in progress.

c) Initial Pt adsorption and dispersion

The *WI - no H₂* on TS2 sample has shown similar ESD behavior as on TS0. This is surprising, because the HER rates over TS2 are stable in in-situ PD measurements. On *in-situ PD* samples, the Pt forms initially bigger NPs on TS2 than on TS0, which determined the lower activity, but the size increase on TS2 is smaller than on TS0 ([Table 6.4](#)). Contrary, on the WI samples (*WI - no H₂* and *WI - H₂*) the observed initial size and size increase on early-stage deactivating samples is similar for TS0 and TS2 ([Table 6.5](#)).

Due to the drying process before HER during the WI deposition, the precursor may be adsorbed and dispersed much better on the surface compared to the *in-situ PD* sample, where the precursor gradually adsorbs on Pt rather than on SiO₂. This gradual

adsorption leads to initially large Pt NPs, while the higher dispersion of the precursor leads to smaller Pt NPs - as shown on the *WI + H₂* sample before HER (0.8 nm).

The increased Pt precursor adsorption amount and dispersion determine; the photoreduction mechanism, i.e. Pt single atoms get reduced and form NPs afterwards (see Equation 6.14); and the reduction kinetics, which are faster when the adsorption is higher (see Equation 6.12). After suspension of the catalyst in the HER reaction solution, some of the precursor may desorb from the surface and dissolve in the solution due to the lack of nucleation sites; however, the increased dispersion still leads to a larger number and smaller size of initially formed Pt NPs during photoreduction. The increased initial dispersion therefore leads to a similar photoreduction mechanism as on TS0, which is connected to the ESD.

This finding further excludes SMSI as the major cause for the deactivation, since the bifunctional effect as well as the geometric effect are considered to be impacted strongly over Pt/SiO₂ interfaces.

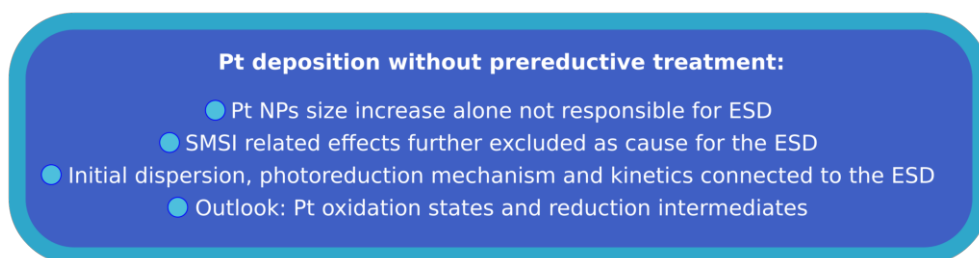


Figure 6.26: Concluding remarks and outlook concerning the Pt deposition methods without reductive pretreatment. The size increase and the photoreduction mechanism and kinetics are both connected to the deactivation. To investigate this, studies determining the nature of Pt at different stages during HER need to be performed.

In summary, the characterizations of the non-reduced samples confirm that a size increase of the Pt NPs is observed in early-stage deactivating samples, while an agglomeration of the NPs was observed less often. To some extent, the deactivation can be explained with a decrease in accessible active sites due to the NPs size increase. It was further suggested, that the slow photoreduction of Pt and possibly different Pt oxidation states during the reduction play an important role for the ESD during HER.

Intriguingly, the size increase and ESD has been observed on samples with and without an SiO₂ shell, which further excludes SMSI related effects to be the major cause for

the ESD. It was found, that the photoreduction kinetics and mechanism are determined by the precursor adsorption and dispersion, respectively, before illumination, which, on SiO₂, is influenced by the deposition method. As my former studies suggest, the photoreduction mechanism and kinetics are connected to the ESD.

2. Samples which were pretreated in reductive atmospheres, i.e. which were fully reduced before HER, show:

- **On TS0:**
 - an HER activity between the maximum and minimum of early-stage deactivating samples
 - no ESD
 - less change in Pt NPs size (< 1 nm over 18 hours)
 - no agglomeration
 - a significant CO generation
- **On TS2:** Generally the same behavior as over TS0, but:
 - smaller HER activities, even though Pt was fully adsorbed and reduced before HER
 - no CO generation

a) Effect of the reductive pretreatment

The reductive pretreatment eliminates the ESD. Pre-reduced samples show a lower starting activity than samples which were not reduced before HER, which could be due to a higher initial size of the Pt NPs. Their long-term rates are higher, i.e. the activity is more stable. A small, almost linear deactivation was observed, which could be due to a small Pt NPs size increase: The deactivation over TS0 and TS2 with *WI* + *H*₂ was ≈15% for both samples. However, the Pt surface area increases ≥50% (from 37 to 19 cm² for TS0, from 47 to 20 cm² for TS2), which is much higher than the loss of activity. This shows, that the relation between surface area and activity is much smaller in pre-reduced samples and that, crucially, the size increase due to the mobility of reduced Pt is not the main cause for the ESD.

Furthermore, CO poisoning of Pt is not a factor either, as the CO generation over TS2

is much smaller than over TS0, even though the deactivation behavior is similar. This indicates that the methanol oxidation mechanism, which determines the CO generation, is not related to the deactivation.

b) Effect of the Pt-SiO₂ interaction

The HER activities over TS2 are generally less than 50% as over the TS0 samples, even in samples where the Pt was reduced before HER, i.e. the amount of deposited Pt was complete. Three possible factors can contribute to this: Either, a) the band structures at the interfaces are affected due to the SiO₂ monolayer, affecting the Pt electron trap efficiency of Pt. I determined in photoluminescence studies that the charge transfer to the liquid is not affected in this thickness regime, but the shell could still affect the electron transfer to the co-catalyst, i.e. the electronic effect. Or, b) the bifunctional effect may be changed due to the SiO₂ layer. I referred to this in a former section as a possible cause for the lower activity in nanocavities containing core-shell samples where a thick SiO₂ layer surrounds the co-catalyst (see [page 128](#)). Or, c) some of the Pt leaches during photocatalysis, even after it has been reduced in a pretreatment. I determined in former studies that less Pt is deposited on the core-shell samples, which could be due to the weaker Pt attachment to SiO₂ than to TiO₂.

In studies correlating the Pt surface area to the HER rates, a monolayer of SiO₂ has not been found to strongly inhibit SMSI related effects, and the lower amount of Pt on the catalysts was found to be the main cause for the lower HER rates ([page 123](#)). The electronic and bifunctional effect are therefore considered as less likely to contribute to the lower activity than the leaching of the co-catalyst. To confirm or exclude its contribution, leaching studies are currently performed.

Pt deposition with preductive treatment:

- Pt NPs size increase connected to a small, almost linear deactivation
- The SiO₂ layer affects the HER activity
- Outlook: Pt leaching studies

Figure 6.27: Concluding remarks and outlook concerning the Pt deposition methods with reductive pretreatment. The Pt size increase is connected to a small deactivation. The effects of the SiO₂ shell on the electron transfer to Pt or possible leaching effects need to be investigated, to determine its effect on the HER activity.

6 Deactivation during HER

In summary, over pre-reduced samples no ESD but a small linear deactivation was observed. It was found that a significant Pt surface area increase correlates with a small deactivation, which suggests that it is not the main cause for the strong deactivation in ESD samples. The SiO₂ layer affects the HER activity, possibly due to leaching of Pt, which will be determined in future studies.

Conclusion of the Pt deposition experiments

The combined results of the Pt deposition methods show that there are several effects contributing to the deactivation, which are connected to the concentration of the Pt precursor and its initial dispersion on the catalyst's surface. This conclusion is summarized in Figure 6.28.

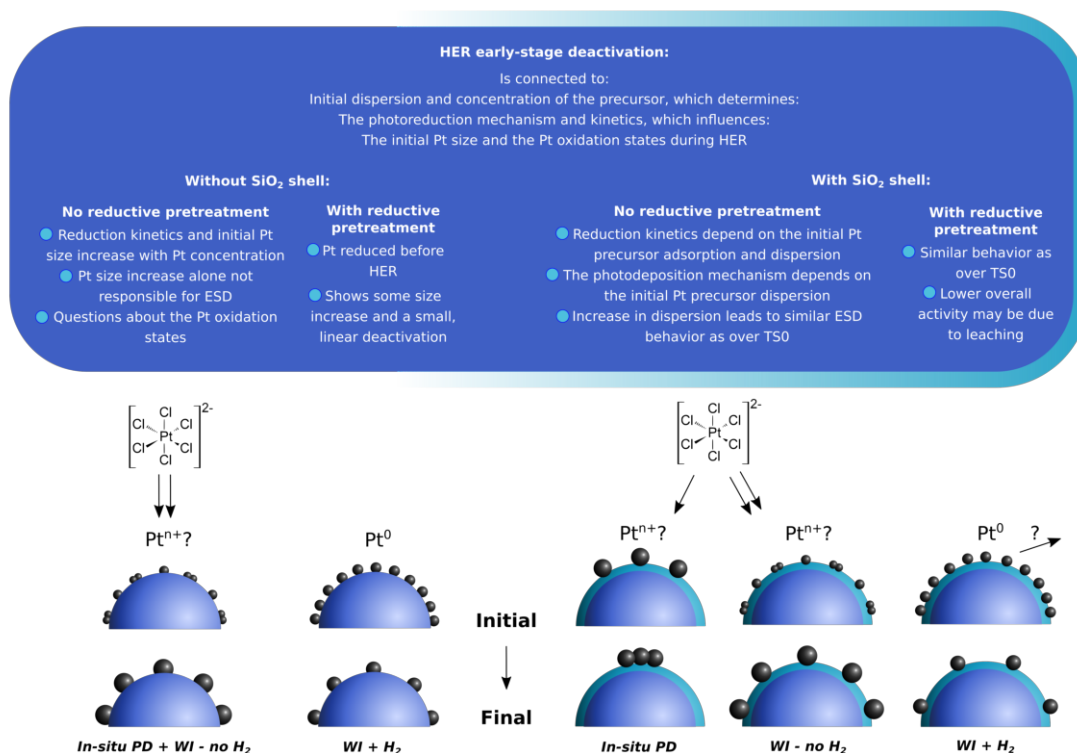


Figure 6.28: Concluding remarks concerning the Pt deposition studies. The ESD depends on the initial dispersion and concentration of the Pt precursor when Pt is photoreduced. The SiO₂ shell changes the photodeposition method and kinetics only for the *in-situ PD sample* - the *WI - no H₂* sample has a similar adsorption and dispersion of the Pt precursor as over TiO₂, which leads to a similar HER behavior over TS2 and TS0. When the samples were reduced before HER (*WI - H₂*) the deactivation and Pt size increase is low - with and without an SiO₂ shell.

When no reductive pretreatment is performed on the catalyst containing 0.2 wt.% (*In-*

situ PD + WI - no H₂), the Pt mobility on TiO₂ leads to a size increase and sometimes agglomeration, which increases the stability of the NPs and lowers the HER activity. However, these effects alone cannot explain the strong deactivation. It was suggested that the slow reduction leads to different oxidation states of Pt on the catalyst over time, which influence the HER activities. The low Pt concentration limits the investigation of the oxidation states of Pt at different stages during HER - characterization methods with a higher sensitivity are needed.

With the introduction of an SiO₂ shell, the deactivation behavior depends on the deposition method. For the *in-situ PD* sample, ESD was significantly decreased over Pt/TS2 and no significant Pt size increase or agglomeration over time was observed, while in *ex-situ* deposition methods without reductive pretreatment (*WI - no H₂*), the deactivation was found to be similar for the reference catalyst Pt/TS0 and the Pt morphology correlated with the values found over Pt/TS0.

When Pt is reduced before HER (*WI - H₂*), the average Pt size and its changes upon HER are significantly smaller, as is the deactivation. No agglomeration was observed in any of these samples. The behavior is similar when an SiO₂ shell is introduced. It was found in former studies, that the amount of deposited Pt on TiO₂-SiO₂ is less than the nominal values, which can be explained with a weak attachment of Pt to the SiO₂ surface; either, less Pt is deposited or it leaches during HER.

Overall, it was found that the ESD is connected to the initial dispersion and concentration of the precursor: A lower concentration and higher dispersion leads to a stronger deactivation. This is probably because they determine the photoreduction mechanism and kinetics, which then influence the initial Pt size and Pt oxidation states at different stages during HER.

6.3 Conclusion & Outlook

In this project, several possibly contributing factors have been investigated on anatase and core-shell samples with SiO₂ shells of different thicknesses between 0.15 and 1 nm to unravel the causes for ESD during photocatalytic HER.

It was found that the overall photocatalytic activity decreases with increasing shell thickness. This has been attributed to a larger size and a lower amount of the deposited Pt on the SiO₂ surfaces, compared to TiO₂. However, a correlation of the activity to the calculated surface area of Pt revealed that SiO₂ shells up to one monolayer considerably reduces the ESD, while largely preserving the overall activity for HER. The decrease in the saturation activity with thicker shells has been attributed to the agglomeration of Pt nanoparticles on the supports surface which increases the average travel distance of electrons and diminishes the access to active sites/TPBs.

Importantly, the samples that experienced an ESD during HER also show an increase of CO generation, which suggests a connection to the oxidation mechanism of the sacrificial agent methanol. Experiments of replacing methanol with formic acid, methyl formate and formaldehyde suggest that the initial reactant adsorption is key to the oxidation mechanism. In-situ studies are needed to determine the first stages of the methanol oxidation.

However, later HER studies show that the generation of CO is not always connected to the ESD of H₂. CO, acting as a catalyst poison, was therefore excluded as the major contributor to the deactivation.

SMSI related effects between Pt and the support could contribute to changes in activity. Possible changes in the geometric or the bifunctional effect were investigated by changing the supports surface and access to TPB with the introduction of an SiO₂ layer. Neither of these effects were found to be responsible for the ESD. However, postcatalytic characterizations, i.e. by TEM, revealed a considerably increase in Pt size and agglomeration in early-stage deactivating samples. Note that a higher Pt concentration does not lead to ESD, which is attributed to a higher initial size and agglomeration and lower Pt mobility. The activity is only slightly higher than over catalysts with a smaller Pt concentration. Overall, these changes in activity and stability are due to a faster reduction rate and lower mobility due to the higher Pt concentration.

The effects of Pt size increase, agglomeration and slow reduction on the ESD were

further investigated by varying the Pt deposition method, including a reductive pretreatment of the co-catalyst. The deposition method influences the initial amount and dispersion of the precursor, which determines its photoreduction mechanism and kinetics and consequently affects the size of the Pt NPs. A size increase during HER correlates with an activity decrease.

In contrast, reductive pretreatment of the samples with hydrogen has resulted in a considerably smaller ESD, although the Pt size increase is comparable. Therefore, the origin for ESD is rather determined by photoreduction mechanism and kinetics, and hence the Pt oxidation states during photocatalysis. In-situ FTIR and XPS measurements with higher sensitivity for low Pt concentrations are required to support this hypothesis.

As a final conclusion, I was able to identify three ways to stabilize the HER rates: 1) via a reductive pretreatment of Pt on the catalyst to ensure full reduction before photocatalysis; 2) by introducing an ultrathin SiO₂ layer, i.e. a non-reducing metal oxide, which influences the dispersion and photodeposition mechanism; and 3) through increasing the Pt precursor concentration, thereby influencing the photoreduction mechanism and kinetics.



Die approbierte gedruckte Originalversion dieser Dissertation ist an der TU Wien Bibliothek verfügbar.
The approved original version of this doctoral thesis is available in print at TU Wien Bibliothek.

7 Size selective hole scavenging

Introduction

Pure titania in pure water usually leads to negligible reaction rates during photocatalytic water splitting ($< 1 \text{ mol h}^{-1}$).¹²⁷ This is mostly due to the endergonic nature of the reaction and the fact that the oxidation of O^{2-} requires four holes. To achieve sufficient activities, sacrificial agents (SAs), whose oxidation is usually thermodynamically and kinetically more favorable, are often used. The available substances are manifold, but most commonly simple organic or inorganic substances, such as methanol or $\text{Na}_2\text{S}_2\text{O}_3$, are used. Methanol is the primary SA used in this research group, and many others, because in general the oxidation is simple: It is oxidized step-wise upon consumption of holes leading to formaldehyde, formic acid and eventually CO_2 . Many studies report that these reactions take place directly on the catalysts surface, via adsorption of a methoxy radical as the first step of the oxidation. However, another mechanism is often proposed, which includes the generation of OH^\bullet radicals, which can oxidize the SA up to 500 nm away from the surface.^{12,170–172,213} Wang et al. have used in situ sum-frequency generation and found that the dominant reaction - direct or indirect oxidation of methanol - depends on the ratio between water and methanol: If the water:methanol ratio is ≥ 300 , indirect oxidation by OH^\bullet radicals is dominant, and below this value the oxidation predominantly takes place on the surface.²¹⁴ However, the method used in their study is highly advanced, and alternative methods could be used to obtain if there is a direct or indirect oxidation mechanism dominant in a specific photocatalytic system.

This part of the work describes how the creation of nanocavities with specific pore sizes around 1 nm in size may select between organic molecules, used as sacrificial agents, to determine their oxidation mechanism: Direct oxidation is allowed for some alcohols, but inhibited for others, whose hydroxyl groups do not reach the surface to

7 Size selective hole scavenging

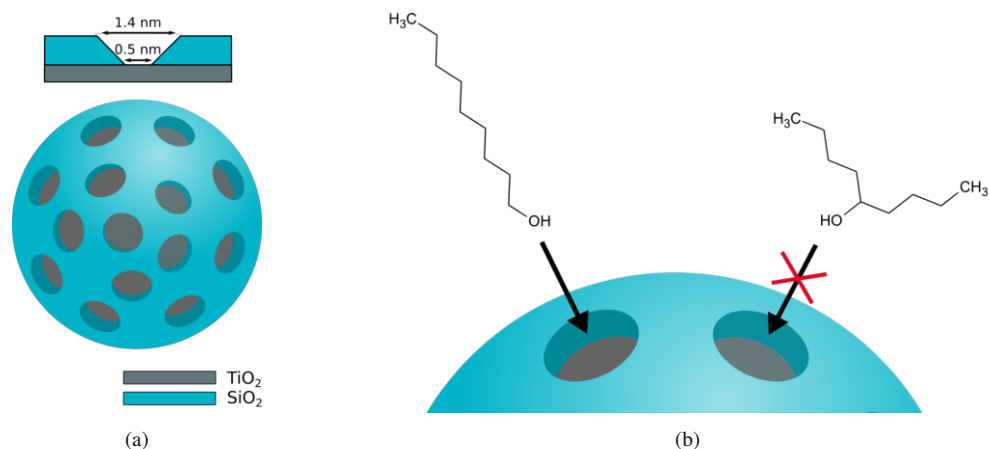


Figure 7.1: (a) A TiO₂-SiO₂ core-shell sample, with a nanocavity containing shell; (b) size-selection of the nanocavities; the OH group of 1-nonanol can access the TiO₂ catalyst, while the OH group of 5-nonanol is sterically hindered.

be adsorbed. Those molecules can only be oxidized indirectly, by OH[•] radicals. This process can be suppressed by the use of specific solvents.

To test this application, the isomers 1-nonanol and 5-nonanol were chosen as SAs. They have a similar structure with just the hydroxyl group on different positions; the branched structure of the latter is expected to sterically hinder its diffusion through the nanocavity, thus allowing for oxidation via OH[•] only. In some studies, the formation of OH[•] radical was prevented by the use of acetonitrile (aCN) as a solvent, as it is known to significantly decrease the lifetime of OH[•]. It is further suitable to dissolve many organic substances, such as nonanol, and it is not competitively oxidized by TiO₂.^{215–217} It has also been found that, in the presence of acetonitrile, heteroatomic sites, such as -OH groups, are more efficiently oxidized than C-C or C-H bonds.²¹⁸

Before HER, it will be verified that the nanocavities discriminate between the two SAs. Then, the ratio of water:aCN and water:SA will be varied to find optimum values for the HER application; enough water to create sufficient amounts of H₂, while still destabilizing OH[•] radicals and keeping the nonpolar SA dissolved; and low enough H₂O and SA concentrations to minimize intermolecular interactions that might further inhibit the SAs from entering the nanocavities.

The aim of this project is to provide a proof-of-concept: To show that the discrimination between different SAs can be deduced from the HER activity, and that nanocavities containing shells can be used to investigate the dominant oxidation mechanism - direct

or indirect - in a specific photocatalytic system.

The nanocavities samples have been created by grafting templates, i.e. 4-tert-butylcalix-[4]arene, on the surface of anatase nanoparticles. A stepwise sol-gel process was used to deposit ultrathin insulating SiO₂ layers with a thickness between 0.5 and 1 nm around the templates. The templates were removed by low-temperature calcination at 325°C. A detailed description of the process can be found in former chapters (subsection 3.1.2).

7.1 Size selection properties of the nanocavities

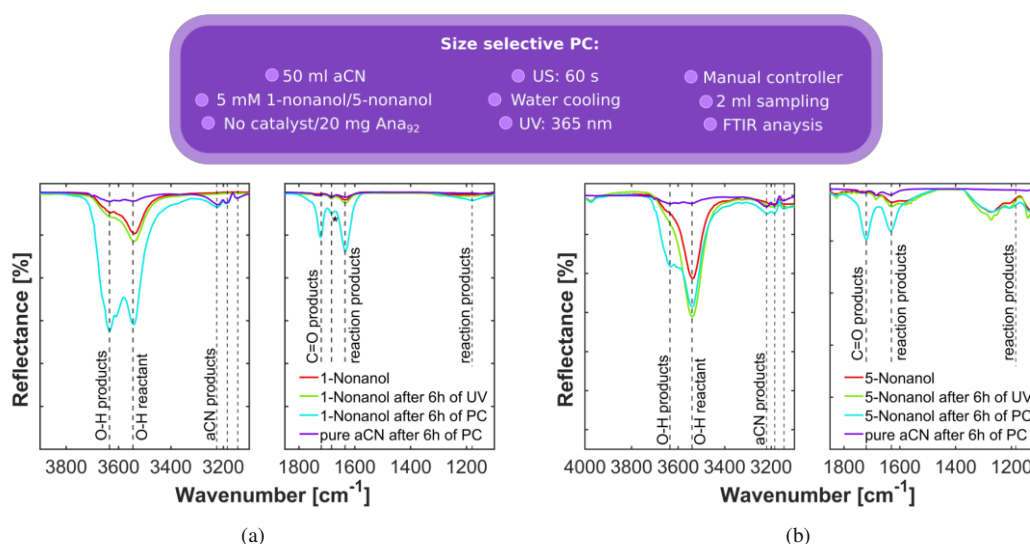


Figure 7.2: FTIR spectra of nonanol in acetonitrile; (a) 1-nonanol and (b) 5-nonanol before and after illumination without and with a catalyst for 6 hours.

To examine the nanocavities towards their size selective properties, 20 mg of the catalyst powder was suspended in a 5 mM solution of 1-nonanol or 5-nonanol and illuminated with UV light (Thorlabs LED, 365 nm) in a photocatalytic reactor which allows the extraction of a liquid sample portion of 2 ml with a syringe (0.45 μ m syringe filter were used to separate the powder from the solution). The experiments were performed with Anatase = Ana₉₂, AG049 = T₉₂S4^{NC}, AG089 = 2ndT₉₂S4^{NC} and AG090 = T₉₂S6^{NC} as catalysts, and a sample portion was taken out every hour and the sample

was analyzed in a thin cell build for FT-IR transmission measurements. The cell has a thickness of 200 μm .

The spectra of 1-nonanol and 5-nonanol in pure acetonitrile and the respective products after 6 hours of UV illumination without and with 20 mg of the catalyst are shown in [Figure 7.2](#). Please note that no water was added to the system, but a low amount of water may be present in the solvent (< 30 ppm); and that this solution was not degassed, and molecular oxygen can react with the reactants during the photocatalytic oxidation.²¹⁹ The peak at 3540 cm^{-1} is assigned to the OH groups of nonanol, while the OH peaks next to it, around 3630 cm^{-1} may stem from the reaction of the product with the HCN in acetonitrile or from the carboxylic acid product from 1-nonanol or from fragments of 5-nonanol.²²⁰ The small peaks around 3200 cm^{-1} are assigned to products from conversion of the solvent acetonitrile. The peak at 1722 cm^{-1} is from carbonyl groups of the oxidized alcohols, while 1680 cm^{-1} may be from C=O vibrations from the carboxylic acid, as it is only visible for the 1-nonanol products (marked with an asterisk *). These peaks are shifted to slightly lower wavenumbers, possibly due to the solvent effect.²²¹ The peaks around 1635 cm^{-1} and 1200 cm^{-1} may be from reactions of the products with the solvent or HCN, but which reaction is not yet clearly defined; the vibrations may be from either N-H or C=N bonds and from C-N bonds, respectively.²²²

[Figure 7.3](#) show the time plots of the intensity of the 1722 cm^{-1} peak which develops during the PC reaction in pure aCN. According to this plot, there is no conversion without an SA or without a catalyst. It also shows that the nanocavities in the shell do not discriminate 1-nonanol (graph a). $\text{T}_{92}\text{S4}^{\text{NC}}$ and $^{2\text{nd}}\text{T}_{92}\text{S4}^{\text{NC}}$ slightly discriminate 5-nonanol, but the effect was not sufficient (graph b). Due to this, I synthesized $\text{T}_{92}\text{S6}^{\text{NC}}$, which includes two more steps of SiO_2 deposition and therefore a thicker shell (1 nm vs. 0.8 nm). As can be seen, its discrimination against 5-nonanol is more efficient than $\text{T}_{92}\text{S4}^{\text{NC}}$; only 1/6 of the molecules get converted. For this reason, $\text{T}_{92}\text{S6}^{\text{NC}}$ was chosen as the nanocavity sample to be used in the following HER experiments.

Photocatalytic HER requires water and therefore the discrimination of the nanocavities was tested again after adding 10% H_2O to the solution of nonanol in acetonitrile. The results can be seen in [Figure 7.4](#): The addition of water clearly decreases the conversion of 1-nonanol over the NC sample, which might be due to interactions of the alcohol with water molecules, i.e. a solvation of the hydroxyl group. It partly inhibits the access of the hydroxyl group to the TiO_2 surface, and the conversion is decreased by

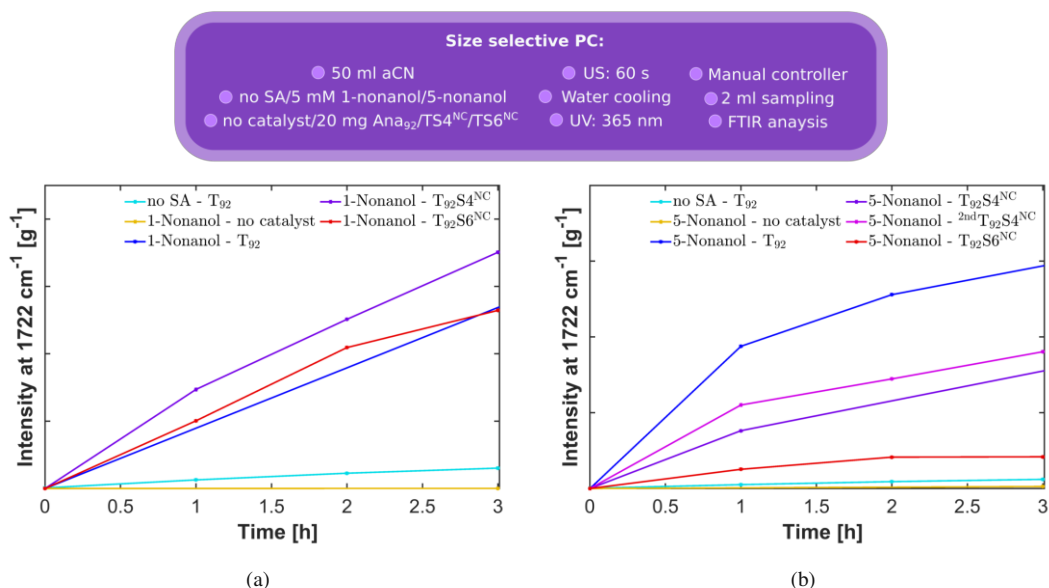


Figure 7.3: Conversion of 5 mM of nonanol in pure acetonitrile with different catalysts; (a) shows how 1-nonanol is converted over pure TiO₂ and the nanocavity samples without inhibition due to the cavities; (b) shows how 5-nonanol is converted less over the nanocavity samples, because it is sterically hindered and cannot enter the cavities. While T₉₂S4^{NC} hinders the molecule only slightly, a thicker shell, as in T₉₂S6^{NC}, increases the inhibition of the conversion.

more than 50%. For 5-nonanol, the extend of this effect is similar: only 1/12 of the molecules get converted, half as much as before the addition of H₂O.

In conclusion, the introduction of a SiO₂ shell of a minimum thickness of 1 nm, that contains nanocavities of an average diameter of 1 nm, it is possible to discriminate between two alcohols: 1-Nonanol can enter the nanocavity, while 5-nonanol cannot enter and shows a greatly reduced activity. The addition of water reduces the conversion for both alcohols over the nanocavities, due the solvation of the hydroxyl group by H₂O. It was shown, that the alcohols can only be oxidized directly on the surface of TiO₂, due to the destabilization of OH[•] radicals in acetonitrile, with and without 10% H₂O.

7.2 Size selection of sacrificial agents during HER

A set of experiments were performed to establish the optimum parameters for size selective HER: 5 mg of catalyst powder was dispersed in 2 ml of a solution of acetonitrile with either 50% or 10% H₂O and 5% (maximum amount that is miscible in a 1:1 acetonitrile:water solution), 1% or 0.08% (equal to 5 mM) of the sacrificial agent.²²³

7 Size selective hole scavenging

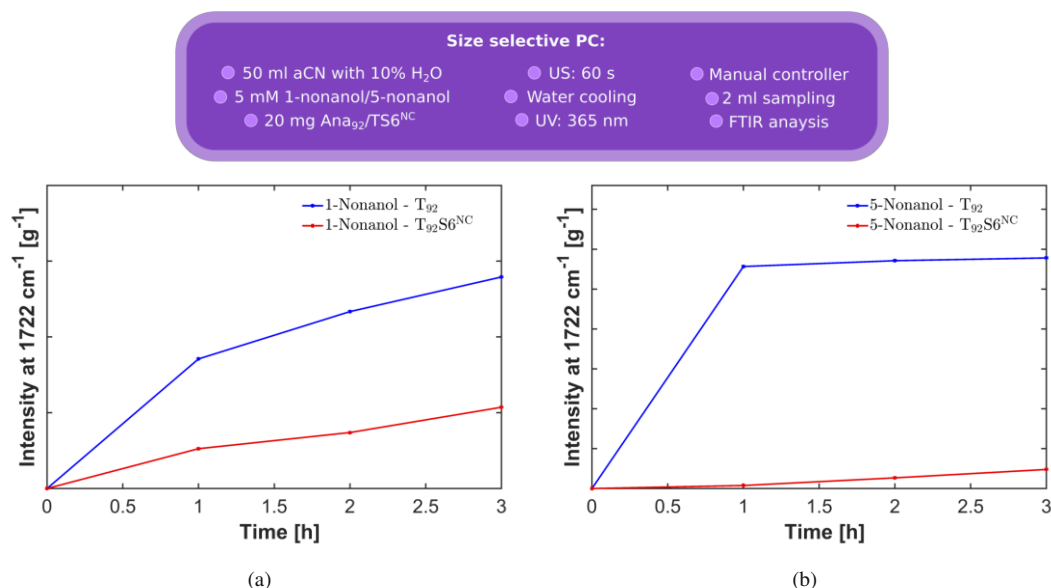


Figure 7.4: Conversion of 5 mM nonanol in acetonitrile with 10% H₂O with different catalysts; (a) the conversion of 1-nonanol is slightly inhibited for the nanocavity sample T₉₂S6^{NC}, due to the formation of a solvation shell of the hydroxyl group; (b) the conversion of 5-nonanol is similarly inhibited further due to solvation.

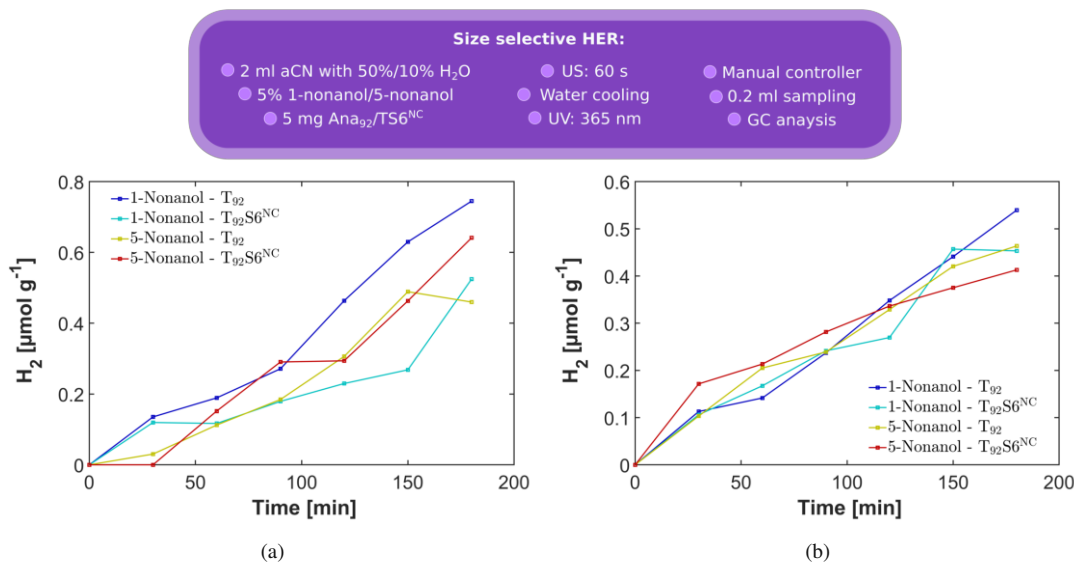


Figure 7.5: Photocatalytic hydrogen evolution with 5% of the sacrificial agents 1-nonanol and 5-nonanol and with different catalysts in acetonitrile with (a) 50% H₂O and (b) 10% H₂O. The introduction of a nanocavities containing shell does not lead to significant differences in the HER.

The suspension was ultrasonicated for 60 seconds and placed in a 5 ml reactor, which was watercooled with 15° and illuminated from the side. The reactor was flushed with Argon for 10 minutes before the reaction and a small gas sample was extracted every

30 minutes with a syringe and analyzed in the GC.

The first set of experiments was done in acetonitrile with 50% H₂O and 5% of the SAs and can be seen in Figure 7.5a. As can be seen, the nanocavities sample did not lead to different H₂ amounts for the two SAs. Since the determined error of this method is 0.1 μmol · g⁻¹, no significant differences in H₂ generation have been detected. It is possible that the high concentration of water leads to intermolecular interactions with the hydroxyl group of nonanol or competitive adsorption on the catalyst's surface, inhibiting its oxidation over each catalyst.

However, when the amount of water is lowered to 10% the differences are even smaller for both catalysts and both SAs (see Figure 7.5b). The high water content is therefore not the cause for the lack of size discriminating effect. Another possibility is that the high concentration of SA leads to a limitation in miscibility in the aCN/water mixture and therefore an inhomogeneous suspension.

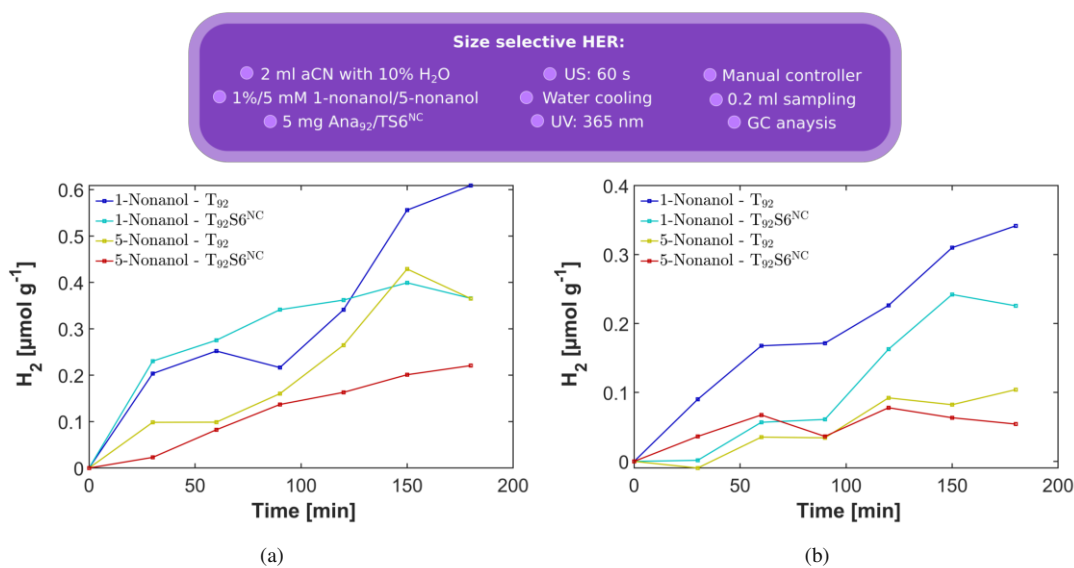


Figure 7.6: Photocatalytic hydrogen evolution with (a) 1% and (b) 5mM of the sacrificial agents 1-nonanol and 5-nonanol and with different catalysts in acetonitrile with 10% H₂O. The introduction of a nanocavities containing shell leads to small differences, that are not easily distinguished due to the low overall activity.

A lower concentration of SAs was chosen for the following experiments. The generated H₂ amount with 1% of SA can be seen in Figure 7.6a. For 1-nonanol, the nanocavity sample slightly decreased the activity by 40% compared to pure TiO₂ after

3 hours of PC. A similar relative difference in activity can be seen when 5-nonanol was the SA.

The SA concentration was lowered further to 5 mM, similar to the discrimination experiments in the former section (see [Figure 7.3](#)). The HER results can be seen in [Figure 7.6b](#): Again, there was only a slight difference in H₂ production for the different SAs when nanocavities samples were used: For 1-nonanol it was decreased by 1/3, and for 5-nonanol by 1/2, but the absolute differences are rather small.

Considering the low activity of the system, it is possible that the sensitivity of the detection is too low to get reliable quantitative results. While I did not define the standard deviation of the blank, the standard deviation of the measurements and the detection of the blank are around 0.1 $\mu\text{mol} \cdot \text{g}^{-1}$ after 3 hours. The limit of quantification was determined to a minimum activity of 0.5-1 $\mu\text{mol} \cdot \text{g}^{-1}$ after 3 hours, which is not met in the systems with 1% and 5 mM of SA. While it was verified that 1-nonanol and 5-nonanol are good choices of reactants for size discrimination with nanocavities, they are not efficient SAs for photocatalytic HER: When methanol is used, the order of magnitude of detected H₂ is two orders of magnitude higher (not shown).

7.3 Conclusion and Outlook

This work has shown that metal oxide catalysts can be made size selective by depositing an ultrathin nanocavities containing layer on the surface, without leading to diffusion limitations. Due to the discrimination of molecules of a certain size (< 1.4 nm), or with a sterically non-hindered structure, only specific reactants have access to the photocatalytically active surface where they can adsorb and undergo redox reactions.

It was also shown that the size selection is decreased, though still significant when 10% water is added to the system, which increases the hydrodynamic radius and inhibits the oxidation over nanocavities containing samples by 50%.

It was found that 5% of SA is too high to observe size discriminating effects during HER. Though with lower SA concentrations size discrimination was determined, the HER activity was too low to observe significant results.

In summary, it was shown that there is a discriminating effect for the oxidation of the alcohols 1-nonanol and 5-nonanol, but it was not possible to observe this size

discrimination by measuring the product of the complementary redox reaction, the reduction of H^+ , due to the low activity.

To increase the activity, a more efficient SA has to be found. It has to fulfill several requirements; it needs to have a fitting redox potential to act as an SA for HER; it needs to be available in two forms with a similar redox potential, where one form is sterically hindered, while the other can pass through the nanocavity; it needs to be miscible with acetonitrile that contains 10% water.

Another possible approach would be to introduce a noble metal co-catalyst which generally increases the HER activity. It must be considered that this co-catalyst, deposited as nanoparticles, will fill some of the nanocavities. A sufficient amount of nanocavities must stay empty for the SA oxidation reaction to occur on the bottom of the cavities, which could be achieved by adjusting the concentration of the co-catalyst. This approach can be easily adapted to the current system and will therefore be used for investigations in future studies.



Die approbierte gedruckte Originalversion dieser Dissertation ist an der TU Wien Bibliothek verfügbar.
The approved original version of this doctoral thesis is available in print at TU Wien Bibliothek.

Bibliography

- [1] Yuzhu Fu and T Viraraghavan. Fungal decolorization of dye wastewaters: a review. *Bioresour. Technol.*, 79(3):251–262, September 2001. doi: 10.1016/s0960-8524(01)00028-1.
- [2] Severin N. Habisreutinger, Lukas Schmidt-Mende, and Jacek K. Stolarczyk. Photocatalytic Reduction of CO₂ on TiO₂ and Other Semiconductors. *Angew. Chem. Int. Ed.*, 52(29):7372–7408, July 2013. ISSN 1521-3773. doi: 10.1002/anie.201207199.
- [3] Intergovernmental Panel On Climate Change. Climate change 2007: The physical science basis: Summary for policymakers. *Geneva: IPCC*, 2007.
- [4] REA Almond, M Grooten, and T Peterson. *Living Planet Report 2020-Bending the curve of biodiversity loss*. World Wildlife Fund, 2020.
- [5] Vincent Moreau, Piero Dos Reis, and François Vuille. Enough metals? Resource constraints to supply a fully renewable energy system. *Resources*, 8(1): 29, 2019. doi: 10.3390/resources8010029.
- [6] UNFCCC. Paris agreement. In *Report of the Conference of the Parties to the United Nations Framework Convention on Climate Change (21st Session, 2015: Paris)*. Retrived December, volume 4, page 2017. HeinOnline, 2015.
- [7] S. E. Braslavsky. Glossary of terms used in photochemistry, 3rd edition (IUPAC recommendations 2006). *Pure Appl. Chem.*, 79(3):293–465, January 2007. doi: 10.1351/pac200779030293.
- [8] A. D. McNaught and A. Wilkinson. *IUPAC. Compendium of Chemical Terminology, 2nd ed. (the "Gold Book")*. Blackwell Scientific Publications, Online version (2019-) created by S. J. Chalk., Oxford 1997. ISBN ISBN 0-9678550-9-8. doi: <https://doi.org/10.1351/goldbook>.

- [9] Frank E. Osterloh. Photocatalysis versus Photosynthesis: A Sensitivity Analysis of Devices for Solar Energy Conversion and Chemical Transformations. *ACS Energy Lett.*, 2(2):445–453, January 2017. doi: 10.1021/acsenergylett.6b00665.
- [10] Zheng Wang, Can Li, and Kazunari Domen. Recent developments in heterogeneous photocatalysts for solar-driven overall water splitting. *Chem. Soc. Rev.*, 48(7):2109–2125, 2019. doi: 10.1039/c8cs00542g.
- [11] Felipe Guzman, Steven S. C. Chuang, and Cheng Yang. Role of methanol sacrificing reagent in the photocatalytic evolution of hydrogen. *Ind. Eng. Chem. Res.*, 52(1):61–65, January 2013. doi: 10.1021/ie301177s.
- [12] Jenny Schneider and Detlef W. Bahnemann. Undesired role of sacrificial reagents in photocatalysis. *The Journal of Physical Chemistry Letters*, 4(20):3479–3483, October 2013. doi: 10.1021/jz4018199.
- [13] Siyuan Fang, Yixin Liu, Zhuxing Sun, Junyu Lang, Chenyu Bao, and Yun Hang Hu. Photocatalytic hydrogen production over rh-loaded TiO₂: What is the origin of hydrogen and how to achieve hydrogen production from water? *Appl. Catal., B*, 278:119316, December 2020. doi: 10.1016/j.apcatb.2020.119316.
- [14] Xue Lu Wang, Wenqing Liu, Yan-Yan Yu, Yanhong Song, Wen Qi Fang, Daxiu Wei, Xue-Qing Gong, Ye-Feng Yao, and Hua Gui Yang. Operando NMR spectroscopic analysis of proton transfer in heterogeneous photocatalytic reactions. *Nat. Commun.*, 7(1), June 2016. doi: 10.1038/ncomms11918.
- [15] ASTM G173-03, standard tables for reference solar spectral irradiances: Direct normal and hemispherical on 37° tilted surface, 2003. URL www.astm.org.
- [16] Solar spectrum en.svg by Nick84. License: CC BY-SA (<https://creativecommons.org/licenses/by-sa/3.0>), size and colors changed by author of this thesis, 2013.
- [17] Perry Sadorsky. Renewable energy consumption, CO₂ emissions and oil prices in the g7 countries. *Energy Econ.*, 31(3):456–462, May 2009. doi: 10.1016/j.eneco.2008.12.010.
- [18] C.A. Gueymard, D. Myers, and K. Emery. Proposed reference irradiance spectra for solar energy systems testing. *Sol Energy*, 73(6):443–467, December 2002. doi: 10.1016/s0038-092x(03)00005-7.
- [19] George W. Crabtree and Nathan S. Lewis. Solar energy conversion. *Phys. Today*, 60(3):37–42, March 2007. doi: 10.1063/1.2718755.

- [20] Takashi Hisatomi, Jun Kubota, and Kazunari Domen. Recent advances in semiconductors for photocatalytic and photoelectrochemical water splitting. *Chem. Soc. Rev.*, 43(22):7520–7535, January 2014. doi: 10.1039/c3cs60378d.
- [21] Zümriye Aksu. Application of biosorption for the removal of organic pollutants: a review. *Process Biochem.*, 40(3-4):997–1026, March 2005. doi: 10.1016/j.procbio.2004.04.008.
- [22] Terri Damstra. Potential effects of certain persistent organic pollutants and endocrine disrupting chemicals on the health of children. *J. Toxicol. Clin.*, 40(4): 457–465, January 2002. doi: 10.1081/clt-120006748.
- [23] Akira Fujishima, Tata N. Rao, and Donald A. Tryk. Titanium dioxide photocatalysis. *J. Photochem. Photobiol., C*, 1(1):1–21, June 2000. ISSN 1389-5567. doi: 10.1016/S1389-5567(00)00002-2.
- [24] Haruna Hori, Mai Takashima, Mai Takase, Mika Kitamura, Fumiaki Amano, and Bunsho Ohtani. Multielectron reduction of molecular oxygen in photocatalytic decomposition of organic compounds by bismuth tungstate particles without cocatalyst loading. *Catal. Today*, 303:341–349, April 2018. doi: 10.1016/j.cattod.2017.08.045.
- [25] Qian Wang, Senlin Tian, and Ping Ning. Degradation mechanism of methylene blue in a heterogeneous fenton-like reaction catalyzed by ferrocene. *Ind. Eng. Chem. Res.*, 53(2):643–649, January 2014. ISSN 0888-5885. doi: 10.1021/ie403402q.
- [26] S.S. Penner. Steps toward the hydrogen economy. *Energy*, 31(1):33–43, January 2006. doi: 10.1016/j.energy.2004.04.060.
- [27] J.O. Abe, A.P.I. Popoola, E. Ajenifuja, and O.M. Popoola. Hydrogen energy, economy and storage: Review and recommendation. *Int. J. Hydrogen Energy*, 44(29):15072–15086, June 2019. doi: 10.1016/j.ijhydene.2019.04.068.
- [28] M. Ball and M. Wietschel. The future of hydrogen – opportunities and challenges. *Int. J. Hydrogen Energy*, 34(2):615–627, January 2009. doi: 10.1016/j.ijhydene.2008.11.014.
- [29] Muhammad Tahir and NorAishah Saidina Amin. Advances in visible light responsive titanium oxide-based photocatalysts for CO₂ conversion to hydrocarbon fuels. *Energy Convers. Manage.*, 76:194–214, December 2013. ISSN 0196-8904. doi: 10.1016/j.enconman.2013.07.046.

- [30] Roland Marschall. Semiconductor Composites: Strategies for enhancing charge carrier separation to improve photocatalytic activity. *Adv. Funct. Mater.*, 24(17): 2421–2440, December 2013. doi: 10.1002/adfm.201303214.
- [31] Cameron J. Shearer, Alexey Cherevan, and Dominik Eder. Application and future challenges of functional nanocarbon hybrids. *Adv. Mater.*, 26(15):2295–2318, February 2014. ISSN 1521-4095. doi: 10.1002/adma.201305254.
- [32] Miloslav Nič, Jiří Jirát, Bedřich Košata, Aubrey Jenkins, and Alan McNaught, editors. *IUPAC Compendium of Chemical Terminology*. IUPAC, Research Triangle Park, NC, 2.1.0 edition, June 2009. ISBN 978-0-9678550-9-7. doi: 10.1351/goldbook.
- [33] Jinfeng Zhang, Peng Zhou, Jianjun Liu, and Jiaguo Yu. New understanding of the difference of photocatalytic activity among anatase, rutile and brookite TiO₂. *Phys. Chem. Chem. Phys.*, 16(38):20382–20386, August 2014. doi: 10.1039/c4cp02201g.
- [34] Fei Qi, Anna Moiseev, Joachim Deubener, and Alfred Weber. Thermostable photocatalytically active TiO₂ anatase nanoparticles. *J. Nanopart. Res.*, 13(3): 1325–1334, March 2011. ISSN 1572-896X. doi: 10.1007/s11051-010-0211-0.
- [35] Yasuhiro Yamada and Yoshihiko Kanemitsu. Determination of electron and hole lifetimes of rutile and anatase TiO₂ single crystals. *Appl. Phys. Lett.*, 101(13): 133907, September 2012. doi: 10.1063/1.4754831.
- [36] Yusuke Kakuma, Atsuko Y. Nosaka, and Yoshio Nosaka. Difference in TiO₂ photocatalytic mechanism between rutile and anatase studied by the detection of active oxygen and surface species in water. *Phys. Chem. Chem. Phys.*, 17(28):18691–18698, July 2015. ISSN 1463-9084. doi: 10.1039/c5cp02004b.
- [37] Thomas W. Woolerton, Sally Sheard, Yatendra S. Chaudhary, and Fraser A. Armstrong. Enzymes and bio-inspired electrocatalysts in solar fuel devices. *Energy Environ. Sci.*, 5(6):7470, 2012. doi: 10.1039/c2ee21471g.
- [38] Greta M. Haselmann, Bettina Baumgartner, Jia Wang, Karin Wieland, Tushar Gupta, Christopher Herzig, Andreas Limbeck, Bernhard Lendl, and Dominik Eder. In situ pt photodeposition and methanol photooxidation on Pt/TiO₂: Pt-loading-dependent photocatalytic reaction pathways studied by liquid-phase infrared spectroscopy. *ACS Catal.*, 10(5):2964–2977, February 2020. doi: 10.1021/acscatal.9b05588.

- [39] Zhi Jiang, Mark A. Isaacs, Zheng Wen Huang, Wenfeng Shangguan, Yifeng Deng, and Adam F. Lee. Active Site Elucidation and Optimization in Pt Co-catalysts for Photocatalytic Hydrogen Production over Titania. *ChemCatChem*, 9(22):4268–4274, 2017. ISSN 1867-3899. doi: 10.1002/cctc.201700901.
- [40] Juan C. Colmenares, Agnieszka Magdziarz, Maria A. Aramendia, Alberto Marinas, José M. Marinas, Francisco J. Urbano, and José A. Navio. Influence of the strong metal support interaction effect (SMSI) of Pt/TiO₂ and Pd/TiO₂ systems in the photocatalytic biohydrogen production from glucose solution. *Catal. Commun.*, 16(1):1–6, November 2011. ISSN 1566-7367. doi: 10.1016/j.catcom.2011.09.003.
- [41] Junya Ohyama, Akira Yamamoto, Kentaro Teramura, Tetsuya Shishido, and Tsunehiro Tanaka. Modification of metal nanoparticles with TiO₂ and metal-support interaction in photodeposition. *ACS Catal.*, 1(3):187–192, March 2011. doi: 10.1021/cs100072k.
- [42] Bastian Mei, Christian Wiktor, Stuart Turner, Anna Pougin, Gustaaf van Tendeloo, Roland A. Fischer, Martin Muhler, and Jennifer Strunk. Evidence for metal-support interactions in Au modified TiO_x/SBA-15 materials prepared by photodeposition. *ACS Catal.*, 3(12):3041–3049, December 2013. doi: 10.1021/cs400964k.
- [43] Roland Resch, Sheffer Meltzer, Thomas Vallant, Helmuth Hoffmann, Bruce E. Koel, Anupam Madhukar, Requicha, and Peter Will. Immobilizing Au nanoparticles on SiO₂ surfaces using octadecylsiloxane monolayers. *Langmuir*, 17(18):5666–5670, September 2001. ISSN 0743-7463. doi: 10.1021/la001296p.
- [44] Qiang Fu and Thomas Wagner. Interaction of nanostructured metal overlayers with oxide surfaces. *Surf. Sci. Rep.*, 62(11):431–498, November 2007. doi: 10.1016/j.surfrep.2007.07.001.
- [45] Ikuma Y. and Bessho H. Effect of pt concentration on the production of hydrogen by a TiO₂ photocatalyst. *Int. J. Hydrogen Energy*, 32(14):2689–2692, September 2007. doi: 10.1016/j.ijhydene.2006.09.024.
- [46] Mi-Young Kim, Jae-Soon Choi, Todd J. Toops, Eun-Suk Jeong, Sang-Wook Han, Viviane Schwartz, and Jihua Chen. Coating SiO₂ Support with TiO₂ or ZrO₂ and Effects on Structure and CO Oxidation Performance of Pt Catalysts. *Catalysts*, 3(1):88–103, March 2013. doi: 10.3390/catal3010088.

Bibliography

- [47] Liuxian Zhang, Qianlang Liu, and Peter A. Crozier. Light induced coarsening of metal nanoparticles. *J. Mater. Chem.A*, 7(19):11756–11763, 2019. doi: 10.1039/c8ta11341f.
- [48] T.C. Watling, A.F. Gusovius, and R. Prins. Synthesis of methanol from CO over ca-promoted pt/SiO₂. *J. Catal.*, 188(1):233–236, November 1999. doi: 10.1006/jcat.1999.2660.
- [49] Kasper Wenderich and Guido Mul. Methods, mechanism, and applications of photodeposition in photocatalysis: A review. *Chem. Rev.*, 116(23):14587–14619, December 2016. doi: 10.1021/acs.chemrev.6b00327.
- [50] Zhen Zhang and John T. Yates. Band bending in semiconductors: Chemical and physical consequences at surfaces and interfaces. *Chem. Rev.*, 112(10):5520–5551, July 2012. doi: 10.1021/cr3000626.
- [51] Shun Kashiwaya, Jan Morasch, Verena Streibel, Thierry Toupance, Wolfram Jaegermann, and Andreas Klein. The work function of TiO₂. *Surfaces*, 1(1): 73–89, September 2018. doi: 10.3390/surfaces1010007.
- [52] Wei-Ning Wang, Woo-Jin An, Balavinayagam Ramalingam, Somik Mukherjee, Dariusz M. Niedzwiedzki, Shubhra Gangopadhyay, and Pratim Biswas. Size and structure matter: Enhanced CO₂ photoreduction efficiency by size-resolved ultrafine pt nanoparticles on TiO₂ single crystals. *J. Am. Chem. Soc.*, 134(27): 11276–11281, July 2012. ISSN 0002-7863. doi: 10.1021/ja304075b.
- [53] M. Sadeghi, W. Liu, T-G. Zhang, P. Stavropoulos, and B. Levy. Role of photoinduced charge carrier separation distance in heterogeneous photocatalysis: oxidative degradation of CH₃OH vapor in contact with Pt/TiO₂ and cofumed TiO₂-Fe₂O₃. *The Journal of Physical Chemistry*, 100(50):19466–19474, January 1996. doi: 10.1021/jp961335z.
- [54] Dong Wang, Zhi-Pan Liu, and Wei-Min Yang. Revealing the size effect of platinum cocatalyst for photocatalytic hydrogen evolution on TiO₂ support: A DFT study. *ACS Catal.*, 8(8):7270–7278, June 2018. doi: 10.1021/acscatal.8b01886.
- [55] S. M. Sze. *Physics of semiconductor devices*. Wiley-Interscience, Hoboken, N.J, 2007. ISBN 9780471143239.
- [56] Sonali Das, Javier Pérez-Ramírez, Jinlong Gong, Nikita Dewangan, Kus Hidayat, Bruce C. Gates, and Sibudjing Kawi. Core-shell structured catalysts for

- thermocatalytic, photocatalytic, and electrocatalytic conversion of CO₂. *Chem. Soc. Rev.*, 49(10):2937–3004, 2020. doi: 10.1039/c9cs00713j.
- [57] Sajjad Ullah, Elias P. Ferreira-Neto, André A. Pasa, Carlos C. J. Alcântara, José J. S. Acuña, Sara A. Bilmes, Maria L. Martínez Ricci, Richard Landers, Taina Zampieri Fermino, and Ubirajara P. Rodrigues-Filho. Enhanced photocatalytic properties of core@shell SiO₂@TiO₂ nanoparticles. *Appl. Catal., B*, 179:333–343, December 2015. ISSN 0926-3373. doi: 10.1016/j.apcatb.2015.05.036.
- [58] Milka Nussbaum and Yaron Paz. Ultra-thin SiO₂ layers on TiO₂: improved photocatalysis by enhancing products' desorption. *Phys. Chem. Chem. Phys.*, 14(10):3392–3399, 2012. doi: 10.1039/C2CP23202B.
- [59] Shaozheng Hu, Fayun Li, and Zhiping Fan. Preparation of SiO₂-Coated TiO₂ Composite Materials with Enhanced Photocatalytic Activity Under UV Light. *Bull. Korean Chem. Soc.*, 33(6):1895–1899, 2012. ISSN 0253-2964. doi: 10.5012/bkcs.2012.33.6.1895.
- [60] Yusuke Ide, Yusuke Koike, and Makoto Ogawa. Molecular selective photocatalysis by TiO₂/nanoporous silica core/shell particulates. *J. Colloid Interface Sci.*, 358(1):245–251, June 2011. ISSN 0021-9797. doi: 10.1016/j.jcis.2011.02.018.
- [61] P. A. Williams, C. P. Ireland, P. J. King, P. A. Chater, P. Boldrin, R. G. Palgrave, J. B. Claridge, J. R. Darwent, P. R. Chalker, and M. J. Rosseinsky. Atomic layer deposition of anatase TiO₂ coating on silica particles: Growth, characterization and evaluation as photocatalysts for methyl orange degradation and hydrogen production. *J. Mater. Chem.*, 22(38):20203–20209, 2012. doi: 10.1039/C2JM33446A.
- [62] Basanti Ekka, Manoj Kumar Sahu, Raj Kishore Patel, and Priyabrat Dash. Titania coated silica nanocomposite prepared via encapsulation method for the degradation of Safranin-O dye from aqueous solution: Optimization using statistical design. *Water Resour. Ind.*, page 100071, August 2016. ISSN 2212-3717. doi: 10.1016/j.wri.2016.08.001.
- [63] Nan Zhang, Siqi Liu, Xianzhi Fu, and Yi-Jun Xu. Synthesis of M@TiO₂ (M = Au, Pd, Pt) core-shell nanocomposites with tunable photoreactivity. *J. Phys. Chem. C*, 115(18):9136–9145, April 2011. doi: 10.1021/jp2009989.
- [64] Mannan Mehta, Satheesh Krishnamurthy, Suddhasatwa Basu, Tony P. Nixon, and Aadesh P. Singh. BiVO₄/TiO₂ core-shell heterostructure: wide range

- optical absorption and enhanced photoelectrochemical and photocatalytic performance. *Mater. Tod. Chem.*, 17:100283, September 2020. doi: 10.1016/j.mtchem.2020.100283.
- [65] N. Ramesh Reddy, U. Bhargav, G. Manoranjani, M. Mamatha Kumari, K. K. Cheralathan, and M. V. Shankar. Low-cost TiO₂-graphitic carbon core/shell nanocomposite for depriving electron, hole recombination. *Mater. Lett.*, 248: 105–108, August 2019. ISSN 0167-577X. doi: 10.1016/j.matlet.2019.03.072.
- [66] Inderpreet Singh Grover, Roop Chand Prajapat, Satnam Singh, and Bonamali Pal. SiO₂-coated pure anatase TiO₂ catalysts for enhanced photo-oxidation of naphthalene and anthracene. *Particuology*, 34:156–161, October 2017. ISSN 1674-2001. doi: 10.1016/j.partic.2017.03.001.
- [67] Yichao Gong, Dan Ping Wang, Renbing Wu, Sarifuddin Gazi, Han Sen Soo, Thirumany Sritharan, and Zhong Chen. New insights into the photocatalytic activity of 3-D core–shell P25@silica nanocomposites: Impact of mesoporous coating. *Dalton Trans.*, 46(15):4994–5002, 2017. doi: 10.1039/C7DT00797C.
- [68] Meiqi Chang, Yanhua Song, Jie Chen, Lei Cui, Zhan Shi, Ye Sheng, and Haifeng Zou. Photocatalytic and Photoluminescence Properties of Core–Shell SiO₂@TiO₂:Eu³⁺,Sm³⁺ and Its Etching Products. *ACS Sustainable Chem. Eng.*, 6(1):223–236, January 2018. doi: 10.1021/acssuschemeng.7b02285.
- [69] Juanmin Hu, Jie Ding, and Qin Zhong. In situ fabrication of amorphous TiO₂/NH₂-MIL-125(Ti) for enhanced photocatalytic CO₂ into CH₄ with H₂O under visible-light irradiation. *J. Colloid Interface Sci.*, 560:857–865, February 2020. doi: 10.1016/j.jcis.2019.11.003.
- [70] Ariane Giesriegl, Jakob Blaschke, Shaghayegh Naghdi, and Dominik Eder. Rate-limiting steps of dye degradation over titania-silica core-shell photocatalysts. *Catalysts*, 9(7):583–594, June 2019. doi: 10.3390/catal9070583.
- [71] S. Aksel and D. Eder. Catalytic effect of metal oxides on the oxidation resistance in carbon nanotube–inorganic hybrids. *J. Mater. Chem.*, 20(41):9149–9154, 2010. doi: 10.1039/c0jm01129k.
- [72] Chun-Jern Pan, Meng-Che Tsai, Wei-Nien Su, John Rick, Nibret Gebeyehu Akalework, Abiye Kebede Agegnehu, Shou-Yi Cheng, and Bing-Joe Hwang. Tuning/exploiting strong metal-support interaction (SMSI) in heterogeneous catalysis. *J. Taiwan Inst. Chem. Eng.*, 74:154–186, May 2017. ISSN 1876-1070. doi: 10.1016/j.jtice.2017.02.012.

- [73] Kiyoshi Miyashita, Shin-ichi Kuroda, So Tajima, Kazuyuki Takehira, Seiji Tobita, and Hitoshi Kubota. Photoluminescence study of electron–hole recombination dynamics in the vacuum-deposited SiO₂/TiO₂ multilayer film with photocatalytic activity. *Chem. Phys. Lett.*, 369(1):225–231, February 2003. ISSN 0009-2614. doi: 10.1016/S0009-2614(02)02009-2.
- [74] Lan Yuan, Chuang Han, Mario Pagliaro, and Yi-Jun Xu. Origin of enhancing the photocatalytic performance of TiO₂ for artificial photoreduction of CO₂ through a SiO₂ coating strategy. *J. Phys. Chem. C*, 120(1):265–273, January 2016. ISSN 1932-7447. doi: 10.1021/acs.jpcc.5b08893.
- [75] Nina Kemnade, Paul Gebhardt, Greta M. Haselmann, Alexey Cherevan, Gerhard Wilde, and Dominik Eder. How to evaluate and manipulate charge transfer and photocatalytic response at hybrid nanocarbon-metal oxide interfaces. *Adv. Funct. Mater.*, 28(17):1704730–1704738, December 2017. doi: 10.1002/adfm.201704730.
- [76] Yaron Paz. Self-assembled monolayers and titanium dioxide: From surface patterning to potential applications. *Beilstein J. Nanotechnol.*, 2:845–861, December 2011. ISSN 2190-4286. doi: 10.3762/bjnano.2.94.
- [77] I. Ichinose, H. Senzu, and T. Kunitake. Stepwise adsorption of metal alkoxides on hydrolyzed surfaces : A surface sol-gel process. *Chem. Lett.*, 10:831–832, 1996. doi: <https://doi.org/10.1246/cl.1996.831>.
- [78] M. Alexander Ardagh, Zhenyu Bo, Scott L. Nauert, and Justin M. Notestein. Depositing SiO₂ on Al₂O₃: A Route to Tunable Brønsted Acid Catalysts. *ACS Catal.*, 6(9):6156–6164, September 2016. doi: 10.1021/acscatal.6b01077.
- [79] T. Vallant, H. Brunner, U. Mayer, H. Hoffmann, T. Leitner, R. Resch, and G. Friedbacher. Formation of self-assembled octadecylsiloxane monolayers on mica and silicon surfaces studied by atomic force microscopy and infrared spectroscopy. *J. Phys. Chem. B*, 102(37):7190–7197, September 1998. ISSN 1520-6106. doi: 10.1021/jp981282g.
- [80] H. B. Profijt, S. E. Potts, M. C. M. van de Sanden, and W. M. M. Kessels. Plasma-assisted atomic layer deposition: Basics, opportunities, and challenges. *J. Vac. Sci. Technol., A*, 29(5):050801, August 2011. ISSN 0734-2101. doi: 10.1116/1.3609974.
- [81] Amit Katiyar, Santosh Yadav, Panagiotis G. Smirniotis, and Neville G. Pinto. Synthesis of ordered large pore SBA-15 spherical particles for adsorption

- of biomolecules. *J. Chromatogr. A*, 1122(1-2):13–20, July 2006. doi: 10.1016/j.chroma.2006.04.055.
- [82] Christian P. Canlas, Junling Lu, Natalie A. Ray, Nicolas A. Grosso-Giordano, Sungsik Lee, Jeffrey W. Elam, Randall E. Winans, Richard P. Van Duyne, Peter C. Stair, and Justin M. Notestein. Shape-selective sieving layers on an oxide catalyst surface. *Nat. Chem.*, 4(12):1030–1036, October 2012. doi: 10.1038/nchem.1477.
- [83] Justin M. Notestein, Enrique Iglesia, and Alexander Katz. Photoluminescence and charge-transfer complexes of calixarenes grafted on TiO₂ nanoparticles. *Chem. Mater.*, 19(20):4998–5005, September 2007. doi: 10.1021/cm070779c.
- [84] Rongyue Wang, Jianguo Liu, Pan Liu, Xuanxuan Bi, Xiuling Yan, Wenxin Wang, Yifei Meng, Xingbo Ge, Mingwei Chen, and Yi Ding. Ultra-thin layer structured anodes for highly durable low-pt direct formic acid fuel cells. *Nano Res.*, 7(11):1569–1580, August 2014. doi: 10.1007/s12274-014-0517-9.
- [85] Jun Di, Jun Xiong, Huaming Li, and Zheng Liu. Ultrathin 2D photocatalysts: Electronic-structure tailoring, hybridization, and applications. *Adv. Mater.*, 30(1):1704548, November 2017. doi: 10.1002/adma.201704548.
- [86] T. Vallant, H. Brunner, J. Kattner, U. Mayer, H. Hoffmann, T. Leitner, G. Friedbacher, G. Schügerl, R. Svagera, and M. Ebel. Monolayer-controlled deposition of silicon oxide films on gold, silicon, and mica substrates by room-temperature adsorption and oxidation of alkylsiloxane monolayers. *J. Phys. Chem. B*, 104(22):5309–5317, June 2000. ISSN 1520-6106. doi: 10.1021/jp000006a.
- [87] Shamil Shaikhutdinov. Strong metal–support interaction and reactivity of ultrathin oxide films. *Catal. Lett.*, 148(9):2627–2635, July 2018. doi: 10.1007/s10562-018-2499-9.
- [88] F. Jiménez-Molinos, F. Gámiz, A. Palma, P. Cartujo, and J. A. López-Villanueva. Direct and trap-assisted elastic tunneling through ultrathin gate oxides. *J. Appl. Phys.*, 91(8):5116–5124, April 2002. doi: 10.1063/1.1461062.
- [89] Roger Mueller, Hendrik K. Kammler, Karsten Wegner, and Sotiris E. Pratsinis. OH surface density of SiO₂ and TiO₂ by thermogravimetric analysis. *Langmuir*, 19(1):160–165, January 2003. doi: 10.1021/la025785w.
- [90] Zhenyu Bo, Sol Ahn, M. Alexander Ardagh, Neil M. Schweitzer, Christian P. Canlas, Omar K. Farha, and Justin M. Notestein. Synthesis and stabilization of

- small Pt nanoparticles on TiO₂ partially masked by SiO₂. *Appl. Catal., A*, 551: 122–128, February 2018. ISSN 0926-860X. doi: 10.1016/j.apcata.2017.11.017.
- [91] Zhenyu Bo, Todd R. Eaton, James R. Gallagher, Christian P. Canlas, Jeffrey T. Miller, and Justin M. Notestein. Size-Selective Synthesis and Stabilization of Small Silver Nanoparticles on TiO₂ Partially Masked by SiO₂. *Chem. Mater.*, 27(4):1269–1277, February 2015. ISSN 0897-4756. doi: 10.1021/cm504243f.
- [92] Sven Tougaard. Universality classes of inelastic electron scattering cross-sections. *Surf. Interface Anal.*, 25(3):137–154, 1997. doi: [https://doi.org/10.1002/\(SICI\)1096-9918\(199703\)25:3<137::AID-SIA230>3.0.CO;2-L](https://doi.org/10.1002/(SICI)1096-9918(199703)25:3<137::AID-SIA230>3.0.CO;2-L).
- [93] D. A. Shirley. High-resolution X-Ray photoemission spectrum of the valence bands of gold. *Phys. Rev. B*, 5(12):4709–4714, June 1972. doi: 10.1103/physrevb.5.4709.
- [94] Mahdiyaz Bagheri and Peter Blaha. DFT calculations of energy dependent XPS valence band spectra. *J. Electron Spectrosc. Relat. Phenom.*, 230:1–9, January 2019. doi: 10.1016/j.elspec.2018.11.002.
- [95] Thomas G. Mayerhöfer, Susanne Pahlow, and Jürgen Popp. The bouguer-beer-lambert law: Shining light on the obscure. *ChemPhysChem*, 21(18):2029–2046, August 2020. doi: 10.1002/cphc.202000464.
- [96] Patrycja Makuła, Michał Pacia, and Wojciech Macyk. How to correctly determine the band gap energy of modified semiconductor photocatalysts based on UV–vis spectra. *The Journal of Physical Chemistry Letters*, 9(23):6814–6817, December 2018. doi: 10.1021/acs.jpcclett.8b02892.
- [97] A. R. Zanatta. Revisiting the optical bandgap of semiconductors and the proposal of a unified methodology to its determination. *Sci. Rep.*, 9(1), August 2019. doi: 10.1038/s41598-019-47670-y.
- [98] Joseph R. Lakowicz. *Principles of Fluorescence Spectroscopy*. Springer US, 2006. doi: 10.1007/978-0-387-46312-4.
- [99] P. Wilhelm and D. Stephan. On-line tracking of the coating of nanoscaled silica with titania nanoparticles via zeta-potential measurements. *J. Colloid Interface Sci.*, 293(1):88–92, January 2006. ISSN 0021-9797. doi: 10.1016/j.jcis.2005.06.047.

- [100] George A. Parks. The isoelectric points of solid oxides, solid hydroxides, and aqueous hydroxo complex systems. *Chem. Rev.*, 65(2):177–198, April 1965. ISSN 0009-2665. doi: 10.1021/cr60234a002.
- [101] Micromeritics Instrument Corporation. Gas adsorption theory, 2021. URL https://www.micromeritics.com/Repository/Files/Gas_Adsorption_Theory_poster.pdf.
- [102] Li Zhang, Haizhen Li, Yan Liu, Zhang Tian, Bo Yang, Zebin Sun, and Shiqiang Yan. Adsorption-photocatalytic degradation of methyl orange over a facile one-step hydrothermally synthesized TiO₂/ZnO–NH₂–RGO nanocomposite. *RSC Adv.*, 4(89):48703–48711, September 2014. ISSN 2046-2069. doi: 10.1039/C4RA09227A.
- [103] Umar Ibrahim Gaya and Abdul Halim Abdullah. Heterogeneous photocatalytic degradation of organic contaminants over titanium dioxide: A review of fundamentals, progress and problems. *J. Photochem. Photobiol., C*, 9(1):1–12, March 2008. ISSN 1389-5567. doi: 10.1016/j.jphotochemrev.2007.12.003.
- [104] M. A. Fardad. Catalysts and the structure of SiO₂ sol-gel films. *J. Mater. Sci.*, 35(7):1835–1841, April 2000. ISSN 0022-2461, 1573-4803. doi: 10.1023/A:1004749107134.
- [105] Sourav Bhattacharjee. DLS and zeta potential - What they are and what they are not? *J. Controlled Release*, 235:337–351, October 2016. ISSN 1873-4995. doi: 10.1016/j.jconrel.2016.06.017.
- [106] Denis Flandre, Alexei N. Nazarov, and Peter L. F. Hemment. *Science and Technology of Semiconductor-On-Insulator Structures and Devices Operating in a Harsh Environment*. Springer Science & Business Media, March 2006. ISBN 978-1-4020-3013-0.
- [107] Chao Chen, Wei Wu, William Z. Xu, and Paul A. Charpentier. The effect of silica thickness on nano TiO₂ particles for functional polyurethane nanocomposites. *Nanotechnology*, 28(11):115709–115722, 2017. ISSN 0957-4484. doi: 10.1088/1361-6528/aa5cf0.
- [108] Ahmed Mohamed El-Toni, Shu Yin, and Tsugio Sato. Control of silica shell thickness and microporosity of titania–silica core–shell type nanoparticles to depress the photocatalytic activity of titania. *J. Colloid Interface Sci.*, 300(1): 123–130, August 2006. ISSN 0021-9797. doi: 10.1016/j.jcis.2006.03.073.

- [109] Muhammad Shariq Vohra and Keiichi Tanaka. Photocatalytic degradation of aqueous pollutants using silica-modified TiO₂. *Water Res.*, 37(16):3992–3996, September 2003. ISSN 0043-1354. doi: 10.1016/S0043-1354(03)00333-6.
- [110] Marek Kosmulski and Egon Matijević. Zeta potential of anatase (TiO₂) in mixed solvents. *Colloids Surf.*, 64(1):57–65, May 1992. ISSN 0166-6622. doi: 10.1016/0166-6622(92)80162-U.
- [111] Nikola Kallay, Darko Babić, and Egon Matijević. Adsorption at solid/solution interfaces II. Surface charge and potential of spherical colloidal titania. *Colloids Surf.*, 19(2):375–386, August 1986. ISSN 0166-6622. doi: 10.1016/0166-6622(86)80346-8.
- [112] Francisco J. Gil-Llambías and A. M. Escudéy-Castro. Use of zero point charge measurements in determining the apparent surface coverage of molybdena in MoO₃/γ-Al₂O₃ catalysts. *J. Chem. Soc., Chem. Commun.*, 0(9):478–479, January 1982. ISSN 0022-4936. doi: 10.1039/C39820000478.
- [113] A. A. Belhekar, S. V. Awate, and R. Anand. Photocatalytic activity of titania modified mesoporous silica for pollution control. *Catal. Commun.*, 3(10):453–458, October 2002. ISSN 1566-7367. doi: 10.1016/S1566-7367(02)00179-6.
- [114] Alexandra Fidalgo and Laura M Ilharco. The defect structure of sol–gel-derived silica/polytetrahydrofuran hybrid films by FTIR. *J. Non-Cryst. Solids*, 283(1): 144–154, May 2001. ISSN 0022-3093. doi: 10.1016/S0022-3093(01)00418-5.
- [115] Christian E. Fischer, János Mink, László Hajba, Zoltán Bacsik, Csaba Németh, Judith Mihály, Alexander Raith, Mirza Cokoja, and Fritz E. Kühn. Vibrational spectroscopic study of SiO₂-based nanotubes. *Vib. Spectrosc.*, 66:104–118, May 2013. ISSN 0924-2031. doi: 10.1016/j.vibspec.2013.01.012.
- [116] Xingtao Gao and Israel E Wachs. Titania–silica as catalysts: Molecular structural characteristics and physico-chemical properties. *Catal. Today*, 51(2):233–254, June 1999. ISSN 0920-5861. doi: 10.1016/S0920-5861(99)00048-6.
- [117] D. C. M. Dutoit, M. Schneider, and A. Baiker. Titania-Silica Mixed Oxides: I. Influence of Sol-Gel and Drying Conditions on Structural Properties. *J. Catal.*, 153(1):165–176, April 1995. ISSN 0021-9517. doi: 10.1006/jcat.1995.1118.
- [118] Yuhui Lin, Jia Yu, Zipeng Xing, Xiaolei Guo, Xiujuan Yu, Bo Tang, and Jinlong Zou. Enhanced generation of H₂O₂ and radicals on Co₉S–

- 8/partly-graphitized carbon cathode for degradation of bio-refractory organic wastewater. *Electrochim. Acta*, 213:341–350, September 2016. doi: 10.1016/j.electacta.2016.07.136.
- [119] Mohong Lu, Yu Sun, Peng Zhang, Jie Zhu, Mingshi Li, Yuhua Shan, Jianyi Shen, and Chunshan Song. Hydrodeoxygenation of guaiacol catalyzed by high-loading ni catalysts supported on SiO₂–TiO₂ binary oxides. *Ind. Eng. Chem. Res.*, 58(4):1513–1524, January 2019. ISSN 0888-5885. doi: 10.1021/acs.iecr.8b04517.
- [120] NIST. Nist X-ray photoelectron spectroscopy database, Version 4.1 (National institute of standards and technology, Gaithersburg, 2012), 2012. URL <http://srdata.nist.gov/xps/>.
- [121] A. E. Danks, S. R. Hall, and Z. Schnepf. The evolution of ‘sol–gel’ chemistry as a technique for materials synthesis. *Mater. Horiz.*, 3(2):91–112, 2016. doi: 10.1039/C5MH00260E.
- [122] Candy Mercado, Zachary Seeley, Amit Bandyopadhyay, Susmita Bose, and Jeanne L. McHale. Photoluminescence of dense nanocrystalline titanium dioxide thin films: Effect of doping and thickness and relation to gas sensing. *ACS Appl. Mater. Interfaces*, 3(7):2281–2288, July 2011. doi: 10.1021/am2006433.
- [123] Dongjiang Yang, Chuncheng Chen, Zhanfeng Zheng, Hongwei Liu, Eric R. Wacławik, Zhimin Yan, Yining Huang, Hongjie Zhang, Jincai Zhao, and Huaiyong Zhu. Grafting silica species on anatase surface for visible light photocatalytic activity. *Energy Environ. Sci.*, 4:2279–2287, 2011. doi: 10.1039/C1EE01182K. URL <http://dx.doi.org/10.1039/C1EE01182K>.
- [124] Rita G. Lerner and George L. Trigg. *Encyclopedia of physics*. Wiley-VCH, 2nd edition, 1991. ISBN 3527269541.
- [125] Tsutomu Hirakawa, Kenta Yawata, and Yoshio Nosaka. Photocatalytic reactivity for O₂- and OH radical formation in anatase and rutile TiO₂ suspension as the effect of H₂O₂ addition. *Appl. Catal., A*, 325(1):105–111, May 2007. doi: 10.1016/j.apcata.2007.03.015.
- [126] Leonie Deilmann. *Nanostructured and Functionalized Transition Metal Oxides and Nitrides for Photocatalytic Hydrogen Production*. University of Muenster, 2018.

- [127] Greta Haselmann. *TiO₂-based photocatalysis : Role of Defects during Photocatalytic Hydrogen Evolution and Oxidation of Methanol*. Technical University of Vienna, 2018.
- [128] Kazuhiko Maeda. Photocatalytic properties of rutile TiO₂ powder for overall water splitting. *Catal. Sci. Technol.*, 4(7):1949–1953, 2014. doi: 10.1039/c4cy00251b.
- [129] Ayad F. Alkaim, Tarek A. Kandiel, Falah H. Hussein, Ralf Dillert, and Detlef W. Bahnemann. Solvent-free hydrothermal synthesis of anatase TiO₂ nanoparticles with enhanced photocatalytic hydrogen production activity. *Appl. Catal., A*, 466:32–37, September 2013. doi: 10.1016/j.apcata.2013.06.033.
- [130] Paula A. Osorio-Vargas, Cesar Pulgarin, Andrzej Sienkiewicz, Luis R. Pizzio, Mirta N. Blanco, Ricardo A. Torres-Palma, Christian Pétrier, and Julián A. Rengifo-Herrera. Low-frequency ultrasound induces oxygen vacancies formation and visible light absorption in TiO₂ p-25 nanoparticles. *Ultrason. Sonochem.*, 19(3):383–386, May 2012. doi: 10.1016/j.ultsonch.2011.11.013.
- [131] Masato Takeuchi, Gianmario Martra, Salvatore Coluccia, and Masakazu Anpo. Verification of the photoadsorption of H₂O molecules on TiO₂ semiconductor surfaces by vibrational absorption spectroscopy. *J. Phys. Chem. C*, 111(27): 9811–9817, July 2007. doi: 10.1021/jp0689159.
- [132] Ryuhei Nakamura, Tomoaki Okamura, Naomichi Ohashi, Akihito Imanishi, and Yoshihiro Nakato. Molecular mechanisms of photoinduced oxygen evolution, PL emission, and surface roughening at atomically smooth (110) and (100)n-TiO₂ (rutile) surfaces in aqueous acidic solutions. *J. Am. Chem. Soc.*, 127(37): 12975–12983, September 2005. doi: 10.1021/ja053252e.
- [133] Jean-Michel Mermet. Limit of quantitation in atomic spectrometry: An unambiguous concept? *Spectrochim. Acta, Part B*, 63(2):166–182, 2008. ISSN 0584-8547. doi: <https://doi.org/10.1016/j.sab.2007.11.029>.
- [134] Jill Carlson, Artur Wysoczanski, and Edward Voigtman. Limits of quantitation — yet another suggestion. *Spectrochim. Acta, Part B*, 96:69–73, 2014. ISSN 0584-8547. doi: <https://doi.org/10.1016/j.sab.2014.03.012>.
- [135] CITAC / EURACHEM GUIDE. *Guide to quality in analytical chemistry, An Aid to Accreditation*. CITAC and Eurachem, 2002.

- [136] A. Bozzi, T. Yuranova, I. Guasaquillo, D. Laub, and J. Kiwi. Self-cleaning of modified cotton textiles by TiO₂ at low temperatures under daylight irradiation. *J. Photochem. Photobiol., A*, 174(2):156–164, August 2005. ISSN 1010-6030. doi: 10.1016/j.jphotochem.2005.03.019.
- [137] Chia-hung Huang, Hsunling Bai, Yaoling Huang, Shuling Liu, Shaoi Yen, and Yaohsuan Tseng. Synthesis of Neutral SiO₂/TiO₂ Hydrosol and It's Application as Antireflective Self-Cleaning Thin Film. *Int. J. Photoenergy*, 2012, June 2012. doi: 10.1155/2012/620764.
- [138] Takashi Kamegawa, Yasushi Ishiguro, Yasuhiro Magatani, and Hiromi Yamashita. Spherical TiO₂/Mesoporous SiO₂ Core/Shell Type Photocatalyst for Water Purification. *J. Nanosci. Nanotechnol.*, 16(9):9273–9277, 2016-09-01T00:00:00//. doi: 10.1166/jnn.2016.12894.
- [139] Sihui Zhan, Dairong Chen, Xiuling Jiao, and Yang Song. Mesoporous TiO₂/SiO₂ composite nanofibers with selective photocatalytic properties. *Chem. Commun.*, 0(20):2043–2045, May 2007. ISSN 1364-548X. doi: 10.1039/B618905A.
- [140] Peter Nadrah, Miran Gaberšček, and Andrijana Sever Škapin. Selective degradation of model pollutants in the presence of core@shell TiO₂@SiO₂ photocatalyst. *Appl. Surf. Sci.*, 405:389–394, May 2017. ISSN 0169-4332. doi: 10.1016/j.apsusc.2017.02.058.
- [141] Tahereh Gholami, Mehdi Bazarganipour, Masoud Salavati-Niasari, and Samira Bagheri. Photocatalytic degradation of methylene blue on TiO₂@SiO₂ core/shell nanoparticles: Synthesis and characterization. *J. Mater. Sci.: Mater. Electron.*, 26(8):6170–6177, August 2015. ISSN 1573-482X. doi: 10.1007/s10854-015-3198-6.
- [142] Iqbal Ahmed Siddiquey, Takeshi Furusawa, Masahide Sato, Kozue Honda, and Noboru Suzuki. Control of the photocatalytic activity of TiO₂ nanoparticles by silica coating with polydiethoxysiloxane. *Dyes Pigm.*, 76(3):754–759, January 2008. ISSN 0143-7208. doi: 10.1016/j.dyepig.2007.01.020.
- [143] F. B. Li, X. Z. Li, M. F. Hou, K. W. Cheah, and W. C. H. Choy. Enhanced photocatalytic activity of Ce³⁺-TiO₂ for 2-mercaptobenzothiazole degradation in aqueous suspension for odour control. *Appl. Catal., A*, 285(1):181–189, May 2005. ISSN 0926-860X. doi: 10.1016/j.apcata.2005.02.025.

- [144] Wei Zhong, Ting Jiang, Yanliu Dang, Junkai He, Sheng-Yu Chen, Chung-Hao Kuo, David Kriz, Yongtao Meng, Andrew G. Meguerdichian, and Steven L. Suib. Mechanism studies on methyl orange dye degradation by perovskite-type $\text{LaNiO}_3\text{-}\delta$ under dark ambient conditions. *Appl. Catal., A*, 549:302–309, January 2018. doi: 10.1016/j.apcata.2017.10.013.
- [145] Ranfang Zuo, Gaoxiang Du, Weiwei Zhang, Lianhua Liu, Yanming Liu, Lefu Mei, and Zhaohui Li. Photocatalytic degradation of methylene blue using TiO_2 impregnated diatomite. *Adv. Mater. Sci. Eng.*, 2014:1–7, 2014. ISSN 1687-8434. doi: 10.1155/2014/170148.
- [146] Q. Y. Li, Y. F. Chen, D. D. Zeng, W. M. Gao, and Z. J. Wu. Photocatalytic characterization of silica coated titania nanoparticles with tunable coatings. *J. Nanopart. Res.*, 7(2):295–299, June 2005. ISSN 1572-896X. doi: 10.1007/s11051-004-5944-1.
- [147] Biswas Pratim Wei-Ning and Soulis Wang Johnathon, Yang Y. Jeffrey. Comparison of CO_2 photoreduction systems: A review. *Aerosol Air Qual. Res.*, 14(2): 533–549, 2014. ISSN 1680-8584. doi: 10.4209/aaqr.2013.09.0283.
- [148] Matumuene Joe Ndolomingo and Reinout Meijboom. Kinetic analysis of catalytic oxidation of methylene blue over $\gamma\text{-Al}_2\text{O}_3$ supported copper nanoparticles. *Appl. Catal., A*, 506:33–43, October 2015. ISSN 0926-860X. doi: 10.1016/j.apcata.2015.08.036.
- [149] M. Arab Chamjangali, G. Bagherian, A. Javid, S. Boroumand, and N. Farzaneh. Synthesis of Ag-ZnO with multiple rods (multipods) morphology and its application in the simultaneous photo-catalytic degradation of methyl orange and methylene blue. *Spectrochim. Acta, Part A*, 150:230–237, November 2015. ISSN 1386-1425. doi: 10.1016/j.saa.2015.05.067.
- [150] Erik Luebke. *Synthesis of Silica-coated TiO_2 Nanoparticles and the Characterisation of their Photocatalytic Properties*. Technical University of Vienna, 2019. Bachelor Thesis.
- [151] Harrison S. Kibombo, Rui Peng, Shivatharsiny Rasalingam, and Ranjit T. Koodali. Versatility of heterogeneous photocatalysis: Synthetic methodologies epitomizing the role of silica support in TiO_2 based mixed oxides. *Catal. Sci. Technol.*, 2(9):1737–1766, August 2012. ISSN 2044-4761. doi: 10.1039/C2CY20247F.

- [152] Nattaya Comsup, Joongjai Panpranot, and Piyasan Prasertthdam. The influence of Si-modified TiO₂ on the activity of Ag/TiO₂ in CO oxidation. *J Ind Eng Chem*, 16(5):703–707, September 2010. doi: 10.1016/j.jiec.2010.07.015.
- [153] Changhua An, Sheng Peng, and Yugang Sun. Facile synthesis of sunlight-driven AgCl:ag plasmonic nanophotocatalyst. *Advanced Materials*, 22(23):2570–2574, May 2010. doi: 10.1002/adma.200904116.
- [154] Chihiro Yogi, Kazuo Kojima, Noriyuki Wada, Hiroshi Tokumoto, Tomoo Takai, Tadashi Mizoguchi, and Hitoshi Tamiaki. Photocatalytic degradation of methylene blue by TiO₂ film and au particles-TiO₂ composite film. *Thin Solid Films*, 516(17):5881–5884, July 2008. doi: 10.1016/j.tsf.2007.10.050.
- [155] Li Li, Methira Krissanasaerane, Sebastian W. Pattinson, Morgan Stefik, Ulrich Wiesner, Ullrich Steiner, and Dominik Eder. Enhanced photocatalytic properties in well-ordered mesoporous WO₃. *Chem. Commun.*, 46(40):7620–7622, October 2010. ISSN 1364-548X. doi: 10.1039/C0CC01237H.
- [156] M. Gouamid, M. R. Ouahrani, and M. B. Bensaci. Adsorption Equilibrium, Kinetics and Thermodynamics of Methylene Blue from Aqueous Solutions using Date Palm Leaves. *Enrgy Proced*, 36:898–907, January 2013. ISSN 1876-6102. doi: 10.1016/j.egypro.2013.07.103.
- [157] Zhijian Wu, Ik-Sung Ahn, Yanxin Lin, Liyao Huang, Xinren Lan, and Kangtaek Lee. Methyl orange adsorption by microporous and mesoporous TiO₂-SiO₂ and TiO₂-SiO₂-Al₂O₃ composite xerogels. *Compos. Interfaces*, 11(2):205–212, January 2004. ISSN 0927-6440. doi: 10.1163/156855404322971459.
- [158] Jeremy A. Bau and Kazuhiro Takanabe. Ultrathin Microporous SiO₂ Membranes Photodeposited on Hydrogen Evolving Catalysts Enabling Overall Water Splitting. *ACS Catal.*, 7(11):7931–7940, November 2017. doi: 10.1021/acscatal.7b03017.
- [159] Alfred B. Anderson and Haleema Aied Asiri. Reversible potentials for steps in methanol and formic acid oxidation to CO₂ adsorption energies of intermediates on the ideal electrocatalyst for methanol oxidation and CO₂ reduction. *Phys. Chem. Chem. Phys.*, 16(22):10587–10599, 2014. doi: 10.1039/c3cp54837f.
- [160] Muhammad Shakeel, Muhammad Arif, Ghulam Yasin, Baoshan Li, Arif Ullah Khan, Faheem Ullah Khan, and Musa Kaleem Baloch. Hollow mesoporous architecture: A high performance bi-functional photoelectrocatalyst for overall

- water splitting. *Electrochim. Acta*, 268:163–172, April 2018. ISSN 0013-4686. doi: 10.1016/j.electacta.2018.02.024.
- [161] J.J. Murcia, J.A. Navío, and M.C. Hidalgo. Insights towards the influence of Pt features on the photocatalytic activity improvement of TiO₂ by platinisation. *Appl. Catal., B*, 126:76–85, September 2012. doi: 10.1016/j.apcatb.2012.07.013.
- [162] Alexey S. Cherevan, Leonie Deilmann, Tobias Weller, Dominik Eder, and Roland Marschall. Mesoporous semiconductors: A new model to assess accessible surface area and increased photocatalytic activity? *ACS Appl. Energy Mater.*, 1(11):5787–5799, October 2018. doi: 10.1021/acsaem.8b01123.
- [163] H. Ahmad, S.K. Kamarudin, L.J. Minggu, and M. Kassim. Hydrogen from photo-catalytic water splitting process: A review. *Ren. Sust. Energ. Rev.*, 43: 599–610, March 2015. doi: 10.1016/j.rser.2014.10.101.
- [164] Greta M. Haselmann and Dominik Eder. Early-Stage Deactivation of Platinum-Loaded TiO₂ Using In Situ Photodeposition during Photocatalytic Hydrogen Evolution. *ACS Catal.*, 7(7):4668–4675, July 2017. doi: 10.1021/acscatal.7b00845.
- [165] Bastian Mei, Kai Han, and Guido Mul. Driving surface redox reactions in heterogeneous photocatalysis: The active state of illuminated semiconductor-supported nanoparticles during overall water-splitting. *ACS Catal.*, 8(10):9154–9164, August 2018. doi: 10.1021/acscatal.8b02215.
- [166] Ekaterina A. Kozlova, Tatyana P. Lyubina, Maxim A. Nasalevich, Alexander V. Vorontsov, Alexander V. Miller, Vasily V. Kaichev, and Valentin N. Parmon. Influence of the method of platinum deposition on activity and stability of Pt/TiO₂ photocatalysts in the photocatalytic oxidation of dimethyl methylphosphonate. *Catal. Commun.*, 12(7):597–601, March 2011. doi: 10.1016/j.catcom.2010.12.007.
- [167] Gian Luca Chiarello, Myriam H. Aguirre, and Elena Selli. Hydrogen production by photocatalytic steam reforming of methanol on noble metal-modified TiO₂. *J. Catal.*, 273(2):182–190, July 2010. doi: 10.1016/j.jcat.2010.05.012.
- [168] J. G. Highfield, M. H. Chen, P. T. Nguyen, and Z. Chen. Mechanistic investigations of photo-driven processes over TiO₂ by in-situ DRIFTS-MS: Part 1. Platinization and methanol reforming. *Energy & Environmental Science*, 2(9): 991, 2009. doi: 10.1039/b907781m.

- [169] Gábor Schubert, Tamás Bánsági, and Frigyes Solymosi. Photocatalytic decomposition of methyl formate over TiO₂-supported pt metals. *J. Phys. Chem. C*, 117(44):22797–22804, October 2013. doi: 10.1021/jp406840n.
- [170] Mohamad El-Roz, Philippe Bazin, Marco Daturi, and Frederic Thibault-Starzyk. On the mechanism of methanol photooxidation to methylformate and carbon dioxide on TiO₂: an operando-FTIR study. *Phys. Chem. Chem. Phys.*, 17(17):11277–11283, 2015. doi: 10.1039/c5cp00726g.
- [171] You Han, Chang jun Liu, and Qingfeng Ge. Effect of Pt clusters on methanol adsorption and dissociation over perfect and defective anatase TiO₂(101) surface. *J. Phys. Chem. C*, 113(48):20674–20682, November 2009. doi: 10.1021/jp907399j.
- [172] Tao Chen, Zhaochi Feng, Guopeng Wu, Jianying Shi, Guijun Ma, Pinliang Ying, and Can Li. Mechanistic studies of photocatalytic reaction of methanol for hydrogen production on Pt/TiO₂ by in-situ fourier transform IR and time-resolved IR spectroscopy. *J. Phys. Chem. C*, 111(22):8005–8014, June 2007. doi: 10.1021/jp071022b.
- [173] Akira Yamakata, Taka aki Ishibashi, and Hiroshi Onishi. Pressure dependence of electron- and hole-consuming reactions in photocatalytic water splitting on Pt/TiO₂ studied by time-resolved IR absorption spectroscopy. *Int. J. Photoenergy*, 5(1):7–9, 2003. doi: 10.1155/s1110662x03000047.
- [174] Krzysztof Czupryn, Ireneusz Kocemba, and Jacek Rynkowski. Photocatalytic CO oxidation with water over Pt/TiO₂ catalysts. *React. Kinet., Mech. Catal.*, 124(1):187–201, December 2017. doi: 10.1007/s11144-017-1334-4.
- [175] Huiting Huang, Jianyong Feng, Song Zhang, Hongna Zhang, Xin Wang, Tao Yu, Chuncheng Chen, Zhiguo Yi, Jinhua Ye, Zhaosheng Li, and Zhigang Zou. Molecular-level understanding of the deactivation pathways during methanol photo-reforming on Pt-decorated TiO₂. *Appl. Catal., B*, 272:118980, September 2020. doi: 10.1016/j.apcatb.2020.118980.
- [176] Ayman D. Allian, Kazuhiro Takanabe, Kyle L. Furdala, Xianghong Hao, Timothy J. Truex, Juan Cai, Corneliu Buda, Matthew Neurock, and Enrique Iglesia. Chemisorption of CO and mechanism of CO oxidation on supported platinum nanoclusters. *J. Am. Chem. Soc.*, 133(12):4498–4517, March 2011. doi: 10.1021/ja110073u.

- [177] Y. Ji, A. Vandereerden, V. Koot, P. Kooyman, J. Meeldijk, B. Weckhuysen, and D. Koningsberger. Influence of support ionicity on the hydrogen chemisorption of Pt particles dispersed in γ zeolite: Consequences for Pt particle size determination using the H/M method. *J. Catal.*, 234(2):376–384, September 2005. doi: 10.1016/j.jcat.2005.06.030.
- [178] Svetlana Schauer mann, Niklas Nilius, Shamil Shaikhutdinov, and Hans-Joachim Freund. Nanoparticles for heterogeneous catalysis: New mechanistic insights. *Acc. Chem. Res.*, 46(8):1673–1681, December 2012. doi: 10.1021/ar300225s.
- [179] Theophilos Ioannides and Xenophon E. Verykios. Charge transfer in metal catalysts supported on doped TiO_2 : A theoretical approach based on metal–semiconductor contact theory. *J. Catal.*, 161(2):560–569, July 1996. doi: 10.1006/jcat.1996.0218.
- [180] S. J. Tauster, S. C. Fung, R. T. K. Baker, and J. A. Horsley. Strong interactions in supported-metal catalysts. *Science*, 211(4487):1121–1125, March 1981. doi: 10.1126/science.211.4487.1121.
- [181] W. M. Haynes. *CRC Handbook of Chemistry and Physics, 92nd Edition*. CRC Press, June 2011. doi: 10.1201/b17379.
- [182] L. Z. Mezey and J. Giber. The surface free energies of solid chemical elements: Calculation from internal free enthalpies of atomization. *Jpn. J. Appl. Phys.*, 21 (Part 1, No. 11):1569–1571, November 1982. doi: 10.1143/jjap.21.1569.
- [183] Qiang Fu, Thomas Wagner, Sven Olliges, and Heinz-Dieter Carstanjen. Metal-oxide interfacial reactions: Encapsulation of Pd on $\text{TiO}_2(110)$. *J. Phys. Chem. B*, 109(2):944–951, January 2005. doi: 10.1021/jp046091u.
- [184] Anupama Shivamurthy, Prashanth G R, Renukappa N M, Sundara Rajan J, and Parameshwara S. Study of surface energy of SiO_2 and TiO_2 on charge carrier mobility of rubrene organic field effect transistor. In *Proceedings of the 3rd International Conference on Theoretical and Applied Nanoscience and Nanotechnology (TANN'19)*. Avestia Publishing, June 2019. doi: 10.11159/tann19.135.
- [185] Wilfrid Jochum, Dominik Eder, Gernot Kaltenhauser, and Reinhard Kramer. Impedance measurements in catalysis: Charge transfer in titania supported noble metal catalysts. *Top. Catal.*, 46(1):49–55, September 2007. ISSN 1572-9028. doi: 10.1007/s11244-007-0314-8.

- [186] Felipe Polo-Garzon, Thomas F. Blum, Zhenghong Bao, Kristen Wang, Victor Fung, Zhennan Huang, Elizabeth E. Bickel, De en Jiang, Miaofang Chi, and Zili Wu. In-situ strong metal–support interaction (SMSI) affects catalytic alcohol conversion. *ACS Catal.*, 11(4):1938–1945, January 2021. doi: 10.1021/acscatal.0c05324.
- [187] Kazuhiro Sayama and Hironori Arakawa. Effect of carbonate salt addition on the photocatalytic decomposition of liquid water over Pt–TiO₂ catalyst. *J. Chem. Soc., Faraday Trans.*, 93(8):1647–1654, 1997. doi: 10.1039/a607662i.
- [188] Liang-Yi Lin, Shalinee Kavadiya, Xiang He, Wei-Ning Wang, Bedia Begum Karakocak, Yu-Chih Lin, Mikhail Y. Berezin, and Pratim Biswas. Engineering stable Pt nanoparticles and oxygen vacancies on defective TiO₂ via introducing strong electronic metal-support interaction for efficient CO₂ photoreduction. *Chem. Eng. J.*, 389:123450, June 2020. doi: 10.1016/j.cej.2019.123450.
- [189] Tepin Hengsawad, Tossaporn Jindarat, Daniel E. Resasco, and Siriporn Jongpatiwut. Synergistic effect of oxygen vacancies and highly dispersed pd nanoparticles over Pd-loaded TiO₂ prepared by a single-step sol–gel process for deoxygenation of triglycerides. *Appl. Catal., A*, 566:74–86, September 2018. doi: 10.1016/j.apcata.2018.08.007.
- [190] A. J. Simoens, R. T. K. Baker, D. J. Dwyer, C. R. F. Lund, and R. J. Madon. A study of the nickel-titanium oxide interaction. *J. Catal.*, 86(2):359–372, April 1984. doi: 10.1016/0021-9517(84)90381-6.
- [191] J.C Yang, Y.C Kim, Y.G Shul, C.H Shin, and T.K Lee. Characterization of photoreduced and decomposition of dichloroacetic acid over photoreduced catalysts. *Appl. Surf. Sci.*, 121-122:525–529, November 1997. doi: 10.1016/s0169-4332(97)00359-0.
- [192] Alexander V Vorontsov, Evgueni N Savinov, and Jin Zhensheng. Influence of the form of photodeposited platinum on titania upon its photocatalytic activity in CO and acetone oxidation. *J. Photochem. Photobiol., A*, 125(1-3):113–117, August 1999. doi: 10.1016/s1010-6030(99)00073-8.
- [193] Jean Marie Herrmann, Jean Disdier, and Pierre Pichat. Photoassisted platinum deposition on TiO₂ powder using various platinum complexes. *The Journal of Physical Chemistry*, 90(22):6028–6034, October 1986. doi: 10.1021/j100280a114.

- [194] Hiroshi Yoneyama, Naritoshi Nishimura, and Hideo Tamura. Photodeposition of palladium and platinum onto titanium dioxide single crystals. *The Journal of Physical Chemistry*, 85(3):268–272, February 1981. doi: 10.1021/j150603a010.
- [195] Yu Hang Li, Jun Xing, Zong Jia Chen, Zhen Li, Feng Tian, Li Rong Zheng, Hai Feng Wang, P. Hu, Hui Jun Zhao, and Hua Gui Yang. Unidirectional suppression of hydrogen oxidation on oxidized platinum clusters. *Nat. Commun.*, 4(1), September 2013. doi: 10.1038/ncomms3500.
- [196] Yun Zhou, Christopher L. Muhich, Brian T. Neltner, Alan W. Weimer, and Charles B. Musgrave. Growth of Pt particles on the anatase $\text{TiO}_2(101)$ surface. *J. Phys. Chem. C*, 116(22):12114–12123, May 2012. doi: 10.1021/jp302273m.
- [197] Søren Bredmose Simonsen, Ib Chorkendorff, Søren Dahl, Magnus Skoglundh, Jens Sehested, and Stig Helveg. Ostwald ripening in a Pt/SiO₂ model catalyst studied by in-situ TEM. *J. Catal.*, 281(1):147–155, July 2011. doi: 10.1016/j.jcat.2011.04.011.
- [198] S. Gan, A. El-azab, and Y. Liang. Formation and diffusion of Pt nanoclusters on highly corrugated anatase $\text{TiO}_2(001)-(1\times 4)$ surface. *Surf. Sci.*, 479(1-3):L369–L374, May 2001. doi: 10.1016/s0039-6028(01)01009-3.
- [199] Huan Qiu, Xujun Ma, Chunyu Sun, Bin Zhao, and Feng Chen. Surface oxygen vacancies enriched Pt/TiO₂ synthesized with a defect migration strategy for superior photocatalytic activity. *Appl. Surf. Sci.*, 506:145021, March 2020. doi: 10.1016/j.apsusc.2019.145021.
- [200] Nathan Daelman, Franziska Simone Hegner, Marcos Rellán-Piñeiro, Marçal Capdevila-Cortada, Rodrigo García-Muelas, and Núria López. Quasi-degenerate states and their dynamics in oxygen deficient reducible metal oxides. *J. Chem. Phys.*, 152(5):050901, February 2020. doi: 10.1063/1.5138484.
- [201] Jingyue Jimmy Liu. Advanced electron microscopy of metal-support interactions in supported metal catalysts. *ChemCatChem*, 3(6):934–948, June 2011. doi: 10.1002/cctc.201100090.
- [202] Xiao Jiang, Xiaowa Nie, Xinwen Guo, Chunshan Song, and Jingguang G. Chen. Recent advances in carbon dioxide hydrogenation to methanol via heterogeneous catalysis. *Chem. Rev.*, 120(15):7984–8034, February 2020. doi: 10.1021/acs.chemrev.9b00723.

- [203] Junyan Ding, Yingju Yang, Jing Liu, and Zhen Wang. Catalytic reaction mechanism of formaldehyde oxidation by oxygen species over Pt/TiO₂ catalyst. *Chemosphere*, 248:125980, June 2020. doi: 10.1016/j.chemosphere.2020.125980.
- [204] R. Schaub, P. Thstrup, N. Lopez, E. Lægsgaard, I. Stensgaard, J. K. Nørskov, and F. Besenbacher. Oxygen vacancies as active sites for water dissociation on Rutile TiO₂(110). *Phys. Rev. Lett.*, 87(26), December 2001. doi: 10.1103/physrevlett.87.266104.
- [205] Gabriel Jeantelot, Muhammad Qureshi, Moussab Harb, Samy Ould-Chikh, Dalaver H. Anjum, Edy Abou-Hamad, Antonio Aguilar-Tapia, Jean-Louis Hazemann, Kazuhiro Takanabe, and Jean-Marie Basset. TiO₂-supported Pt single atoms by surface organometallic chemistry for photocatalytic hydrogen evolution. *Phys. Chem. Chem. Phys.*, 21(44):24429–24440, 2019. doi: 10.1039/c9cp04470a.
- [206] J.J. Murcia, M.C. Hidalgo, J.A. Navío, V. Vaiano, P. Ciambelli, and D. Sanino. Ethanol partial photooxidation on Pt/TiO₂ catalysts as green route for acetaldehyde synthesis. *Catal. Today*, 196(1):101–109, November 2012. doi: 10.1016/j.cattod.2012.02.033.
- [207] L. Piccolo, P. Afanasiev, F. Morfin, T. Len, C. Dessal, J. L. Rousset, M. Aouine, F. Bourgain, A. Aguilar-Tapia, O. Proux, Y. Chen, L. Soler, and J. Llorca. Operando X-ray absorption spectroscopy investigation of photocatalytic hydrogen evolution over ultradispersed Pt/TiO₂ catalysts. *ACS Catal.*, 10(21):12696–12705, October 2020. doi: 10.1021/acscatal.0c03464.
- [208] Anthony Martino, Allen G. Sault, Jeffrey S. Kawola, Elaine Boespflug, and Mark L.F. Phillips. A sintering study of novel sol–gel-based nanocluster catalysts. *J. Catal.*, 187(1):30–38, October 1999. doi: 10.1006/jcat.1999.2614.
- [209] B.A. Sexton, A.E. Hughes, and K. Foger. Xps investigation of strong metal-support interactions on group iii-a–va oxides. *J. Catal.*, 77(1):85–93, 1982. ISSN 0021-9517. doi: [https://doi.org/10.1016/0021-9517\(82\)90149-X](https://doi.org/10.1016/0021-9517(82)90149-X).
- [210] Kohki Ebitani and Hideshi Hattori. Combined temperature-programmed reduction (TPR)- temperature-programmed desorption (TPD) study of supported platinum catalysts. *Bull. Chem. Soc. Jpn.*, 64(8):2422–2427, August 1991. doi: 10.1246/bcsj.64.2422.

- [211] C. Nützenadel, A. Züttel, D. Chartouni, G. Schmid, and L. Schlapbach. Critical size and surface effect of the hydrogen interaction of palladium clusters. *The European Physical Journal D - Atomic, Molecular and Optical Physics*, 8(2): 245–250, January 2000. doi: 10.1007/s100530050033.
- [212] L. Gomathi Devi and R. Kavitha. A review on plasmonic metal TiO₂ composite for generation, trapping, storing and dynamic vectorial transfer of photogenerated electrons across the schottky junction in a photocatalytic system. *Appl. Surf. Sci.*, 360:601–622, January 2016. doi: 10.1016/j.apsusc.2015.11.016.
- [213] Jian Chen, David F. Ollis, Wim H. Rulkens, and Harry Bruning. Photocatalyzed oxidation of alcohols and organochlorides in the presence of native TiO₂ and metallized TiO₂ suspensions. Part (II): Photocatalytic mechanisms. *Water Res.*, 33(3):669–676, 1999. ISSN 0043-1354. doi: [https://doi.org/10.1016/S0043-1354\(98\)00262-0](https://doi.org/10.1016/S0043-1354(98)00262-0).
- [214] Chuan yi Wang, Henning Groenzin, and Mary Jane Shultz. Direct observation of competitive adsorption between methanol and water on TiO₂: an in situ sum-frequency generation study. *J. Am. Chem. Soc.*, 126(26):8094–8095, June 2004. doi: 10.1021/ja048165l.
- [215] Susan Mitroka, Stephanie Zimmeck, Diego Troya, and James M. Tanko. How solvent modulates hydroxyl radical reactivity in hydrogen atom abstractions. *J. Am. Chem. Soc.*, 132(9):2907–2913, March 2010. ISSN 0002-7863. doi: 10.1021/ja903856t.
- [216] Juan C. Colmenares, Weiyi Ouyang, Manuel Ojeda, Ewelina Kuna, Olga Chernyayeva, Dmytro Lisovytskiy, Sudipta De, Rafael Luque, and Alina M. Balu. Mild ultrasound-assisted synthesis of TiO₂ supported on magnetic nanocomposites for selective photo-oxidation of benzyl alcohol. *Appl. Catal., B*, 183:107–112, April 2016. ISSN 0926-3373. doi: 10.1016/j.apcatb.2015.10.034.
- [217] Marta Bettoni, Pietro Candori, Fabio Marmottini, Nicoletta Perenze, Cesare Rol, Giovanni V. Sebastiani, and Franco Vecchiocattivi. Photocatalytic activity in CH₃CN related to the surface properties of TiO₂ powders prepared by sol-gel method. *Int J Photoenergy*, 2009:1–6, 2009. doi: 10.1155/2009/905987.
- [218] Marye Anne Fox and Maria T Dulay. Heterogeneous photocatalysis. *Chemical reviews*, 93(1):341–357, 1993.

Bibliography

- [219] Omima S. Mohamed, Abd El-Aal M. Gaber, and A.A. Abdel-Wahab. Photocatalytic oxidation of selected aryl alcohols in acetonitrile. *J. Photochem. Photobiol., A*, 148(1-3):205–210, May 2002. doi: 10.1016/s1010-6030(02)00044-8.
- [220] Peter Linstrom. NIST Chemistry WebBook, NIST Standard Reference Database 69, 1997.
- [221] Branislav Jovic, Jovana Ajdukovic, Evgenija Djurendic, and Aleksandar Nikolic. FTIR investigation of solvent-induced carbonyl band shifts of 17 β -hydroxy-17 α -picolyl-androst-4-en-3-one. *Acta Periodica Technologica*, 45: 191–199, 2014. doi: 10.2298/apt1445191j.
- [222] Sigma Aldrich. IR Spectrum Table & Chart, 2021. URL <https://www.sigmaaldrich.com/technical-documents/articles/biology/ir-spectrum-table.html>.
- [223] C. Narasigadu, J. D. Raal, P. Naidoo, and D. Ramjugernath. Ternary liquid-liquid equilibria of acetonitrile and water with heptanoic acid and nonanol at 323.15 K and 1 atm. *Journal of Chemical & Engineering Data*, 54(3):735–738, January 2009. doi: 10.1021/je800404f.
- [224] Tery L. Barr and Sudipta Seal. Nature of the use of adventitious carbon as a binding energy standard. *J. Vac. Sci. Technol., A*, 13(3):1239–1246, May 1995. doi: 10.1116/1.579868.

Appendix

Characterization of core-shell nanoparticles

TEM images of core-shell samples after upscaling the sol-gel synthesis

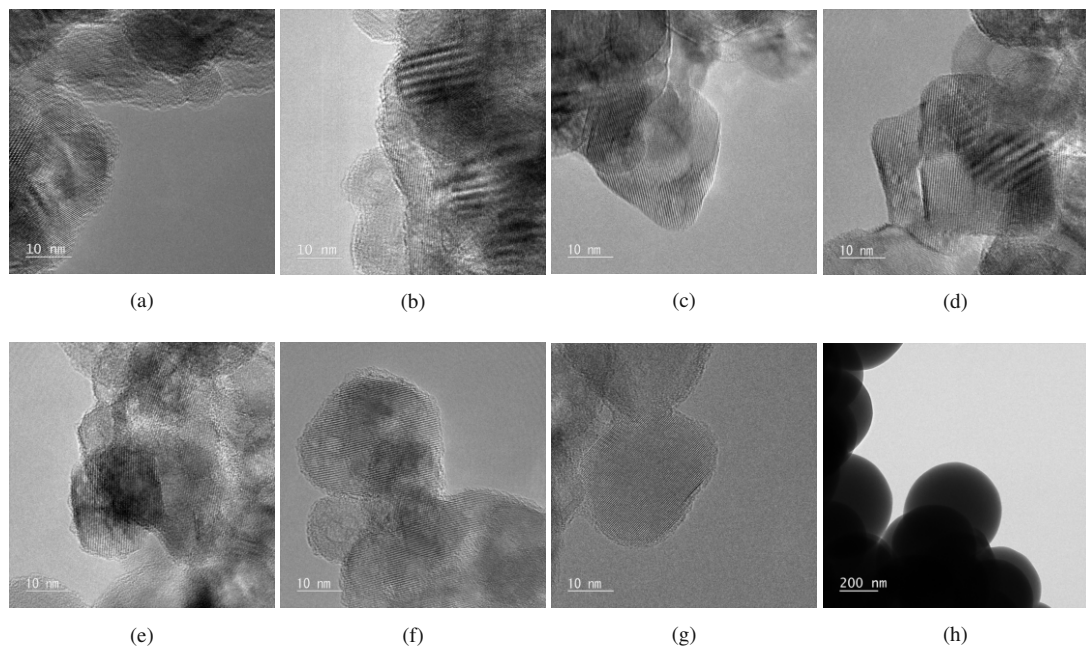


Figure A.1: Transmission electron microscopy (TEM) images of sol-gel TiO_2 – SiO_2 core-shell nanoparticles after upscaling the synthesis. (a) 2-step sample ${}^{2nd}\text{T}_{92}\text{S}_{28\%}^{\text{SG}5}$ has a thicker shell than $\text{T}_{92}\text{S}_{28\%}^{\text{SG}5}$; (b) 4-step ${}^{2nd}\text{T}_{92}\text{S}_{15\%}^{\text{SG}5}$ is similar to $\text{T}_{92}\text{S}_{15\%}^{\text{SG}5}$; (c) 1-step $\text{T}_{70}\text{S}_{3\%}^{\text{SG}5}$ has no visible layer; (d) 2-step $\text{T}_{70}\text{S}_{6\%}^{\text{SG}5}$ and (e) 3-step $\text{T}_{70}\text{S}_{9\%}^{\text{SG}5}$ have a patchy, visible layer, (f) 4-step $\text{T}_{70}\text{S}_{12\%}^{\text{SG}5}$ and (g) 5-step $\text{T}_{70}\text{S}_{14\%}^{\text{SG}5}$ have a thicker, more homogeneous layer that is a bit more patchy than in "core-shell SG set 1"; (h) is a pure SiO_2 reference sample.

PL emission spectra

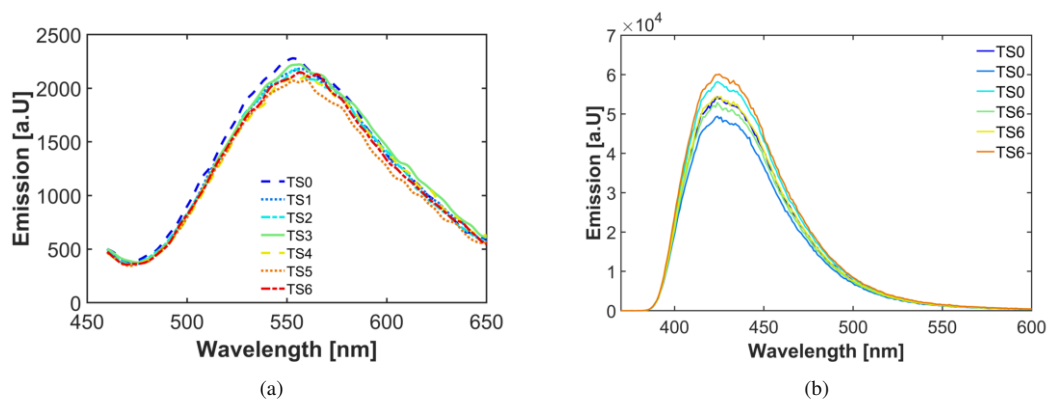


Figure A.2: Emission spectra of (a) the sample suspensions in pure water upon laser illumination at 378 nm; (b) terephthalic acid solution after Xe lamp illumination at 315 nm of selected sample suspensions of samples $T_{70}S0^{SG6}$ and $T_{70}S6^{SG6}$, each measured three times.

PL emission peak fits

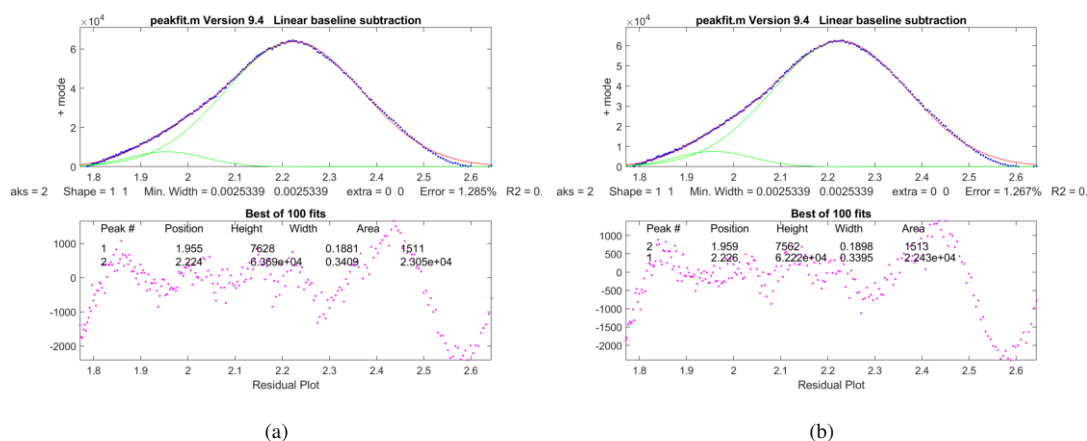


Figure A.3: Gaussian peakfits performed on photoluminescence emission spectra of (a) $T_{70}S0^{SG6}$ and (b) $T_{70}S2^{SG6}$. While those samples show the highest differences in PL lifetimes, their emission spectra are very similar, as are the peaks that were fitted to the signal.

EDX example spectrum

The EDX results show a) absence of any foreign impurities (Figure A.4), b) Si is well distributed over the entire sample and c) Si content increases with increasing number of steps.

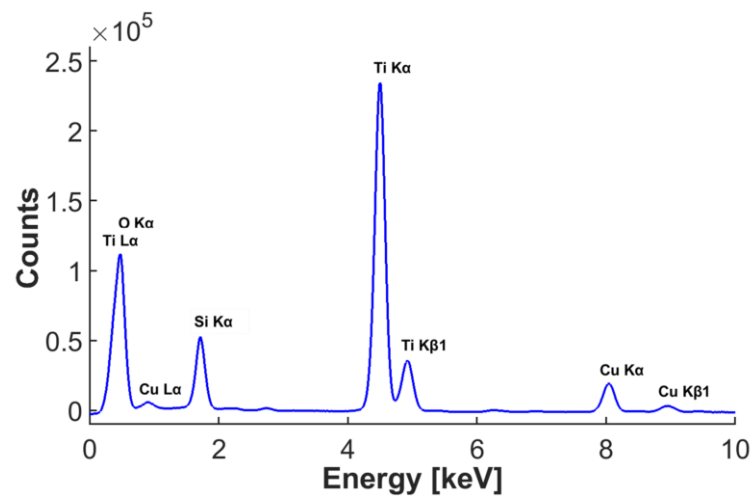


Figure A.4: Energy dispersive X-Ray spectrum of sample T₉₂S₄^{SG5}_{15%}.

XPS details and survey spectra

The chemical composition of the samples was obtained with X-ray photoelectron spectroscopy (XPS) using a custom-built SPECS XPS-spectrometer equipped with a monochromatized Al-K α X-ray source (μ 350) and a hemispherical WAL-150 analyzer (acceptance angle: 60 $^\circ$).

All samples were mounted onto the sample holder using double-sided carbon tape. Pass energies of 100 eV and 30 eV and energy resolutions of 1 eV and 100 meV were used for survey and detail spectra, respectively (excitation energy: 1486.6 eV, beam energy and spot size: 70 W onto 400 μ m, angle: 51 $^\circ$ to sample surface normal, base pressure: $5 \cdot 10^{-10}$ mbar, pressure during measurements: $2 \cdot 10^{-9}$ mbar).

To reduce charging effects, a broad-spot low energy electron source (SPECS FG 22 flood gun) was used for charge compensation in some samples. Data analysis was performed using CASA XPS software with Shirley backgrounds. Charge correction was applied so the adventitious carbon peak (C–C peak) was shifted to 284.8 eV binding energy (BE)²²⁴.

Table A.1: Details about peak positions and full width half maxima (FWHM) of the Ti 2p and Si 2p signals measured via XPS of sample set 2.

Sample	Ti 2p peak position [eV]	Ti 2p FWHM [eV]	Si 2p peak position [eV]	SI 2p FWHM [eV]
Ana ₇₀	458.66	1.06	-	-
T ₇₀ S1 ^{SG6} _{3%}	458.72	1.03	102.32	0.84
T ₇₀ S2 ^{SG6} _{6%}	458.76	1.05	102.44	1.16
T ₇₀ S4 ^{SG6} _{11%}	458.74	1.38	103.12	1.42
T ₇₀ S6 ^{SG6} _{16%}	459.09	1.37	103.25	1.63

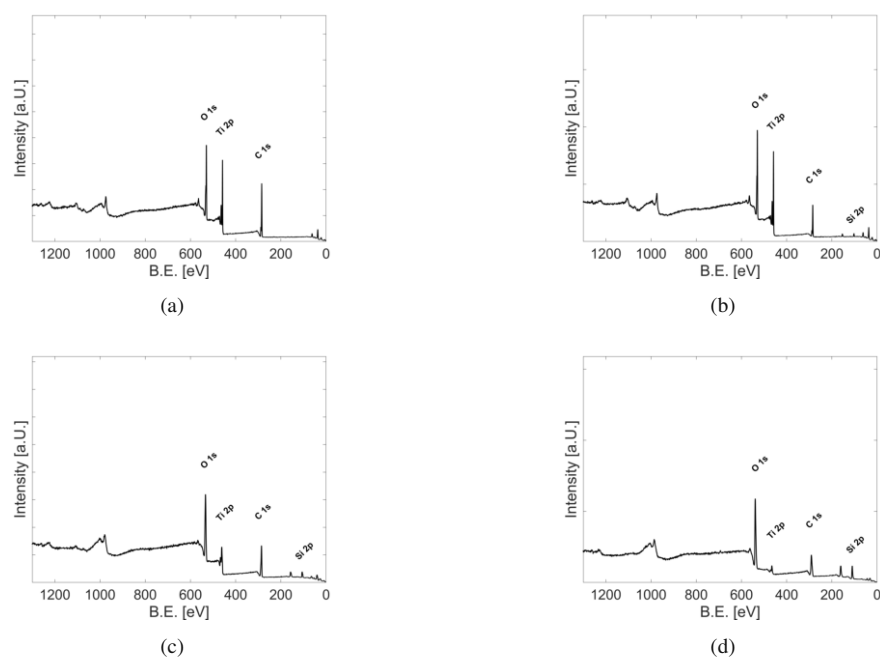


Figure A.5: Survey XPS spectra of the samples a) TS0, b) TS2, c) TS4, d) TS8 of sample set 1

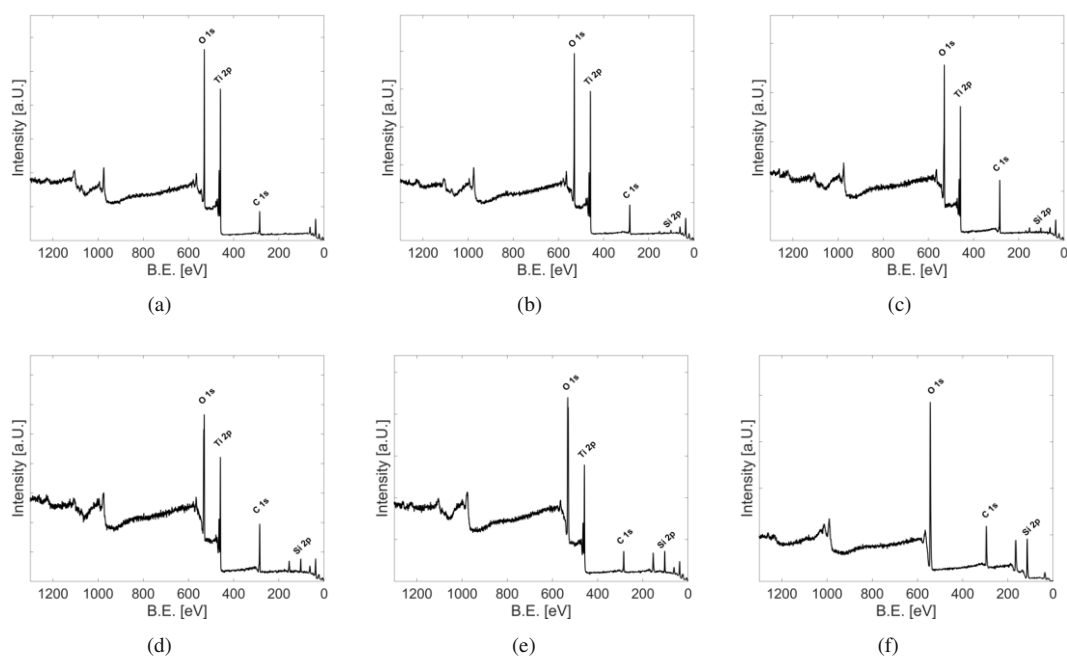
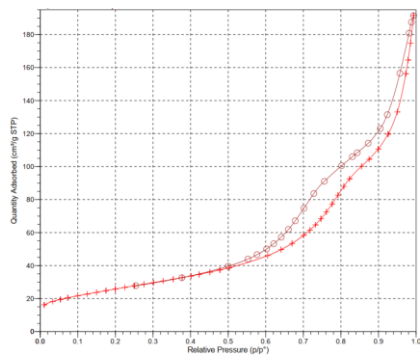
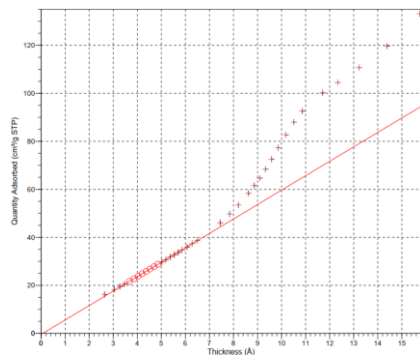


Figure A.6: Survey XPS spectra of the samples a) TS0, b) TS1, c) TS2, d) TS4, e) TS6 and f) S1 of sample set 2

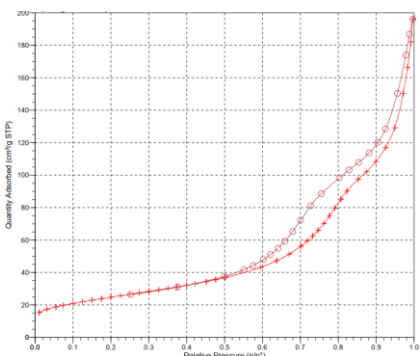
N₂ physisorption isotherms and t-plots



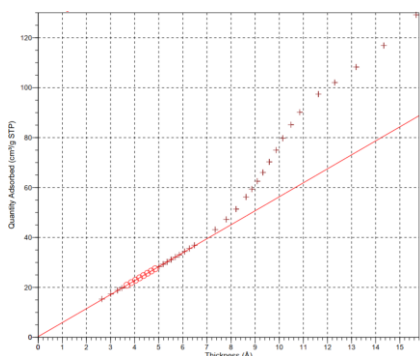
(a)



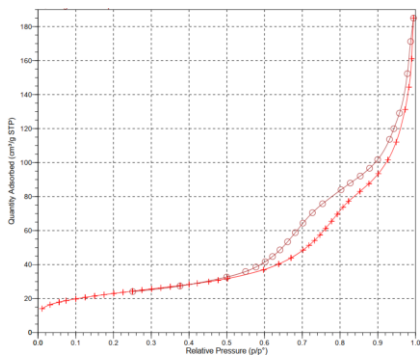
(b)



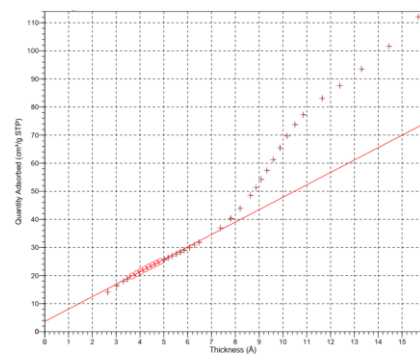
(c)



(d)



(e)



(f)

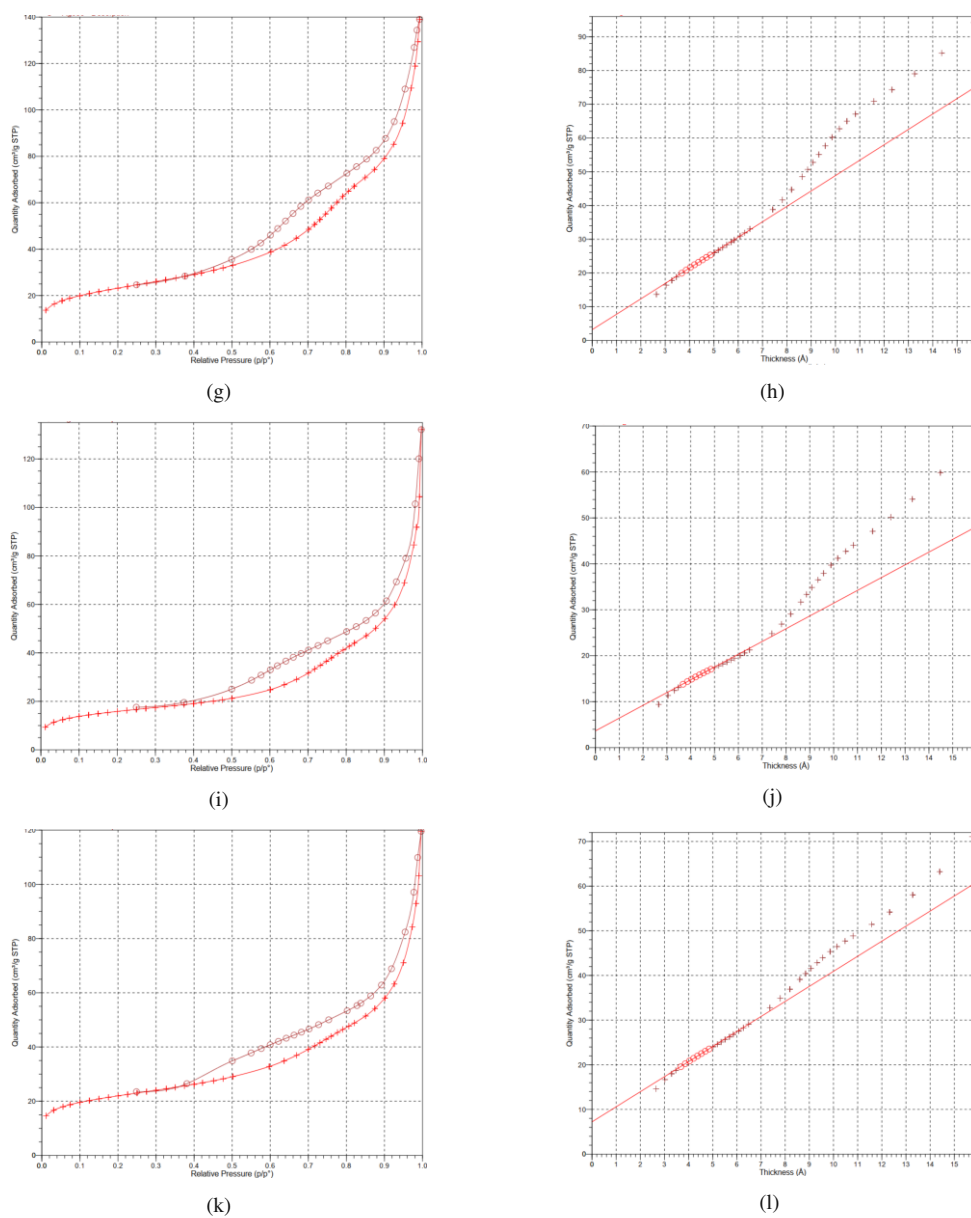
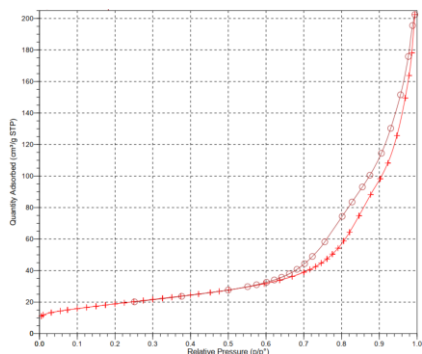
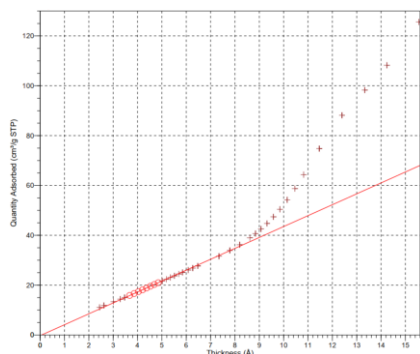


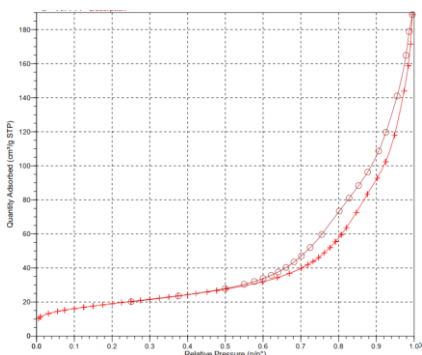
Figure A.7: N_2 physisorption isotherms and t-plots of sample set 1; (a) and (b) are the isotherms and t-plots of TS0, respectively; (c) and (d) are the isotherms and t-plots of TS1, respectively; (e) and (f) are the isotherms and t-plots of TS2, respectively; (g) and (h) are the isotherms and t-plots of TS3, respectively; (i) and (j) are the isotherms and t-plots of TS4, respectively; (k) and (l) are the isotherms and t-plots of TS5, respectively;



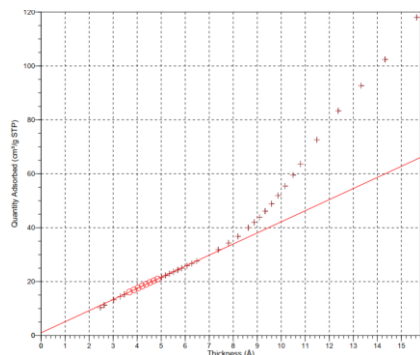
(a)



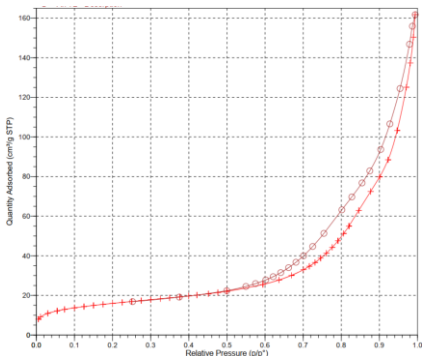
(b)



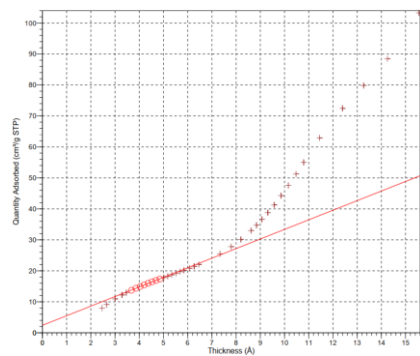
(c)



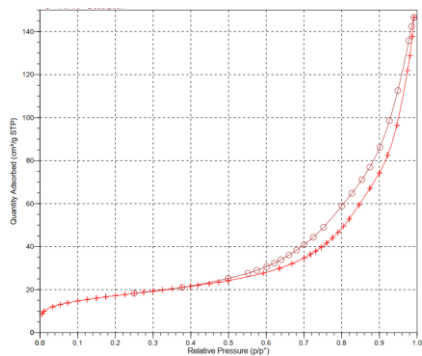
(d)



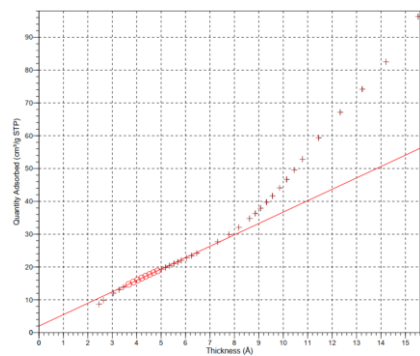
(e)



(f)



(g)



(h)

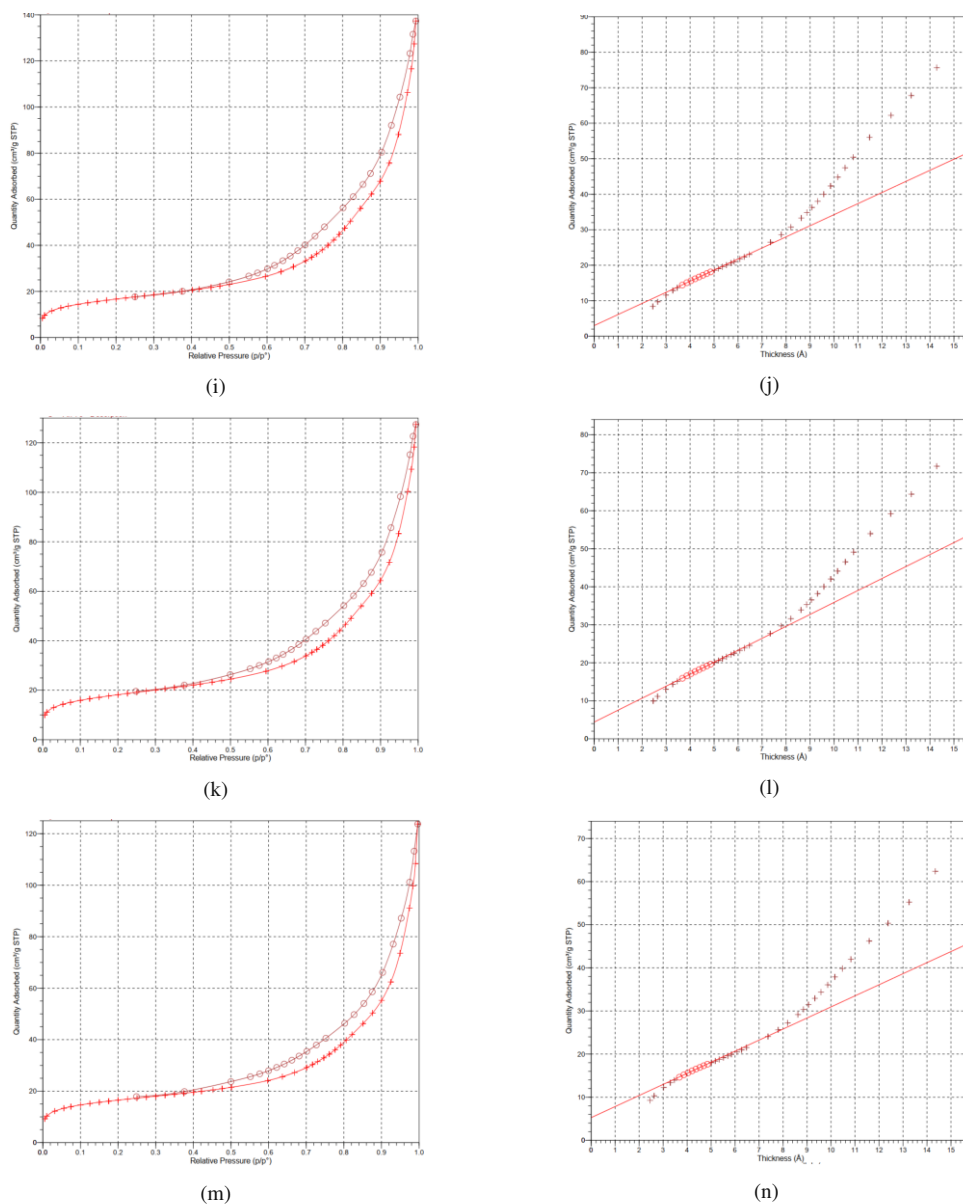


Figure A.8: N_2 physisorption isotherms and t-plots of sample set 2; (a) and (b) are the isotherms and t-plots of TS0, respectively; (c) and (d) are the isotherms and t-plots of TS1, respectively; (e) and (f) are the isotherms and t-plots of TS2, respectively; (g) and (h) are the isotherms and t-plots of TS3, respectively; (i) and (j) are the isotherms and t-plots of TS4, respectively; (k) and (l) are the isotherms and t-plots of TS5, respectively; (m) and (n) are the isotherms and t-plots of TS6, respectively;

Original UV-vis reflectance data

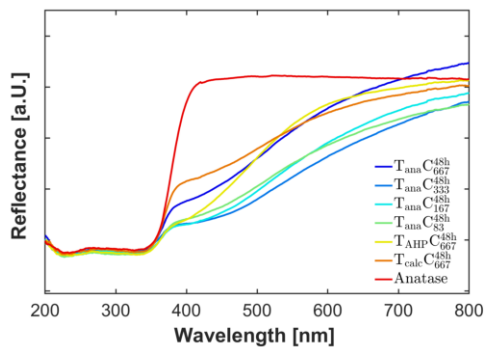


Figure A.9: Original data of the spectroscopic analysis to quantify the amount of calixarenes chemisorbed on the surface of Ana₉₂ after different synthesis methods.

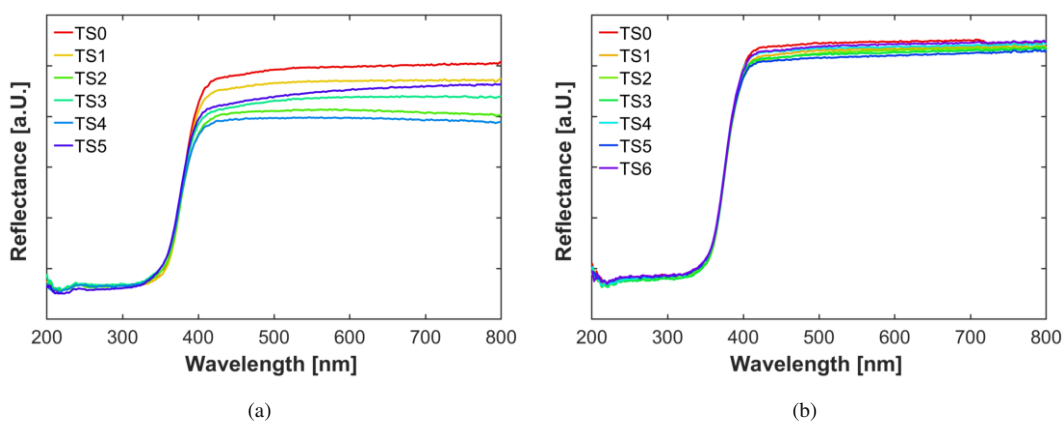


Figure A.10: Original DRS UV-vis reflectance data of sol-gel core-shell samples; (a) set 1; (b) set 2.

Deactivation with Pt/TiO₂ – SiO₂

Pt surface area

Determined values of the determined surface area of Pt NPs can be seen in [Table A.2](#), which were calculated according to the following equation:

$$A_{\text{tot}} = A_{\text{hs}} \cdot N = \frac{m}{\rho \cdot r} \quad (\text{A.1})$$

where A_{tot} is the total surface area, A_{hs} is the surface area of one hemispherical nanoparticle, N is the determined amount of nanoparticles, m is the measured mass of Pt, r is the mean measured radius, and ρ is the density of Pt.

Further details about the calculation can be found in [section 3.4.2](#).

Table A.2: The platinum amount determined via Total Reflection X-Ray Fluorescence (T-XRF). The Pt diameter was determined from TEM images (15 particles). The calculated surface area (A) used in an HER experiment is displayed in the last column.

Sample	Pt amount [wt. %]	Size [nm]	Calc. A 10 ⁻³ [m ²]
Pt/TS0	0.20 ± 0.02	1.7 ± 0.3	2.2 ± 0.2
Pt/TS1	0.22 ± 0.02	2.0 ± 0.5	2.1 ± 0.2
Pt/TS2	0.12 ± 0.01	2.1 ± 0.4	1.1 ± 0.1
Pt/TS3	0.16 ± 0.02	2.3 ± 0.7	1.3 ± 0.2
Pt/TS4	0.10 ± 0.01	2.7 ± 0.7	0.7 ± 0.1
Pt/TS5	0.10 ± 0.01	2.6 ± 0.6	0.7 ± 0.1
Pt/TS6	0.11 ± 0.01	3.0 ± 0.9	0.7 ± 0.1

HER activities of sample set 2

Table A.3: The activities at the maximum point and after 2.5 hours of illumination for each sample are displayed in this table. The activities normalized with the calculated Pt surface area as seen in Table 6.2 are shown as well.

Sample	Max. H ₂ activity [$\mu\text{mol} \cdot \text{h}^{-1}$]	After 2.5 hours [$\mu\text{mol} \cdot \text{h}^{-1}$]	Max. H ₂ activity norm. [$\mu\text{mol} \cdot \text{h}^{-1} \text{m}^{-2}$]	After 2.5 hours norm. [$\mu\text{mol} \cdot \text{h}^{-1} \text{m}^{-2}$]
Pt/TS0	365 ± 37	162 ± 2	1663 ± 170	739 ± 5
Pt/TS1	163 ± 15	121 ± 13	794 ± 74	589 ± 64
Pt/TS2	89 ± 2	76 ± 8	832 ± 24	709 ± 78
Pt/TS3	65 ± 2	53 ± 2	497 ± 14	411 ± 18
Pt/TS4	28 ± 6	23 ± 0	409 ± 92	329 ± 2
Pt/TS5	17 ± 1	12 ± 2	236 ± 12	163 ± 28
Pt/TS6	16 ± 5	10 ± 2	240 ± 66	148 ± 33

Table A.4: The activities at the maximum point and after 2.5 hours of illumination for each sample are displayed in this table. The activities normalized with the calculated Pt surface area as seen in Table 6.2 are shown as well.

Sample	Max. CO ₂ activity [$\mu\text{mol} \cdot \text{h}^{-1}$]	After 2.5 hours [$\mu\text{mol} \cdot \text{h}^{-1}$]	Max. CO activity [$\mu\text{mol} \cdot \text{h}^{-1} \text{m}^{-2}$]	After 2.5 hours [$\mu\text{mol} \cdot \text{h}^{-1} \text{m}^{-2}$]
Pt/TS0	1.93 ± 0.277	1.68 ± 0.229	0.28 ± 0.069	0.39 ± 0.083
Pt/TS1	1.08 ± 0.06	1 ± 0.082	0.13 ± 0.04	0.18 ± 0.039
Pt/TS2	0.83 ± 0.269	0.7 ± 0.083	0.04 ± 0.03	0.01 ± 0.008
Pt/TS3	0.59 ± 0.057	0.59 ± 0.027	0.07 ± 0.04	0.1 ± 0.031
Pt/TS4	0.46 ± 0.057	0.36 ± 0.131	0.03 ± 0.026	0.04 ± 0.023
Pt/TS5	0.44 ± 0.063	0.19 ± 0.01	0.11 ± 0	0.1 ± 0.016
Pt/TS6	0.41 ± 0.114	0.18 ± 0.039	0.13 ± 0.066	0.12 ± 0.054

Acknowledgements

First of all, I would like to thank my supervisor Prof. Dr. Dominik Eder for giving me the opportunity to work in his research group. I am grateful for his support, helpful advice, and fruitful discussions along my PhD study. I also would like to thank Prof. Dr. Roland Marschall and Prof. Dr. Jürgen Fleig for the time they will spend reading and evaluating this thesis.

I want to thank several group mates for their help with some characterization techniques and sharing theoretical knowledge: Shaghayegh for BET, and Pablo for TXRF, and Greta and Jasmin for XPS and their optimistic and relaxed view on my results. I also want to thank Jakob Blaschke for many measurements done during his research internship, and for building and optimizing the in-situ DRIFTS setup for CO₂ reduction; it was a long and difficult process, and it was, sadly, not finished in time to contribute to this thesis.

Furthermore, I want to thank the whole group for the friendly and positive working atmosphere, their support and their entertainment.

I especially want to thank my best friend Aida for proofreading my thesis, again, and her motivating comments, such as "very entertaining!", "interesting!" and "AHA!".

Last but not least, I would like to thank my whole family, friends and flatmates for their support and motivation, especially in the last weeks.



Die approbierte gedruckte Originalversion dieser Dissertation ist an der TU Wien Bibliothek verfügbar.
The approved original version of this doctoral thesis is available in print at TU Wien Bibliothek.

Giesriegl Ariane

Curriculum Vitae



Info

Name Ariane Giesriegl
Birth: 24. November 1988, Vienna, Austria

Education

- 2017–today **PhD student**, *Vienna University of Technology*, Vienna, Austria.
2014–today **Bachelor student of Physics**, *Vienna University of Technology*, Vienna, Austria.
2012–2015 **Master student of Chemistry**, *University of Vienna*, Vienna, Austria.
2008–2012 **Bachelor student of Chemistry**, *University of Vienna*, Vienna, Austria.

Experience

- 2017–today **University assistant**, *VIENNA UNIVERSITY OF TECHNOLOGY*, A-1010 Vienna.
2013–2016 **Research & Development**, *QUANTARED TECHNOLOGIES GMBH*, A-1100 Vienna.
2012–2013 **Chemical Technical Assistant**, *INSTITUTE OF PHYSICAL CHEMISTRY, UNIVERSITY OF VIENNA*, A-1090 Vienna.

Academic publications:

- o P. Ayala, A. Giesriegl, S. P. Nandan, S. N. Myakala, P. Wobruschek, A. Cherevan*, “Isolation Strategy towards Earth-Abundant Single-Site Co-Catalysts for Photocatalytic Hydrogen Evolution Reaction“, **Catalysts** 11, 417 (2021)
- o J. S. Schubert, J. Popovic, G. M. Haselmann, S. P. Nandan, J. Wang, A. Giesriegl, A. S. Cherevan, D. Eder*, “Immobilization of Co, Mn, Ni and Fe oxide co-catalysts on TiO₂ for photocatalytic water splitting reactions“, **J. Mater. Chem. A** 7, 18568-18579 (2019)
- o A. Giesriegl, J. Blaschke, S. Naghdi, D. Eder*, “Rate-Limiting Steps of Dye Degradation over Titania-Silica Core-Shell Photocatalysts“, **Catalysts** 9, 583 (2019)

- o T. O. Nagy, U. Pacher, A. Giesriegl, M. J. J. Weimerskirch, W. Kautek*, “Depth profiling of galvanoaluminium–nickel coatings on steel by UV- and VIS-LIBS”, **Appl. Surf. Sci** 418, 508-516 (2017)
- o T. O. Nagy, U. Pacher, A. Giesriegl, L. Soyka, G. Trettenhahn, W. Kautek*, “Laser-induced electrochemical de- and repassivation investigations on plasma-oxidized aluminium alloys”, **Appl. Surf. Sci** 302, 184 (2014)